Alma Mater Studiorum – Università di Bologna

DOTTORATO DI RICERCA IN

FISICA

Ciclo XXIV

Settore Concorsuale di afferenza: 02/A1

Settore Scientifico disciplinare: FIS/04

Study of the X(3872) state with the CMS Experiment at LHC

Presentata da: Dott. Daniele Fasanella

Coordinatore Dottorato **Relatore**

Prof. Fabio Ortolani **Chiar.mo Prof. Antonio Maria Rossi**

Esame finale anno 2012

Contents

Introduction

At the end of 2009 the world's largest and highest-energy particle accelerator, the Large Hadron Collider (LHC), started its operations at the CERN laboratories in Geneva. The scope of this accelerator is to answer some of the fundamental open questions in physics, concerning the basic laws governing the interactions and forces among the elementary particles. LHC has already provided 2 years of proton-proton collisions at a center-of-mass energy of 7 TeV to the experiments placed at its four interaction points. One of the main experiments is CMS (Compact Muon Solenoid), a general purpose detector projected to address a wide range of physical phenomena, in particular the search of the Higgs boson,the only still unconfirmed element of the Standard Model (SM) of particle interactions and, new physics beyond the SM itself. Main features of CMS are a superconducting solenoid magnet, providing a field of 3.8 T, an inner tracking detector able to reconstruct charged tracks and primary and secondary vertexes with high resolution, and a efficient and redundant muon spectrometer located in the return yoke of the magnet.

I've started my Ph.D in the CMS Collaboration in 2009 when the detector was still in its commissioning phase. My activities inside the Collaboration have covered many aspects ranging from the operation of the Drift Tube (DT) Detector to data analysis. The DTs are a gaseous detector for the measure of muons in the central part of CMS. I've become one of the experts for its hardware maintenance and the responsible for the software that controls its very complex powering system (composed by more than 14000 high and low voltage channels). I've also worked for the development of the software for the triggering and reconstruction of muons tracks.

During 2010 I started to work in the CMS group dedicated to the study of quarkonium, which has an important role as a probe to improve the understanding of Quantum ChromoDynamics (QCD) theory. In the last years many new particles have been discovered in the charmonium mass range. The first of these states was announced by the Belle experiment in 2003, where a new resonance was found in the $J/\psi\,\pi^+\pi^-$ spectrum with an invariant mass of about 3872 MeV/c^2. This announcement was very surprising because it was soon realized that the apparent quantum numbers, mass and decay patterns of this new state, called $X(3872)$, were not compatible with a standard charmonium state interpretation. Many new theoretical models have been developed in order to explain the $X(3872)$ nature, but no one can account all its properties and additional experimental studies are needed.

The results on the $X(3872)$ obtained at Tevatron have shown the great contribution that can be given in this kind of study by hadron collider experiments. Even if designed to study higher energy physics, the features of the CMS experiment make it an good instrument for the study of the X(3872) in its $J/\psi\,\pi^+\pi^-$ decay channel. In fact, in CMS interesting events can be easily identified thanks to the subsequent decay of J/ψ in a pair

of muons.

In this thesis are reported the studies I made on the $X(3872)$ using the data collected by the CMS experiment in the first two years of operations, when the low LHC luminosity has been used to collect large samples of low energy physics data.
This document is organized as follows. Chapter 1 proposes a wide review of the actual experimental knowledge on $X(3872)$ and of the main theoretical models proposed. A brief review is made of the basic concepts of Quantum Chromodynamics in order to better understand how regular mesons are described and why the $X(3872)$ features are so puzzling. Among the alternative models I will focus on the molecular and the tetraquark hypothesis that seem the more promising.

In Chapter 2 is presented a general description of the experimental apparatus, comprising the LHC accelerator and the CMS experiment. Particular focus is posed on the characteristics of proton-proton collisions.

I have studied the $X(3872)$ in the $J/\psi\,\pi^+\pi^-$ decay channel. In the CMS experiment pions are reconstructed as charged particles in the inner tracker, while muons are also detected in the external muon spectrometer. Chapter 3 will focus on how this reconstruction is made, and particular detail is given on the muon trigger, that has an important role in my analysis.

In the 4th chapter is described my analysis on the $X(3872)$ with all the data collected by the CMS experiment, equivalent to 40 nb^{-1}. Taking advantage of the whole acceptance region of the detector, a clear peak of the $X(3872)$ containing about 500 candidates has been found. With these data I performed the measurement of the cross section ratio of the $X(3872)$ with respect to the $\psi(2S)$, a charmonium meson which decays as the $X(3872)$ into $J/\psi\,\pi^+\pi^-$. The analysis reported here has been the first one of this kind on the $X(3872)$. I've taken care of the approval inside the CMS Collaboration and made the first public presentation of the results. This analysis has been made available as a public document by the CMS Collaboration.

In 2011 LHC has ramped up it's instantaneous luminosity and new strategies had to be developed to continue the study on the $X(3872)$. In fact more than $5fb^{-1}$ of data have been delivered to the CMS experiment, but the higher instantaneous luminosity forced to drop part of the produced J/ψ. With the 2011 data I've worked on expanding the study done in 2010, thanks to the higher statistics (more than 11.000 $X(3872)$ candidates have been reconstructed). Using a similar method, the cross section ratio measurement between $X(3872)$ and $\psi(2S)$ has been repeated as a function of the transverse momentum in a reduced kinematic region.

Experiments at Tevatron have shown that the production of $X(3872)$, like for the other charmonium state, is composed by a prompt component and a non-prompt one, the latter arising from the decay of B-hadron. In Chapter 6 is detailed the method I used for separating these two components for the $X(3872)$ reconstructed during 2011. This is the first measurement of the non-prompt component of the $X(3872)$ performed as a function of its transverse momentum. The content of chapters 5 and 6 is under internal review from the Collaboration, and will be proposed for a publication in the next months.

Finally a Summary of the results is proposed, containing also the prospectives for future study on the $X(3872)$ with CMS.

Chapter 1

The X(3872): a theoretical and experimental review

The X(3872) is a new state discovered by the Belle experiment in 2003. It has attracted much theoretical interest because its properties don't match any expected state of quarkonium spectroscopy and has opened the possibilities to more "exotic" interpretations. In this chapter it will be first briefly reviewed the concepts of the Standard Model and the Quark Model, with particular emphasis on the $c\overline{c}$ meson. The known experimental facts on the X(3872) and the proposed theoretical models will be reviewed.

1.1 Review of Standard Model concepts

The Standard Model (SM) of particle physics is a gauge theory of the elementary particles that describes the interactions of three of the four fundamental forces of nature: the electromagnetic and weak forces, which are unified as the electroweak interaction at high energy, and the strong interaction. It's among the most successful achievements of modern science being able to explain a wide range of experimental facts passing precise test at the 0.1% to 1% level.

1.1.1 Fundamental particles and forces

Within the Standard Model, nature is described using half-integer (fermionic) and integer (bosonic) fields whose quantization implies the existence of point-like particles. Matter is described by elementary spin $\frac{1}{2}$ fermions of two kinds: leptons and quarks. There are three generations of quarks, each one made of an up-type quark (up, charm and top) and a down-type quark (down, strange and bottom). The leptons also come in three flavours with their corresponding neutrinos: the electron, the muon and the tau. Corresponding elements in different generations of the same family have an equal electric charge, but different masses.

The properties of quarks and leptons are reported in Table 1.1. Each of these twelve elementary particles is associated to a corresponding anti-particle of opposite electric charge. In the SM, the neutrinos are predicted to be massless. However, observations of neutrino flavour oscillations have demonstrated that neutrinos have small, but non-zero,

	First Generation	Second Generation	Third Generation	Q
Quarks	Up (u) $1.7 < m_u < 3.3\, MeV/c^2$	Charm (c) $m_c = (1.27^{+0.07}_{-0.09})\, GeV/c^2$	Top (t) $m_t = (172.0 \pm 0.9) GeV/c^2$	$\frac{2}{3}$
	Down (d) $4.1 < m_d < 5.8\, MeV/c^2$	Strange (s) $m_s = 101^{+29}_{-21}\, MeV/c^2$	Botton (b) $m_b = 4.19^{+0.18}_{-0.06}\, GeV/c^2$	$-\frac{1}{3}$
Leptons	Electron (e) $m_e = 0.51\, MeV/c^2$	Muon (μ) $m_\mu = 105.66\, MeV/c^2$	Tau (τ) 1776.82 ± 0.16	-1
	Electron Neutrino (ν_e)	Muon Neutrino (ν_μ)	Tau Neutrino (ν_τ)	0

Table 1.1: *Quark and lepton Families and their electric charge Q and masses. Quark masses are model-dependent estimates. Neutrinos are considered massless in the SM and, even if later experimental results suggest they are massive, their mass is below 2 eV [66]*

mass differences. However, only upper limits on the absolute masses have been obtained. In any case, the SM needs an extension to explain neutrino's non-zero masses.

The interaction between particles arises asking the invariance of the field Lagrangian under $SU(3)_C \oplus SU(2)_L \oplus U(1)_Y$ gauge transformations, where $SU(3)_C$ is responsible of the strong (colour) interaction while $SU(2)_L \oplus U(1)_Y$ describes the electroweak sector of the SM on the basis of left-handed lepton doublets and hypercharge singlets. The interactions are described in term of exchange of bosons which are the carriers of the fundamental forces. The main characteristic of bosons and corresponding interactions are summarised in Table 1.2. Quarks are subject to all forces, while leptons interact only through electroweak forces.

	Electromagnetic	Weak		Strong
Boson Carrier	Photon γ	$W^\pm$	Z	Gluons (g)
Mass $[GeV/c^2]$	0	80.399 ± 0.023	91.1876 ± 0.0021	0
Coupling Constant	$\alpha(Q^2 = 0) \approx \frac{1}{137}$	$\frac{G_F}{(\hbar c)^3} \approx 1.2 \cdot 10^{-5} GeV^{-2}$		$\alpha_s(m_Z) \approx 0.1$
Range [cm]	∞	10^{-16}		10^{-13}

Table 1.2: *Fundamental interactions in the Standard Model and corresponding carriers*

Mixing between quark generation is explained using the CKM (Cabibbo-Kobayashi-Maskawa) mechanism and further separation between weak and electromagnetic interactions is obtained introducing a spontaneous-symmetry-breaking mechanism, known as Higgs mechanism, which is also responsible of the generation of the masses of the weak interacting vector bosons. The adoption of spontaneous-symmetry-breaking allows to preserve the gauge invariance of the theory that would be manifestly violated in the case of the insertion of ad-hoc mass terms in the field lagrangians. Moreover, as a consequence of the Higgs mechanism, the existence of a scalar bosonic particle, the Higgs boson, is predicted.

Three discrete symmetries play an important role in the Standard Model. Parity P represents a space inversion, where the three spatial coordinates are reversed. Charge conjugation C interchanges a particle with its own anti-particle. The third discrete symmetry is the time-reversal transformation T. Parity is known to be maximally violated by the weak interaction, which only couples left-handed components of particles and right-handed components of anti-particles. The weak interaction also maximally violates C, because a left-handed particle is transformed into a left-handed anti-particle, which doesn't interact with the weak interaction mediators. The violation of the CP conjugated

symmetry has been observed in the neutral kaon decay $K_L \rightarrow \pi^+\pi^-$, mediated by the weak interaction.

There is however one symmetry which is conserved by all interactions, it's the CPT, the operation by which space and time are reversed at the same time as particles are changed into their anti-particles. The CPT theorem states that any Lorentz invariant local quantum field theory with a Hermitian Hamiltonian must have CPT symmetry. This fundamental symmetry implies that the masses and lifetimes of a particle and the corresponding anti-particle are equal, and that their charges are of equal value with an opposite sign. Finally, as a consequence of the CPT invariance and the violation of the CP symmetry by the weak interaction, the T symmetry is also expected to be violated.

1.1.2 Quantum ChromoDinamics

The strong interaction is so defined due to the fact that it couples particles with a strength 10^2 times larger than the electromagnetic force and 10^{13} times larger than the weak interaction. It is also called the nuclear force as it is responsible for the cohesion of quarks in the hadrons and of hadrons together, like the neutrons and the protons in an atomic nucleus. The behaviour of strong interaction is modelled by a $SU(3)_C$ gauge theory named Quantum ChromoDynamics (QCD). Quarks have an additional freedom (or one property, more exactly speaking) named colour which is the charge of strong interaction.

Each quark carries one different colour, which could be red(r), green(g), blue(b), anti-red($\overline{r}$), anti-green($\overline{g}$) and anti-blue($\overline{b}$). Sum of the three colours or three anti-colours leads to white (neutral-colour). So does the combination of one colour and its anti-colour.

Quarks have, by convention, positive parity, while antiquarks have negative parity. For quarks are also defined an addictive baryon number $\frac{1}{3}$ ($-\frac{1}{3}$ for antiquarks) and addictive quantum numbers reflecting their flavour. These quantum numbers are related to the charge Q (in units of the elementary charge e) through the generalized Gell-Mann-Nishijima formula

$$Q = I_z + \frac{\mathbf{B} + S + C + B + T}{2} \tag{1.1}$$

where **B** is the baryon number. The convention is that the flavour of a quark (I_z, S, C, B, or T) has the same sign as its charge Q. The strong force is mediated between quarks by eight massless and electrically neutral gluons, which carry both colour and anti-colour. Carrying colour charge, gluons can interact among themselves.

There are two important properties in QCD, asymptotic freedom and colour confinement. The asymptotic freedom means that quarks and gluons will have arbitrarily weak interactions at short distances and high energy scale, i.e. they act as free particles. The asymptotic freedom determines that the renormalized QCD coupling is small in high energy collisions, which could so be described by perturbation theory. The colour confinement refers to the fact that interactions between quarks increase sharply with distance. Thus, colour confinement forbids the existence of any free quarks because the energy to separate two quarks is bigger than the energy needed to produce a new pair of quark-antiquark out of the vacuum. All particles that can be observed are colour-neutral, meaning that quarks are always observed in bound states, called hadrons. The Quark Model is the theory which describes the static composition of hadrons. In order to have colourless states, quarks can combine in groups of three, named barions (where

each quark has a different colour), or two, called mesons (composed by a quark and an anti-quark with the same colour).

1.1.3 Mesons

Mesons are bosons made of a quark q and an anti-quark $\overline{q}'$ (q and q' can have different flavour), so their baryon number is 0 [66]. If the orbital angular momentum of the $q\overline{q}'$ state is ℓ, then the parity P is $(-1)^{\ell+1}$. The meson total angular momentum J is given by $|\ell - s| \leq J \leq |\ell + s|$, where the spin s is 0 (antiparallel quark spins) or 1 (parallel quark spins). The charge conjugation, or C-parity, $C = (-1)^{\ell+s}$, is defined only for the $q\overline{q}$ states made of quarks and their corresponding antiquarks. The C-parity can be generalized to the G-parity, $G = (-1)^{I+\ell+s}$, for mesons made of quarks and their corresponding antiquarks (isospin $I_z = 0$), and for the charged $u\overline{d}$ and $d\overline{u}$ states (isospin $I_z = 1$).

The mesons are classified in J^{PC} multiplets. The $\ell = 0$ states are the pseudoscalars (0^{-+}) and the vectors (1^{--}). The orbital excitations $\ell = 1$ are the scalars (0^{++}), the axial vectors (1^{++}) and (1^{+-}), and the tensors (2^{++}). Radial excitations are denoted by the principal quantum number n. The very short lifetime of the t quark makes it likely that bound-state hadrons containing t quarks and/or antiquarks do not exist. States in the natural spin-parity series $P = (-1)^J$ must, according to the above, have s = 1 and hence, $CP = +1$. Thus, mesons with natural spin-parity and $CP = -1$ ($0^{+-}, 1^{-+}, 2^{+-}, 3^{-+}$, etc.) are forbidden in the $q\overline{q}'$ model. The $J^{PC} = 0^{--}$ state is forbidden as well.

Lattice calculations predict the spectrum of bound states in QCD from first principles, beginning with the Lagrangian of full QCD or of various approximations to it. In QCD, the field variables correspond to gauge fields and quark fields. In a lattice calculation, the lattice spacing (which serves as an ultraviolet cutoff) and the (current) quark masses are inputs; hadron masses and other observables are predicted as their functions. The lattice spacing is unphysical, and it is necessary to extrapolate to the limit of zero lattice spacing. Lattice predictions are for dimensionless ratios of dimensionful parameters (like mass ratios), and predictions of dimensionful quantities require the use of one experimental input to set the scale. Interpolation or extrapolation of lattice results in the light quark masses involves formulas of chiral perturbation theory. Calculations with heavy quarks typically use Non-Relativistic QCD (NRQCD) or Heavy Quark Effective Theory (HQET), which are systematic expansions of the QCD Lagrangian respectively in powers of the heavy quark velocity, or the inverse heavy quark mass. Terms in the Lagrangian have obvious quark model analogs, but are derived directly from QCD. The heavy quark potential is a derived quantity, measured in simulations.

1.1.4 Charmonium

The bound state of two charm quarks is usually named charmonium. The first charmonium state, the J/ψ, was discovered in November 1974 simultaneously at Brookhaven [65] and SLAC [68]. This discovery has been of pivotal importance for the development of the Standard Model of particles. On one hand its existence confirmed the GIM [71] prediction of a fourth quark, the charm. On the other hand, the impressive narrowness of the J/ψ peak (about 90keV) was realized to be the footprint of the asymptotic freedom of quan-

tum chromodynamics. Thus, the J/ψ discovery opened a new route to the theory of weak interactions and pointed to the most striking feature of the theory of strong interactions, namely the quark freedom on very short scales.

The charmonium system has become the prototypical hydrogen atom of meson spectroscopy and information on quarkonium levels has grown to the point that more is known about the $c\bar{c}$ system than about its namesake positronium, the bound state of an electron and a positron.

The reduced mass system of the two charm quarks is subject to a central potential which has an approximately Coulomb form at small distances [2],

$$V(r) \sim -\frac{4}{3}\frac{\alpha_S(1/r^2)}{r} \tag{1.2}$$

and is confining at large distances

$$V(r) \sim Kr \tag{1.3}$$

where K is the string tension. The experimentally clear spectrum of relatively narrow states below the open-charm threshold of 3.73 GeV can be easily identified with $c\bar{c}$ levels predicted by this kind of potential models. Spin-dependent interquark forces are evident in the splitting of states within these multiplets, and the observed splittings are consistent with the predictions of a one gluon exchange (OGE) Breit-Fermi Hamiltonian, combined with a linear scalar confining interaction.

The open-charm threshold value is twice the mass of the lightest charmed particles, which are the D-mesons. Charmonium states which lay above this threshold are expected to be broad resonances which decay rapidly into pairs of charmed particles, through a mechanism involving the creation of a light quark-antiquark pair. In contrast, below this threshold, the charmonium state decays much more slowly to non charmed hadrons (or leptons) through a mechanism involving the annihilation of the charmed quark-antiquark pair. The suppression of processes involving the creation or annihilation of $c\bar{c}$ and $b\bar{b}$ pairs, as opposed to those involving the creation or annihilation of light quark-antiquark pairs ($u\bar{u}$, $d\bar{d}$. $s\bar{s}$) is a general characteristic of strong iterations. It is often referred to as the OZI rule, after Okubo, Zweig and Izuka. It does not apply to weak or electromagnetic interactions.

The present status of charmonium levels is shown in Fig. 1.1.The levels are labelled by S, P, D, corresponding to relative orbital angular momentum L = 0, 1, 2 between quark and antiquark. (No candidates for $L \geq 3$ states have been seen yet). The spin of the quark and antiquark can couple to either S = 0 (spin-singlet) or S = 1 (spin-triplet) states. The parity of a quark-antiquark state with orbital angular momentum L is $P = (-1)^{L+1}$; the charge-conjugation eigenvalue is $C = (-1)^{L+S}$. Values of J^{PC} are shown at the bottom of each figure. The states are often denoted by $^{2S+1}[L]_J$, with [L]= S, P, D.... Thus, L=0 states can be $^1S_0$ or $^3S_1$; L=1 states can be $^1P_1$ or $^3P_{0,1,2}$; L = 2 states can be $^1D_2$ or $^3D_{1,2,3}$, and so on. The radial quantum number is denoted by n.

The direct charmonium production over a wide range of environments (leptons and hadrons collisions or photo-production) is given by the Colour Singlet Model (CSM), developed since the 1980. For example, in the CSM model the J/ψ production is described in two steps: at first the charmonium state is produced with a quantum number in a colour singlet state, and then it is calculated the binding of the $c\bar{c}$ into charmonium

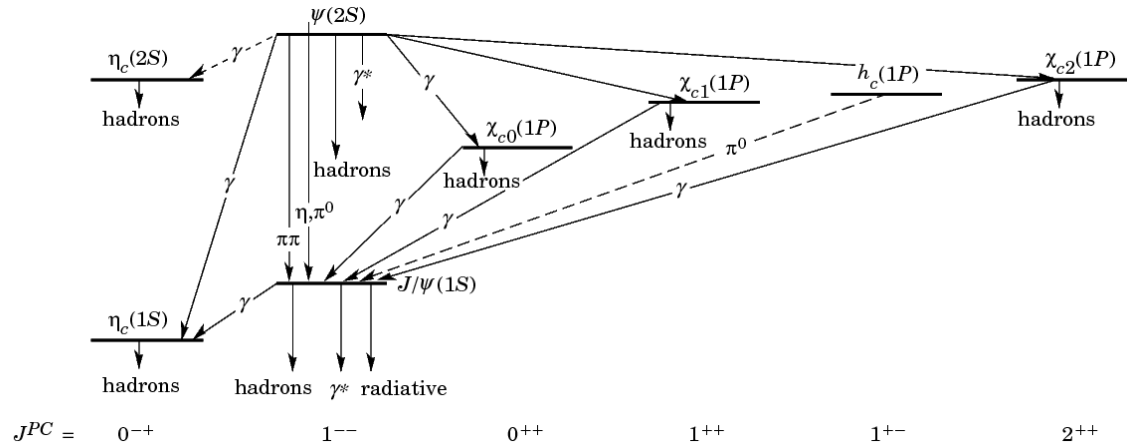

Figure 1.1: *Charmonium levels spectrum and decays [67]*

state. The CSM model can predict the radiative decay of the charmonium states, such the $\chi_{cn} \to J/\psi + \gamma$.

Another way to compute the production is performed by the Non Relativistic QCD, NRQCD [**?**]. This theory treats the quarkonium state as a non relativistic system. The production is achieved in two steps: first the perturbative level generation and then the evolution to colourless meson through a gluon emission at non perturbative domain. The $c\bar{c}$ is produced often as a colour octet state, and this also gives the name of Colour Octet Mechanism (COM) to the model. The matrix elements used in this model calculations greatly increase the predictive power of the NRQCD and leave the calculation process independent.

Charmonium is also produced by the decay of particles containingthe b quark: ($B \to c\bar{c} + other$). The relatively long lifetime of the b hadrons moves the decay vertex to few mm from the interaction point. This allows the identification of the secondary vertex of the decay.

1.2 Established experimental results on X(3872)

The $X(3872)$ was the first state that was found not to fit in charmonium spectroscopy. It was initially observed by the Belle experiment in $B \to X(3872)\, K$, in the decay channel $X(3872) \to J/\psi\, \pi^+\pi^-$ (Fig. 1.2 [37]). It was later confirmed by BaBar [26] and in inclusive hadronic $p\bar{p}$ production by CDF [17] [14] [10] and $D\emptyset$ [11] (see Fig. 1.3). It has been widely studied, but yet its interpretation demands much more experimental attention. Its apparent quantum numbers, mass, and decay patterns make it an unlikely conventional charmonium candidate, and no consensus explanation has been found([32, 55, 86].

1.2.1 X(3872) Decay channels

The $X(3872)$ has been firstly observed decaying into $J/\psi\, \pi^+\pi^-$. This channel is easy to identify also in hadronic collision thanks to the subsequent decay of the J/ψ in 2 muons. Studies made on the dipion mass distribution by CDF [13] and Belle [38] favours high $M_(\pi^+\pi^-)$ values. This is not atypical for charmonium states (cf. $\psi(2S) \to J/\psi\, \pi^+\pi^-$),

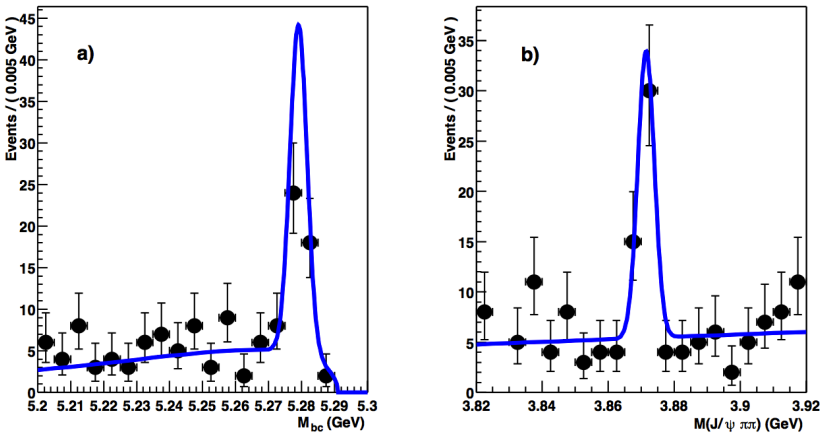

Figure 1.2: *Discovery of X(3872) in the $B \to J/\psi\,\pi^+\pi^- K$ channel by Belle. Mass Spectrum of a) M_b, b) $M_{J/\psi\pi^+\pi^-}$ for the $X(3872) \to J/\psi\,\pi^+\pi^-$ signal region. The curves are the results of unbinned fits [37].*

but could be an indication that the pion pair might even be produced in a ρ configuration; if that were indeed the case the X(3872) could not be a charmonium state.

Belle also provided a measurement of the relative $B^{/pm}$ branching fraction:

$$\frac{\mathcal{B}(B^\pm \to X(3872)K^\pm)\cdot\mathcal{B}(X(3872)\to J/\psi\,\pi^+\pi^-)}{\mathcal{B}(B^\pm \to \psi(2S)\,K^\pm)\cdot\mathcal{B}(\psi(2S)\ \to J/\psi\,\pi^+\pi^-)} = 0.063 \pm 0.012\,(stat) \pm 0.007\,(syst). \tag{1.4}$$

The decay $X(3872) \to J/\psi\,\pi^+\pi^-\pi^0$ was observed at a rate comparable to that of $J/\psi\pi^+\pi^-$ [12] with a statistical significance of 5.8σ. The relative width for this decay was found to be:

$$\frac{\Gamma(X(3872)\to J/\psi\,\pi^+\pi^-\pi^0)}{\Gamma(X(3872)\to J/\psi\,\pi^+\pi^-)} = 0.8 \pm 0.3\,(stat) \pm 0.1\,(syst). \tag{1.5}$$

The $M_{\pi^+\pi^-\pi^0}$) distribution is concentrated at the highest values, coinciding with the kinematic limit, which spurred speculations that the decay might proceed through (the low-side tail of) an ω. This decay has been confirmed also by BaBar [52]. Both Belle [87] and BaBar [27] have reported X(3872) signals in the $D^{*0}\overline{D^0}$ final state with branching fractions about ten times higher than for $J/\psi\,\pi^+\pi^-$.

Using a data sample of 465 million $B\overline{B}$ pairs, BaBar searched for $B \to c\bar{c}\,\gamma K$ decays and found evidence for $X(3872) \to J/\psi\,\gamma$ and $X(3872) \to \psi(2S)\,\gamma$ with $3.6\,\sigma$ and $3.5\,\sigma$, respectively [28]. They measured the product of branching fractions

$$\mathcal{B}(B^\pm \to X(3872)K^\pm)\cdot\mathcal{B}(X(3872)\to J/\psi\,\gamma) = (2.8 \pm 0.8 \pm 0.1)\times 10^{-5} \tag{1.6}$$

and

$$\mathcal{B}(B^\pm \to X(3872)K^\pm)\cdot\mathcal{B}(X(3872)\to \psi(2S)\gamma) = (9.5 \pm 2.7 \pm 0.6)\times 10^{-6} \tag{1.7}$$

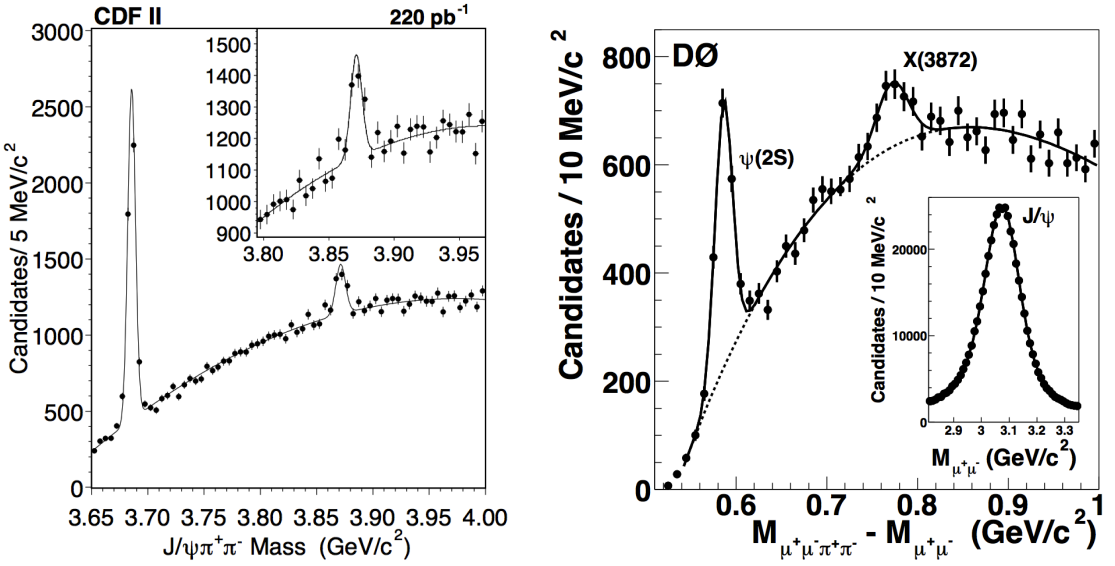

(a) (b)

Figure 1.3: *Observation of X(3872) in $p\bar{p}$ collisions. On (a) the $J/\psi\,\pi^+\pi^-$ invariant mass distribution for X(3872) candidates at the CDF experiment, on (b) the same spectrum at the DØ experiment.*

and obtained the ratio

$$\frac{\mathcal{B}(X(3872) \to \psi(2S)\,\gamma)}{\mathcal{B}(X(3872) \to J/\psi\,\gamma)} = 3.4 \pm 1.4 \tag{1.8}$$

With 772 million $B\overline{B}$ events, Belle observed $X(3872) \to J/\psi\gamma$ in the charged decay $B^+ \to X(3872)K^+$, with a significance of 4.9σ, while in a search for $X(3872) \to \psi(2S)\gamma$ no significant signal was found [18]. They measured the branching fractions

$$\mathcal{B}(B^\pm \to X(3872)K^\pm) \cdot \mathcal{B}(X(3872) \to J/\psi\,\gamma) = (1.78^{+0.48}_{-0.44} \pm 0.12) \times 10^{-6} \tag{1.9}$$

and provided an upper limit on the branching fraction

$$\frac{\mathcal{B}(X(3872) \to \psi(2S)\gamma)}{\mathcal{B}(X(3872) \to J/\psi\,\gamma)} < 2.1\ (at\ 90\%\ CL). \tag{1.10}$$

While the result for $X(3872) \to J/\psi\gamma$ is consistent between the two experiments, the one for $X(3872) \to \psi'\gamma$ is in disagreement and new experimental study is needed. Belle has also set limits on other radiative decays in charmonium states [12]:

$$\frac{\Gamma(X(3872) \to \chi_{c1}\,\gamma)}{\Gamma(X(3872) \to J/\psi\,\pi^+\pi^-)} < 0.89\ (at\ 90\%\ CL) \tag{1.11}$$

$$\frac{\Gamma(X(3872) \to \chi_{c2}\,\gamma)}{\Gamma(X(3872) \to J/\psi\,\pi^+\pi^-)} < 1.1\ (at\ 90\%\ CL). \tag{1.12}$$

1.2.2 X(3872) Mass

CDF has reconstructed $\approx$ 6000 $X(3872)$ candidates with 2.4 fb^{-1} of data measuring a mass $M_X = 3871.61 \pm 0.16\,(stat) \pm 0.19\,(syst)\,MeV/c^2$, which is the most precise determination to date. In EPS2011, LHCb presented measurements of the X(3872) mass, with $M_X = 3871.97 \pm 0.46 \pm 0.1$ with 35 pb^{-1} of data. Belle also updated the mass and width measurements with 711 fb^{-1} data and set an upper limit on the decay width

$$\Gamma(X(3872)) < 2.3MeV\ (at\ 90\%\ CL). \tag{1.13}$$

A new world average, that includes these new measurements and other results using the $J/\psi\,\pi^+\pi^-$ decay mode, is $M_X = 3871.67 \pm 0.17 MeV/c^2$.

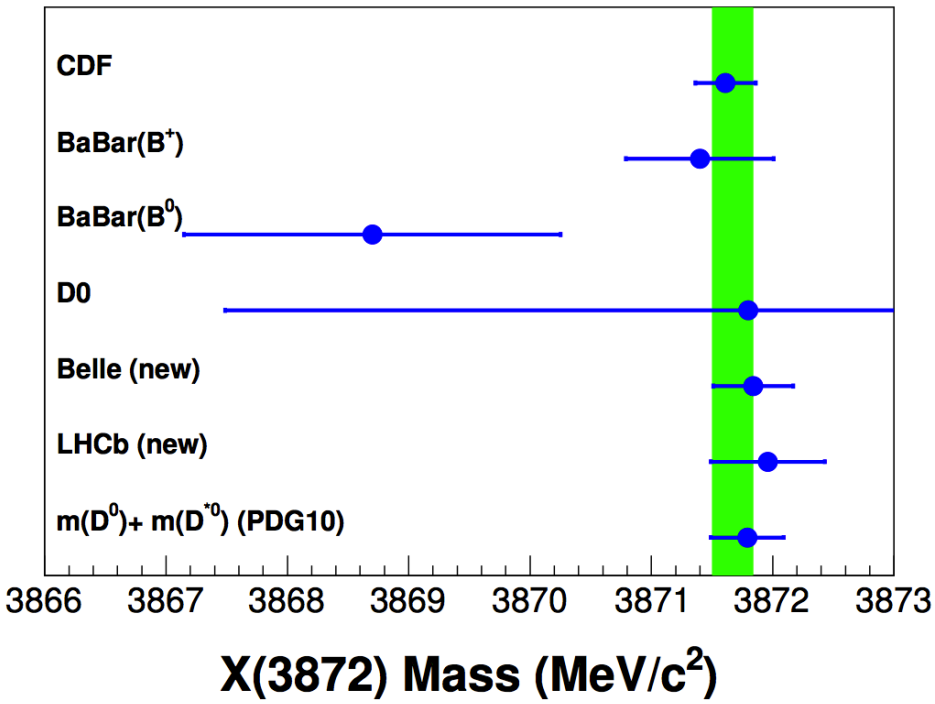

Figure 1.4: *Comparison of the mass measurements of the* $X(3872)$.

An important feature of the X(3872) is that its mass is close to the $D^{*0}\overline{D^0}$ threshold. This has opened to the interpretation of the X(3872) as a molecule-like arrangement comprised of D^{*0} and $\overline{D^0}$. Important for this idea is whether the X(3872) mass is above or below M(D^{*0}) + M($\overline{D^0}$). Taking the D^{*0} and $\overline{D^0}$ from the PDG [66],$M(D^{*0})+M(\overline{D^0}) = 3871.79 \pm 0.30 MeV/c^2$, that is 0.12 $\pm$ 0.35MeV/c^2 above the actual world average of the X(3872). The most updated results on the X(3872) mass are reported in Fig. 1.4.

Another actual problem on the measurement of the mass of the X(3872) is the discussion on whether there is more than one state with similar mass or not. The two options being investigated are that either the neutral and charged B mesons decay to different linear combinations of the two possible X states or that the two states decay into different final states (in particular $J/\psi\,\pi^+\pi^-$ and $D^{*0}\overline{D^0}$). The first possibility (different B^0 and $B^{\pm}$ decays) has been investigated by CDF [10], where the $J/\psi\,\pi^+\pi^-$ spectrum has been fitted searching for evidence of multiple structures. The negative result of such a

search has allowed to establish that the eventual two states would have a mass difference smaller than 3.2 MeV at 90% CL. BaBar and Belle have instead measured the masses of the states observed in B^0 and $B^{\pm}$ decays separately, arriving at similar conclusions, $\Delta M = 1.2 \pm 0.8 MeV$. Measuring the X mass with the $D^{*0}\overline{D^0}$ decay is considerably more challenging than with $J/\psi\,\pi^+\pi^-$, and has been performed by both BaBar and Belle.

The BaBar X mass from $D^{*0}\overline{D^0}$ decays resulted more than 3 MeV larger than the world average from $J/\psi\,\pi^+\pi^-$. This result engendered the speculation that the $D^{*0}\overline{D^0}$ enhancement might be a different state than the one observed in $J/\psi\,\pi^+\pi^-$, but the smaller value observed by Belle in $D^{*0}\overline{D^0}$ seems to make that possibility unlikely. The two $X(3872)$ mass measurements using $D^{*0}\overline{D^0}$ decays are inconsistent by 2.2σ, and are 1.8σ and 4.7σ higher than the $J/\psi\,\pi^+\pi^-$-based mass.

1.2.3 X(3872) Quantum Numbers

While the exact nature of the $X(3872)$ is still not been fully determined, most quantum numbers J^{PC} could be largely excluded. Angular distributions of $X(3872)$ decays were analyzed by CDF [14] yielding non-negligible probabilities only for 1^{++} and 2^{-+}. The Belle experiment claims to rule out all J^{PC} states except 1^{++} and 2^{++}. The existence of radiative decay modes in $J/\psi\,\gamma$ and not in $\chi_{c1}\,\gamma$ verifies a positive C-parity assignment. This fact also disfavours the 2^{-+} assumption, because this would involve a high-order multipole transition which would be more strongly suppressed than the observed rates allow. Also, the observation of decays into $D^0\overline{D^0}\pi^0$ [72] disfavours a 2^- assignment. This considerations led to several years in which the favored option has been $J^{PC} = 1^{++}$. Recently, in a comparison of the observed $M(3\pi)$ mass distribution with that of MC simulations in $X(3872) \to J/\psi\,\omega$ decay, BaBar found that the inclusion of one unit of orbital angular momentum in the $J/\psi\,\omega$ system, with its consequent negative parity, substantially improves the description of the data. Hence the X(3872) quantum number assignment of $J^{PC} = 2^{-+}$ is preferred in the BaBar analysis with respect to the 1^{++} hypothesis that has only 7.1% probability to match data (so not being ruled out).

1.2.4 X(3872) Production

Studies made by BaBar and Belle found no evidence of prompt production of the X(3872) in e^+e^- collisions. Both experiments have also estimated the ratio of branching fractions, Belle result is

$$\frac{\mathcal{B}(B^0 \to X(3872)K^0)}{\mathcal{B}(B^+ \to X(3872)K^+)} = (0.82 \pm 0.22 \pm 0.05) \tag{1.14}$$

while BaBar measures

$$\frac{\mathcal{B}(B^0 \to X(3872)K^0)}{\mathcal{B}(B^+ \to X(3872)K^+)} = (0.41 \pm 0.24 \pm 0.05). \tag{1.15}$$

It's interesting to compare the production characteristics of the $X(3872)$ to those of other charmonium states in B meson decays to have a better insight on its behaviour. One common characteristic of all of the known charmonium states that are produced in

B meson decays is that, when they are produced in association with a $K\pi$ pair, the $K\pi$ system is always dominated by a strong $K^*(890) \to K\pi$ signal.

Belle [19] studied the question of whether or not the $X3872$ tends to be produced more strongly in $B^0 \to K^{*0}X$ relative to nonresonant (NR) $B^0 \to (K^+\pi^-)_{NR}X$. Using $J/\psi\,\pi^+\pi^-$ decays, they limit the $K^{*0}/(K^+\pi^-)_{NR}$ ratio to be < 0.5 at 90% CL, contrasted with ratios closer to 3 for other charmonium states. The only search in $\gamma\gamma$ production has been performed by CLEO [53]. It did not return a signal and a limit was set:

$$(2J+1)\Gamma_{\gamma\gamma}\mathcal{B}(X(3872) \to J/\psi\,\pi^+\pi^-) < 12.9eV at 90\% CL. \tag{1.16}$$

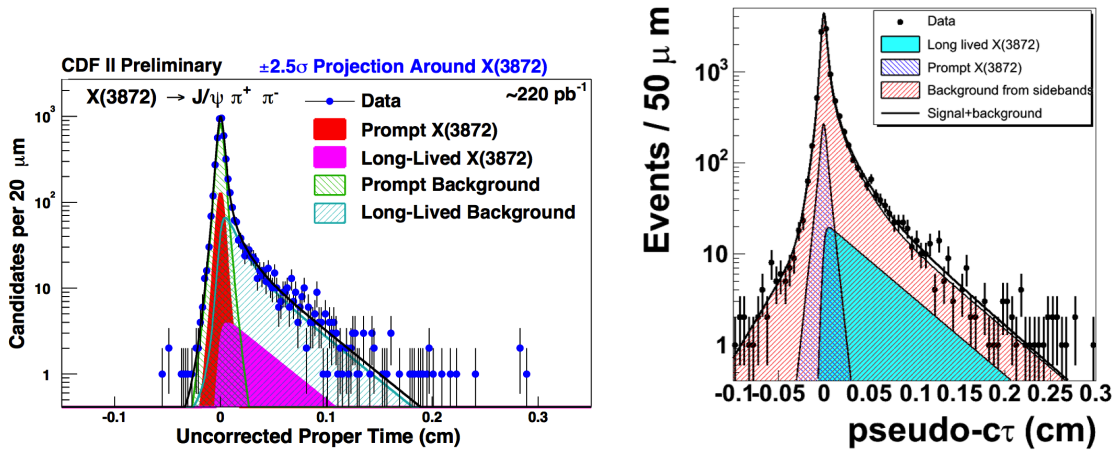

(a) (b)

Figure 1.5: *Lifetime distribution fits for CDF (a) and DØ (b)*

For what regards the hadron colliders, detailed studies at the Tevatron have shown that prompt production, i.e. without the typical lifetime signature indicating the presence of B-hadrons in the event, is actually dominant in $p\bar{p}$ collisions. Both $D\emptyset$ and CDF [3] measured the long-lived fraction for their sample of $X(3872) \to J/\psi\,\pi^+\pi^-$ with a pseudo-decay-length fit as showed in Fig. **??**. $D\emptyset$ obtained a non-prompt fraction of $30.0 \pm 6.66(stat)\%$ for the X(3872) (and $22.9 \pm 1.29(stat)\%$ for their $\psi(2S)$ in the same decay channel), while CDF obtained $16.1 \pm 4.9(stat) \pm 2.0(sys)$ % (to be compared to $28.3 \pm 1.0(stat) \pm 0.7(sys)\%$ for $\psi(2S)$).

1.3 Theoretical interpretations for the $X(3872)$

Starting from the experimental results is Section 1.2 many theoretical interpretations have been formulated on the true nature of the X(3872). Moreover, the X(3872) has been just the first of a wide range of new states discovered in the last years. Nowadays about 20 new states have been found above the open charm threshold, even if many of them still require confirmation. The widely studied X(3872) is therefore the starting point in the search for a theory able to describe this new chapter in QCD studies.

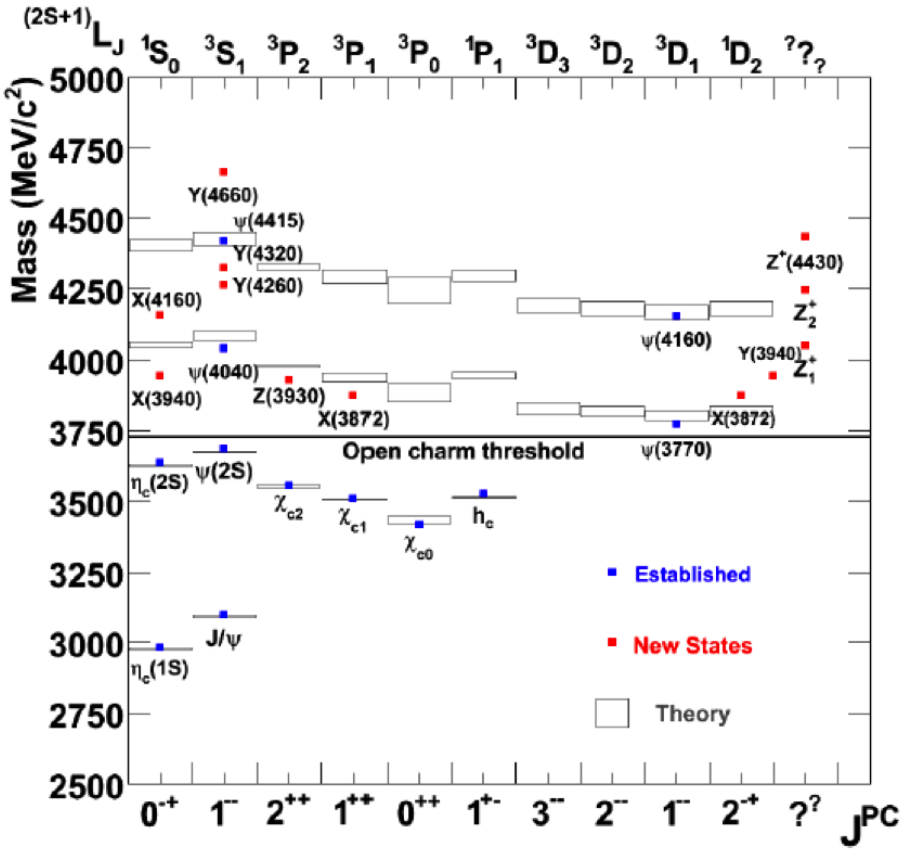

Figure 1.6: *The charmonium state spectrum from theory (see Chapter 1.1.4) and experimentally observed states [2]*

1.3.1 Charmonium interpretation

In Fig 1.6 are reported the theoretical states expected from the QCD $c\bar{c}$ model (see Section 1.1.4) in comparison to the experimentally observed ones. Below the open charm threshold the agreement with theory is strong, while just some on the new discovered states above it have a plausible charmonium assignment. In particular this is true for the $J^{PC} = 1^{--}$ family, produced at Belle and BaBar via e^+e^- annihilation (so their quantum number is the same that of the photon).

For the X(3872) observed spin-parity, only two charmonium assignements are still possible: $1^1D_{2^{-+}}$ and $2^3P_{1^{++}}$. The $1^1D_{2^{-+}}$ decay via the open-charm channel $D\overline{D}$ is suppressed due to spin-parity conservation. The positive C-parity of this state and the negative C-parity of the J/ψ ($J^{PC} = 1^{--}$) forces the pions in the decay $1^1D_{2^{-+}} \rightarrow J/\psi\,\pi^+\pi^-$ to have a negative C-parity, i.e. odd L. This needs to the necessity of having isospin I=0 in the final state, while the charmonium in the initial state has isospin I=0. So that the decay of $1^1D_{2^{-+}}$ into a $J^{PC} = 1^{--}$ breaks the conservation of isospin and the decay in $J/\psi\,\pi^+\pi^-$ should be highly suppressed. On the other hand this would force the decay through the weaker short-distance $c\bar{c}$ annihilation processes, radiative decays and closed-flavour hadronic transition, with a predicted total width of about 1 MeV, consistent with the observed one of the $X(3872)$. Also the predicted mass is near the $X(3872)$ one.

Against this interpretation there is also the fact that the isospin conserving decay to

$\eta_c\pi^+\pi^-$ has not yet been observed, and that it should be possible to produce it in $\gamma\gamma$ fusion where the X(3872) has not been found.

The predicted value for the $2^3P_{1^{++}}$ is about $80\,MeV/c^2$ higher then the observed mass of the X(3872), but if its mass is forced to be the experimental one ,it would have a narrow width of about 1-2 MeV. Other shortcomings of the $2^3P_{1^{++}}$ assignment include a small partial width to $J/\psi\,\pi^+\pi^-$ and dominant decay to $J\psi\,\gamma$ and $\psi(2S)\gamma$ in contradiction to Belle's results.

1.3.2 Molecular hypothesis

X(3872) mass lays very close to the $D^{*0}\overline{D^0}$ threshold, with a difference being compatible with zero. This characteristic leads many authors to identify the $X(3872)$ with a $D^{*0}\overline{D^0}$ molecule at threshold. Since $M_{X(3872)} < M_{\overline{D^0}} + M_{D^{*0}}$, in the $J/\psi\pi^+\pi^-$, the state could be considered as a proper bound state, i.e. with negative binding energy. On the other side this small binding energy would make this state very large in size: $4.9^{+13.4}_{-1.3}\,fm$, that is order of ten times bigger than the typical range of strong interactions. Relying on intuition, this feature, per se, would discourage to pursue the molecular picture of the $X(3872)$, also taking into account that this loosely bound state should rearrange its quarks to produce a $J/\psi\,\rho$ final state. This kind of interpretation is valid only for a $X(3872)$ with $J^{PC} = 1^{++}$ and would be ruled out by a definitive assignment of $J^{PC} = 2^{-+}$.

The particle content in the molecular model would be [25]:

$$X(3872) = \frac{1}{\sqrt{2}(D^{*0}\overline{D^0} + D^0\overline{D^{*0}}} \equiv (D^{*0}\overline{D^0})_+ \tag{1.17}$$

In this theoretical framework it would be also possible to explain a different measurement of the mass of $X(3872)$ in $J/\psi\pi^+\pi^-$ and $D^{*0}\overline{D^0}$ decays. The X lineshape in this decay mode is determined by the binding energy, the D^{*0} natural width and the natural width of the $X(3872)$ itself, which is at least as large as the D^{*0} width. Because the binding energy of the $X(3872)$ is less than 1 MeV, whether or not its mass peak is below $D^{*0}\overline{D^0}$ threshold, substantial fractions of the lineshape will lay both above and below that threshold. The portion of the X lineshape below $D^{*0}\overline{D^0}$ threshold, by definition, cannot decay to $D^{*0}\overline{D^0}$. However, $D^{*0}\overline{D^0}\gamma$ and $D^{*0}\overline{D^0}\pi^0$ final states are possible from decays of a bound, effectively off-shell, D^{*0}, as there is adequate phase space available above $D^{*0}\overline{D^0}\pi^0$ threshold. Due to imperfect experimental resolution, these final states are indistinguishable from $D^{*0}\overline{D^0}$ even though the D^{*0} decay products have masses below that of D^{*0}. Furthermore, the analysis procedure which mass-constrains a D^{*0} candidate in each event distorts the purported $X(3872)$ mass distribution for below-threshold decays. Conversely, that portion of the $X(3872)$ lineshape above $D^{*0}\overline{D^0}$ threshold can, of course, decay to $D^{*0}\overline{D^0}$, but the $D^{*0}\overline{D^0}$ mass distribution should, by definition, be exactly zero below threshold.

Therefore the kinematic constraint on the reconstructed $D^0\pi^0$ to the D^{*0}-mass, as carried out by Belle and BaBar, results in a broad $D^{*0}\overline{D^0}$ mass peak above threshold that should not be misconstrued as the true $X(3872)$ lineshape: neither the mass nor width results from $D^{*0}\overline{D^0}$ reflect the true mass or width of the $X(3872)$. Rather, the lineshapes for $J/\psi\,\pi^+\pi^-$, $D^{*0}\overline{D^0}$, and $D^{*0}\overline{D^0}\pi^0$(and $D^{*0}\overline{D^0}\gamma$) final states are related but slightly different from one another, as shown in Fig. 1.7.

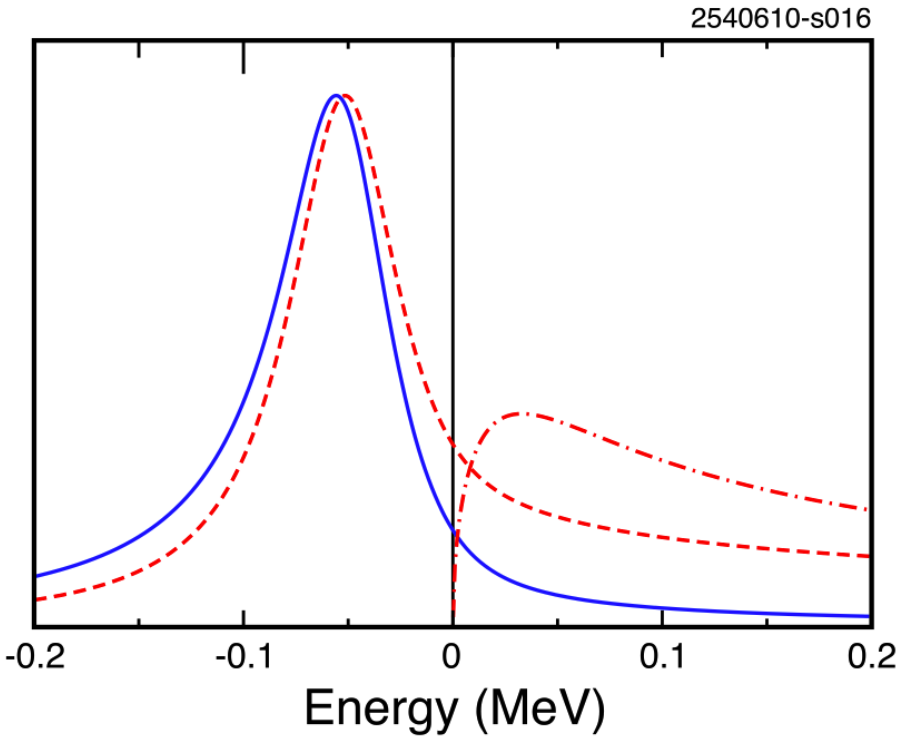

Figure 1.7: *The X(3872) lineshapes extracted from a fit to the Belle $D^{*0}\overline{D^0}$ events, unfolding the effects of experimental resolution, for $J/\psi\pi^+\pi^-$ (solid curve), $D^{*0}\overline{D^0}\pi^0$ (dashed), and, when always constraining one $D^0\pi^0$ pairing per event to a D^{*0} mass, $D^{*0}\overline{D^0}$(dot-dashed). The horizontal axis is the invariant mass of the decay products relative to $D^{*0}\overline{D^0}$ threshold, and the solid and dashed curves are normalized so as to have the same peak height [31]*

Another argument against this interpretation is its large prompt production cross section in hadron collisions. In fact the typical relative momentum between D^{*0} and $\overline{D^0}$ produced at high p_T in $p\overline{p}$ collisions is about 1.5 GeV, while the typical relative momentum between D^{*0} and $\overline{D^0}$ bound in the X(3872) is about 28 MeV. From naive calculation in this scenario, the expected cross section at Tevatron should have been 3 orders of magnitude less than the measured one.

Recent developments have nevertheless showed that, taking into account the large rescattering length in the near threshold phase space, this incompatibility can be overcome. In this scenario the prompt production of $X(3872)$ proceeds via the production of a charm-quark pair with small relative momentum (see Fig. 1.8) and it's possible to use NRQCD framework to factorize all the effects from momentum scales much smaller than M_c:

$$\sigma[(X(3872)] = \sum_n \hat{\sigma}[c\overline{c}_n] \left\langle \mathcal{O}_n^X \right\rangle \tag{1.18}$$

Using this model in the NRQCD framework and renormalizing using Tevatron result, prediction on the expected production cross section at LHC has been made [25]. For CMS and Atlas a phase space for $X(3872)$ with $p_T > 5GeV/c$ and a rapidity range $|y| < 2.4$ is considered. The p_T distributions integrated over the rapidity and the rapidity distributions integrated over p_T are shown in Fig. 1.9. Two hypothesis are considered (see

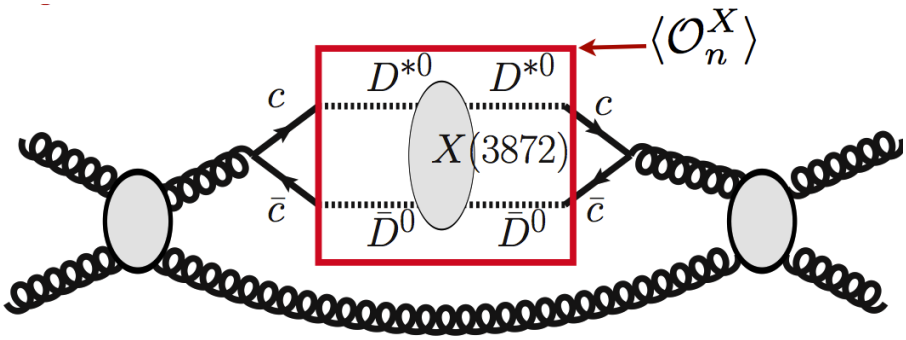

Figure 1.8: *Scheme for the production of the prompt production of the $X(3872)$ from rescattering of $c\bar{c}$ [31]*

also charmonium production at the end of Section 1.1.4):

- S-wave dominance. The X(3872) is equally likely to be formed from any $c\bar{c}$ pair that is created with small relative momentum in a S-wave state, regardless of the colour or spin state of the $c\bar{c}$ pair.

- Colour-octet $^3S_1$ dominance. The X(3872) can be formed only from a $c\bar{c}$ pair that is created with a small relative momentum in a colour-octet $^3S_1$ state.

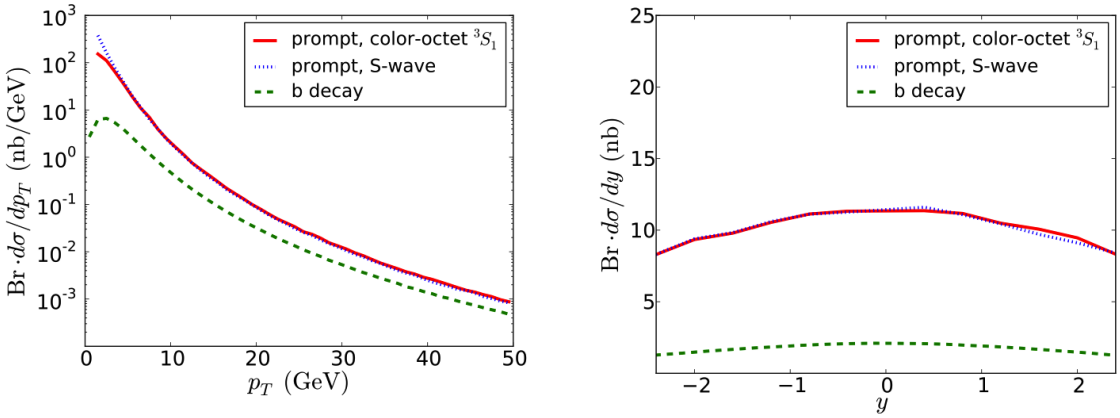

Figure 1.9: *Cross sections for $X(3872) \to J/\psi\pi^+\pi^-$ in pp collisions at $\sqrt{s} = 7\,TeV$. The graphs are the transverse momentum (p_T) distribution for $|y| < 2.4$ (on the left) and the rapidity (y) distribution for $p_T > 5GeV/c$ (on the right). The curves are for prompt production assuming colour-octet $^3S_1$ dominance (solid) or S-wave dominance (dotted) and for production from b-hadron decay (dashed) [25].*

The prompt and b-decay cross sections integrated in the complete phase space region, showed in Fig. 1.9, are predicted to be about 49 nb and 8.2 nb, respectively. The fraction of X(3872) events from b-hadron decay is predicted to increase from 10% at $p_T = 5GeV/c$ to 35% at $p_T = 50GeV$.

1.3.3 Tetra-quark hypothesis

A rather natural, and more fundamental possibility, would be that of thinking of other forms of aggregation of quarks in hadrons, like diquarks. A diquark is a coloured quark-quark state which could neutralize its colour, binding with an antidiquark. The resulting meson is a particular realization of a tetraquark. Indeed as for the colour, the diquark is like an antiquark and the antidiquark is just like a quark. It follows that the resulting tetraquarks are a kind of standard $q\overline{q}$ mesons but with the notable difference that at the end of the electric colour string there are diquarks instead of quarks.

Following the same line of reasoning, a tetraquark is expected to decay into two baryons upon colour string breaking. The X(3872) on the other hand has not enough mass to decay into two charmed baryons because of phase space. This forces the diquark-antidiquark system to rearrange itself into a $J/\psi\,\rho$ or $J/\psi\,\omega$ configuration. Contrary to the picture given in molecular models, such a rearrangement happens inside the boundaries of $1/\Lambda_{QCD}$. Some of the newly discovered hadrons have enough mass to decay into two baryons. The Y(4660), for example, appears to decay prominently into $\Lambda_c\Lambda_c^-$ baryons, as expected for a tetraquark.

The tetraquark model has more challenging predictions though. Charged states are expected, such as $[cu][\overline{c}d]$ and even doubly charged states as $[cu][d\overline{s}]$. The $Z^+(4430)$, the first of a series of three newly discovered charged particles, decays in a charmonium state plus a charged pion and is a strong candidate to be a charged tetraquark state. Even if Belle observes it at more than 6 σ significance, it has not yet been confirmed by other experiments.

In order to explain in the tetraquark model the peculiar decay pattern of the $X(3872)$ which dissociates with equal rate into $J/\psi\,\rho$ and $J/\psi\,\omega$, one needs to consider two neutral states with a difference in mass of few MeV. One can call them $X_u = [cu][\overline{cu}]$ and $X_d = [cd][\overline{cd}]$. Once these states are mixed by $u\overline{u} \leftrightarrow d\overline{d}$ annihilations, we can end up with isospin pure mixtures of the kind $(X_u \pm X_d)/\sqrt{2}$. The expected difference in mass between the two X states must be $\Delta M \sim M_d - M_u$, but CDF excludes [10] a mass difference greater than 3.2 MeV at 90% CL. Moreover the tetraquark model predicts charged partners of the $X(3872)$ with a very similar mass. This partners has not yet been observed even if searches have been performed by BaBar in the $J/\psi\,\rho^+$ channel.

The main drawback of the tetraquark picture is the proliferation of expected states. There isn't any clue of selection rules which could limit the production of tetraquark particles at the fragmentation level. Moreover is not possible to predict the fragmentation probabilities of tetraquark states, so it is also difficult to estimate their production rates.

1.3.4 Other theoretical interpretations

Many other exotic models have been proposed to explain the $X(3872)$ and other states observed above the open charm threshold:

- **Hadrocharmonium** [57]: In this picture, states that decay prominently in one of the two charmonium states J/ψ and $\psi(2S)$ and with the decay into open-charm mesons highly suppressed, are interpreted as the indication of an hadronic structure in which a standard charmonium state is stuck into a light hadron. This charmonium state embedded inside light hadronic matter is referred to as hadro-charmonium or

hadro-quarkonium in general. The light hadronic matter acts as a spatial extended environment in which the more compact J/ψ or $\psi(2S)$ moves.

This picture is at least able to explain why the decay into J/ψ or $\psi(2S)$ is favored or suppressed, depending on which charmonium state is stuck inside the hadron. The reason why the $c\bar{c}$ state interacts with the light hadronic stuff, although being neutral with respect to colour charge, is that it has a chromo-electric polarizability. Thus its chromo-electric dipole moment interacts with the chromo-electric field generated by the light hadronic matter. This interaction can be treated with the multipole expansion in QCD used for the charmonium binding inside nuclei. The possibility that such a bound state exists depends on the relation between the mass M_X and the spatial extension of the light hadron. In particular in [56] it has been shown that a quarkonium state does form a bound state inside a sufficient highly excited light hadron.

- **Hybrids**: Both the molecular and tetraquark hadrons are built with quarks and antiquarks. However the QCD Lagrangian contains also the gluons, which can act as dynamical degrees of freedom besides being the particles which mediate strong interactions. One can indeed suppose the existence of gluonic hadrons, bound states of gluons and quarks, i.e. a $c\bar{c}g$ system. Such states were proposed back in 1976 [**?**]. The main drawback for the hybrid interpretation for the X(3872) is that the expected masses for the hybrids in the charmonium family are around 4.3 GeV, with an estimated uncertainty of 100/200 MeV.

- **Glueballs**: An extreme consequence to the hybrid idea is to consider the X(3872) to be a glueball, a bound state containing no quarks, but only gluons, with a small (about 3%) admixture of $c\bar{c}$. A lattice QCD calculation [77] in 1990 predicts a 3-gluon vector glueball with mass $3850 \pm 50 \pm 190 MeV/c^2$ and $J^{PC} = 1^{--}$. The pure glueball does not couple to e^+e^-, which explains why the $X(3872)$ has not been found in direct production at e^+e^- collisions, despite the suitable spin-parity supposed. In this model the $c\bar{c}$ admixture is the $\psi(2S)$ and that is responsible for the observed decay $X(3872) \to J/\psi\pi^+\pi^-$. The model predicts decays $X(3872) \to J/\psi\pi^0\pi^0$ and $X(3872) \to J/\psi\,\eta$. The decays of X(3872) to $J/\psi\,\gamma$, $J/\psi\,\rho$ and to $J/\psi\,\omega$ are forbidden because of the negative C-parity of the $X(3872)$ in this model.

1.4 Summary

From the totality of the experimental information on the X(3872) available today, the $X(3872)$ appears as a narrow resonant structure with the most probable quantum numbers $J^{PC} = 1^{++}$ and I=0, and a mass within 1 MeV the $D^{*0}\overline{D^0}$ threshold. It may have comparable decay rates to $\gamma\,\psi(2S)$ and (often-slightly-below-threshold)$D^{*0}\overline{D^0}$, but has an order of magnitude smaller rate to both $J/\psi\,\omega$ and $J/\psi\,\rho$. If there are two components of the observed enhancements, they must be closer in mass than a few MeV. It is produced and observed in Tevatron $p\overline{p}$ collisions with a rate similar to conventional charmonia, and at the B-factories in $B \to K\,X$ decays. Unlike conventional charmonia, $B \to K^*\,X$ is suppressed with respect to $B \to K\,\pi\,X$.

The summarized properties of X(3872) do not comfortably fit those of any plausible charmonium state. Alternative theories have been proposed, prominently interpreting the X(3872) as a $D^{*0}\overline{D^0}$ molecule loosely bound or a tetraquark state, but both theories don't explain in a satisfactory way all the experimental results. Better understanding of the X(3872) demands more experimental constraints and theoretical insight.

Chapter 2

The CMS Experiment at LHC

2.1 The Large Hadron Collider

The Large Hadron Collider (LHC) is the world's largest and highest-energy particle accelerator and it is situated 100 m underground beneath the Franco-Swiss border near Geneva, Switzerland. LHC is the latest and most advanced accelerating machine built by the European Organization for Nuclear Research (CERN). CERN is an international organization founded on 29 September 1954, its main function is to provide the particle accelerators and other infrastructure needed for high-energy physics research.

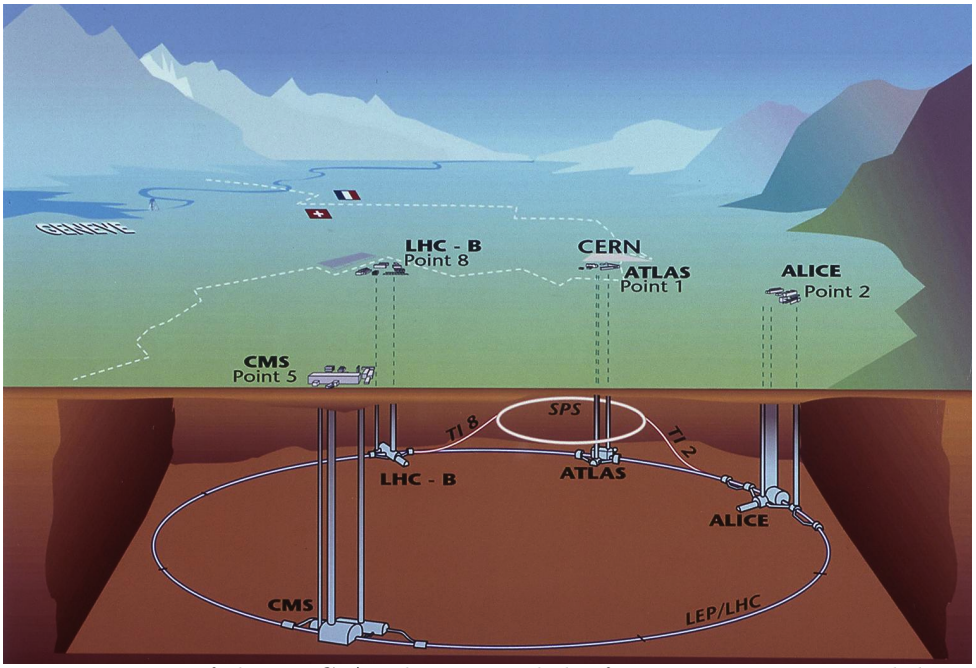

Figure 2.1: *Map of the LHC Accelerator and the four main experimental detectors.*

The LHC project [34] was approved by the Cern Council on 16 December 1994 and the actual construction started in 2002. The decision was to construct a proton collider to study the Standard Model physics at the TeV energy scale (in particular the Higgs mechanism) and to investigate a wide range of possible scenarios beyond the SM.

The design choice to collide proton-proton beams has several advantages. The loss of energy due to synchrotron radiation in case of circular motion of charged particles is proportional to the inverse of the fourth power of the particle mass. So using the proton, which has a mass about 2000 times the one of the electron, it has been possible to reuse the same tunnel of the CERN Large ElectronPositron Collider (LEP [4]) and to design a machine that will be able to reach a beam energy of 7 TeV (with respect to the 100 GeV of LEP).

Moreover protons are not elementary particles, hence, in hard collisions, the pp interaction involves the particle constituents, which do not carry a fixed fraction of the hadron energy. So at a fixed energy of the beams it's possible to explore phenomena in a wide range of energies, key feature for a discovery machine. With respect to the Tevatron accelerator at FermiLab, which collides protons with anti-protons, it was also decided to use only protons for different reasons. In fact, the difference pp and $p\overline{p}$ total cross sections becomes very small at high energies, and the proton production is faster and more efficient with respect to the antiproton one, thus allowing to reach higher luminosity and keep beam stability. LHC is also able to accelerate heavy ions up to lead with unprecedented energy, up to 1148 TeV in the center of mass, opening a new frontier in the study of Quark-Gluon Plasma, which existed in the early universe.

The LHC beams cross at four interaction points, as shown in Fig. 2.1, where four detectors are placed. ATLAS (**A** **T**oroidal **L**HC **A**pparatu**s**) and CMS (**C**ompact **M**uon **S**olenoid) are general pourpose detectors devoted to the study of Standard Model and to the search of new physics beyond it. ALICE (**A** **L**arge **I**on **C**ollider **E**xperiment) is especially designed for the heavy ions collisions focusing on the study of the Quark-Gluon Plasma and LHCb (**LHC** **b**eauty experiment) will perform precise measurements of CP violation in the b-hadron sector. Two further experiments, TOTEM and LHCf, are much smaller in size. They are designed to focus on forward physics in order to study the total proton cross section, elastic scattering and diffraction dissociation. They are positioned respectively near the CMS and ATLAS detectors.

2.1.1 The accelerator

The LHC accelerator takes advantage of a series of pre-existing CERN accelerators (shown in Fig. 2.2) in order to obtain an injection energy of 450 GeV per beams. In the first step the protons are produced by hydrogen ionization (750 keV) and then accelerated to the energy of 50 MeV by a linear accelerator (LINAC). Protons are then injected into the Proton Synchrotron Booster (PSB), where the energy reaches 1.4 GeV and subsequently the Proton Synchrotron (PS) accelerates them to 25 GeV. The last step of acceleration is made by the 6.9 Km Super Proton Synchrotron (SPS) where the beams reach the injection energy of 450 GeV. They are then transferred to the 27 Km LHC ring. Here the proton bunches are accumulated, accelerated to their peak energy, and finally circulated for 10 to 24 hours while collisions occur at the four intersection points.

When LHC operates as a heavy ion accelerator, lead ions are first accelerated by the linear accelerator LINAC 3, and the Low-Energy Ion Ring (LEIR) is used as an ion storage and cooler unit. The ions then are further accelerated by the PS and SPS before being injected into LHC ring, where they will reach an energy of 2.76 TeV per nucleon (or 575 TeV per ion).

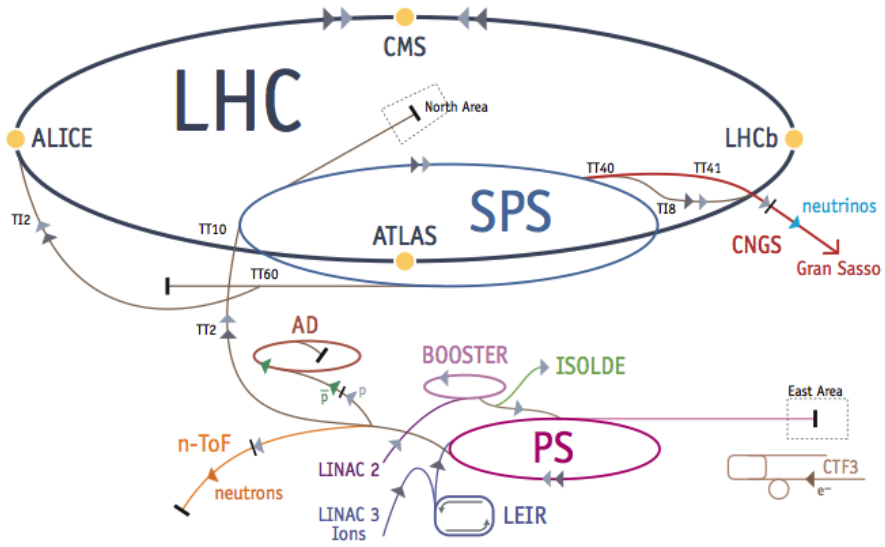

Figure 2.2: *The CERN accelerator complex.*

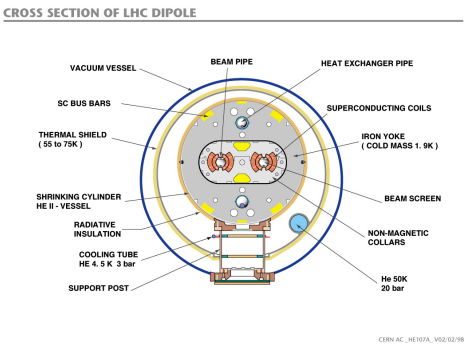

Figure 2.3: *Section of a LHC Dipole*

Machine Parameter	Value
Circumference [Km]	26.659
Beam Radius at interaction point [μm]	15
Number of dipoles	1232
Lengh of dipoles [m]	14.3
Field of dipoles at injection [T]	0.535
Field of dipoles for 7 TeV beams [T]	8.33
Number of quadrupoles	520

Figure 2.4: *LHC technical parameters.*

Accelerating two beams of same charge requires two separate acceleration cavities with two different magnetic field configurations. The bending power needed to keep the beam circulating is the limiting factor to the achievable centre of mass energy. In case of LHC it's supplied by about 1200 superconducting dipoles (Fig. 2.3), able to reach a stable 8.3 T field. 392 quadrupole magnets are used to keep the beams focused, in order to maximize the chances of interaction between the particles in the four intersection points. In total, over 1,600 superconducting magnets are installed, with most weighing over 27 tonnes. Approximately 96 tonnes of liquid helium is needed to keep the magnets, made of copper-clad niobium-titanium, at their operating temperature of 1.9 K, making the LHC the largest cryogenic facility in the world at liquid helium temperature.

2.1.2 Luminosity

A key parameter for the discovery potential of experiments at LHC is the machine luminosity ($\mathcal{L}$). In the general case of two colliding beams, the luminosity writes:

$$\mathcal{L} = f_{rev}\, n_b\, \frac{N_1\, N_2}{A} \tag{2.1}$$

where f_{rev} is the revolution frequency, n_b is the number of bunches per beam, N_1 and N_2 are the number of particles in the bunches of each colliding beam , and A is the cross section of the beams. At LHC, the bunches are filled with an identical number of protons so $N_1 = N_2 = N_b$. The cross section of the beam writes:

$$A = 4\pi\epsilon_n \frac{\beta^\star}{\gamma_r} \tag{2.2}$$

where ϵ_n is the normalized transverse beam emittance (which measures the extent occupied by the particles of the beam in position and momentum phase space), and $\beta^\star$ is the beta function at collision point, which measure the beam focalization. That is then corrected by the relativistic gamma factor γ_r. Finally, the expression in 2.1 has to be corrected by a geometric luminosity reduction factor, F, due to the crossing angle at the interaction point. Hence, the final expression of the luminosity writes:

$$\mathcal{L} = \frac{f_{rev}\, n_b\, N_b^2\, \gamma_r}{4\pi\epsilon_n\beta^\star}\, F \tag{2.3}$$

CMS and ATLAS experiments are designed to take advantage of the high luminosity deliverable by LHC. The design values for the collision at their interaction points are reported in Table 2.1. LHCb target luminosity is of the order of $10^{32} cm^{-2} s^{-1}$. The luminosity is even lower for ALICE which is designed for the Pb-Pb collisions (Alice design luminosity is $2 \cdot 10^{27} cm^{-2} s^{-1}$).

Parameter	Value
Luminosity ($\mathcal{L}$)	$10^{34} cm^{-2} s^{-1}$
Number of particles per bunch (N_b)	$1.1 \cdot 10^{11}$
Number of bunches (n_b)	2808
Beta function at impact point ($\beta^\star$)	0.55 m
Normalized transverse beam emittance (ϵ_n)	3.75 μm
Relativistic gamma γ_r	479.6
Geometric luminosity reduction factor F	0.836
Luminosity lifetime	10 h
Time between collisions	24.96 ns
Bunch crossing rate	40.08 MHz
Stored energy in the beams	362 MJ
Circulating beam current	0.582 A

Table 2.1: *LHC design parameter for collisions at ATLAS and CMS*

2.1.3 LHC operations

Beams were circulated for the first time in LHC on 10 September 2008, but just 8 days after, a major technical incident forced a long stop. Investigations showed that cause of the incident was a faulty electrical connection between two of the accelerator's magnets. This fault resulted in mechanical damage and release of helium from the magnet cold mass into the tunnel. The repairs and the deployment of a better protection system took more than one year, nevertheless, in order to operate the accelerator safely, it was decided to limit the maximum beam energy to 3.5 TeV. Higher energies will be achieved after a long shut down scheduled for 2013, when extensive intervention will be performed on the machine. On 23 November 2009 the accelerator produced the first proton-proton collision. After a few pilot runs at energies of 450 GeV and 1.18 TeV per beam, the energy was ramped up to 3.5 TeV, reaching the first collision at a centre-of-mass energy of 7 TeV on 30th March 2010, the highest ever reached at a particle collider. With respect to the design parameters of Table 2.1 the luminosity has been gradually increased up to $2 \cdot 10^{32} cm^{-2} s^{-1}$ with a maximum of 400 bunches spaced down to 150 ns. In Fig 2.5 the evolution of instantaneous and integrated luminosity during 2010 is shown.

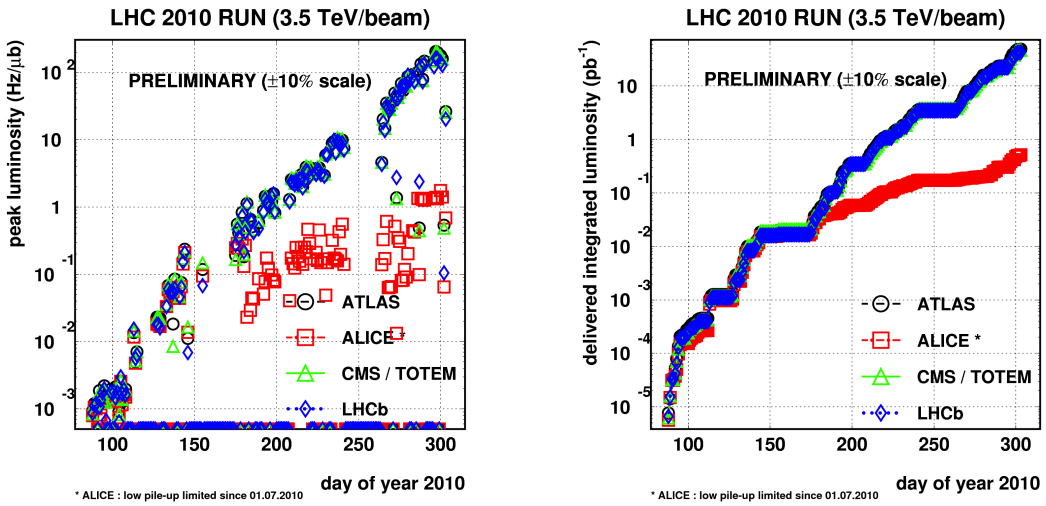

(a) (b)

Figure 2.5: *LHC maximum istantaneus luminosity (a) and delivered integrated delivered luminosity (b) to the four experiments during the 2010 proton run.*

The proton-proton operation continued smoothly also in 2011 when a record instantaneous luminosity of $3.6 \cdot 10^{33} cm^{-2} s^{-1}$ was reached, with up to 1380 bunches of $1.4 \cdot 10^{11}$ protons spaced down to 50 ns. By the end of the 2011 run, more than $5 fb^{-1}$ of integrated luminosity has been delivered to CMS and ATLAS, as shown in Fig 2.6. At the end of both 2010 and 2011 proton runs, four weeks have been dedicated to ions collisions, delivering to the experiments $10 \mu b^{-1}$ and $150 \mu b^{-1}$ respectively. The next year will be the last one at 3.5 TeV per beam, with the objective to add a recorded luminosity of about $20 fb^{-1}$ per experiment before the long shut-down of 2013.

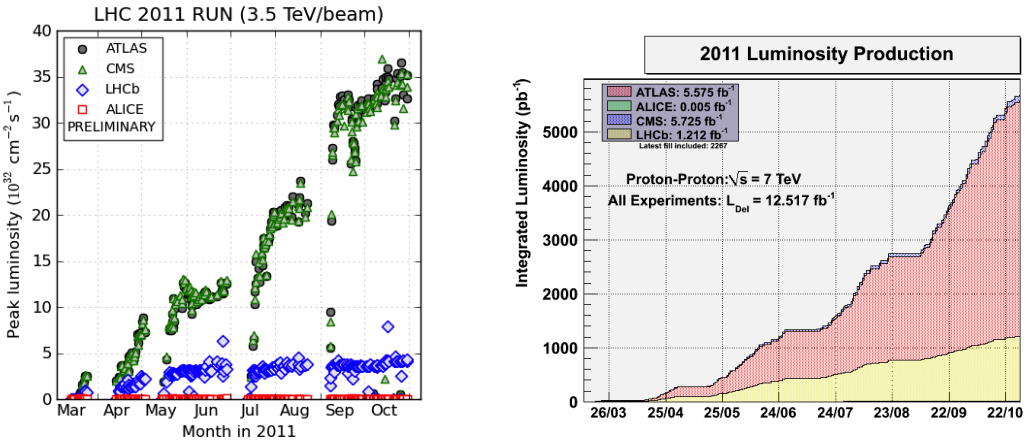

(a) (b)

Figure 2.6: *LHC maximum istantaneus luminosity (a) and delivered integrated luminosity (b) to the four experiments during the 2011 proton run.*

2.1.4 Proton-proton collision at LHC

The event rate of a process with cross section σ at a certain instantaneous luminosity (Equation 2.3) is given by

$$R = \mathcal{L} \cdot \sigma \tag{2.4}$$

The total inelastic cross section for proton-proton collision was expected to be $\sigma_{pp} = 80mb$ at design condition, while by the various experiments it has been measured to be around 70 mb (see Fig. 2.7) at 3.5 TeV.

The inelastic cross section includes two classes of interactions. In the first the two incoming protons can just transfer a small momentum at large distance (*soft collision*). In this case particle scattering at large angle is suppressed and most of the final state particles escape down the beam pipe.

In the second type of interaction, since protons are not elementary particles, collisions occur between two of their constituents (partons, i.e quarks and gluons), and this results in a high transferred momentum in the direction transverse to the beam direction (p_T). These are called *hard collisions*, which usually contain the most interesting physics events. The rate of hard collisions is more orders of magnitude lower than that of soft interactions so, even if particles produced in soft collisions are mostly distributed in the forward region, the residual tail at high p_T is competitive with the hard interaction rate, and constitutes a background to high p_T signal events.

In hard interactions the effective centre-of-mass energy $\sqrt{\hat{s}}$ is given by the centre-of-mass energy of the two partons, and it's proportional to the fraction of energy carried by the two partons. The distribution of the fractional momentum of partons inside protons is called *parton distribution function* (PDF). These distributions are different for each parton and are functions of the exchanged momentum Q^2. At high Q^2 the contribution of gluons and sea quarks increases with respect to that of valence quarks.

Due to the high luminosity of the machine at the design condition, the collision rate (Equation 2.4) would be of the order of $10^9 Hz$, which would result in about 25 collisions every bunch crossing. The presence of more than one collision event per bunch crossing is

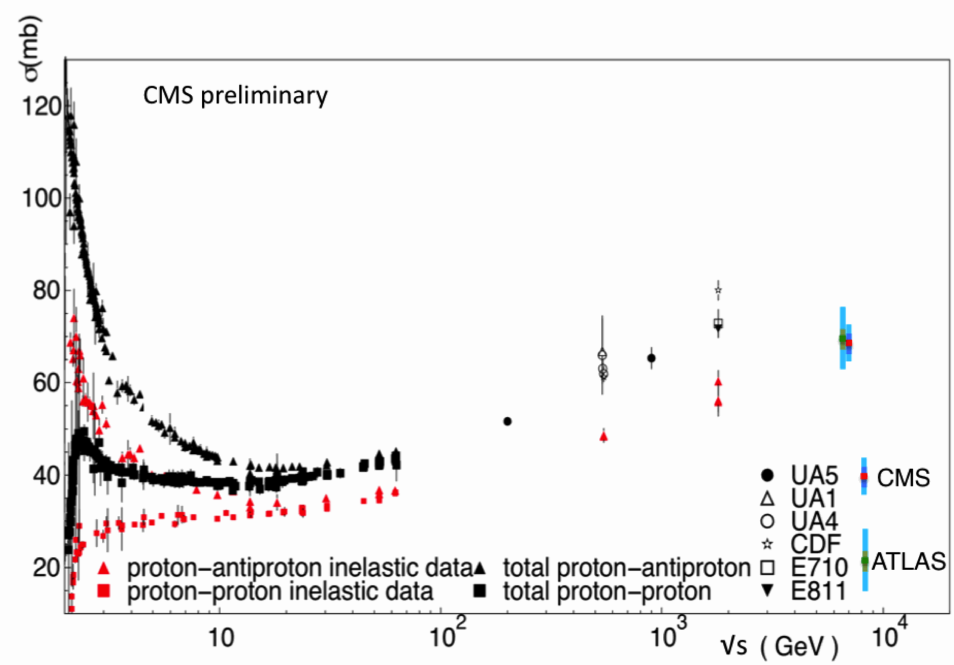

Figure 2.7: *Compilation of total inelastic pp and $p\bar{p}$ cross section values. CMS analysis uncertainty is shown in dark blue while the model-dependent extrapolation is shown in light blue (dark green and light blue for ATLAS) [7] [15]*

usually referred as *pile-up*, and only ATLAS and CMS experiment have been designed to take data in a high pile-up environment. Pile-up has been almost negligible in the 2010 run, but already in 2011 the average collision in a bunch crossing has been about ten. The inconvenience of pile-up is needed in order to achieve a sufficient rate for very rare processes with small cross section. Cross sections and events rates for the main processes produced at the LHC are reported in Fig. 2.8 as a function of centre-of-mass energy.

2.1.5 The LHC data management

One of the main challenges of the experiments at LHC will be the management of the huge amount of data that will be recorded. At design condition the Large Hadron Collider will produce annually roughly 15 petabytes of data, that have to be accessible to thousands of scientists around the world. In order to cope with this need CERN is collaborating with institutions in 34 different countries to operate a distributed computing and data storage infrastructure: the Worldwide LHC Computing Grid (WLCG [60]). The GRID is structured in several layers, called Tiers, as shown in Fig. 2.9.

The original raw data emerging from the data acquisition systems will be recorded at the "Tier-0" centre at CERN. The first-pass reconstruction will take place at the Tier-0, where a copy of the reconstructed data will be stored. The Tier-0 will then distribute this data across the Tier-1 centres (large computer centres in Canada, France, Germany, Italy, the Netherlands, the Nordic countries, Spain, Taipei, the UK, and two sites in the USA) where sufficient storage capacity is available for a large fraction of the data, and with round-the-clock support for the computing grid. These so-called "Tier-1" centres make the data available to over 200 "Tier-2" centres for specific analysis tasks. Individual

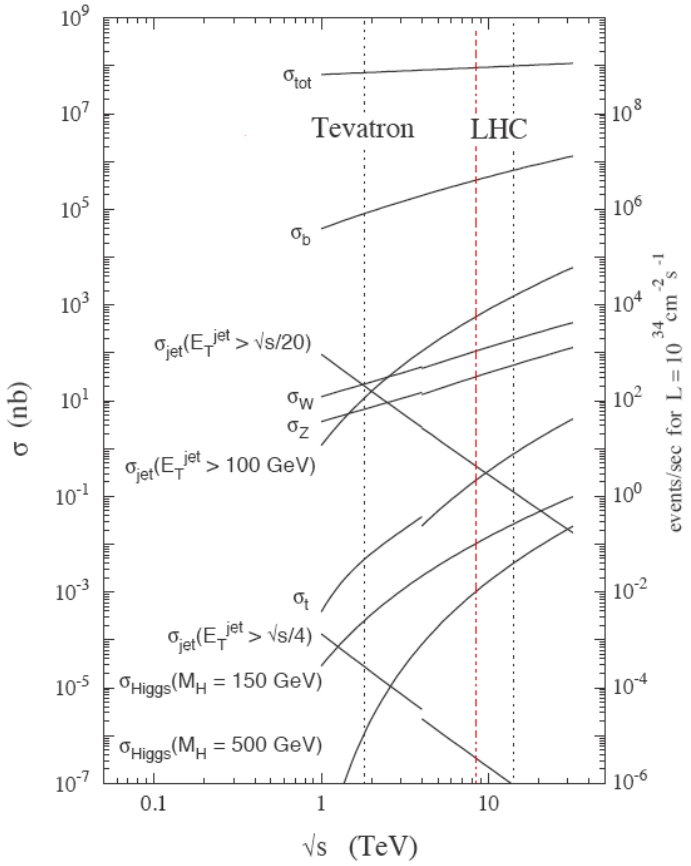

Figure 2.8: *Cross Section and event rates of several processes as a functions of the centre-of-mass energy of p-p collisions. For LHC are considered the design energy (black) and the actual one (7 TeV, in red)*

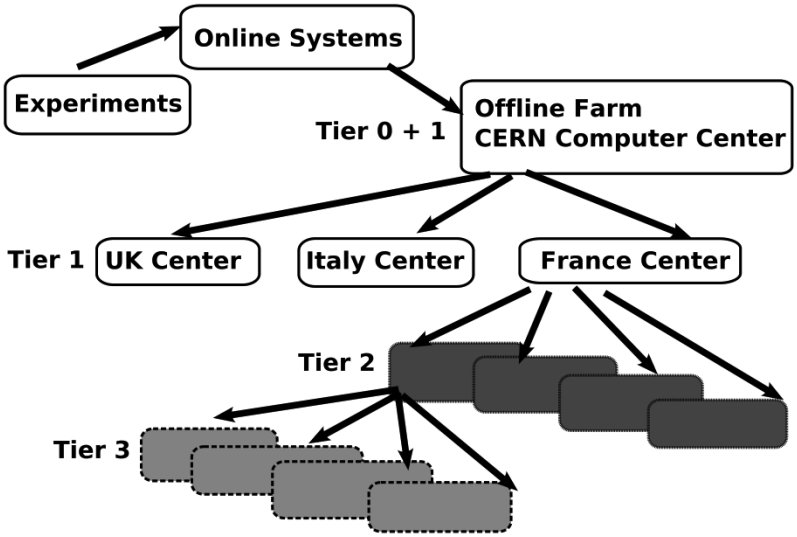

Figure 2.9: *Schematic structure of the LHC Computing Grid Tier system [36]*

scientists can then access the LHC data from their home country, using local computer clusters ("Tier-3" or even individual PCs). This new type of globally distributed model for data storage and analysis - a computing Grid - was chosen instead of a centralized one because it provides several key benefits. In particular:

- the significant costs of maintaining and upgrading the necessary resources for such a computing challenge are more easily handled in a distributed environment, where individual institutes and participating national organizations can fund local computing resources and retain responsibility for these, while still contributing to the global goal.

- in a distributed system there are no single points of failure. Multiple copies of data and automatic reassigning of computational tasks to available resources ensure load balancing of resources and facilitate access to the data for all the scientists involved, independently of geographical location. Spanning all time zones also facilitates round-the-clock monitoring and support.

2.2 The CMS experiment

The Compact Muon Solenoid [40] is one of the two "general purpose" detectors at the Large Hadron Collider. Its aim is to study a large spectrum of physical phenomena, starting from the completion of the Standard Model predictions looking for the Higgs Boson and up to the search for new physics beyond the Standard Model at the TeV scale. The experiment is located in an underground cavern at LHC experimental point number five, near the french town of Cessy. The main characteristic of the detector is a strong super-conductive solenoidal magnet, which can reach a 4 T field and dictates the cylindrical shape of the experiment. Another characteristic of CMS is its modularity. This had made it possible to build CMS on surface, while the experimental cavern was being excavated, and it was lowered one section at the time in 2007. The magnet occupies the central region of the detector, called *barrel*, which is externally subdivided in 5 wheels. The wheels compose the iron yoke for the return of the magnetic fields, and contain the chambers for the detection of muons. The central wheel (designated wheel 0) is also the structural support for the magnet to which it's connected (see Fig. 2.10(a)). The *barrel* region is closed on both ends by three instrumented iron disks called *endcaps* (see Fig. 2.10(b). Once closed, the detector is quite compact (at least with respect to ATLAS), being a cilinder 21.6 m long and with a diameter of 14.6 m. Its total weight is of about 14500 t. In Fig. 2.11 an expanded section of the CMS detector is shown, with highlighted the main sub-detectors.

2.2.1 CMS Coordinate system

The CMS coordinate system used to describe the detector is a right-handed Cartesian frame, centred in the interaction point and with the z axis along the beam line (this direction is referred to as *longitudinal*). The x axis is chosen to be horizontal and pointing towards the centre of the LHC ring, and the y axis is vertical and pointing upwards. The x-y plane is called *transverse* plane.

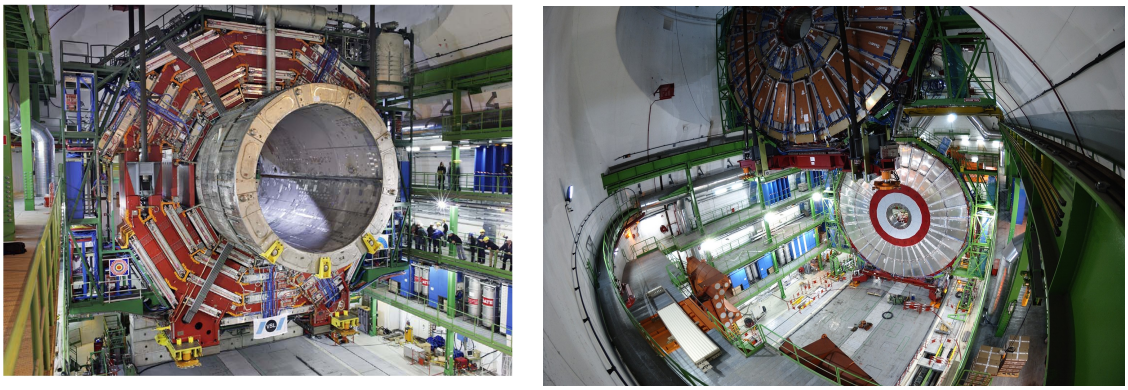

(a) (b)

Figure 2.10: *Lowering in the experimental cavern of the central barrel wheel and magnet (a) and of two endcaps disks (b) at the beginning of 2007.*

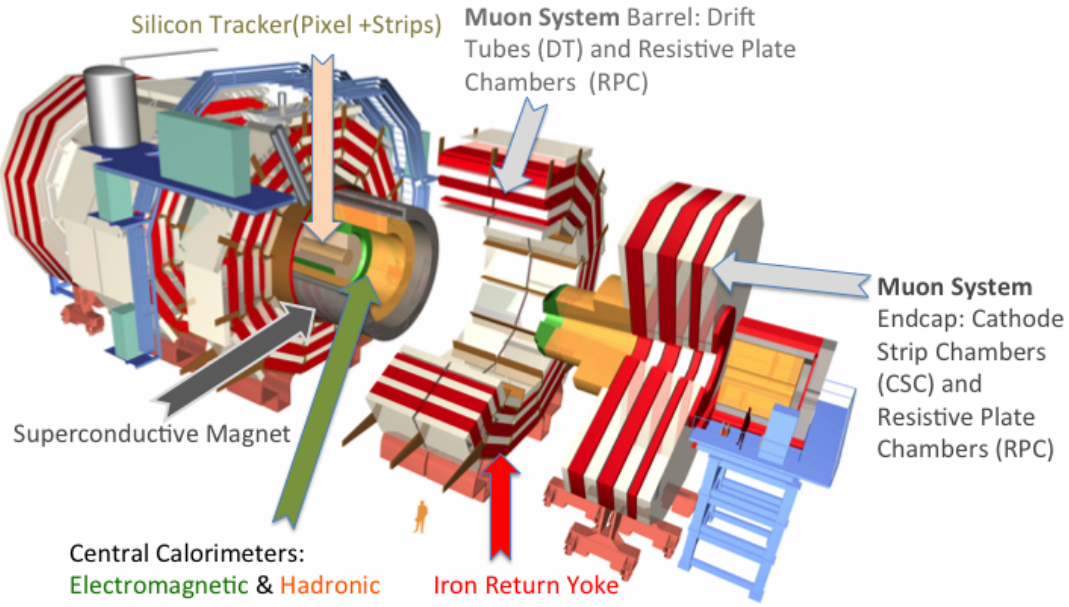

Figure 2.11: *Schematic structure of the LHC Computing Grid Tier system [36]*

Given the cylindrical symmetry of the CMS design, usually a (ϕ, θ) cylindrical coordinate system is used in the reconstruction of the tracks of particles. ϕ is the polar angle, laying in the x-y plane, measured from the x-axis in mathematical positive direction (i.e. the y-axis is at $\phi = 90°$). The azimuthal angle θ is measured from the z-axis towards the x-y plane. The angle θ can be translated into the pseudo-rapidity η by

$$\eta = -ln\left(\tan\frac{\theta}{2}\right) \tag{2.5}$$

The actual value of η can be seen in the longitudinal view of the detector in Fig. 2.12(b). Using these parameters, the distance between two particles can be defined as

$$\Delta R = \sqrt{\Delta\phi^2 + \Delta\eta^2} \tag{2.6}$$

Referring to the Cartesian system, the momentum of a particle can be divided in two components: the *longitudinal momentum* p_z and the *transverse momentum* p_T, defined as:

$$p_T = \sqrt{p_z^2 + p_y^2} \tag{2.7}$$

The magnet bends charged tracks on the ϕ plane, so what is effectively measured is the p_T of the particles. For a particle of energy E, the variable *rapidity* (y) is also introduced, defined as

$$y = arctanh\frac{|\vec{p}|c}{E} = \frac{1}{2}\ln\left(\frac{E + p_z c}{E - p_z c}\right) \tag{2.8}$$

For high energy particles rapidity can be approximated by pseudorapidity. Both rapidity and p_T are used because parton collision (see Section 2.1.4) can have the center-of-mass of the interaction boosted along the z direction; both these quantities have invariance properties under this kind of boost.

2.2.2 Inner Tracing System

Outside the beam pipe, the first sub-detector found by particles coming from the interaction point is the inner tracking system ("Tracker"), a system of silicon sensors designed to provide a precise and efficient measurement of the trajectories of charged particles. The Tracker consists of two major parts, an internal silicon pixel detector and an outer silicon strip detector. The overall length of the Tracker is 5.4 m with an outer diameter of 2.4 m.

The Pixel Detector

The pixel detector [54] consists of three cylindrical layers of hybrid pixel modules surrounding the interaction point at radii of 4.4, 7.3 and 10.2 cm. Two disks of pixel modules on each side complement the pixel detector, as shown in Fig. 2.13(a). It is built to ensure precise 3D vertex reconstruction to allow efficient τ and b jets identification and covers a pseudorapidity range up to $|\eta| < 2.5$ (see Fig. 2.13(b), 2.13(c)).

The 66 million active silicon sensors are realized on high-resistance n-substrate, with an implanted pn-junction and a pixel cell size of 100x150 μm^2. The minimal pixel cell area is dictated by the readout circuit surface required for each pixel and the small pixel

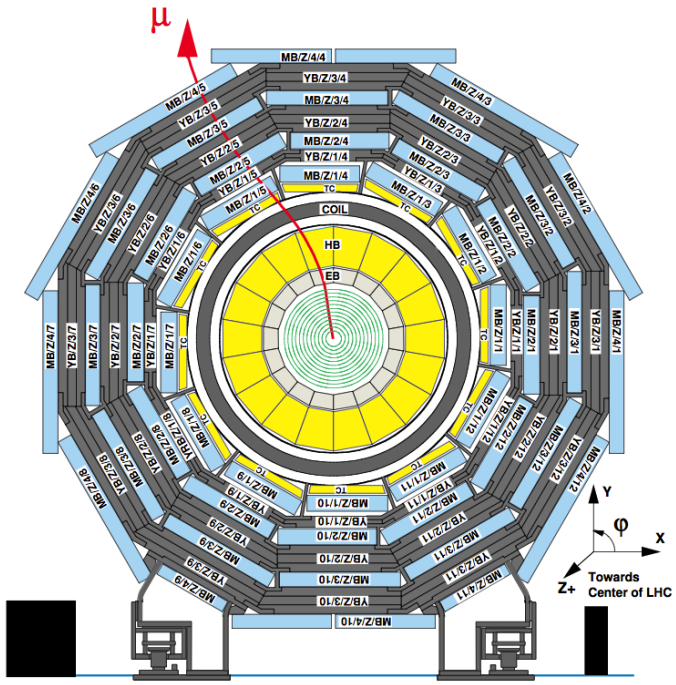

(a)

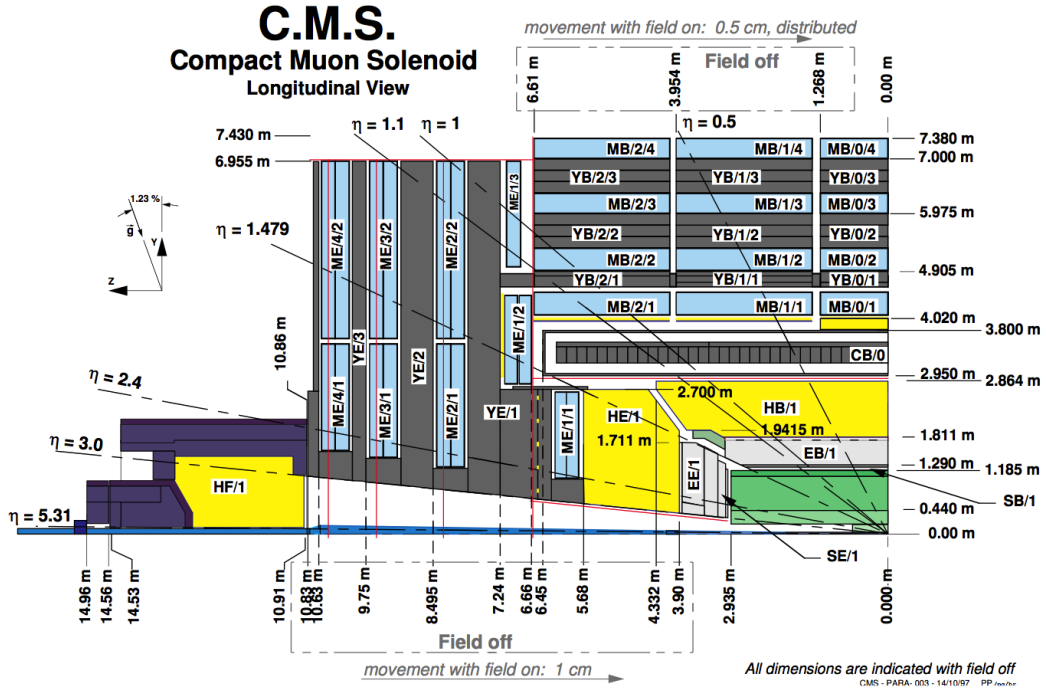

(b)

Figure 2.12: *On (a) a transverse view of CMS in the barrel region. On (b) a longitudinal view of one quarter of the detector.*

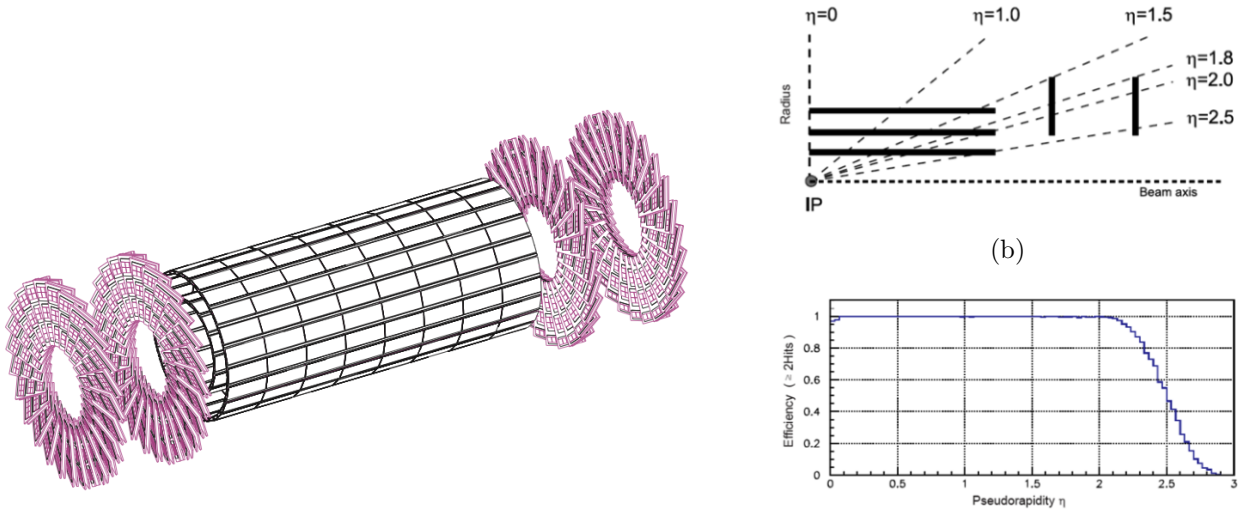

(a) (b) (c)

Figure 2.13: *Overview of the pixel detector layout (a); longitudinal view of one quarter of the pixel detector (b) and its hit coverage as a function of (c).*

size allows to keep single channel occupancy per bunch crossing around 10^{-4} even in the future high flux scenario (10^7 particles/s at 10 cm).

In localizing secondary decay vertices, both transverse and longitudinal coordinates are important and a nearly square pixel shape is adopted. Indium bumps are deposited onto the sensors for subsequent connection to the readout electronics. Movable electrons and holes are created in silicon by ionisation, if a charged particle traverses it. Applying high voltage, these movable charge carriers can be separated and measured as a current, as illustrated in Fig. 2.14(a).

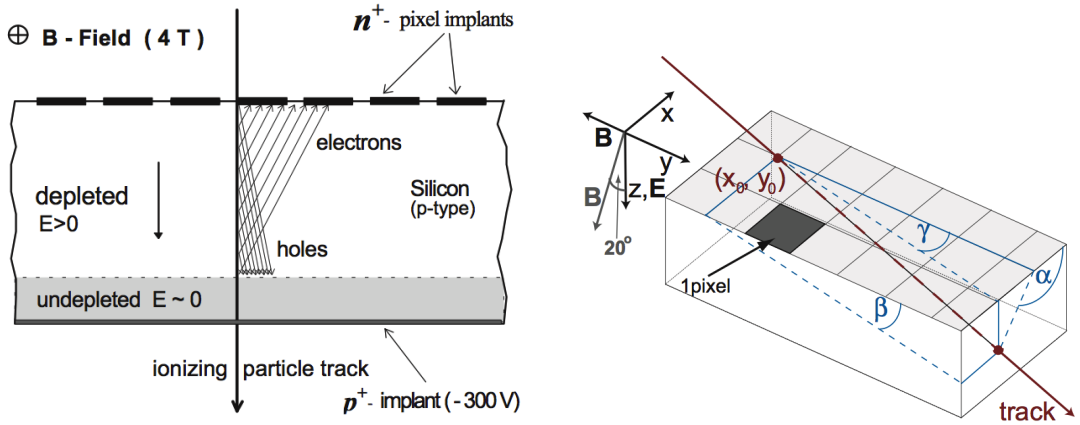

(a) (b)

Figure 2.14: *Functionality of silicon based particle detection (a). On (b) sketch of the track impact angles with respect to a pixel sensor. The magnetic field vector is anti-parallel to the y axis for the barrel sensors and at 20° with respect to the z axis for the endcap sensors.*

Since the deposited charge is often shared among several pixels, an analog charge readout is implemented. Charge sharing enables interpolation between pixels, which im-

proves the spatial resolution. In the barrel section the charge sharing in the $r\phi$-direction is largely due to the Lorentz effect: the charges drift at an angle (Lorentz angle) relative to the direction of the electric field. The pixel hit reconstruction exploits this effect to improve the spatial resolution by interpolating the charge collected in a cluster. Once the interpolation is done the resulting position is adjusted to account for the Lorentz drift. Because the pixel barrel sensor planes are parallel to the magnetic field, the Lorentz drift is both maximal and in the azimuthal direction. In the endcap pixels the sharing is enhanced by arranging the blades in the turbine-like layout. The spread of the charge over neighboring pixels depends on the particles incidence angle and has a minimum for tracks parallel to the drift direction of the charge carriers. The Lorentz angle is extracted by finding the minimum of the mean cluster size along the local x coordinate measured as a function of the cotangent of the incidence angle α, as shown in Fig. 2.14(b).

The resulting hit resolution depends on the cluster size and position, and is in general between 10 and 25 μm (Fig. 2.15(a)). In the first two years of operation the detector has shown a hit reconstruction efficiency of about 99%, as shown in Fig 2.15(b).

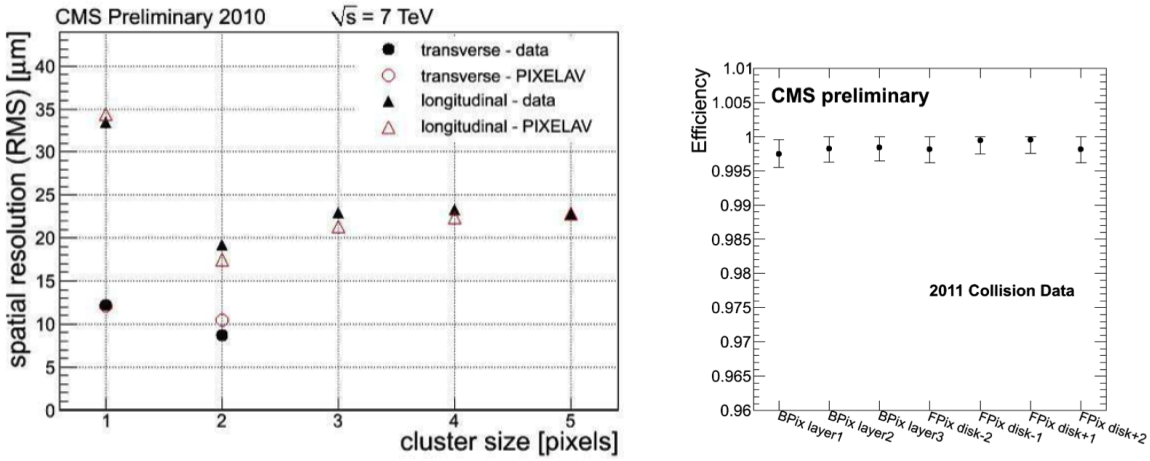

(a) (b)

Figure 2.15: *In (a) transverse and longitudinal pixel spatial resolution as a function of the cluster size. Full dots and triangles are measurements, open symbols are simulations. In (b) it reconstruction efficiency as measured for all layers of the pixel tracker*

The strip detector

The pixel system is surrounded by the Silicon Strip Tracker (SST). With its more than 9.3 million detector channels, 15000 silicon modules and a total active detector area of about 200 m^2, it is the largest silicon tracker ever built. The SST was completed at CERN using the tracker integration facility, a clean room with facilities to assemble, connect and operate parts of the tracker in turn. The sealed SST was finally transported to the experimental area and lifted down into the cavern.

The SST consists of four main subsystems, shown in Fig. 1: the four-layer Tracker Inner Barrel (TIB), the six-layer Tracker Outer Barrel (TOB) and, on each side of the barrel region, the three-disk Tracker Inner Disks (TID), and the nine-disk Tracker End Caps (TEC). Each TID disk is made of three rings of modules, while TEC disks have seven

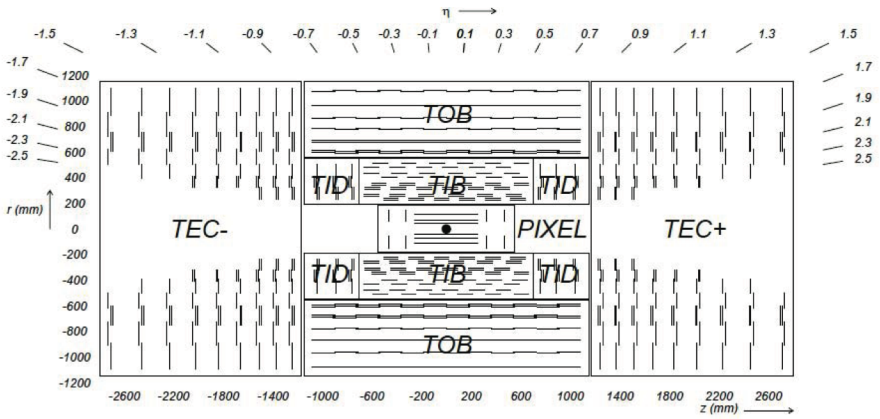

Figure 2.16: *The tracker schematic structure*

rings. The entire system is operated at a temperature below 10°C. The active detector elements, the silicon modules, consist of a carbon or graphite fibre frame, which supports the silicon sensor and the associated front-end readout electronics. The silicon sensors are made up of single-sided p^+ strips on n-bulk sensors with two different thicknesses: 320 μm and 500 μm in the inner four and outer six layers of the barrel, respectively; 320 μm in the inner disks, and 320 μm and 500 m in the inner four and outer three rings of the end cap disks, respectively. More than 20 different module geometries exist, with differences in terms of strip length, pitch and material resistivities, to ensure that the single strip occupancy is low even at full LHC luminosity. Both single-sided and double-sided modules (two single-sided modules mounted back to back with a stereo angle of 100 mrad) are used. The final single hits resolution depends on the type of sensors and their position, and has been measured to be between 15 and 45 μm, in accordance to the design expectation (Fig. **??**).

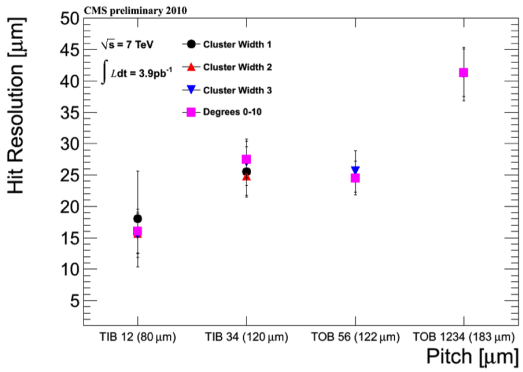

Figure 2.17: *Silicon strip hit resolution as a function of strip pitch*

2.2.3 The Eletromagnetic Calorimeter

The CMS Electromagnetic Calorimeter is composed of 75848 lead tungstate ($PbWO_4$) crystals, chosen because of their excellent energy resolution. The detector consists of a barrel region, extending to a pseudorapidity $|\eta|$ of 1.48, and two endcaps, which extend coverage to $|\eta| = 3.0$. The Barrel section (EB) has an inner radius of 129 cm, and

is structured as 36 identical supermodules, each covering half the barrel length. Each supermodule is composed by 1700 crystals with a front face cross-section of about $22 \times 22mm^2$ and a length of 230 mm, corresponding to 25.8 radiation lengths (X_0). The crystal axes are inclined at an angle of 3° relative to the direction of the nominal interaction point, in both the azimuthal (ϕ) and η projections.

The two ECAL endcaps (EE) are located at a distance of 314 cm from the vertex and are constructed from four half-disk dees, each consisting of 3662 tapered crystals, with a frontal area of $2.68 \times 2.68\ cm^2$ and a length of 22 cm (corresponding to 24.7 X_0), arranged in a quasi-projective geometry. The crystals are focussed at a point 1.3 m farther than the nominal interaction point along the beam line, with off-pointing angles between 2° and 8°. The crystals in each dee are organised into 138 standard 5×5 supercrystal units, and 18 special shaped supercrystals that are located at the inner and outer radii.

The Endcaps (EE) are located at a distance of 314 cm from the vertex. The endcap crystals have a front face cross section of $28.6 \times 28.6\ mm^2$ and a length of 220 mm, corresponding to 24.7 X_0. A Preshower detector (ES) is placed in front of the crystal calorimeter over the endcap pseudorapidity range $1.653 < |\eta| < 2.6$. Its active elements are two planes of silicon strip detectors, with a pitch of 1.9 mm, which lie behind disks of lead absorber at depths of 2 X_0 and 3 X_0. A schematic layout of ECAL is reported in Fig. 2.18.

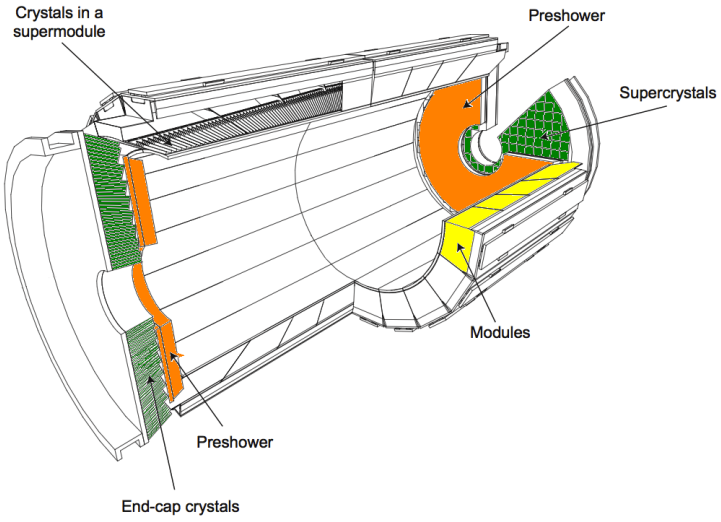

Figure 2.18: *View of the CMS ECAL structure: Barrel (one supermodules in yellow), Endcap (in green), Preshower (in orange).*

The scintillation light produced in the crystals is read-out by a pair of avalanche photodiodes (APD) for each EB crystal, and a vacuum phototriode for each EE crystal. The small Moliere radius (RM = 2.2 cm) in combination with the large number of crystals results in a fine granularity for the lateral shower shape. In the forward region the granularity is further improved by the Preshower detector.

In order to achieve the desired energy resolution of the ECAL it is necessary to maintain the stability of the per-channel energy calibration over time. This places stringent requirements on the stability of the temperature of the ECAL and of the high voltage applied to the APDs. This is due to the temperature dependence of the crystal light

yield, as well as the sensitivity of the APD gains to variations in both temperature and high voltage (the VPT response is much less sensitive to temperature and high voltage variations). The ECAL energy resolution measured in electron test beams is parametrized as

$$\left(\frac{\sigma}{E}\right)^2 = \left(\frac{\alpha}{\sqrt{E}}\right)^2 + \left(\frac{\sigma_n}{E}\right)^2 + c^2 \tag{2.9}$$

for electrons incident on the center of crystals [33]. The three contributions correspond to the stochastic term, the noise term and the constant term. The stochastic term depends on the event-by-event fluctuations in the electromagnetic shower development, on the photo-statistics and on the photodetector excess noise factor. The noise term depends on the level of the electronic noise and event pile-up. The constant term depends on the non-uniformity of the longitudinal light collection, on the leakage of energy from the rear face of the crystals and on the accuracy of the detector inter-calibration constants.

For electromagnetic showers of energies above 100 GeV the energy resolution is dominated by the constant term. As a consequence, in the CMS environment the detector's performance will depend mainly on the quality of its inter-calibration and monitoring. Of particular importance are changes in crystal transparency under irradiation that have to be tracked in order to apply the needed correction, as can be seen in the example is Fig. 2.19 and Fig. 2.20.

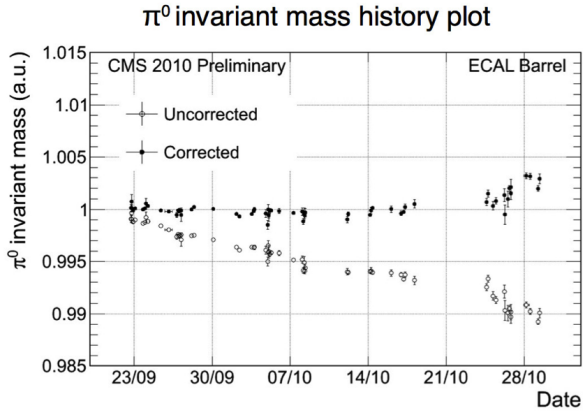

Figure 2.19: *π_0 invariant mass history plot in 2010 for the ECAL Barrel detector, before and after the corrections for the crystal transparency loss.*

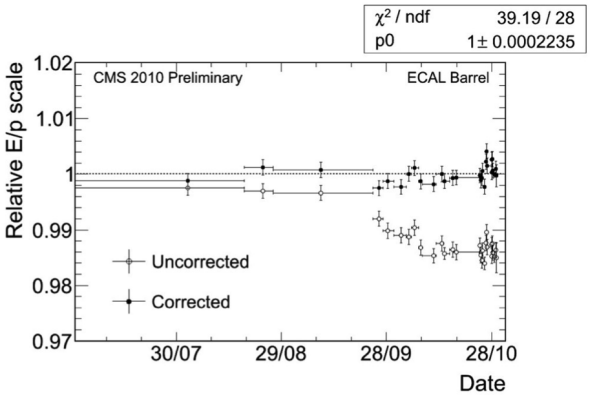

Figure 2.20: *E/p history plot, with E = ECAL elctron energy and p = Tracker electron momentum, for $W \to e\nu$ decays measured in 2010 with the ECAL Barrel detector.*

2.2.4 The Hadronic Calorimeter

The Hadron Calorimeter (HCAL) is used, together with the ECAL, to perform measurements on direction and energy of hadronic jets and to estimate the amount of missing transverse energy (missing ET) of each event. The request to perform precise missing ET measurement implies the development of a very hermetic system, whose design is constrained by compactness requests and by the high magnetic field. In order to fulfill these requirements a sampling calorimeter system based on brass absorber layers alternated to active plastic scintillators has been built.

The signal coming from active scintillators is read out with embedded wavelength-shifting fibers (WLS) and conveyed via clear fiber wave-guides to hybrid photodiodes. The choice of brass as absorber material has been driven from its short interaction length λ_I and its non-magnetic nature. The HCAL consists of the following parts:

- **HCAL Barrel region (HB).** It is located between the EB (see Section 2.2.3) and the solenoid and covers a range of $|\eta| < 1.3$. The HB contains brass absorber plates alternating with layers of plastic scintillator tiles, which have wavelength shifting fibres embedded for the signal readout. As this setup results in a material thickness of $10.6 \cdot \lambda_I$ at $|\eta| = 1.3$ and only $5.82 \cdot \lambda_I$ at $|\eta| = 0$, the additional HCAL outer region is necessary. The segments of the HB have a tower-like readout, i.e. all the light collected by the scintillator tiles of one segment is directed to one Hybrid Photo Diode via fibres. Thus a two-dimensional resolution of $\Delta\phi = 5°$ and $\Delta\eta = 0.087$ is obtained.

- **HCAL Outer region (HO).** In order to guarantee the containment of lately developing and high energetic hadronic showers within the calorimeter of the CMS barrel, an additional layer, the HO, is needed. It is also located in the barrel region, but outside the solenoid, and covers $|\eta| < 1.3$ as well. It consists of five wheels, placed in front of the iron return yoke. As the central region of the HB has the lowest material thickness with regard to the trajectory of the hadrons, for the central HO wheel two layers of scintillator tiles surround an absorber (iron). The other four wheels are made of scintillator only, using the solenoid coil as absorber. The segmentation and readout of the HO reflects the HBs tower structure, in order to form combined HCAL towers. Considering all contributions from ECAL, HCAL, the solenoid, support structure and the first layer of the iron return yoke, a minimum material thickness of $11.8 \cdot \lambda_I$ is achieved.

- **HCAL Endcaps (HE).** They cover a range of $1.3 < |\eta| < 3.0$ and basically work the same way as the HB. As in the HB, scintillator tiles are being read out collectively as HCAL towers. Their granularity decreases from $\Delta\phi = 5°$ and $\Delta\eta = 0.087$ for $|\eta| < 1.6$ to $\Delta\phi = 10°$ and $\Delta\eta = 0.17$ for $|\eta| > 1.6$. Together with the ECAL, the total material thickness is about $10 \cdot \lambda_I$.

- **HCAL Forward region (HF).** It covers a range of $2.9 < |\eta| < 5.2$, which is not covered by any other detector part. To handle the very high particle fluxes in the forward region of the detector, the design of the HF has to be quite different from the rest of the HCAL. Radiation tolerant quartz fibres are embedded in a $10 \cdot \lambda_I$ long steel absorber. The charged shower particles generate Cherenkov light within the fibres, which are bundled into towers of about $\Delta\phi = 10°$ and $\Delta\eta = 0.175$.

Together, the components of the HCAL cover a range of $|\eta| < 5.2$, which is illustrated in Fig. 2.21 , and only a small range of $< 0.7°$ around the beam direction remains uncovered.

2.2.5 The Muon System

The presence of the term "Muon" in the name of the experiment underlines the importance given to the detection of this kind of particles in CMS. Muons are characterized by a great

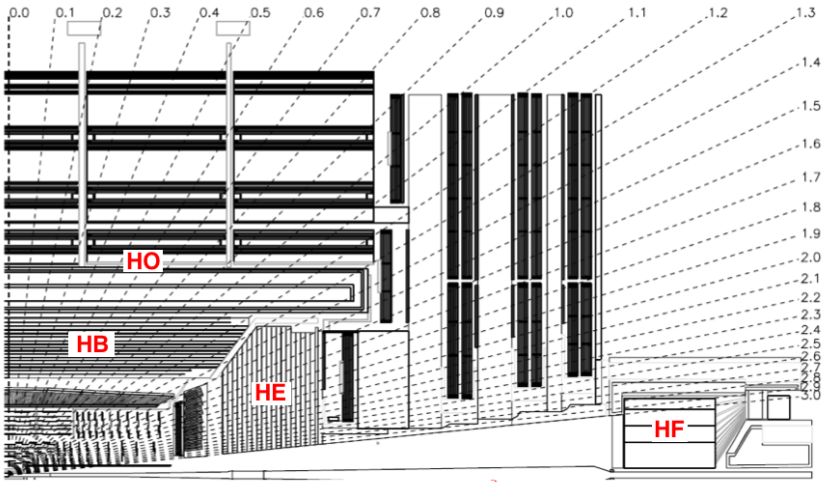

Figure 2.21: *Longitudinal view of one quarter of the HCAL subsystem.*

penetrating power, so they can easily go through the calorimeters and are easy to detect being charged particles. Moreover many of the interesting physical processes in the LHC program are characterized by final states which will involve the presence of high p_T muon. Hence a robust and redundant muon spectrometer is needed to provide precise muon identification, high resolution p_T measurements and effective trigger capabilities.

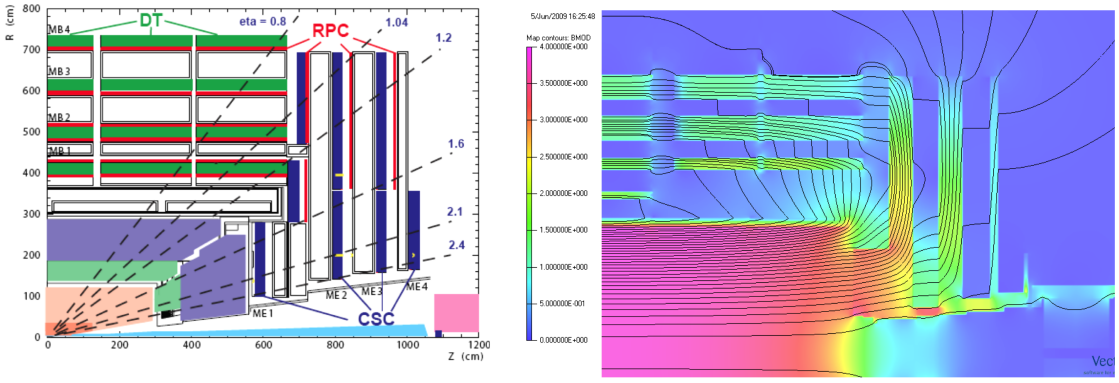

(a) (b)

Figure 2.22: *Longitudinal view of on quarter of the CMS detector. In (a) are showed the various system composing the CMS muons spectrometer, while in (b) are reported the value for the magnetic field in the same regions as calculated by the Tosca [41] simulation.*

The muon system [47] is the outermost group of subdetectors of the CMS experiment, it covers an η region up to 2.4 and is located in the iron yoke for the return of the magnetic field, as shown in Fig. 2.22. It consists of three different types of gaseous detectors, chosen in function of the large surface to be covered, and whose design is driven by the differences in the radiation environment and magnetic field at different values of η. Drift Tubes Chambers (DTs) are used in the barrel (up to $|\eta| < 1.2$) where low track occupancy and residual magnetic field are expected. The endcaps ($0.8 < |\eta| < 2.4$) are instead equipped with Cathode Strip Chambers (CSCs), chosen to cope with the high particle flux and non uniformity of the magnetic field at large η.

In order to ensure redundancy and improve trigger capabilities, Resistive Plate Cham-

bers (RPCs) complement DT and CSC based detectors, both in barrel and endcaps, covering an η region up to 2.1. RPCs allow only coarse spatial resolution measurements, however they are characterized by fast response and their excellent time resolution provides unambiguous BX identification to the muon trigger. For muons up to $p_T \approx 200\ GeV/c$ the system resolution is limited by the multiple scattering of the particle before reaching the first spectrometer station, at higher p_T the precision of the chamber measurements dominates thanks to the larger bending radius.

The resolution is directly proportional to the square root of the amount of material in the muon system in units of X_0 (radiation length) and inversely proportional to the magnetic field. For high p_T ($\sim 1TeV/c$) the momentum resolution is proportional to the spatial resolution of the muon chambers. Up to the last muon station the thickness of the absorber is 16 interaction lengths.

Good muon identification is achieved by absorption of charged particles before the muon system in ECAL and HCAL, and in the muon system by the iron yoke. Moreover, the muon system is able to measure the charge of the muons up to about 1 TeV. The muon system can withstand the harsh radiation environment produced by high rate interactions.

An important issue for the muon system is its alignment, both internally and with respect to the inner tracker. The misalignment originates from imperfect assembly, temperature instabilities or deformations related to the magnetic field. It is important to monitor the alignment, as the measurement of muons is based on the combination on data from muon chambers and from the tracker.

Drift Tubes chambers

The Drift Tubes (DT) are used for the barrel of the CMS muon system because of the large dimensions of the surface to be covered. The CMS regions inside the return yoke of the magnet have the lowest particle rate and radiation doses. The DT system is segmented in 5 wheels along the z direction, each about 2.5 m wide and divided into 12 azimuthal sectors, covering $\sim 30^\circ$ each. Drift tubes are arranged in 4 concentric cylinders - called stations - within each wheel, at different distances from the interaction point, and interleaved with the iron of the yoke.

Each station consists of 12 chambers, with the exception of the outermost station MB4, whose top and bottom sectors are equipped by two chambers each (instead of only one), thus yielding a total of 14 chambers in that station. The overall CMS detector is thus equipped with a total of 250 DT chambers. The dimensions of each chamber are station-dependent. Each chamber is azimutally staggered with respect to the preceeding inner one, in order to maximize the geometrical acceptance.

The basic detector element of the DT muon system is a drift tube cell, whose section is shown in Fig. 2.23(a). The dimensions of a cell are $42mm \times 13mm$ and it has a stainless steel anode wire with diameter $50\mu m$ and length varying from 2 to 4 m. A layer of cells is obtained by two parallel aluminum planes within which a series of I-shaped aluminum beams - 1.2 mm thick and 9.6 mm high - define the boundaries among adjacent cells. Aluminum strips, deposited on either faces of each I-beam and electrically isolated from the I-beam body using Mylar tape, serve as cathodes. Anode wires and cathodes are put at positive and negative voltage (+3600 V, -1800 V) respectively, and provide the electric field within the cell volume.

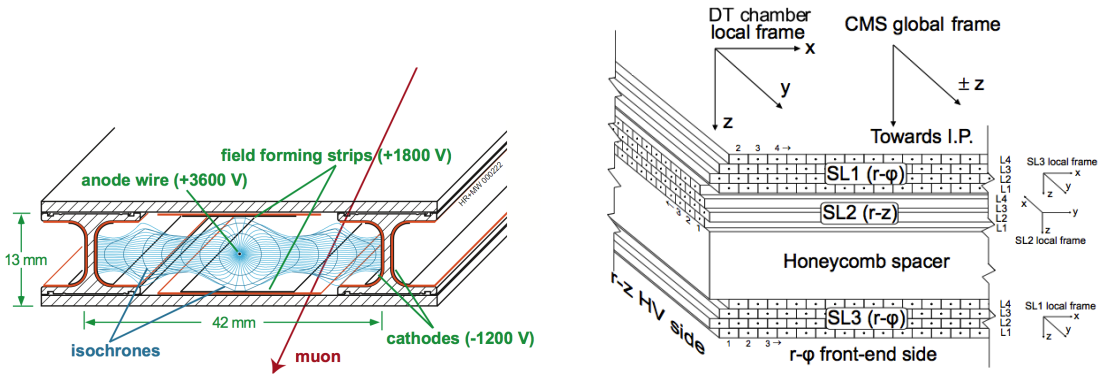

(a) (b)

Figure 2.23: *In (a) transverse view of a drift tube cell, with drift lines and isochrones for a typical voltage configuration of the electrodes. In (b) Cross-section of a barrel muon chamber with the local and global reference frames*

The distance of the traversing track to the wire is measured by the drift time of ionization electrons; for this purpose, two additional positively-biased strips are mounted on the aluminum planes (with an insulator in between) on both inner surfaces in the center of the cell itself, just in correspondence of the anode wire, in order to provide additional field shaping to improve the space-to-distance linearity over the cell (which is crucial for triggering purposes). Typical voltages are +3600 V, +1800 V and -1800 V for wires, strips and cathodes respectively. The tubes are filled with a 80%/20% gas mixture of Ar/CO_2, which provides good quenching properties.

A cross-sectional view of a muon chamber is shown in Fig 2.23(b). Each muon station is instrumented in the transverse plane and in the longitudinal $\theta - z$ plane. The drift cells are assembled in layers, the number of cells depending on the chamber dimensions. Four layers are assembled together to form a quadruplet called superlayer (SL), with neighbouring planes staggered by half a tube, allowing to resolve the left-right ambiguity of a single layer. Each DT station is composed of 3 superlayers, two of which are devoted to the position measurement in the bending plane $r\phi$ (the wires are parallel to the beam line), and one to the measurement of the z-coordinate in the longitudinal plane θz (the wires are disposed orthogonally to the z direction). The only exception is the outermost station MB4, which lacks the SL in the θ-view. In addition, a 128 mm thick honeycomb plate, acting as a rigid but light spacer, is inserted between the inner $\phi - view$ SL and the outer ones. It increases the lever-arm in the bending plane, thus improving the angular resolution.

Cathode Strip Chambers

In the 2 endcap regions of CMS, where the muon rates and background levels are high and the magnetic field is large and non-uniform, the muon system uses Cathode Strip Chambers. CSC chambers are multi-wire proportional chambers with fast response time, fine segmentation, and radiation resistance, so that they can operate at high occupancy levels and in the presence of a large inhomogeneous magnetic field. CSC chambers identify muons between $|\eta|$ values of 0.9 and 2.4, and are arranged in four stations placed between the iron disks of the yoke. The innermost station consists of three concentric rings, the

first (ME1/1) being closer to the interaction point than the other two. The other stations are composed by two disks only.

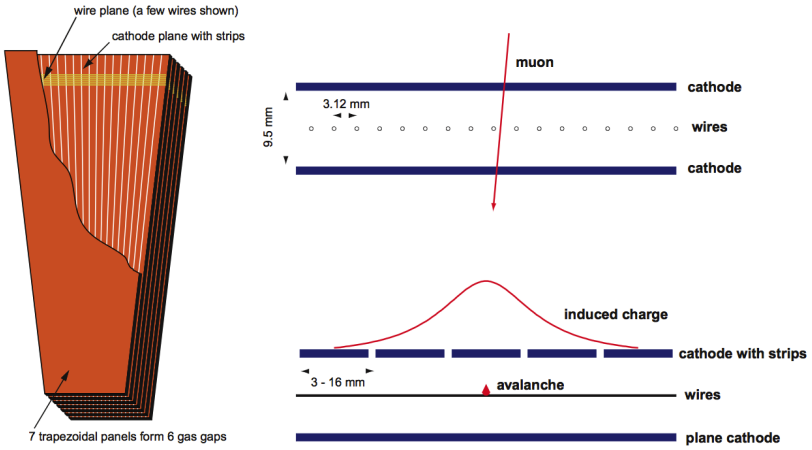

Figure 2.24: *Schematic representation of a CSC chamber (left), and of the effect of a traversing muon in one gap (right)*

The rings are formed by 18 or 36 trapezoidal chambers, which, with the exception of the outermost ring of ME1, are staggered with a small overlap in ϕ. Chambers are composed of six layers, each consisting of an array of anode wires between two cathode planes, as sketched in Fig. 2.24. The gap is 9.5 mm thick and is filled with a 30%/50%/20% mixture of $Ar/CO_2/CF_4$. One of the two cathode planes is segmented into strips orthogonal to the wires.

The avalanche produced in the gap by a crossing charged particle induces a charge in several adjacent strips, an interpolation of the signals gives a precise spatial measurement. Strips are radial and measure the ϕ coordinate. The orthogonal coordinate (r) is measured by the wires which, to reduce the number of channels, are read out in groups of 5 to 16. The resolution is of the order of $\sim 0.5cm$, to be compared with $\sim 150\mu m$ of the strip measurement.

Resistive Plate Chambers

For improving the ability of muon system trigger and measuring the correct beam crossing time when the LHC reaches full luminosity, a complementary, dedicated trigger system consisting of resistive plate chambers (RPC) was added in both the barrel and endcap regions. The RPCs provide a fast, independent, and highly-segmented trigger with a sharp p_T threshold over a large portion of the rapidity range ($|\eta| < 1.6$) of the muon system.

The RPCs are double-gap chambers, operated in avalanche mode to ensure good operation at high rates (in Fig. 2.25 a graphical representation of its operation). They produce a fast response, with good time resolution but coarser position resolution than the DTs or CSCs. They also help to resolve ambiguities in attempting to make tracks from multiple hits in a chamber.

A total of 6 layers of RPCs are embedded in the barrel muon system, 2 in each of the first 2 stations, and 1 in each of the last 2 stations. The redundancy in the first 2 stations allows the trigger algorithm to work even for low-p_T tracks that may stop before

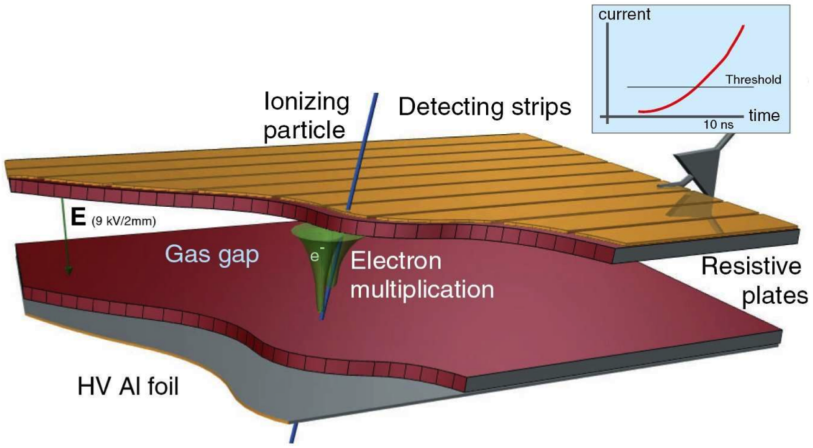

Figure 2.25: *Graphical representation of an RPC gap.*

reaching the outer 2 stations. In the endcap region, there is a plane of RPCs in each of the first 3 stations in order for the trigger to use the coincidences between stations to reduce background, to improve the time resolution for bunch crossing identification, and to achieve a good p_T resolution.

2.2.6 CMS Trigger System

When running at its design luminosity, the LHC will deliver bunch crossings every 25 ns, each causing about 20 particle interactions. Most of these events are soft, i.e. no new particles are produced during the collision. Storing the data of all of these events is neither practicable with todays technology nor necessary. In order to select only interesting events and thus to reduce the event rate which has to be processed, a trigger system has been developed for CMS. It consists of two logic stages (Fig. 2.26).

- The Level 1 triggers (L1 [48]) are hardware based online triggers, meaning that they decide whether to save the events or not, directly after they have been recorded by the detector. In fact, the decision has to be made within 3 μs after each collision, because the data saved in the buffer are overwritten after this period. The L1 triggers lead to a reduction of the event rate from 40 MHz to 100 kHz, which is low enough to be saved and transferred to a computer farm.

- Events passing the L1 trigger are transferred to a computer farm, where they are processed by the second stage of the trigger system, the High Level Trigger (HLT [49]). It is a software based offline trigger, that has more time for making decisions. Thus, it can use reconstruction algorithms to further reduce the event rates. Only permanently storing events that at least passed one HLT criteria, leads to a reduction of the event rate from 100 kHz to 100 Hz, which corresponds to the manageable rate 100 MB/s to be stored on tape.

Different triggers exist for each of the trigger stages, which are specialised for finding special event types. L1 trigger is organized into three major parts: the L1 calorimeter trigger, the L1 muon trigger, and the L1 global trigger. For sub-L1-systems, the calorimeter trigger preserves the tower energy sums from the ECAL, HCAL and HF individual cells

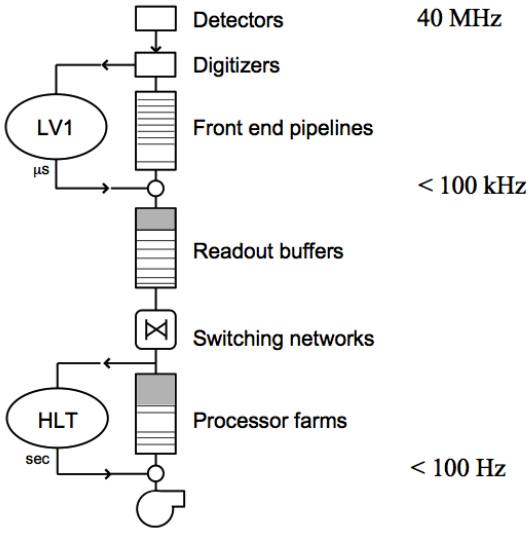

Figure 2.26: *Data flow in the CMS Trigger system. Two consecutive processing stages are implemented: level-1 and High Level Triggers.*

(or towers) and reconstructed candidates of electrons, photons, taus and jets. Thresholds are added on these particle candidates.

In design, for instance, the transverse missing energy trigger requires the events with MET (Transverse Missing Energy) greater than 100 GeV, but at the very first low luminosity this trigger was not enabled. The muon subtrigger focuses on μ preselecting. Information from DT, CSC and RPC is used to drop events with low quality muons. The global muon trigger converts muon tracks from different chambers into the same η, ϕ and p_T scale, then to correlate the tracks.

Another important task for global muon trigger is to identify whether the muon is isolated or not via vetoing the event with an $\eta\phi$ grid of unquiet calorimeter towers. The global L1-subtrigger holds a time match on these information from both calorimeter and muon chambers, and decides to accept or reject each bunch crossing based on the programmed logical combination. The CMS data acquisition system processes events accepted by the first-level trigger at a maximum input rate of a few 100 kHz. Event data are read out from the detector and stored in readout buffers at a total rate of 1 Terabit/s. The event-builder then assembles event fragments into full events employing a large switching network.

The high-level trigger algorithms run on a farm of commercial processors. Each event is processed by a single processor, which has access to the full raw event data. High level-trigger reconstruction code will be as close as possible to the full offline analysis code, the main differences resulting from limited processing time and the possible lack of precise calibration constants. The following three key features of HLT software guarantee minimal processing time:

- *Reconstruction on demand.* Trigger objects are only reconstructed if needed in the trigger decision. Unnecessary calculations are avoided by rejecting events as early as possible using fast algorithms. The reconstruction and selection therefore take place in several stages (virtual trigger levels), which roughly correspond to the functions of traditional second and third trigger levels. There is no limitation to the

number of virtual trigger levels or to the algorithms employed except for CPU time. For historic reasons the terminology Level- 2 is used for a first high-level trigger stage based on data from the muon systems and calorimeters while Level-3 refers to algorithms including tracker data.

- *Partial/Region reconstruction*: only parts of detector information are analysed guided by the trigger objects found in the preceding trigger levels.
- *Conditional reconstruction.* Reconstruction is aborted if further calculations would not alter the result (for example when reconstructing additional tracks in an isolation algorithm) or if the condition arises that resulting trigger object would not be relevant to the trigger decision.

HLT available algorithm changed a lot since the startup, in order to follow the luminosity delivered by LHC. Events that have passed the HLT reach the CERN Tier 0 (Section 2.1.5) for the recostruction and are then distributed on the GRID for an easy access for all the CSM collaboration.

Chapter 3

Charged Particle and Muons in CMS

3.1 Recostruction Software in CMS

The objects reconstruction in CMS is implemented in the CMSSW [43] software framework. A schematic overview of the software framework is given in Fig. 3.1.

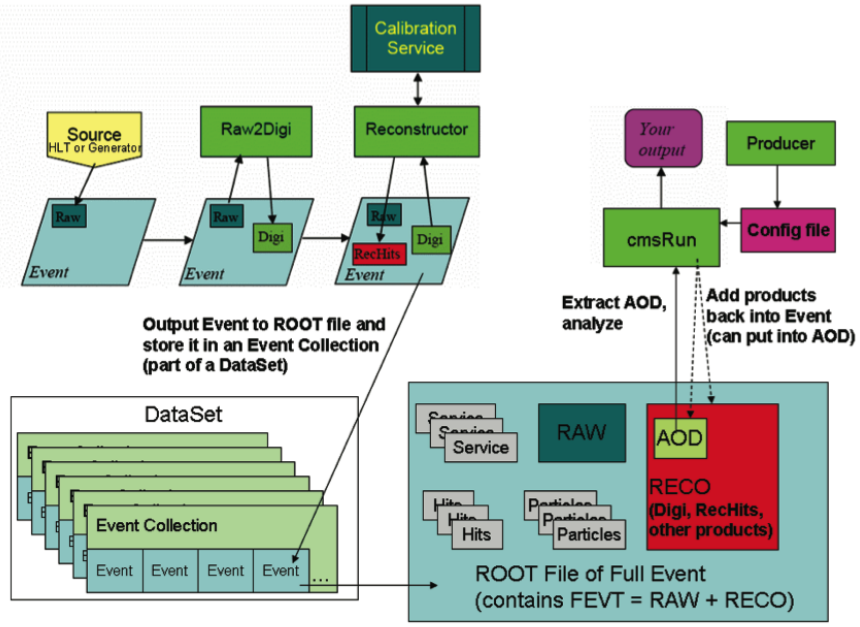

Figure 3.1: *A schematic overview of the software framework.*

Data is stored in the EDM, which is capable to hold different types of data from Monte Carlo simulations, raw detector readout, or reconstructed high level objects needed for the physics analysis. The CMSSW framework is modularized so that are loaded only those parts of the software which are necessary for the individual job. As mentioned in Chapter 2.2.6, on the HLT computer farm a lighter and faster version of the CMS software is run for preselecting the events coming from the detector.

The CMS event data model is centred around the concept of an Event as a C++ object container for all RAW and reconstructed data pertaining to a physics event. During processing, data are passed from one module to the next via the Event, and are accessed

only through the Event. The CMSSW framework implements a software bus model wherein there is one executable and many plug-in modules which run algorithms. This allows to use the same executable for both detector and Monte Carlo data. The CMSSW executable, cmsRun, is configured at run time by the users job-specific configuration file programmed in Python. This file tells cmsRun which data to use, which modules to run, which parameter settings to use for each module, and in what order to run the modules. Required modules are dynamically loaded at the beginning of the job.

In order to compare the results obtained in data with the predictions, various Monte Carlo (MC) techniques are used in CMS to produce simulated events. Standard Model samples are produced with the CTEQ6L [80] set of parton distribution functions and different event generators are used depending on the considered process. The more common are PYTHIA 6 [84], Evtgen [75], POWHEG [81] and Madgraph [23]. Generated events are processed through a full GEANT4 [21, 22] detector simulation, trigger emulation and event reconstruction chain.

3.2 Charged particles reconstruction in the CMS tracker

The CMS tracking software [20] is implemented in the computing framework of the experiment (CMSSW) and is known as the 'Combinatorial Track Finder' (CTF). Before this standard track reconstruction sequence begins, a fast pixel-only track and vertex reconstruction step is run in order to locate the primary vertices in the event. Pixel hits from at least three layers are found and fit using a fast pattern recognition and helix fitter [51]. These pixel standalone tracks are used both in the online, high-level trigger, and in the full general tracking that will be described in the next sections. These standalone pixel tracks are also used to make fast vertexes in the high level trigger to find the z-position of primary hard interactions. In the high level trigger, this information is used for b-hadron tagging, τ-lepton tagging, and to help calculate calorimetric isolation quantities.

In CMS, the standard track collection is derived from multiple passes of the track reconstruction sequence in a process called *iterative tracking* [79]. The basic philosophy of iterative tracking is that by removing the hits associated with already found tracks, it is possible to find additional tracks by reducing the combinatorics and relaxing the selection criteria. Each iteration is designed to find a particular class of tracks and the number and configurations are frequntly changed accordingly with the LHC operation. At the beginning of each iteration, hits already used to produce a good quality track in the previous iterations are masked off.

Each reconstruction iteration proceeds in four steps:

- The seed generation provides initial track candidates using only a few (2 or 3) hits. A seed defines the initial trajectory parameters and uncertainties.
- The track finding is based on a global Kalman filter [69] and extends the seeds to find other hits on a potential track, corresponding to the trajectory taken by a charged particle.
- The final track fitting module is used to provide the best possible estimate of the parameters of the trajectories by means of a Kalman filter and smoother.

- The final track selection sets quality flags and discards tracks which fail certain criteria.

The main differences in the configuration of the iterations are the seed generation and final track selection.

3.2.1 Seed generation

The trajectory seeds define the starting trajectory parameters and uncertainties of potential tracks. In the uniform magnetic field present in the track, charged particles follow helices and therefore five parameters (including the trajectory curvature) are needed to define a starting trajectory. To obtain these five parameters requires at least 3 hits, or 2 hits and a beam constraint. To limit the hit combinations, seeds are required to satisfy loose criteria such as minimum transverse momentum and consistency with originating from the proton-proton interactions region.

Seeds are constructed starting from the pixel layer because granularity of the pixel detector ensures that the average occupancy of the inner pixel layer is much less than the average occupancy of the outer strip layer (Fig. 3.2) and to maintain high efficiency.

In fact due to the mass of the Tracker, many particles produced in LHC collisions suffer destructive interactions before exiting the Tracker. Although most high p_T muons traverse the entire Tracker, between 5% and 15% of the produced pions interact inelastically in the Tracker (Fig. 3.3). In addition, many electrons lose a significant fraction of their energy due to bremsstrahlung radiation in the Tracker.

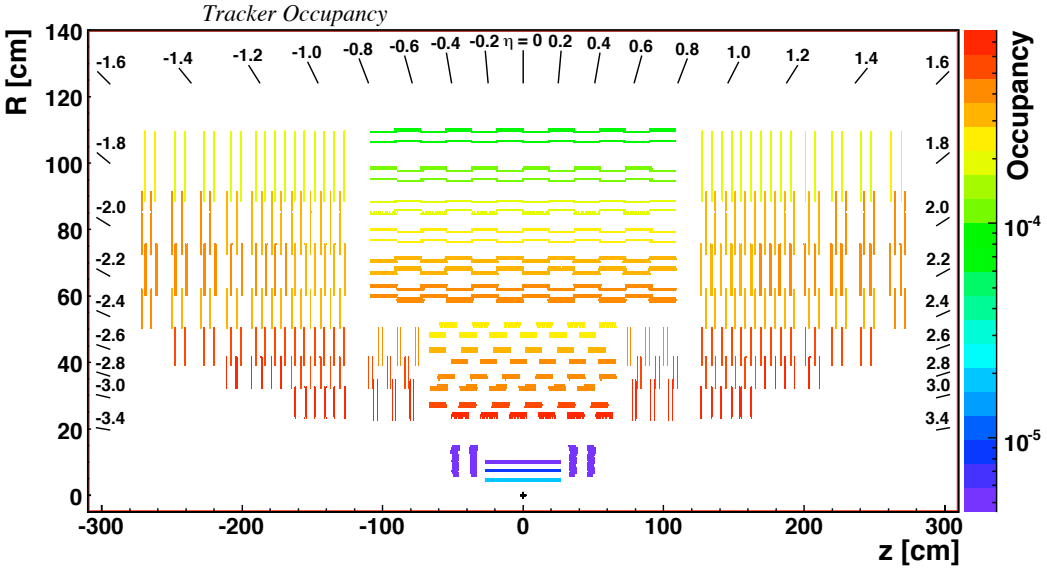

Figure 3.2: *Occupancy of the Silicon Tracker detectors for Minimum Bias events simulated with superimposed pile-up collisions.*

More than 90% of charged particles produced in LHC collisions inside the geometrical acceptance of the Tracker cross 3 pixel layers and therefore can be reconstructed starting from trajectory seeds obtained from triplets of pixel hits. To recover inefficiencies in the pixel detector (from gaps in coverage, non-functioning modules, and saturation of

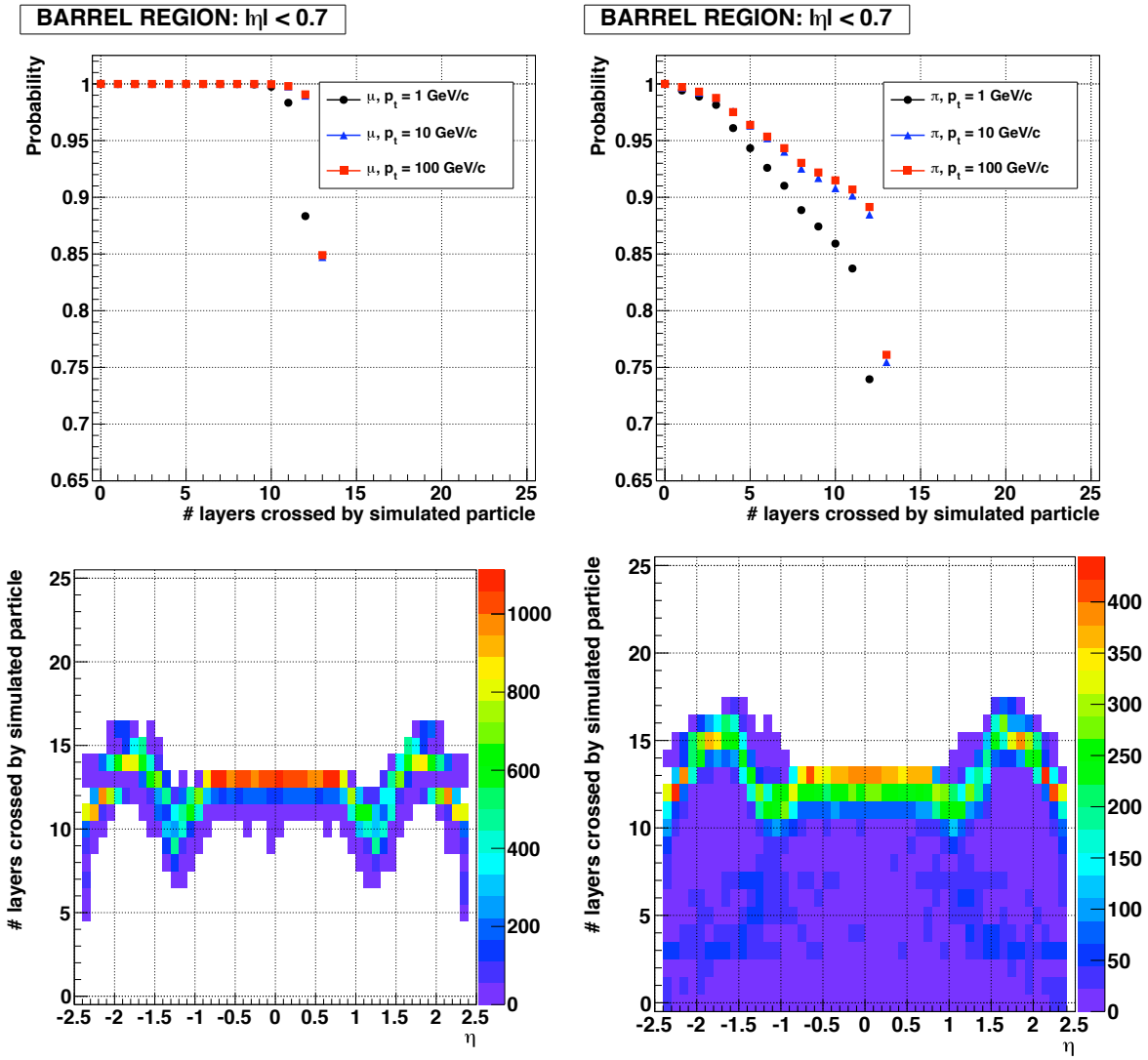

Figure 3.3: *The top plots show the probability that muons (left) and pions (right) of different momenta are not absorbed by the detector material as a function of the number of Tracker layers crossed in the barrel region. The bottom plots show the number of crossed layers versus pseudorapidity for muons (left) and pions (right) with transverse momentum equal to 10 (1) GeV/c [20].*

the readout) and to reconstruct particles not originating directly from the proton-proton collisions other kind of seeds are created using mixing information coming from the strip detector.

3.2.2 Track Finding

The track finding module of the CTF algorithm is based on the Kalman filter method. The filter proceeds iteratively from the seed layer, starting from a coarse estimate of the track parameters provided by the trajectory seed, and includes the information of the successive detection layers one by one. The information provided at each layer includes the location and uncertainty of any found hit as well as the amount of material crossed which is used to estimate the uncertainty arising from multiple Coulomb scattering. Each iteration of the Kalman filter is implemented in four steps.

The first step, navigation, uses the parameters of the track candidate, evaluated at the current layer, to determine which adjacent layer(s) of the tracking detector would be intersected by the extrapolated trajectory, allowing for the current uncertainty on that trajectory.

The second step is a search for compatible *detectors* on the layers returned by the navigation step.

The third step forms groups of hits, obtained by collecting all the hits from each detector.

The fourth and last step is to update the trajectory state. One or more new track candidates are formed from each of the original ones, by adding to them exactly one of the compatible hits from each detector grouping (where this hit may be the invalid hit). The candidate's trajectory parameters are then updated at the new detector surface, by combining the information from the hit with the extrapolated track trajectory of the original candidate.

For the second, third and fourth steps above, a more accurate *material propagator* is used which includes the effect of material in Tracker. This differs from the simple analytical propagator, in that it inflates the uncertainty on the trajectory parameters according to the predicted rms scattering angle in the Tracker material. It also adjusts the momentum of the trajectory according to the mean energy loss predicted by the Bethe-Bloch equation.

After a track candidate has completed the outward search for hits, an inward search for hits is begun. This is started by taking all of the hits assigned to the track, excluding those belonging to the track seed, and using them to make a new trajectory. Then, following the steps above, this trajectory is propagated inward through the seeding layers and then further inwards until the inside edge of the detector is reached or too many invalid hits are found.

The track of a single charged particle may be reconstructed more than once, either by starting from different seeds or when a given seed develops into more than one track candidate. To remedy this feature, a "trajectory cleaner" is applied after all the track candidates in a given iteration have been found. The trajectory cleaner calculates the fraction of shared hits between two track candidates:

$$f_{shared} = \frac{N_{shared}^{hits}}{min(N_1^{hits}, N_2^{hits})} \tag{3.1}$$

where N_1^{hits} (N_2^{hits}) is the number of hits in the first (second) track-candidate. If this fraction exceeds the (configurable) set value of 19%, the trajectory cleaner removes the track with the least number of hits; if both tracks have the same number of hits, the track with the largest χ^2 value is discarded. The procedure is repeated iteratively on all pairs of track candidates. The same algorithm is applied when tracks from the six iterations are combined into a single track collection.

3.2.3 Track Fit

For each trajectory, the track finding stage results in a collection of hits and an estimate of the track parameters. However, the full information is only available at the last hit of the trajectory and the estimate can be biased by constraints applied during the seeding stage.

The Kalman filter is initialized at the location of the innermost hit with the trajectory estimate obtained during seeding. The corresponding covariance matrix is scaled up by a large factor in order to avoid any bias. The fit then proceeds in an iterative way through the full list of hits, updating the track trajectory estimate with each hit in turn. For each valid hit, the hit's position estimate is re-evaluated using the current values of the track parameters. To obtain ultimate precision, this filtering and smoothing procedure uses a *Runge-Kutta propagator* to extrapolate the track trajectory from one hit to the next. This not only takes into account the effect of material, but is also able to accommodate an inhomogeneous magnetic field.

Estimates of the track trajectory at other points, such as the point of closest approach to the beam-line, can be obtained by extrapolation from the trajectory evaluated at the nearest hit. This extrapolation also uses the Runge-Kutta propagator.

After filtering and smoothing, a search is made for spurious hits (*outliers*), wrongly associated to the track. These hits can be correlated with the otherwise well-defined track, e.g. from δ-rays, or uncorrelated, such as hits from nearby tracks or electronic noise. There are two methods which are used to find outliers.

3.2.4 Pions Track Reconstruction

The CMS tracker doesn't have a particle recognition system and the trajectory parameters propagator assumes that the mass of the particle is that of a pion, which is the most common particle among those originating from LHC collisions. Charged pions undergo multiple scattering and energy loss by ionization, as they cross the tracker volume. Moreover, like all hadrons, pions are also subject to elastic and inelastic *nuclear* interactions.

The elastic nuclear interactions introduce long tails in the distribution of the scattering angle, beyond what would be expected assuming simple Coulomb scattering. The current implementation of the track finding algorithm assumes that the track trajectory is modelled by the 'material propagator'. This takes into account Coulomb scattering, but neglects elastic nuclear interactions. As a result, the building of a track can be interrupted if it undergoes a large elastic nuclear scatter.It may then be reconstructed as a single track with fewer hits, or as two separate tracks. Or it may not be found at all. Elastic nuclear interactions, not only reduce the global efficiency of the track finding software, but they also lower the algorithmic efficiency, since the hits are present, but not assigned to the

track.

Inelastic nuclear interactions are the main source of tracking inefficiency for hadrons, in particular in those regions of the Tracker where the material budget is large, so that the probability of particles undergoing nuclear interactions is higher. The products of the nuclear interaction are usually emitted with trajectories approximately tangential to that of the incoming particle. As a result, it is not uncommon for the trajectory builder to combine the hits of the primary particle with those of a secondary particle, in a single track.

The degradation in the purity of the hits on track is more accentuated for high energy hadrons than for low energy ones: indeed the probability that the trajectory builder merges together separate tracks increases with the energy of the primary hadrons because of the larger number of secondary particles that are produced in the interaction and because of the smaller variation between the curvature of the primary particle and that of the secondary particles.

The merging of hadron trajectories affects significantly the efficiency and fake rate distributions depending on which cut is used in the definition of correctly-reconstructed tracks.

In general, the merging of separate trajectories during reconstruction is more common in the transition and end-cap regions of the tracker, due to the higher material budget. In the barrel-end-cap transition region, the probability the reconstruction algorithm returns merged trajectories is even higher because of the large extrapolation length during some iterations of the track finding module in which the trajectory builder navigates from barrel to end-cap layers. The result of this effects is shown in the efficiency of single particle simulation as function of η reported Fig. 3.4(a). While the fake rate is generally lower than 1% for pions with a transverse momentum of 1 or 10 GeV/c, the probability that a 100 GeV/c pion is incorrectly reconstructed peaks to about 10% for particles produced with $|\eta|$ around 1.5.

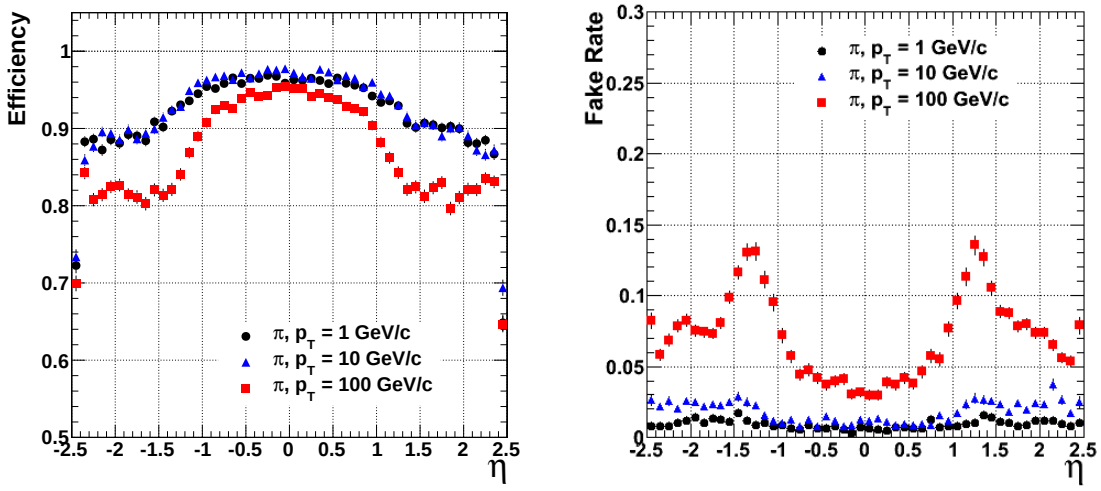

(a) (b)

Figure 3.4: *Global track reconstruction efficiency (left) and fake reconstruction (right) rate as a function of η for simulated pions of transverse momenta of 1, 10 and 100 GeV/c [20].*

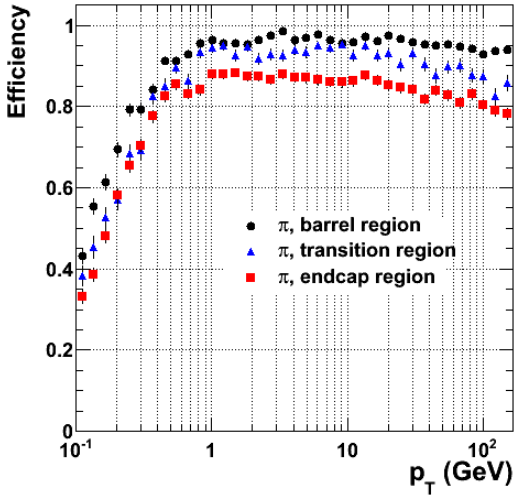

Figure 3.5: *Global track reconstruction efficiency for simulated pions as a function of p_T in different regions of the Tracker [20]*

In Fig. 3.5 the tracking efficiency as a function of the particle transverse momentum showed. It is approximately constant in the p_T range between 5 and 30 GeV/c, but below 5 GeV/c it starts decreasing because lower energy pions have a larger nuclear cross section.For transverse momenta below 0.8 GeV/c it decreases quickly from about 80% to zero.

Pion Tracking Efficiency from data

In the previous paragraph pions efficiency were extracted from simulation With the start of LHC operation the relative efficiency of reconstructing pion tracks in data and simulation can be determined by measuring the ratio of neutral charm-meson decays to final states of four or two charged particles ([6]). Specifically, it's measured the production rate for $D^0 \to K^-\pi^+\pi^-\pi^+$ ("$K3\pi$") relative to that for the two-body decay $D^0 \to K^-\pi^+$ ("$K\pi$") in both data and simulated samples. To increase the purity and provide a common production source, D^0 decays are reconstructed in the chain $D^{*+} \to D^0\pi^+$. Assuming that the kinematic properties of the two decay modes are properly reproduced in the simulation, the ratio of efficiency-corrected signal yields,

$$\mathcal{R} = \frac{N_{K3\pi}}{N_{K\pi}} \cdot \frac{\epsilon_{K\pi}}{\epsilon_{K3\pi}}, \tag{3.2}$$

should be equal to the world-average ratio of branching fractions $\mathcal{R}$(PDG). The relative tracking efficiency for pions in data and simulation can then be estimated as

$$\frac{\epsilon(\text{data})}{\epsilon(\text{MC})} = \sqrt{\frac{\mathcal{R}}{\mathcal{R}(\text{PDG})}}, \tag{3.3}$$

where $\mathcal{R}(\text{PDG}) = 2.08 \pm 0.05$ [24].

The yields in data and simulated samples are determined using an unbinned maximum-likelihood fit to the ΔM distributions for events reconstructed using the same selection criteria. For data events are reconstructed in a sample corresponding to an integrated

luminosity of approximately 0.47 nb^{-1}. Figure 3.6 shows fits of ΔM for the $K\pi$ and $K3\pi$ samples requiring $p_T > 5.5 GeV/c$ for the D^* candidates, which are used for the primary measurement result since it balances the two competing effects of background level and the kinematic range for the lowest momentum tracks.

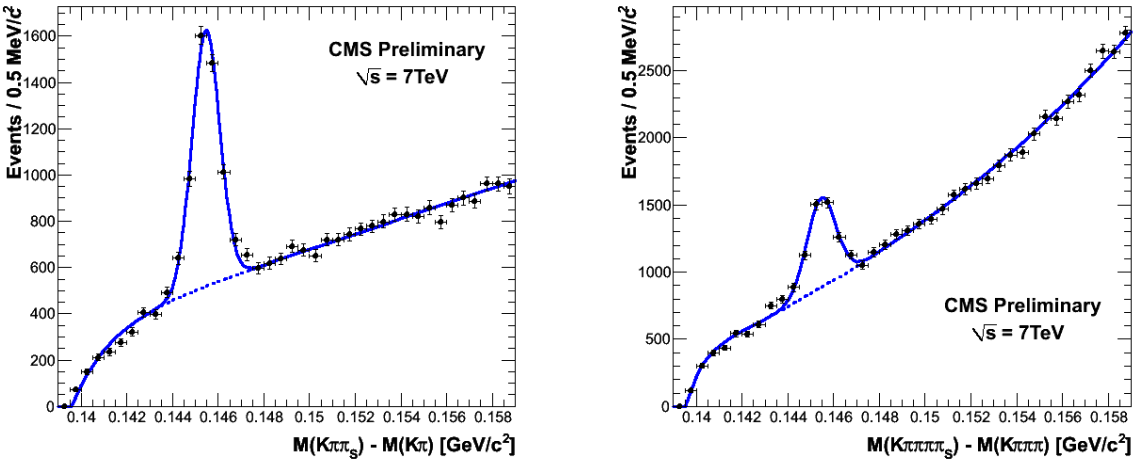

Figure 3.6: *Distribution of ΔM for $K\pi$ (left) and $K3\pi$ (right) events reconstructed in data requiring $p_T > 5.5 GeV/c$ on the D^* candidates.*

The ratio $\mathcal{R}$ is measured from the fitted signal yields and efficiencies obtained from simulation, and then Eq. 3.3 is used to determine the ratio of tracking efficiencies in data and simulation as a function of the minimum p_T on the D^* candidates. Fig. 3.7 shows the resulting ratio of tracking efficiencies, where values consistent with unity, within the statistical uncertainties, are found.

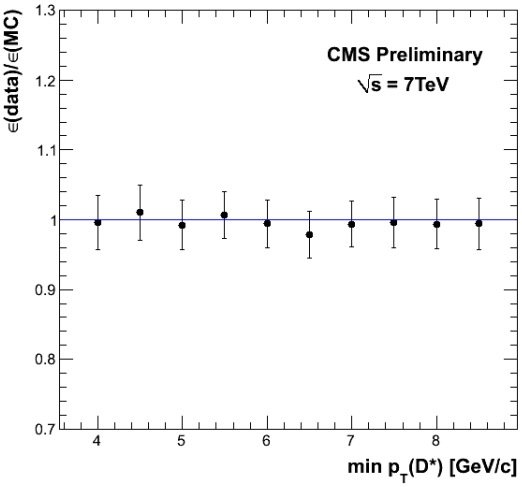

Figure 3.7: *The ratio of tracking efficiency in data and simulation as a function of the minimum p_T for the D^* candidate. The uncertainties are statistical only, and are correlated between bins due to the overlapping data samples.*

Several sources of systematic uncertainty have been considered on the measurement of $\mathcal{R}$, and its interpretation as the square of the ratio of tracking efficiency in data and simulation. The final result is $\epsilon(\text{data})/\epsilon(\text{MC}) = 1.007 \pm 0.034 \pm 0.014 \pm 0.012$, where the first uncertainty is statistical, the second is systematic, and the third comes from the error on $\mathcal{R}$(PDG). The total uncertainty on pion tracking efficiency is then estimated to be 3.9%.

3.3 Primary Vertex Reconstruction

The term "Primary Vertex" refers to the reconstruction of the point of the proton-proton interaction. Vertexes originated from the subsequent decay of prompt particles are referred as "Secondary Vertex". In the primary vertex reconstruction [82], the measurements of the location and uncertainty of an interaction vertex are computed from a given set of reconstructed tracks. The prompt tracks originating from the primary interaction region are selected based on the transverse impact parameter significance with respect to the beam line (see section 3.3.1), number of strip and pixel hits, and the normalized track χ^2. To ensure high reconstruction efficiency in the minimum bias events, there is no requirement on the track transverse momentum.

In the reconstruction of CMS data in 2009 and 2010, the selected tracks were then clustered based on their z coordinates at the point of closest approach to the beam line. Vertex candidates were formed by grouping tracks that are separated in z by less than a distance z_{sep} (typically in the range 2 mm to 1 cm) from their nearest neighbour. Small values of z_{sep} can lead to splitting tracks from one interaction into two separate vertices. However, vertices closer than z_{sep} will always be merged. This algorithm is therefore inefficient for running with multiple pp interactions per crossing.

For the reconstruction of CMS data in 2011, when pile-up becomes more relevant, tracks are clustered using a deterministic annealing (DA) algorithm [58, 73]. The z-coordinates of the points of closest approach of the tracks are referred to as z_i, and the associated uncertainty is σ_i. The tracks must be assigned to some unknown number of vertices at positions z_k. The assignment probability of track i to vertex k is described by p_{ik}, having values between 0 and 1. The procedure then finds the most likely distribution of assignments for a given $< \chi^2 >= \sum_{ik} p_{ik} \frac{(z_i - z_k)^2}{\sigma_i^2}$, referred to as the "principle of maximum entropy".

Candidates containing at least two tracks are then fit with an adaptive vertex fit [70] to compute the best estimate of vertex parameters such as position and covariance matrix, as well as the indicators of the success of the fit, such as the number of degrees freedom of the vertex and track weights of the tracks in the vertex.

In the adaptive vertex fit, to each track in the vertex is assigned a track weight between 0 and 1 based on its compatibility with the common vertex. For a track consistent with the common vertex, its weight is close to 1. The number of degrees of freedom is defined as $n_{\text{dof}} = 2 \sum_{i=1}^{nTracks} w_i - 3$, where w_i is the weight of the i^{th} track. It is thus strongly correlated to the number of tracks compatible with the primary interaction region. For this reason, the number of degrees of freedom of the vertex can be used to select real proton-proton interactions.

The primary vertex resolution depends strongly on the number of tracks used in fitting

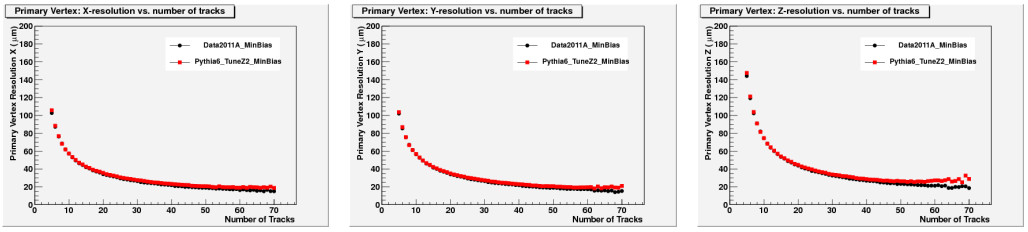

(a) (b) (c)

Figure 3.8: *Primary vertex resolution in x (a), y (b), and z (c) as a function of the number of tracks used in the fitted vertex [20]. The Pythia8 Tune 1 is used in the simulation.*

the vertex and the p_T of those tracks. It's also of great importance to have a good vertex resolution in particular for estimating the life-time of long lived prompt particles, like the b-mesons, which is done by measuring the distance between primary and secondary vertexes. In order to measure in a data sample the resolution as a function of the number of tracks in the vertex a method as been developed,called *split method*.

The tracks used in the vertex in an event are split evenly into two different sets. During the splitting procedure, the tracks are ordered in descending order of p_T first and then grouped in pairs starting from the track with largest p_T. In each pair, tracks are randomly assigned to one or the other track set. This procedure ensures that the two split track sets have the same kinematic distributions on average. These two different track sets are then fitted independently with the adaptive vertex fitter. The distributions of the difference in the fitted vertex positions for a given number of tracks are fit with a single Gaussian distribution to extract the resolution.

Fig. 3.8 shows the measured primary vertex resolutions in x (a), y (b), and z (c) as a function of the number of tracks. Results are shown for both minimum-bias-triggered data and simulation and a good agreement in the curves is seen. The resolutions in x and y are observed to be consistent. For minimum bias events, the resolutions in $x(y)$ and z are found to be below $20\mu m$ and $25\mu m$ for the primary vertexes using more than 50 tracks.

In order to estimate the vertex reconstruction efficiency given a set of tracks clustered in z which forms a reconstructed vertex, it's checked how often its position is consistent with the true value. Similar to the primary vertex resolution, the primary vertex efficiency also strongly depends on the number of tracks in the cluster. The split method can be used to measure the primary vertex reconstruction efficiency as a function of the number of tracks in the cluster. Fig. 3.9 shows the measured primary vertex efficiency as a function of the number of tracks that are clustered in z. The results obtained using the split method described above are applied to both data and simulation and good agreement between the two is observed. The primary vertex efficiency is estimated to be close to 100% if there are more than two tracks with transverse momenta greater than 0.5 GeV/c in the vertex.

3.3.1 Reconstruction of the LHC Beam Line

The beam line (referred also as *beamspot*) represents the three-dimensional profile of the luminous region where the LHC beams collide at CMS. The beam line is determined in an

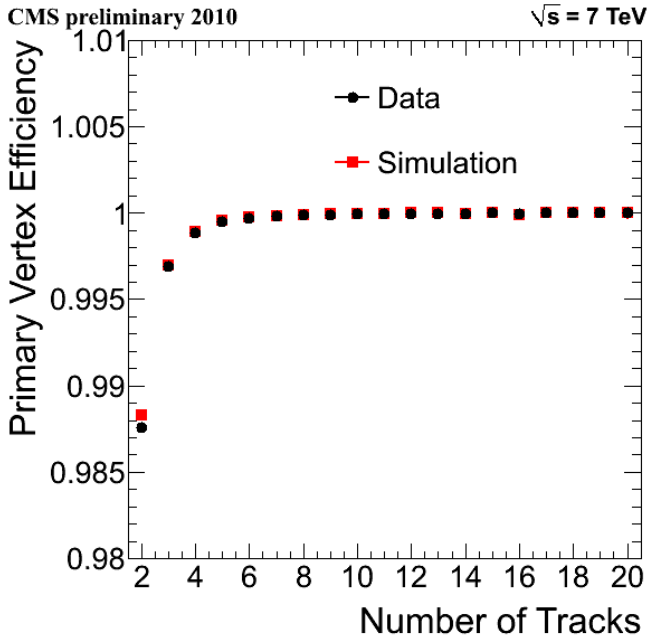

Figure 3.9: *Primary vertex efficiency as a function of the number of tracks in a cluster [20]*

.

average over many events, in contrast to the event-by-event primary vertex which gives the precise position of a single collision. A good measurement of the position and slope of the beam line is an important component of the event reconstruction. The beam line position can be used, especially in the high level trigger, as an estimate of the primary interaction point prior to the reconstruction of the primary vertex and even as the primary interaction point in low multiplicity data. This position can be determined in two ways. The first is through the reconstruction of primary vertexes. The reconstructed vertexes map out the collisions and thus the shape of the beam line. The mean position in x, y, and z can be determined from a likelihood fit to the 3D distribution of vertexes.

The second method exploits a correlation between the transverse impact parameter (d_{xy}) and the azimuthal angle of tracks (ϕ_0) that exists when the beam line is displaced from the expected position. To first order the d_{xy} for tracks coming from the primary vertex can be parametrized by

$$d_{xy}(\phi_0, z) = x_0 \cdot \sin\phi_0 + \frac{dx}{dz} \cdot \sin\phi_0 \cdot z - y_0 \cdot \cos\phi_0 - \frac{dy}{dz} \cdot \cos\phi_0 \cdot z, \tag{3.4}$$

where x_0 and y_0 are the position of the beam at $z = 0$, and $\frac{dx}{dz}$ and $\frac{dy}{dz}$ are the x and y slopes of the beam. The beam line fit [76] uses an iterative χ^2 fit to exploit this correlation between d_{xy} and ϕ_0. With a sample of 1000 tracks, the position can be determined with a statistical precision of ~ 5 μm.

Figure 3.10 shows the fitted positions as a function of time during one part of one fill in which LHC performed a luminosity scan. While the beam position is normally stable, during this scan the position in y was adjusted by LHC operators during the fill. No points are plotted for LS where an insufficient number of tracks or vertexes were reconstructed to fit the beam line. The plots show that the two methods give consistent results and CMS is able to track well the movements of the beam.

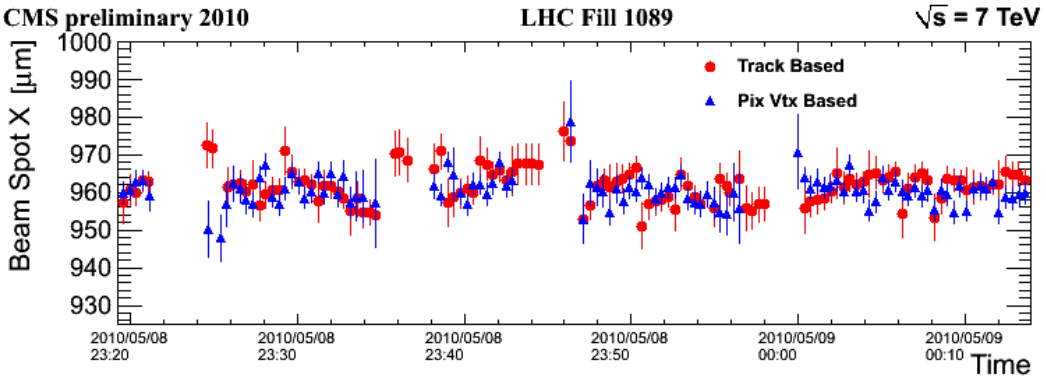

Figure 3.10: *Fitted x_0 (top), y_0 (middle) and z_0 (bottom) positions of the beam line as a function of time during an LHC fill where a luminosity scan was performed [20].*

3.4 Muon reconstruction

In Section 3.2 the charged tracks reconstruction in the central tracker has been described. In the charged tracks also muons are included, which then can reach the muon chamber in the return yoke of the magnetic field. In the standard CMS reconstruction for pp collisions [35, 39], tracks are first reconstructed independently in the silicon tracker (*tracker track*) and in the muon spectrometer (*standalone-muon track*). Based on these, two reconstruction approaches are used:

1. *Global Muon reconstruction (outside-in).*Sstarting from a standalone muon in the muon system, a matching tracker track is found and a *global-muon track* is fitted combining hits from the tracker track and standalone-muon track. At large transverse momenta ($p_T \gtrsim 200$ GeV/c), the global-muon fit can improve the momentum resolution compared to the tracker-only fit [35, 39].

2. *Tracker Muon reconstruction (inside-out).* In this approach, all tracker tracks with $p_T > 0.5$ GeV/c and $p > 2.5$ GeV/c are considered as possible muon candidates and are extrapolated to the muon system, taking into account the expected energy loss and the uncertainty due to multiple scattering. If at least one muon segment (i.e. a short track stub made of DT or CSC hits) matches the extrapolated track, the corresponding tracker track qualifies as a *tracker-muon track*. The extrapolated track and the segment are considered to be matched if the distance between them in local x is less than 3 cm or if the value of the pull for local x is less than 4. At low momentum (roughly $p < 5$ GeV/c) this approach is more efficient than the global muon reconstruction, since it requires only a single muon segment in the muon system, whereas global muon reconstruction is designed to have high efficiency for muons penetrating through more than one muon station.

The majority of muons from collisions (with sufficient momentum) are reconstructed either as a Global Muon or a Tracker Muon, or very often as both. However, if both approaches fail and only a *standalone-muon track* is found, this track is also added to the general collection of muons (and classified as Standalone-muon), even if muons of this kind are not usually used in the physics analyses.

The final result is a a single collection of muon candidates, each one containing information from the standalone, tracker, and global fit, when available. Candidates found both by the Tracker Muon and the Global Muon approach that share the same tracker track are merged into a single candidate. Similarly, standalone-muon tracks not included in a Global Muon are merged with a Tracker Muon if they share a muon segment.

The combination of different algorithms provides a robust and efficient muon reconstruction. A given physics analysis can achieve the desired balance between identification efficiency and purity by applying a selection based on the muon identification variables. The default algorithm for muon momentum assignment, dubbed the "sigma-switch", chooses the global fit if both the global and tracker-only fit estimate the muon transverse momentum (p_T) to be above 200 GeV/c and if the results of the two fits for q/p agree to within two sigma of the tracker-only fit, otherwise it chooses the tracker-only fit.

3.4.1 Muons reconstruction in the Inner Tracker

Muons are the charged particles that are best reconstructed in the Tracker. They mainly interact with the silicon detector through ionization and their energy loss by bremsstrahlung is generally negligible, except when muons are produced with an initial energy higher than about 100 GeV. Therefore these particles usually cross the whole volume of the tracking system, producing detectable hits on *all* the sensitive layers of the apparatus. Finally, muon trajectories are scattered exclusively by Coulomb scattering, whose effects are straightforward to include inside the Kalman filter formalism. For isolated muons with a transverse momentum between 1 GeV/c and 100 GeV/c, the tracking efficiency is higher than 99% in the full η-range of the Tracker acceptance and the efficiency does not depend on the transverse momentum of the particles.

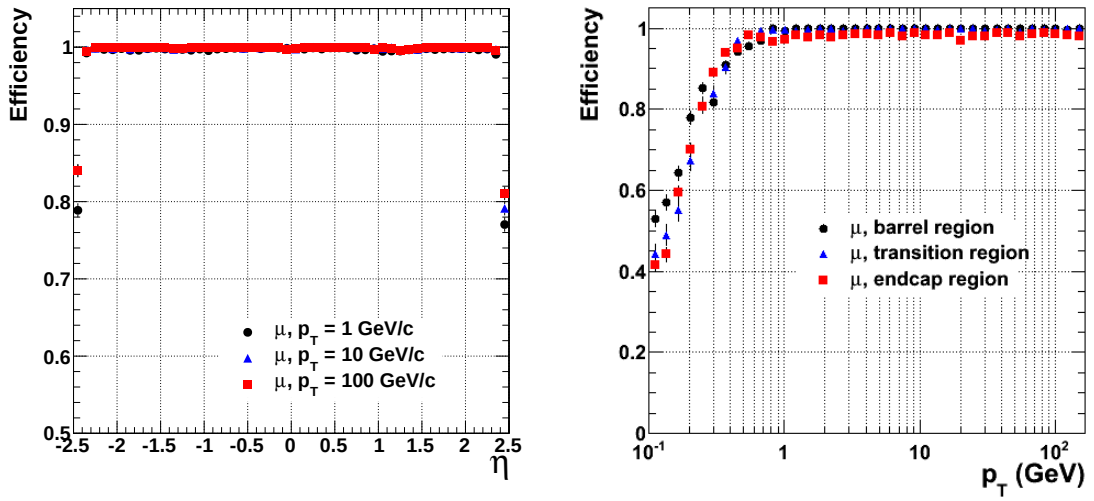

(a) (b)

Figure 3.11: *Global track reconstruction efficiency extracted from single track simulation as a function of η (a) and p_T (b) for muons of transverse momenta of 1, 10 and* 100 GeV/c.

The average hit-finding efficiency (Fig. 3.11(a)) is higher than 99% both in the barrel and in the endcaps; it is still above 97% in the barrel-transition region where the layer

navigation is more complicated and the material budget of the Tracker is more significant. The trajectory contamination due to spurious hits produced by electrical noise or δ-rays is of the order of 10^{-3} (Fig. 3.11(b)).

3.4.2 Muon Recostruction in the Muon Spectrometer

The basic element to construct a muon track in the muon systems is the result of the local reconstruction [83]. Its goal is the reconstruction of basic hits and segments in individual muon chambers, starting from the output of the Data Acquisition system. Different implementations are used to reflect the hardware differences in the 3 types of chambers:

- Local reconstruction in the DTs begins with the reconstruction of mono dimensional hits in individual drift cells. The only information contained in these hits is their distance from the anode, with an intrinsic left/right ambiguity and without any information about their position along the wire. The cell hits are the starting point for the reconstruction of segments in the $r\phi$ and rz projections separately. The 3D position and direction of the muon crossing the chamber are obtained combining the two projections, obtaining segments with an angular resolution of about 0.7 mrad in ϕ and about 6 mrad in θ [63].

- In a CSC chamber each plane measures a point in two dimensions. The radial coordinate r is measured by the wires, the azimuthal coordinate ϕ by the strips. The hits in a chamber are used to fit a three-dimensional straight line segment (made of up to six points). The position resolution of segments varies from about 50 μm in the first CSC station to about 250 μm in the fourth [62]. The directional resolution varies with the chamber type, with an average of about 40-50 mrad in ϕ and slightly worse in θ.

- The RPCs have a spatial resolution limited by the strip pitch. The resolution on ϕ is around l cm, while the orthogonal coordinate is only constrained by the strip length [64].

The results are track segments in the single DT and CSC chambers and individual points in the RPCs that are then used to form the stand-alone track, following a step-by-step method similar to the one used in the track and described in Section 3.2:

- *Fist step: seed generation.* The seeding algorithm takes DT and CSC segments as input and combines them to produce a set of initial states which are the starting point for the reconstruction of muon tracks. The efficiency of building a muon seed is mainly determined by detector acceptance and, in part, by the efficiency of segment reconstruction.

- *Second step: pattern recognition and fit.* Tracks are built using the Kalman filter technique, a recursive algorithm which performs the pattern recognition layer by layer and, at the same time, updates the trajectory parameters. Once all the hits have been collected, a final fitting step (smoothing) can be applied, updating the trajectory state at the location of all intermediate hits with the information from all the collected measurements, thus obtaining the optimal track parameters. The

algorithm is flexible enough to allow different possible strategies: the fit can be applied in either direction, from the innermost layer towards the outermost or vice versa (forward or backward), possibly multiple times to remove a bias from the initial seed, and using either segments or individual hits to update the trajectory parameters.

- *Third step: ghost suppression.* The trajectory building algorithm is run for each seed. If the seeding algorithm fails to merge all the track segments from the same muon, several seeds can be built from a single muon, giving rise to duplicates of the same tracks. These duplicates, called ghosts, usually share a fraction of their measurements. In order to remove them, all the track candidates that share at least one hit are compared with each other and only the best candidate is kept. The algorithm proves very effective, especially in the barrel region, where the rate of duplicate tracks is reduced by several orders of magnitude.

- *Fourth step: beam spot constrain*: In order to improve the momentum resolution of tracks, the beam spot (see Section 3.3.1) position is used to constrain the track parameters. Although the beam position in the transverse plane is known within few tens of microns, the beam spot position uncertainty is set to l mm in the constraint. The constrained tracks are stored and made available to the global re- construction. The unconstrained tracks are kept for reference and saved in a separate collection.

3.4.3 Global muon recostruction

After the completion of the reconstruction of the stand-alone tracks (see Section 3.4.2) and in the inner tracker (described in Section 3.4.1) the reconstruction of global muon tracks can begin. Each standalone track is matched to a compatible tracker track and a fit of all the available measurements is performed.

The process of identifying the tracker track to combine with a given stand-alone muon track is referred to as "track matching" and consists of two steps.

The first step is to define a Region Of Interest (ROI) in the track parameter space that roughly corresponds to the standalone muon track, and to select the subset of tracker tracks inside this ROI. The matching is performed by comparing the parameters of both tracks by propagating them onto a common reference surface, the de- tector layer of the innermost stand-alone track hit.

The second step is to iterate over this subset, applying more stringent spatial and momentum matching criteria to choose the best tracker track to combine with the standalone muon.

Finally, a global track is fitted using all hits belonging to the matching tracker and standalone tracks. The global refit algorithm attempts to perform a fit for each tracker-standalone track pair. If more than one global track is produced for a given standalone, the one with the best χ^2 is chosen. Thus, for each standalone muon there is a maximum of one global muon that will be reconstructed.

In Fig. 3.12, the efficiency of global track reconstruction is shown for simulated muons with a flat η distribution between -2.5 and 2.5 and with design geometry and alignment. A large inefficiency appears in the barrel region for muons with $p_T = 5$ GeV/c. At low p_T, muons easily stop in yoke without crossing all muon stations, especially in the barrel

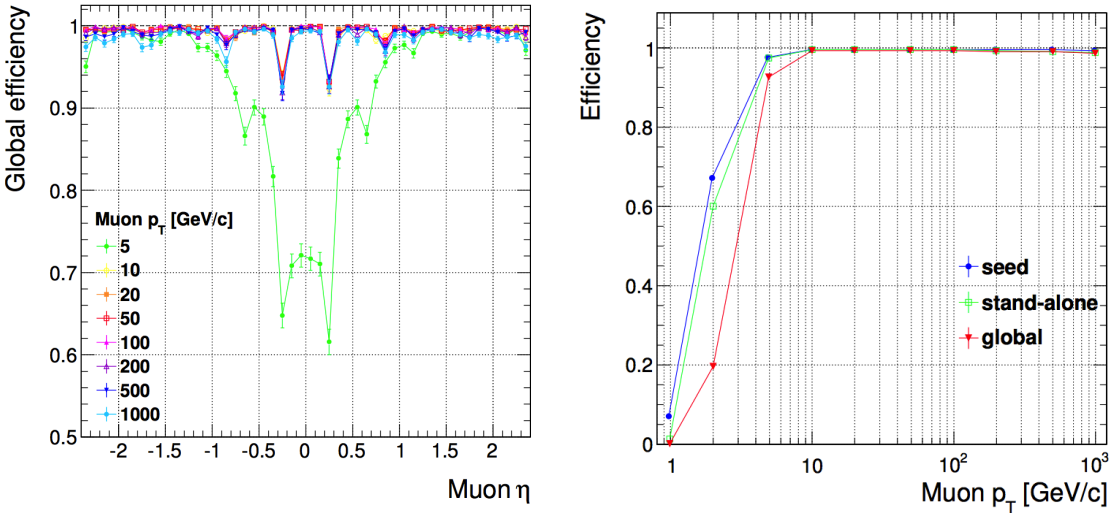

(a) (b)

Figure 3.12: *Global Muon track efficiencies from simulation (a) vs η and (b) vs p_T [83]*

region, and stand-alone tracks are reconstructed with a relatively low number of hits and with a poorer momentum resolution. This makes the matching with tracker tracks more difficult and less efficient.

3.4.4 Tracker Muons Reconstruction

As explained in Section 3.4, the standard muon track reconstruction starts from the muon system and combines stand-alone muon tracks with tracks reconstructed in the inner tracker. This approach naturally identifies the muon tracks in the detector. However, a large fraction of muons with transverse momentum below 6-7 GeV/c (cf Figure 3.8c) does not leave enough hits in the muon spectrometer to be reconstructed as standalone muons. Moreover, some muons can escape in the gap between the wheels. In order to recover the loss of efficiency for low p_T muons present in the Global Muon approach (see 3.12(b) a complementary approach has been designed to identify off-line these muons and hence improve the muon reconstruction efficiency. It consists in considering all silicon tracker tracks and identifying them as muons by looking for compatible signatures in the muon system. The algorithm for the muon identification of the tracker tracks starts with the extrapolation of each silicon track outward to its most probable location in the muon system. After collecting the associated signals the algorithm determines compatibility variables corresponding to how well the observed signals fit with the hypothesis that the silicon track is produced by a muon. For each crossed or nearly crossed chamber in the muon system the algorithm looks for at least one associated segment and the resulting muon is called "tracker-muon". Since each track is treated individually, if two or more tracks are near to each other, it is possible that the same segment or set of segments is associated to more than one track, resulting in duplicate tracker muons. This ambiguity can be resolved by the arbitration algorithm, which assigns segments to tracks by looking at the best ΔR match.

Fig. 3.13 shows the q/p_T resolution of muons tracks resulting from the different fits: standalone, tracker-only and global. In the different η range, the resolution of global

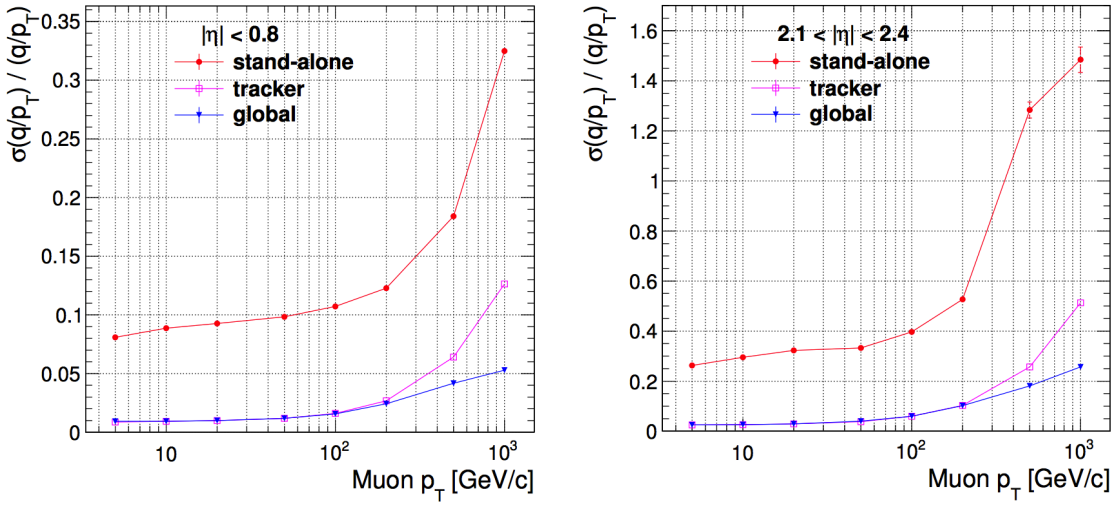

(a) (b)

Figure 3.13: *Muon q/p_T resolution vs. p_T for the three different types of fit: standalone(red), tracker-only(magenta) and global (blue) in the central part of the barrel (a) and in the forward region (b) [83]*

tracks is always dominated by the tracker resolution up to $p_T \sim 200$ GeV/c. For higher p_T, the contribution of the muon system becomes significant and improves the global resolution by 10-20% at 1 TeV/c.

3.4.5 Muon High Level Trigger

The CMS muon trigger, as explained in Section 2.2.6, is structured in a first hardware level, the Level-1 Trigger (Ll), and a software part, the High Level Trigger (HLT).

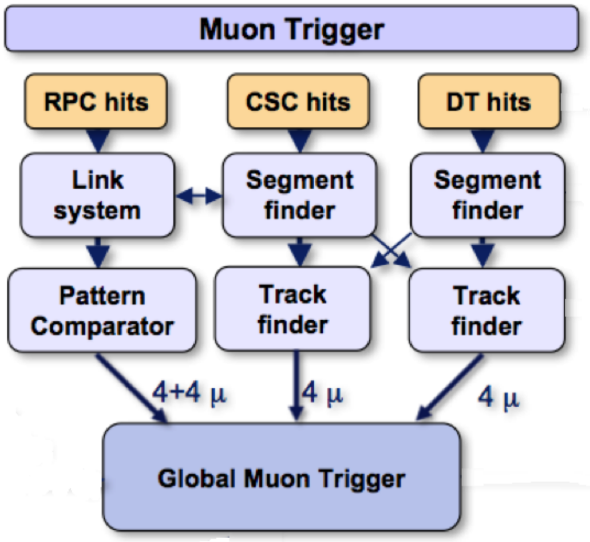

Figure 3.14: *Scheme of the L1 Muon Trigger*

In Fig. **??** is reported the logic scheme of the L1 Muon Trigger. The muon $Level-1$ electronics uses groups of segments from DTs and CSCs, and hit patterns from RPCs. It

identifies muon candidates, determines their position and quality, and provides a transverse momentum estimate in a discretely binned form, based on segment slopes in DTs and CSCs, and on predefined hit patterns in RPCs.

It also provides event timing and assigns events to a particular bunch crossing. Finally, the Global Muon Trigger (GMT) matches DT, CSC and RPC candidates, and rejects unconfirmed candidates of low quality. Up to four muon candidates, satisfying some minimal quality criteria and with the highest p_T, are transmitted to the HLT for further processing.

The HLT is implemented in software and runs on the CMS online filter farm. Muon HLT performs a full track reconstruction, using the same algorithms and software employed in the offline reconstruction. The muon HLT is structured in two main levels, called *"Level-2"* and *"Level-3"*. This allows for a first reduction of the rate, based on a limited part of the information, which saves time for a more detailed reconstruction of the selected events.

After each HLT reconstruction level, a selection is applied on the reconstructed muon candidates. The main selection variables that can be used are the number of muon candidates in the event, their quality, p_T, η, impact parameter, and isolation variables. The trigger requirements are implemented in software modules called filters. A sequence of reconstruction steps and filters is called trigger path. Different trigger paths can be defined by varying the filter cuts. In such a way, the muon trigger can be specialised to fulfil the needs of different physics analyses.

It is important to stress that a trigger path is considered successful only if the requirements of all the three levels are satisfied. When a muon candidate passes a trigger level, all the candidates in the event are transmitted to the following level, even those that failed the selection. In particular, a muon candidate failing to pass the L1 filter of a given path may still be reconstructed at L2 and L3, if the event passes to the next trigger levels, because of another trigger requirement; such a candidate ("volunteer") is not considered for the trigger path which failed at L1.

HLT Level-2

The $Level-2$ (L2) uses muon system information to perform a standalone reconstruction, as in Section 3.4.2. A separate module in L2 computes the isolation of each muon candidate using calorimeter information. The L2 muon reconstruction starts from an initial seed state.

Unlike the offline case, where seeds are obtained combining segments in the muon system, in the online reconstruction the L1 muon candidates are used as external seeds, with a significant reduction of seeding time. The full muon reconstruction is then performed on a regional basis, only where a L1 candidate is found. Although faster, this approach limits the HLT efficiency to the L1 efficiency: there cannot be a L2 muon reconstructed if no corresponding L1 muon object is present.

For each L1 muon candidate promoted by the GMT to the HLT, a L2 seed is built. An initial state is created from the position and momentum of the L1 candidate and fixed errors are assigned to all the parameters. Finally, the seed state is propagated to the innermost compatible muon chamber. Starting from each L2 seed, the reconstruction of L2 tracks proceeds exactly as in the off-line case: the local reconstruction and trajectory

building are performed only in those regions of the muon system where a L1 candidate/L2 seed was built, in order to comply with the time requirements of the trigger.

The flexibility of the software allows a variety of different reconstruction schemes: it is possible to configure which muon detectors to use, the direction and granularity of the pattern recognition, whether to apply the final fitting-smoothing step, etc.

HLT Level-3

After the completion of Level-2 muon reconstruction and Level-2 filtering steps, the algorithm proceeds to reconstruct Level-3 muon candidates. In the HLT environment, the full tracker reconstruction cannot be performed because it is too CPU intensive. Therefore, track reconstruction algorithm is modified in the following ways:

- Rather than trying to reconstruct all tracks in the event, "regional" track reconstruction is performed. The software only attempts to reconstruct tracks laying within a specified η-ϕ region around an object of interest (which might be a muon, electron or jet candidate reconstructed using the calorimeters or muon chambers). This saves a large amount of CPU time. It is accomplished by using 'regional seeding' that only forms seeds from combinations of hits which would be consistent with a track heading into the desired η-ϕ region.

- Further gains in speed can be made by only using a single iteration in the iterative tracking, such that only seeds made from pairs of pixel hits are considered, and these hits must be compatible with a track originating within a few millimetres of the pixel primary vertex.

- Track finding can use 'partial track reconstruction'. With this technique, the building of each track candidate is stopped once a specified number of tracker hits have been assigned to it (typically 8). In consequence, the hits in the outermost few layers of the tracker tend not to be used. Such partially reconstructed tracks will have slightly poorer momentum resolution and fake rates than fully reconstructed ones. However, they take less CPU time to find.

The best tracker tracks to be combined with a given L2 muon are then selected, following the same matching criteria as in the offline reconstruction. Finally, for each L2-tracker match, a global fit is performed, using the whole set of hits in the tracker and muon system. If more than one global L3 track is built from the same L2 muon, only the one with the best χ^2 is kept. Thus, for each L2 muon, there is a maximum of one global L3 muon that is reconstructed.

To reproduce the trigger rate accurately, the simulation must reproduce the correct sample composition, the correct trigger efficiency, and also correctly describe the resolution for muons from different sources including the resolution tails. The current level of agreement between the L1 and HLT trigger performance in data and the Monte Carlo simulation is generally good, as shown in Fig. 3.15. The results suggest that the trigger simulation is a useful tool to predict muon trigger rates and confirms that the performance of the CMS muon trigger system is close to the design expectation.

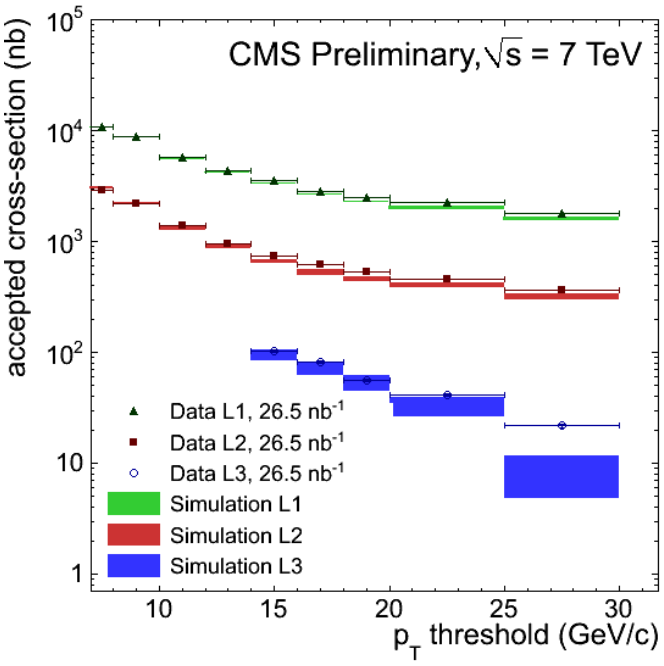

Figure 3.15: *The accepted cross-section of events is shown as a function of trigger p_T threshold for the actual L1, L2, L3 trigger objects processed online in data, compared to the emulated L1 and HLT trigger in simulation*

Chapter 4

Integrated Cross Section Ratio

In this section it's presented the measure of the ratio between the production cross section of the $X(3872)$ and $\psi(2S)$ into their decay channel $J/\psi\pi^+\pi^-$, i.e. the quantity

$$R = \frac{\sigma(pp \to X(3872) + anything) \cdot \mathcal{B}(X(3872) \to J/\psi\,\pi^+\pi^-)}{\sigma(pp \to \psi(2S) + anything) \cdot \mathcal{B}(\psi(2S) \to J/\psi\,\pi^+\pi^-)} \tag{4.1}$$

using the data collected during 2010 by the CMS detector in pp collisions at $\sqrt{s} = 7\,TeV$. The procedure followed is similar to that adopted by CDF and DØ experiments at Tevatron (see Section 1.2).

The events are identified using the decay of the J/ψ in two oppositely charged muons ($\mathcal{B}(J/\psi \to \mu^+\mu^-) = 5.93 \pm 0.06\,\%$) and then two good tracker tracks are paired to the J/ψ in order to reconstruct the $X(3872)$ and $\psi(2S)$ candidates. When a ratio is measured, uncertainties related to the triggering and reconstruction of J/ψ mesons as well, as external normalization errors (e.g. the integrated luminosity), largely cancel. Remaining acceptance and efficiency differences are accounted for by correction factors determined from Monte Carlo simulation. Data-driven methods to verify the simulations are used.

The ratio is finally calculated from

$$R = \frac{N_{X(3872)}}{N_{\psi(2S)}} \cdot \frac{1}{C} \tag{4.2}$$

where $N_{X(3872)}$ and $N_{\psi(2S)}$ are the yields for the two states extracted from the invariant mass spectrum, and C is the correction factor for efficiency and acceptance.

4.1 Data sample and triggers

The sample used for the present analysis covers the data collected by the CMS experiment during 2010. Events are taken from a collection of runs The events are required to fulfil a good-run selection for muons, that is data of good quality from the central tracker and the muon system, and no additional requirement on the calorimeters status during the data taking.

The sample is selected in order to have consistent trigger requirements throughout the analysis, and corresponds to a total integrated luminosity of 40 pb^{-1}. During this data acquisition period, LHC delivered a maximum instantaneous luminosity of 2.1 $\times$

$10^{32}\,cm^{-1}s^{-1}$, with an average of 2.2 inelastic pp collisions per bunch crossing at the CMS interaction region.

The J/ψ, coming from the $X(3872)$ and $\psi(2S)$ decays, is reconstructed in the $\mu^+\mu^-$ decay channel. The analysis is based on events triggered by double-muon triggers that exploit advanced processing at the HLT level. All the three muon systems, as well as the tracker, are used to perform the final trigger decision. Both muons are required to be consistent with a L1 muon signal and to be reconstructed from at least two independent segments in the muon chambers (L2). Moreover, they have to be matched to a track reconstructed in the region defined by the L2 direction (L3), as described in Section 3.4.5.

Thanks to the low luminosity regime of LHC during 2010, a trigger with no explicit requirement on the transverse momentum has been kept during the entire year. After the first $8.7\,pb^{-1}$ of collected data, in order to cope with the higher luminosity, it has been added to the trigger the requirement that the invariant mass of the di-muon system should be within $1.5\,GeV/c^2$ and $14.5\,GeV/c^2$. This loose requirement does not effect the J/ψ yield.

4.2 Simulation samples

Simulated events are used to tune the selection criteria, check the agreement with data, compute the acceptance, and derive efficiency corrections, as well as for systematic studies.

As seen by the experiment at Tevatron the $X(3872)$ (as the $\psi(2S)$) can be produced both promptly and from B-mesons decay. For the production of the events it has been used Pythia 6.422 [84], which generates events based on the leading-order color-singlet and color-octet mechanisms. Color-octet states undergo a shower evolution. The NRQCD matrix elements tuning, obtained by fitting NRQCD calculations to CDF data [30, 74], is used.

The prompt $\psi(2S)$ has been produced using the color-octet formalism developed in PYTHIA for the J/ψ, where the mass of the color-octet $c\bar{c}$ state is set to a value sufficient to produce the $\psi(2S)$.

The $X(3872)$ in not included in PYTHIA. As has been summarized in Section 1.4, up to the last experimental results, the favoured J^{PC} state for the X(3872) is 1^{++}. Moreover, the Tevatron results haven't shown any particular difference in the general production properties of the $X(3872)$ with respect to the other charmonium states. For this reason, the prompt production of the $X(3872)$ has been simulated in PYTHIA changing the mass of the χ_{c1} (which has $J^{PC} = 1^{++}$) to the $X(3872)$ one. For the production, the colour-singlet mechanism $gg \to \chi_{c1}g$ has been used. In the absence of consistent theoretical and experimental information about the $X(3872)$ and $\psi(2S)$ polarization, both particles are produced unpolarized.

The particles generated by PYTHIA are then decayed using the EvtGen package [75], for a more accurate treatment of the phase space of the decays. Through EvtGen is possible to force the decay channels of both particles. The $\psi(2S)$ has been forced into $J/\psi\,\pi^+\pi^-$ final state, using a three body decay model available in the package. For the $X(3872)$, following the result on the dipion invariant mass from Belle and CDF, the two body decay in $J/\psi\,\rho$ has been implemented. In both cases the J/ψ is forced to decay in $\mu^+\mu^-$.

Simulated events with b-hadron decays have been also generated via Pythia, and the b-hadrons are forced to decay inclusively into $\psi(2S)$ and $X(3872)$ by EvtGen. The $X(3872)$ has been added to EvtGen with the appropriate mass, width and J^{PC} and its decays from $B^{\pm}$ and B^0, seen at b-factories, have been implemented. QED final-state radiation (FSR) is implemented using PHOTOS [29] package.

For all these four types of simulation (prompt and non-prompt both for $\psi(2S)$ and $X(3872)$), two kinds of sample have been produced:

- Samples without any type of cuts, with particles produced only at generator level. This kinds of samples contains about ten million events and are used for acceptance studies.
- Samples with loose acceptance cuts on muons based on the geometry of the detector. These simulated events are passed through the GEANT4-based [21] detector simulation, and processed with exactly the same software used for collision events, including the simulation of trigger up to HLT.

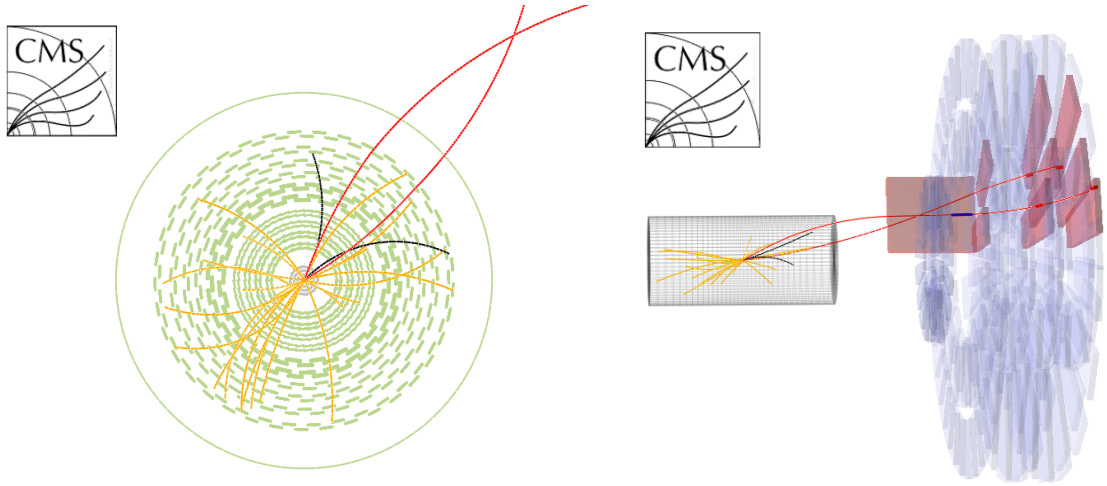

(a) (b)

Figure 4.1: $X(3872)$ *event simulation. In black the 2 pions track and in red the 2 muons track from the* $X(3872)$ *decay. In orange the other track with* $p_T > 0.4 GeV/c$ *in the event. In (a) zoom on the central tracker (tracker and pixel layers in green), in (b) 3D view of the detector and of the muon chambers reached by the two muons.*

In Fig. 4.1 is shown an $X(3872)$ event inside the CMS detector. The opposite charge tracks of the pions are detected by the silicon layers in the tracker, while the two muons from the J/ψ reach the chambers of the muon system.

4.3 J/ψ Reconstruction

The reconstruction of J/ψ candidates closely follows the selection used in the J/ψ cross section analysis published by CMS [50].

The events are selected with two identified muon candidates, tracker muon or global muons, following the definition in Section 3.4. The reconstructed inner tracks are required

to have at least two hits in the pixel detector and at least 12 hits in the tracker (pixel and strips combined). The track fit of the inner track is required to fulfil the condition $\chi^2/NDF < 1.8$ (NDF is the Number of Degree of Freedom).

For global muons, there must be at least one valid hit in the muon system and the global fit to the inner track and the outer muon track must yield a value of $\chi^2/NDF < 20$. The two identified muon candidate tracks are required to originate from a common vertex, with a probability $> 0.01\%$.

The identified muons are also required to match with the muons that have fired the trigger for that event. This is done comparing the muon tracks obtained by the off-line full reconstruction with the muons reconstructed in the various steps of the trigger. The parameter for this check are the ΔR and the relative p_T difference $\Delta p_T/p_T$ between the two objects. At L1 level is requested $\Delta R < 0.3$ while at HLT level $\Delta R < 0.1$, and in both cases $\Delta p_T/p_T < 10\%$.

The two muons are also required to lay in the acceptance region of the detector. This acceptance takes into account the finite geometrical coverage of CMS and the momentum threshold introduced by the material in front of the muon detectors (that acts as absorber), the curvature in the magnetic field and has been studied with large simulation samples in [50]. The detectability contours in the two planes $p_T^\mu - \eta^\mu$ and $p^\mu - \eta^\mu$ are shown in Fig. **??**.

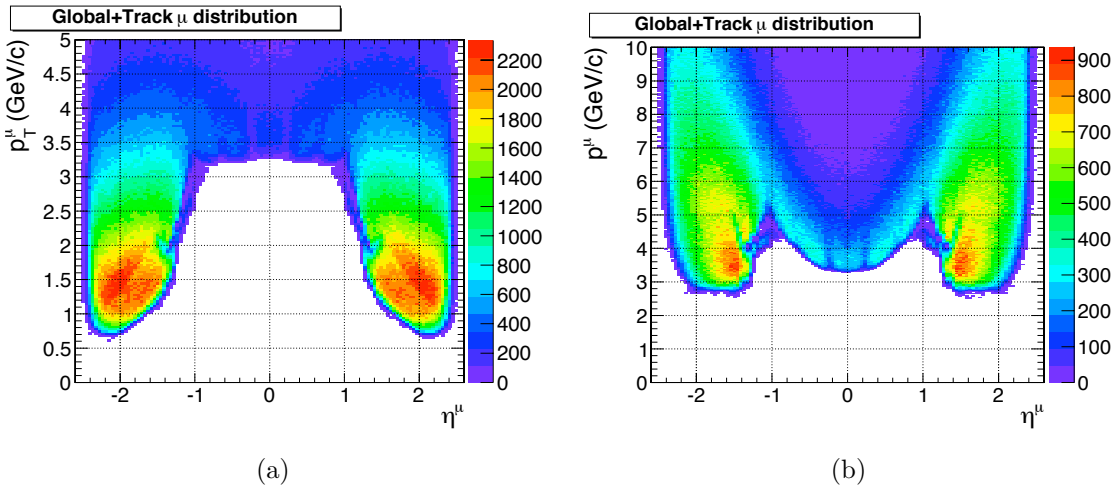

(a) (b)

Figure 4.2: *Distribution of the detectable muons from J/ψ as a function of p_T^μ versus η^μ (a) and p^μ versus η^μ (b).*

The following kinematic cuts, defining the acceptance region, are then required so as to guarantee a single-muon detectability exceeding 10%:

$$\begin{aligned} p_T^\mu &> 3.3 \text{ GeV/c} \quad \text{for} \quad |\eta^\mu| < 1.3 \\ p^\mu &> 2.9 \text{ GeV/c} \quad \text{for} \quad 1.3 < |\eta^\mu| < 2.2 \\ p_T^\mu &> 0.8 \text{ GeV/c} \quad \text{for} \quad 2.2 < |\eta^\mu| < 2.4 \end{aligned}$$

The invariant mass distribution in the data sample of the two opposite charged muons, after these requirements, is shown in Fig. 4.3 for the full range of rapidity. It is also shown separately for the barrel region ($|y| < 1.3$, covered by the DT system), the forward region

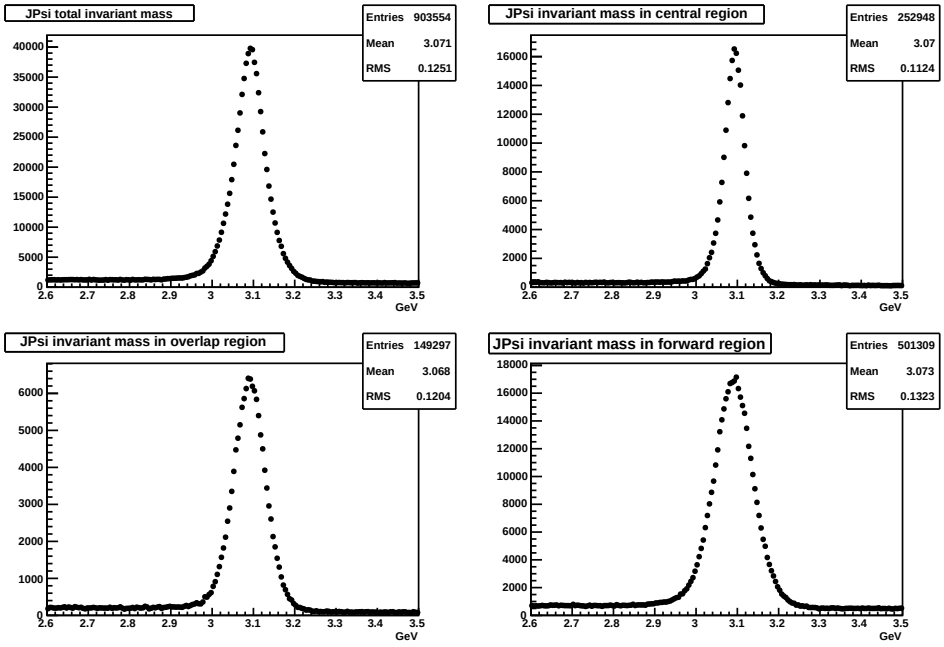

Figure 4.3: *The invariant mass distribution of the two opposite charged muons after the selection cuts for the J/ψ, in the full range of rapidity, and separately for the three different ranges of rapidity $|y| < 1.3$, $1.3 < |y| < 2.2$, $2.2 < |y| < 2.4$.*

($2.2 < |y| < 2.4$, covered by the CSC) and the overlap region ($1.3 < |y| < 2.2$, where information from DT and CSC are combined to reconstruct the muon track). About 9×10^5 J/ψ mesons have been reconstructed in the full data sample. The differences in the invariant mass resolution depend on the spatial resolution of the different detectors, the quantity of material crossed by the muons, their arm in the magnetic field and kinematic distribution. The distribution of the transverse momentum and rapidity of the J/ψ candidates are shown in Fig. 4.4. The mean p_T is around 8 GeV/c and the majority of the J/ψ is produced at high rapidity.

4.4 Selection of $J/\psi\,\pi^+\pi^-$ candidates

In order to select the good J/ψ meson candidates for the next step of the analysis, the invariant mass distribution in the three rapidity regions has been fitted using, for the signal, two Gaussian functions (to describe the detector resolution) and an exponential tail (for modelling the radiative tail from internal bremsstrahlung). The shape of the underlying continuum is described by an exponential. The sum of the σ of the two Gaussians, scaled for their weight in the total signal function, has been taken as the σ for the J/ψ peak. Due to the low underlying background and in order to keep as much signal as possible, a window has been defined with a width of 3 σ (keeping 99% of the signal). The values for this window in the different regions of the detector are reported in Table 4.1.

For the reconstruction of the $J/\psi\pi^+\pi^-$ system, the J/ψ meson candidates are combined with pairs of oppositely charged pion track candidates. These pion tracks are checked not to match kinematically the muon track in the inner silicon detector, in or-

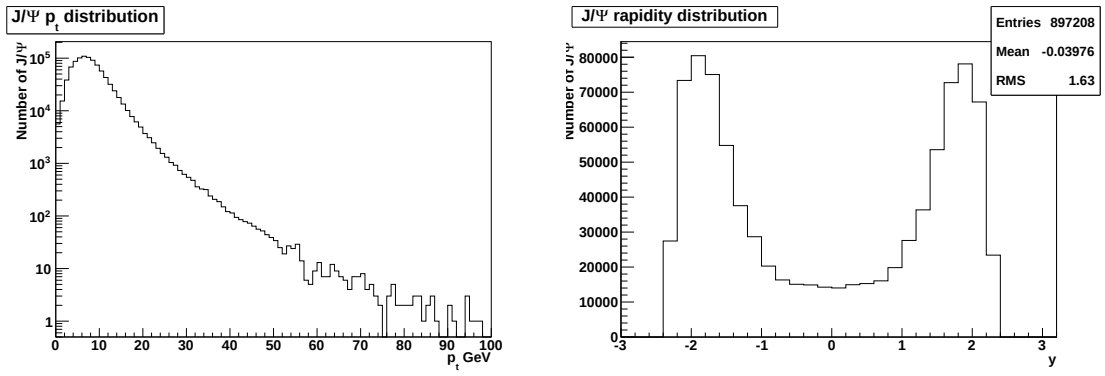

(a) (b) Caption of Second Figure

Figure 4.4: *The distributions of the transverse momentum and rapidity of the J/ψ candidates as measured in data.*

$\|y\|$ range	Weighted σ (MeV)	Mass Range (MeV)
$\|y\| < 1.3$	29	$3019 < m_{J/\psi} < 3167$
$1.3 < \|y\| < 2.2$	42	$2981 < m_{J/\psi} < 3198$
$2.2 < \|y\| < 2.4$	51	$2959 < m_{J/\psi} < 3221$

Table 4.1: *J/ψ selection mass windows.*

der to avoid duplicates. Random combinations of tracks form a significant non-resonant background beneath the $X(3872)$ and $\psi(2S)$ signals. To suppress this background, several track quality and selection criteria are applied, and the four final state tracks are refitted, assuming that the particles come from one common vertex and constraining the mass of the muon pair to that of the J/ψ. Candidate track combinations yielding a vertex fit probability larger than 0.01 % are retained.

Selection criteria for track in the CMS tracker have been studied in various physics analysis in CMS [42, 45], and a review of pions track reconstruction in the experiment has been proposed in Section 3.2.4. Based on these results the refitted pion track candidates are selected if their transverse momentum is larger than 400 MeV/c, they have at least two hits in the pixel detector, five hits in the strip detector, and a track fit yielding a $\chi^2/NDF < 5$. These selection criteria are at the limits of the sensibility of the CMS tracker and additional studies have been carried out in order to evaluate better the efficiency (see Section 4.8).

After the above selection requirements, the data sample consists of 1.7×10^7 candidates with an invariant mass of the $J/\psi\pi^+\pi^-$ system less than 5 GeV.

In order to decrease further the combinatorial background, additional cuts have been studied on the final collection of candidates.

In Fig. 4.5 the transverse momentum distribution $p_T(\pi^+\pi^-)$ of the pion pair (after the fit) and the opening angle ΔR of the pion pair with respect to the direction of the J/ψ candidate are shown. The truncation of the ΔR distribution is related to the preselection cut $\Delta R < 1.2$ between the original tracks and the J/ψ candidate.

The ΔR distribution is shown separately for mass window and sidebands (described in Section 4.10 in Fig. 4.6). In the upper plots the data are shown for signal and sideband.

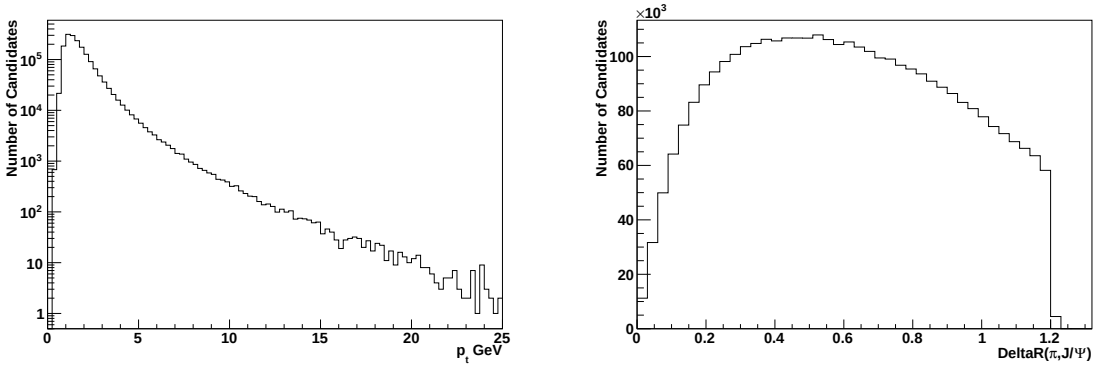

(a) (b)

Figure 4.5: *The transverse momentum distribution of the $\pi^+\pi^-$ system and the opening angle between the pion pair and the J/ψ in the experimental data.*

The sideband entries are scaled to correct for the difference in the width of the sidebands. The lower plots show the difference between the signal and sideband distributions. The data are compared with the simulations normalized to the data. From this distribution it has been decided to apply a cut $\Delta R < 0.7$.

In Fig. 4.7 the MC simulated $p_T(\pi^+\pi^-)$ distributions for signal and background are shown. In order to increase the signal over background ratio for the $X(3872)$, a $p_T(\pi^+\pi^-) > 1.5$ GeV/c is required. The cuts applied on ΔR and $p_T(\pi^+\pi^-)$ reduce the data sample by a factor of about 40, while retaining about 85% of the signal. The list of final cuts is given in Table 5.1.

pion track fit χ^2/NDF	< 5
number of hits in Pixel detector	≥ 2
number of hits in Strip detector	≥ 5
$p_T(\pi)$	> 400 MeV/c
4-track fit vertex probability P_{Vtx}	$> 0.01\%$
ΔR	< 0.7
$p_T(\pi^+\pi^-)$	> 1.5 GeV/c

Table 4.2: *List of cuts on the $J/\psi\pi^+\pi^-$ system.*

4.5 Acceptance and efficiency studies

The Monte Carlo samples are used to study the acceptance for $\psi(2S)$ and $X(3872)$ as a function of their transverse momentum and rapidity. The correction factor of the signal yield (C in Equation 4.2) can be factorized into four components, i.e. the acceptance $A_{J/\psi}$ and efficiency $\epsilon_{J/\psi}$ for the reconstruction of the J/ψ, the acceptance correction for the kinematic cuts imposed on the pion pair $A_{\pi\pi}$ and the reconstruction efficiency of the pion pair $\epsilon_{\pi\pi}$. The overall correction C on the ratio of $X(3872)$ and $\psi(2S)$ signals is then given by:

$$C = \frac{A_{J/\psi}(X(3872)) \cdot \epsilon_{J/\psi}(X(3872)) \cdot A_{\pi\pi}(X(3872)) \cdot \epsilon_{\pi\pi}(X(3872))}{A_{J/\psi}(\psi(2S)) \cdot \epsilon_{J/\psi}(\psi(2S)) \cdot A_{\pi\pi}(\psi(2S)) \cdot \epsilon_{\pi\pi}(\psi(2S))}. \qquad (4.3)$$

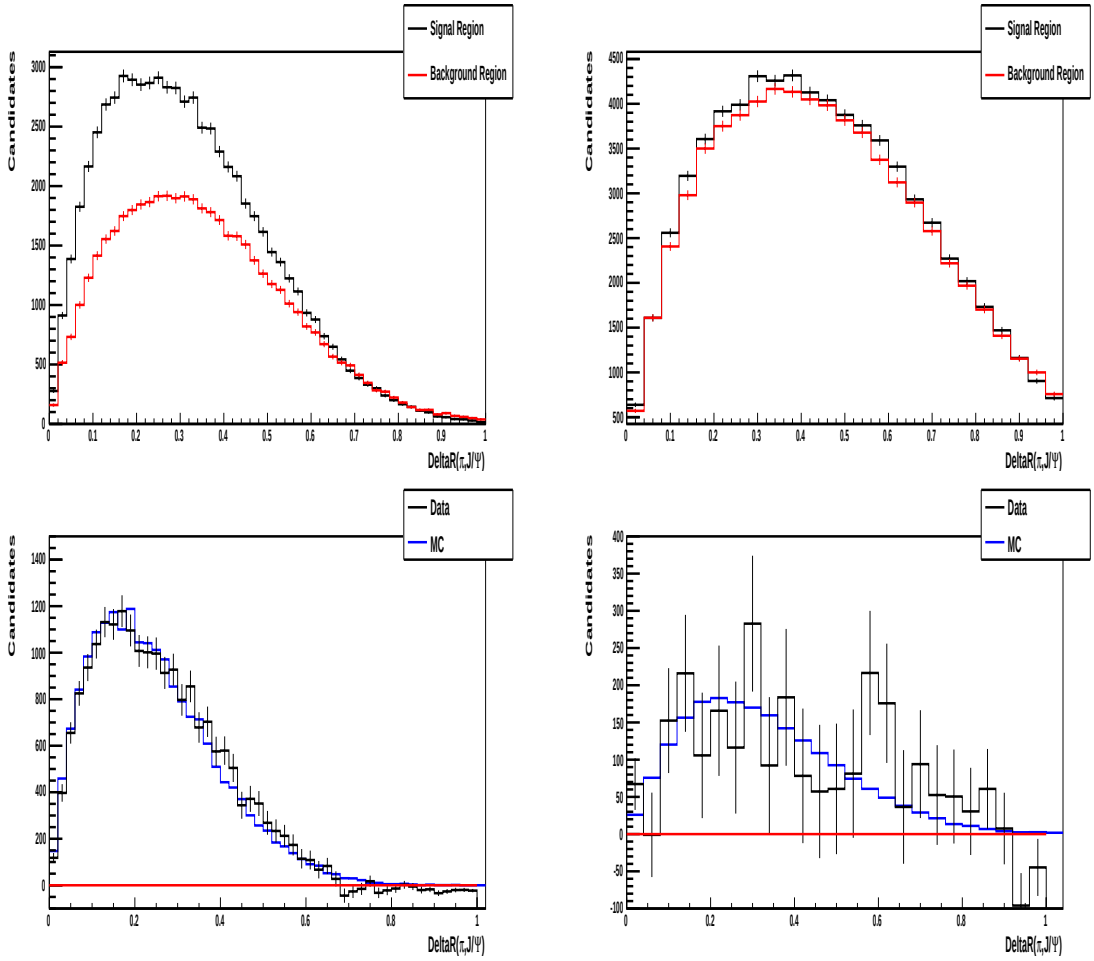

(a) (b)

Figure 4.6: *The opening angle between the pion pair and the J/ψ for the mass interval (black) and the sidebands (red). The left (right) histograms correspond to the $\psi(2S)$ ($X(3872)$), respectively. The bottom histograms show the mass window distributions after subtraction of the distribution from the sidebands (in black) and the Monte Carlo simulation scaled to the number of entries in the data (in blue).*

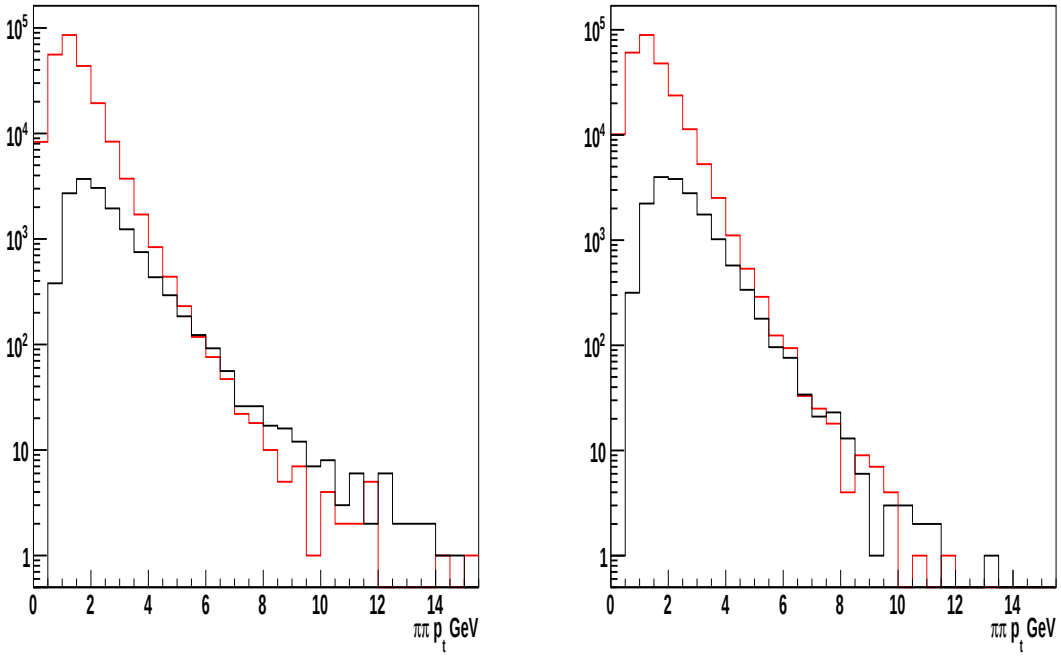

(a) (b) Caption of Second Figure

Figure 4.7: *The Monte Carlo $p_t(\pi^+\pi^-)$ distributions for signal (in black) and background (in red) for $\psi(2S)$ (left) and $X(3872)$ (right).*

Due to the similar properties of the $X(3872)$ and the $\psi(2S)$, the ratio of each of the four components and their product is close to, but not identical to unity.

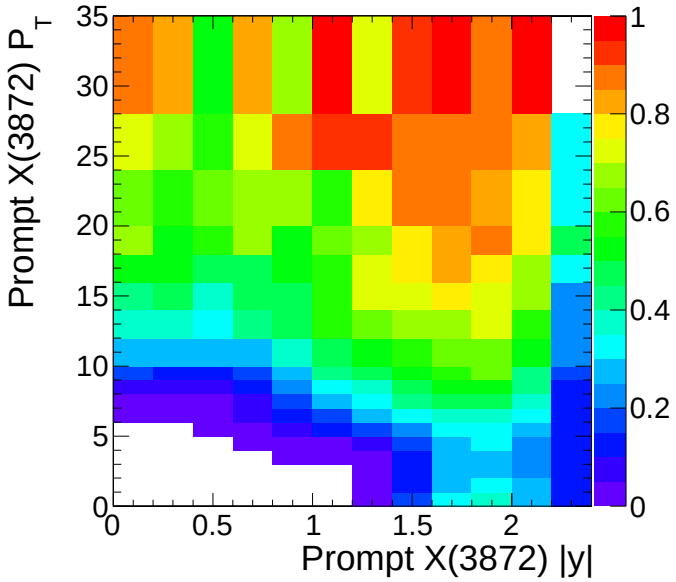

Figure 4.8: *Acceptance map $A_{J/\psi}(X(3872))$ as a function of p_t and $|y|$ for promptly produced $X(3872)$*

In figure 4.8 the acceptance $A_{J/\psi}$ is shown for the measurement of promptly produced $X(3872)$. Sufficiently large acceptance is found in the kinematic region of $p_T(X) > 8$ GeV/c and $|y|(X(3872)) < 2.2$. This kinematic region is chosen for the measurement.

The ratio of the $A_{J/\psi}$ terms between the $X(3872)$ and the $\psi(2S)$ in this kinematic region is close to unity (Fig. 4.9), steeply decreasing at the smallest values of p_T and $|y|$, with an average value of $0.876 \pm 0.002(stat.)$ for the ratio between prompt $X(3872)$ and prompt $\psi(2S)$ production.

In Fig. 4.10 the distributions of promptly produced $X(3872)$ are shown for all simulated candidates and subsequent cuts, after the application of the kinematic cuts on the decay muons from the J/ψ, the transverse momentum and pseudo-rapidity cut on the $X(3872)$, $p_T(X) > 8$ GeV/c and $|y(X(3872)|) < 2.2$, and the selection cuts on the $J/\psi\pi^+\pi^-$ system.

The same study has been performed for simulated samples of non-prompt $\psi(2S)$ and $X(3872)$ production, yielding very similar results, with prompt to non-prompt $A_{J/\psi}$ ratios of 0.97 ± 0.01 and 0.94 ± 0.01 for $\psi(2S)$ and $X(3872)$ respectively. The ratio $A_{J/\psi}(X)/A_{J/\psi}(\psi(2S))$ for the non-prompt simulations is found to be 0.91 ± 0.01.

The term $\epsilon_{J/\psi}$ accounts for the J/ψ reconstruction and trigger efficiency. The ratio of the $\epsilon_{J/\psi}$ terms between the prompt $X(3872)$ and the prompt $\psi(2S)$ production is 0.842 ± 0.007 (Fig 4.11). Using non-prompt components $\epsilon_{J/\psi}$ is found to be 0.94 ± 0.01.

The ratio $A_{\pi\pi}(X) \cdot \epsilon_{\pi\pi}(X)/(A_{\pi\pi}(\psi(2S)) \cdot \epsilon_{\pi\pi}(\psi(2S)))$ of the number of reconstructed $X(3872)$ and $\psi(2S)$ candidates, inside the acceptance region for the J/ψ selection, is

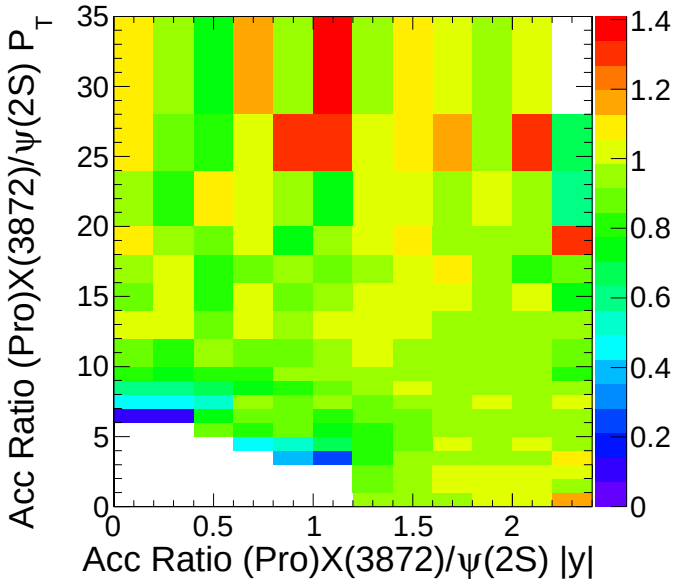

Figure 4.9: *Ratio between acceptance maps for $X(3872)$ prompt and $\psi(2S)$ prompt.*

determined from a Monte Carlo sample of true $X(3872)$ and $\psi(2S)$ candidates extracting the number of truth-matched particles after all cuts divided by the number of true $X(3872)$ and $\psi(2S)$ with a reconstructed J/ψ candidate, after trigger selection. This ratio is found to be $(0.367 \pm 0.004)/(0.334 \pm 0.004) = 1.098 \pm 0.016$. Table 4.3 contains the detailed results for the prompt component, where the combined pion acceptance and efficiency term has been divided in its components. The acceptance term includes all the kinematics cuts on the pions, and an efficiency term the quality ones. For the non-prompt component the combined ratio is found to be 1.199 ± 0.017.

The overall correction factor C of Equation 5.3 is obtained multiplying the previously described ratios. For the prompt component: $A_{J/\psi}$ (0.876), $\epsilon_{J/\psi}$ (0.842) and $A_{\pi\pi} \cdot \epsilon_{\pi\pi}$ (1.098) and the correction is found to be $0.809 \pm 0.014(stat.)$. The overall correction factor for the non-prompt component is $0.990 \pm 0.018(stat.)$.

In order to apply to the data a combined C value for the prompt and non-prompt components, which are extracted separately from the simulations, it was decided to assume a non prompt component fraction of 30%. This rough assumption is based on the results of $D\emptyset$ and CDF, and on the first results of the charmonium non-prompt component at CMS [50]. In this thesis in Chapter 6 a more precise measurement, based on 2011 data, wil be presented. Variations of the non-prompt fraction from the 30% assumption are considered to estimate a systematic uncertainty, as reported in Section 5.10.

The overall correction factor in the scenario with 30% of non-prompt component for both $X(3872)$ and $\psi(2S)$ is:

$$\mathrm{C} = 0.863 \pm 0.015(\mathrm{stat.}) \tag{4.4}$$

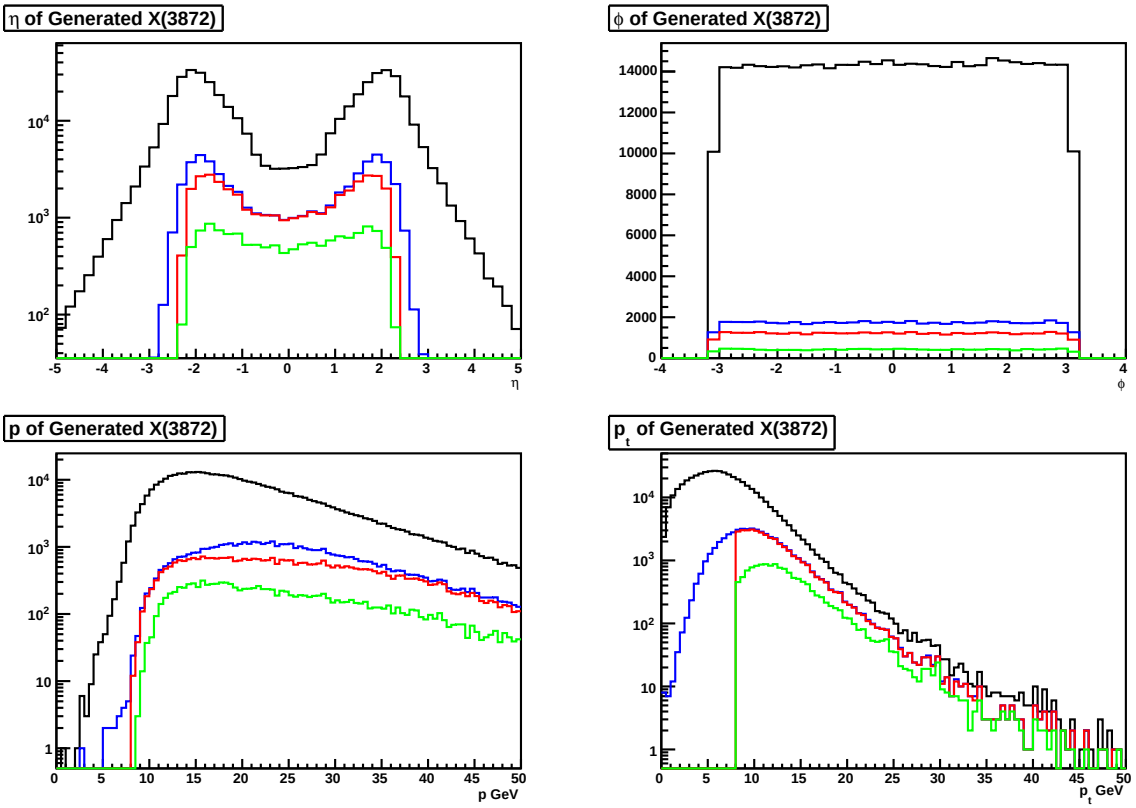

Figure 4.10: *Acceptance and efficiency of $X(3872)$ candidates as a function of $\eta(X)$, $\phi(X)$, $p(X)$ and $p_t(X)$. The black line shows all candidates, the blue line shows the sample after the cut on the J/ψ. The red line shows the sample after a cut on the transverse momentum and rapidity of the $X(3872)$ candidates ($p_t > 8$ GeV, $|y| < 2.2$), and the green line shows the sample of candidates for which the $X(3872)$ candidate is successfully reconstructed.*

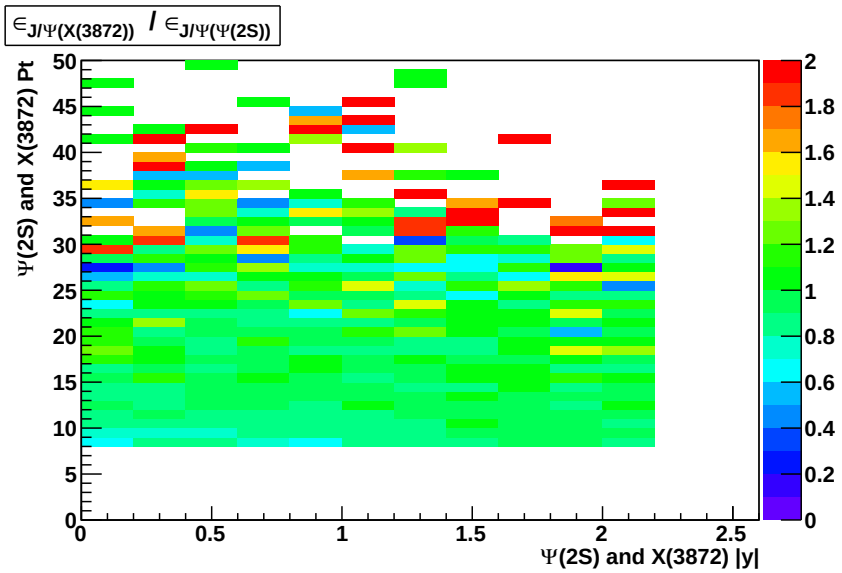

Figure 4.11: *Ratio between $\epsilon_{J/\psi}$ for prompt X and prompt $\psi(2S)$ production.*

Particle	Yield	Cand. after J/ψ cuts	Cand. passing J/ψ and pions cuts	$A_{\pi\pi}$	$\epsilon_{\pi\pi}$	$A_{\pi\pi} \cdot \epsilon_{\pi\pi}$
X(3872)	13398	36529	21233	0.581 ± 0.005	0.631 ± 0.007	0.367 ± 0.004
ψ(2S)	11543	34540	17918	0.519 ± 0.003	0.644 ± 0.006	0.317 ± 0.004

Table 4.3: *Signal yields, acceptance and efficiency $A_{\pi\pi} \cdot \epsilon_{\pi\pi}$ for $\psi(2S)$ and $X(3872)$ prompt components.*

4.6 Signal and background determination

The ratio of signal yields is extracted from the $J/\psi\pi^+\pi^-$ invariant mass spectrum in the kinematic region in which the $J/\psi\pi^+\pi^-$ system has a transverse momentum $p_T > 8$ GeV/c and the absolute value of rapidity $|y| < 2.2$. The mass spectrum is shown in Fig. 5.13. Clear signals of the $\psi(2S)$ and $X(3872)$ states are observed.

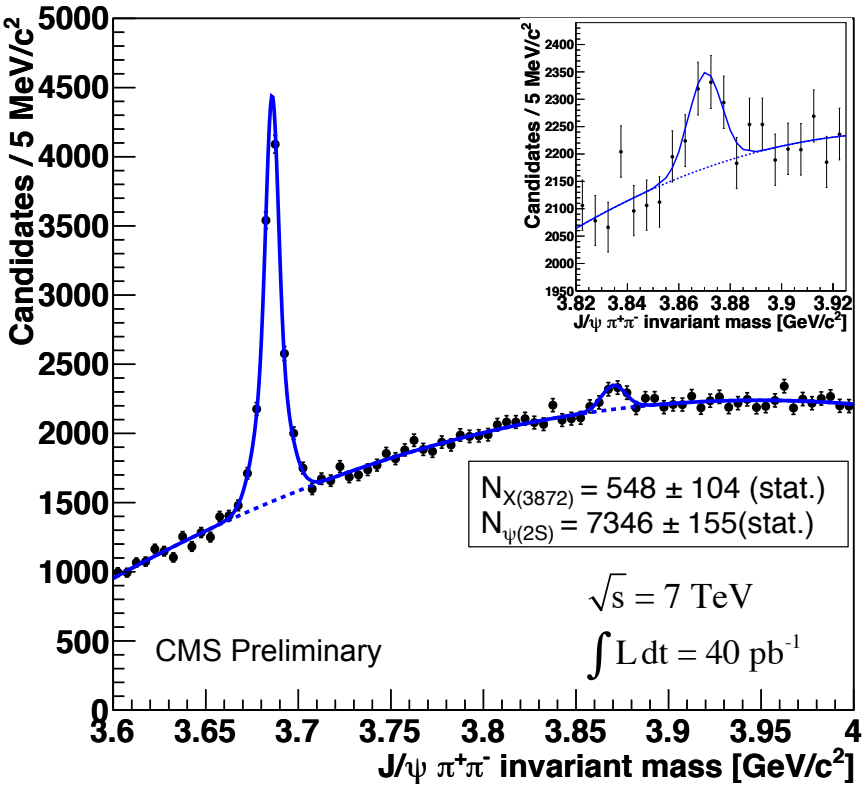

Figure 4.12: *$J/\psi\pi^+\pi^-$ invariant mass spectrum in the region $p_T > 8$ GeV/c and $|y| < 2.2$. The curve represents the result from an unbinned log likelihood fit. The insert shows the mass region around the $X(3872)$.*

In order extract the number of signal events for the $\psi(2S)$ and $X(3872)$ an unbinned log likelihood fit is performed to the invariant mass spectrum of the $J/\psi\pi^+\pi^-$ system, in a range from 3.6 GeV/c^2 to 4.0 GeV/c^2, which includes about the 40 % of the remaining candidates, with an average of 2.4 candidates for an accepted event. The $\psi(2S)$ signal is parametrized using a double Gaussian function, while a single Gaussian is used for the

Parameter	Value
$M_{\psi(2S)}$	3.6859 ± 0.0001
$\sigma_{1\,\psi(2S)}$	0.0081 ± 0.0006
$\sigma_{2\,\psi(2S)}$	0.0033 ± 0.0003
$M_{X(3872)}$	3.8702 ± 0.0019
$\sigma_{X(3872)}$	0.0063 ± 0.0013
$N_{\psi(2S)}$	7346 ± 155
$N_{X(3872)}$	548 ± 104
$N_{\text{Background}}$	149189 ± 412
$S/B_{2\sigma}\ \psi(2S)$	0.05 ± 0.01
$S/B_{2\sigma}\ X(3872)$	0.93 ± 0.02
χ^2_{fit}	0.769

Table 4.4: *Parameters obtained from the fit to the invariant mass spectrum.*

$X(3872)$ signal. A second order Chebyshev polynomial [1] is used for the background. Chebyshev polynomials are chosen over regular polynomials because of their superior stability in fits. Chebyshev polynomials and regular polynomials can describe the same shapes, but a clever reorganization of power terms in Chebyshev polynomials results in much lower correlations between the coefficients in a fit, and thus to a more stable fit behaviour.

The full set of parameters returned from the unbinned fit are given in Table 5.2. $M_{\psi(2S)}$ and $M_{X(3872)}$ are the means of the Gaussian peaks, and σ their standard deviation. The values of the ratio $\frac{Signal}{Background}$ (S/N) are calculated in a mass window of 2σ around the mean of the two particles mass peaks. Even if the error is only statistical, the value for the mass of the $X(3872)$ appear compatible with the world average of $3871.79 \pm 0.30\, MeV/c^2$

The yield is obtained using the extended version of the log likelihood formalism. In this framework, the fitting model M_E is expressed directly in terms of the number of signal (N_S) and background (N_B) events

$$M_E(x) = N_S\, S(x) + N_B\, B(x) \tag{4.5}$$

In this expression $M_E(x)$ is not normalized to 1 but to $N_S + N_B = N$, the number of events in the data sample. Therefore it is not a proper probability density function, but rather a shorthand notation for two expressions: the shape of the distribution and the expected number of events. The normalized model M(x) can be written as:

$$M(x) = \left(\frac{N_S}{N_S + N_B}\right) S(x) + \left(\frac{N_B}{N_S + N_B}\right) B(x). \tag{4.6}$$

The expected number of events is defined as:

$$N_{expected} = N_S + N_B \tag{4.7}$$

$N_{expected}$ and M(x) can be jointly constrained in the extended likelihood formalism as:

$$-logL(p) = -\sum_{data} logM(x_i) - log\ Poisson(N_{expected}, N_{observed}) \tag{4.8}$$

The operators for this calculation are implemented in the RooFit [85] packake used for all the fits presented in this thesis. The statistical error on the $X(3872)$ yield is of order 20%, and is the main source of uncertainty in the analysis.

4.7 Systematic uncertainties

The systematic error on the cross section ratio is composed of those contributions to the uncertainty that are uncorrelated between the $X(3872)$ and the $\psi(2S)$. The list of these contributions is given in the following.

- The systematic error on the signal extraction is determined by variation of the fit parametrizations in the following way. For the background a third and fourth order Chebyshev polynomial and a fourth order regular polynomial are used. For the signal, the sum of a Breit-Wigner and a Gaussian function is used for the $\psi(2S)$; other functions were tried, but they all failed to describe correctly the $\psi(2S)$ peak. The maximum difference between the standard result and the values obtained changing the PDFs is assigned as systematic uncertainty. For the $\psi(2S)$ yield it amounts to 10%. For the ratio of the yields $\frac{N_{X(3872)}}{N_{\psi(2S)}}$ the largest difference amounts to 5.3%., when using the fourth order regular polynomial for the modelling of the background.

- According to the Monte Carlo simulation, the efficiency for the successful reconstruction of a single pion track with at least two pixel and five strip detector hits and a transverse momentum of 400 MeV/c is about 70%. In a similar kinematic region, the absolute uncertainty on the efficiency to reconstruct a single pion track successfully has been determined to be 3.9%, with the data-driven analysis reported in Section 3.2.4. For the pair of pions the uncertainty is correspondingly larger. However, for the measurement of the cross section ratio, the uncertainty on the track finding efficiency is expected to partially cancel. The uncertainty on the ratio is conservatively estimated to be no larger than 4%.

- Variations of the non-prompt fractions of $X(3872)$ and $\psi(2S)$ to 20% and 40% result in differences as large as 6% with respect to the nominal assumption of non-prompt fractions of 30% . This uncertainty is quoted as systematic error.

- The production mechanism of the $X(3872)$ is unknown. The p_T dependence of the result is evaluated by reweighting the prompt $X(3872)$ p_T distribution such that possible discrepancies between the data and the simulation are covered, and the reweighted spectra are used to derive the corrections. A function based on the normalized p_T spectrum coming from PYTHIA is used to extract an event by event weight. On the basis of this weight all the correction factors are recalculated. Figure 4.13(a) shows the final effect of applying an opportune third order polynomial or its inverse to the original Monte Carlo. On 4.13(b) is presented the ratio between the new obtained shape and the original one, showing variation from -50% up to +250%. The results applying this reweighing method are summarized in Table 4.5. Half of the maximum difference between the standard result and the results from the variations is assigned as systematic uncertainty. It amounts to 3.5%.

- The uncertainty introduced by finite Monte Carlo statistics is determined to be 1.8%. The largest impact comes from the determination of the efficiency and acceptance of the pion pair.

- In the kinematic range under study the trigger selection efficiency for both $X(3872)$ and $\psi(2S)$ is very high and, in the ratio, the uncertainty originating from the trigger selection is negligibly small.

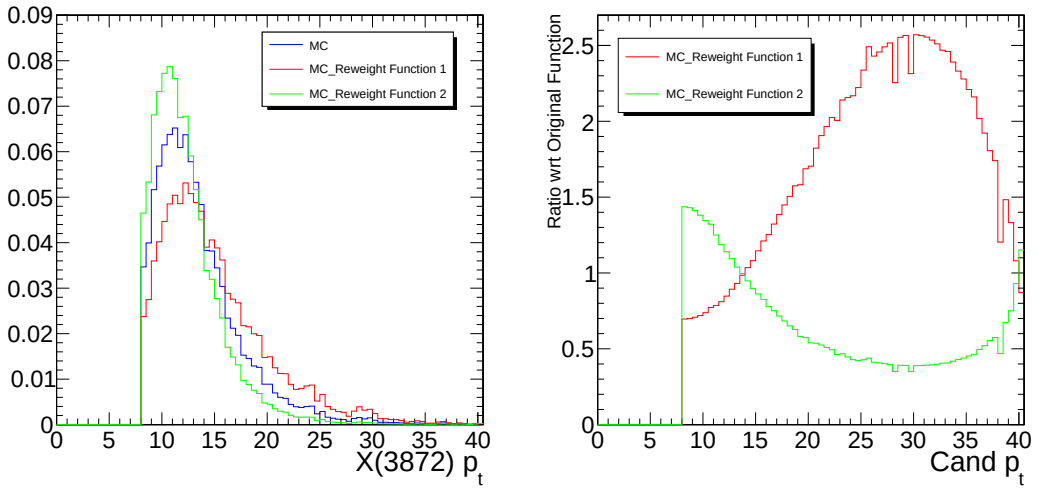

(a) (b)

Figure 4.13: *Reconstructed $X(3872)$ p_t distribution in Monte Carlo (blue) and variations due to reweighting using a polynomial (red) and its inverse (green) on (a), ratio of these two new shapes w.r.t. the original one on (b)*

	Function 1	Function 2
J/ψ Acceptance Ratio	0.835 ± 0.002	0.857 ± 0.002
J/ψ Efficiency Ratio	0.968 ± 0.009	1.076 ± 0.009
$A_{\pi\pi} \cdot \epsilon_{\pi\pi}$	1.08 ± 0.02	0.95 ± 0.01
C	0.873 ± 0.015	0.877 ± 0.018
$X(3872)/\psi(2S)$ Final ratio	0.085 ± 0.016	0.087 ± 0.016
Difference From Central Value	−7%	−5.3%

Table 4.5: *Parameters obtained from the fit to the invariant mass spectrum.*

The different contributions to the systematic error are listed in Table 4.6. The total relative systematic error on the cross section ratio is estimated to be 10%. This is a conservative estimate, however, significantly smaller than the statistical uncertainty.

To gain further confidence in the result and evaluate possible bias, a cut variation study has been performed, regarding especially the cuts on the pion selection. This has been done taking one at the time the cuts, and changing their value in an opportune window. For each of this variations the yield from experimental data are again extracted from the new mass spectrum, and modified corrections factors are calculated from the simulation, in a pure prompt component scenario.

The cuts that have been chosen for this kind of check are the minimum number of hits in the Strip detector, the minimum pion transverse momentum, the minimum 4-track vertex fit probability, the maximum $\Delta R(\pi - J/\psi)$, and the minimum transverse momentum of the $\pi\pi$ system. The results of this study are shown in Table 4.7. Due

track finding efficiency of pions	4%
signal extraction	5.3%
non-prompt fraction	6.0%
$X(3872)$ p_T shape	3.5%
MC statistics	1.8%
Full systematic error	10%

Table 4.6: *Summary of the evaluated systematic uncertainties.*

to the small size of $X(3872)$ signal, the variations on the final result (see column 5 of Table 4.7) are dominated to a large extent by statistics. Thus it was decided not to include these results as additional terms in the total systematic uncertainty.

Nevertheless it's worth noting than when the p_T region of the analysis has been varied, which implies recalculating all the terms of the correction factor and a new confidence region for the data, a good stability of the final results has been found in the limits of the statistical uncertainty. This shows a good description in the simulation of the kinematical distribution of the real events.

4.8 Data-driven pion pair acceptance and efficiency

A data-driven verification of the simulated pion pair acceptance and efficiency has been performed by measurement of the candidate yields of the two decay channels of the $\psi(2S)$:

$$\psi(2S) \to \pi^+\pi^-(J/\psi \to \mu^+\mu^-) \tag{4.9}$$

and

$$\psi(2S) \to \mu^+\mu^-. \tag{4.10}$$

Correcting for branching ratios and differences in acceptance and efficiency of the muon pair, the difference between the two decay channels can be attributed to the efficiency and acceptance of the pion pair. The same study has been performed in the data and simulation samples, such that a difference in the results would indicate problems in the description of the pion pair reconstruction by the simulation.

The study has been performed in the same kinematic range as the measurement, i.e. $p_T(\psi(2S)) > 8$ GeV/c and $|y_{(\psi(2S))}| < 2.2$. In order to extract the yields for data, the same dataset and trigger selection has been chosen. The mass spectrum for the $\mu^+\mu^-$ invariant mass is shown in Figure 4.14. To extract the number of candidates, an unbinned log likelihood fit to the $\mu^+\mu^-$ system invariant mass spectrum has been performed. The $\psi(2S)$ signal has been parametrized using a double Gaussian, while, for the background, an exponential function has been used. The full set of parameters returned from the unbinned fit is given in Table 4.8.

From the experimental, data the obtained yields for the $J/\psi\pi^+\pi^-$ channel and the $\mu^+\mu^-$ channel are 7346± 156 and 13080± 170, respectively. Their ratio is 0.561 ± 0.014.

The acceptance ratio for the two decay channels is shown in Fig. 4.15. In the kinematic range under investigation an average value of 0.8476 ± 0.0018 is found.

Cut variation	$N(X(3872))$	$N(\psi(2S))$	$A_{\pi\pi} \cdot \epsilon_{\pi\pi}$	Measurement	% difference
$N_{Strip\ hits} > 7$	416 ± 102	6151 ± 144	1.102 ± 0.019	0.083 ± 0.020	-9.7%
$N_{Strip\ hits} > 9$	398 ± 85	5258 ± 132	1.107 ± 0.020	0.093 ± 0.020	+0.6%
$N_{Strip\ hits} > 11$	326 ± 71	4017 ± 112	1.109 ± 0.022	0.099 ± 0.022	+7.2%
$p_T(\pi) > 350$ MeV	600 ± 144	7676 ± 175	1.087 ± 0.016	0.097 ± 0.024	+5.7%
$p_T(\pi) > 450$ MeV	500 ± 120	6894 ± 165	1.120 ± 0.017	0.088 ± 0.021	-4.7%
$p_T(\pi) > 500$ MeV	489 ± 113	6468 ± 146	1.131 ± 0.017	0.091 ± 0.020	-1.6%
$p_T(\pi) > 550$ MeV	469 ± 99	5961 ± 146	1.144 ± 0.018	0.093 ± 0.020	+0.1%
$p_T(\pi) > 600$ MeV	434 ± 95	5306 ± 112	1.148 ± 0.019	0.097 ± 0.021	+5.1%
$\Delta R < 0.55$	432 ± 104	7286 ± 170	0.969 ± 0.015	0.083 ± 0.020	-10.0%
$\Delta R < 0.6$	482 ± 111	7365 ± 172	1.030 ± 0.015	0.086 ± 0.020	-6.4%
$\Delta R < 0.65$	526 ± 120	7302 ± 172	1.074 ± 0.016	0.091 ± 0.021	-1.4%
$\Delta R < 0.75$	518 ± 124	7383 ± 176	1.112 ± 0.016	0.086 ± 0.021	-7.2%
$\Delta R < 0.8$	533 ± 105	7479 ± 171	1.117 ± 0.016	0.086 ± 0.017	- 6.2%
$\Delta R < 0.85$	511 ± 116	7430 ± 163	1.118 ± 0.016	0.083 ± 0.019	-9.5 %
$P_{Vtx} > 0.02$	527±121	7272 ±158	1.082 ± 0.018	0.091 ± 0.020	-1.5%
$P_{Vtx} > 0.05$	524±120	7128 ±156	1.080 ± 0.018	0.092 ± 0.021	+0.2%
$p_T(\pi^+\pi^-) > 1.2$	561±142	8380±181	1.024 ± 0.015	0.086 ± 0.023	-6.9%
$p_T(\pi^+\pi^-) > 1.3$	544±183	8133±187	1.047 ± 0.015	0.087 ± 0.029	-6.0%
$p_T(\pi^+\pi^-) > 1.4$	526±188	7788±126	1.070 ± 0.016	0.086 ± 0.031	-7.0%
$p_T(\pi^+\pi^-) > 1.6$	536±120	7050±200	1.123 ± 0.017	0.092 ± 0.021	-0.3%
$p_T(\pi^+\pi^-) > 1.7$	534±119	6595±160	1.152 ± 0.018	0.095 ± 0.021	+3.2%
$p_T(\pi^+\pi^-) > 1.8$	515±90	6059±129	1.175 ± 0.018	0.098 ± 0.017	+6.3%
$\pi_{track}\ \chi^2 < 4$	479±124	7253±162	1.098 ± 0.018	0.082±0.021	-11.5%
$\pi_{track}\ \chi^2 < 3$	486±115	7069±167	1.096 ± 0.018	0.085± 0.020	-7.7%
$Candidate p_T > 9$	562±115	7032±172	1.087 ± 0.017	0.096± 0.020	+4.6%
$Candidate p_T > 10$	505±114	6466±165	1.070 ± 0.017	0.092± 0.021	-0.3%
$Candidate p_T > 11$	480±104	5797±151	1.061 ± 0.019	0.092± 0.021	+2.1%
$Candidate p_T > 12$	394±84	4973±133	1.060 ± 0.021	0.092± 0.019	-4.0%

Table 4.7: *Results for the yields and the corrected ratios for the prompt component due the different choices in the selection cuts affecting the $\pi\pi$ system. The transverse momentum is in units of GeV/c.*

The ratio of the efficiencies for the reconstruction of $\psi(2S)$ in the decay channel $\psi(2S) \to J/\psi\pi^+\pi^-$ and in the channel $\psi(2S) \to \mu^+\mu^-$ is shown in Fig. 4.16. The average for the kinematic range under investigation is 0.737 ± 0.007.

Correcting for the branching ratios [78], as summarized in Table 5.4, and for acceptance and efficiencies as obtained from the Monte Carlo simulation (described above), a value of 0.35 ± 0.04 has been obtained, where the main source of uncertainty is related to the knowledge of $\mathcal{B}(\psi(2S) \to)\mu^+\mu^-$ from PDG. This value, as obtained from the data, compares very well with the corresponding result from the Monte Carlo simulation, i.e. $(A_{\pi\pi}(\psi(2S)) \cdot \epsilon_{\pi\pi}(\psi(2S)) = 0.334 \pm 0.004$.

Finally, to estimate an average pion-pair and subsequently single pion reconstruction efficiency for the range of the measurement, the value extracted from the data, 0.35 ± 0.04, has been divided by the pion pair acceptance, $A_{\pi\pi} = 0.519 \pm 0.003$ as determined from MC and listed in Table 4.3, yielding $\epsilon_{\pi\pi}^{data-driven}$ 0.67 ± 0.08.

The square root of this value, 0.82 ± 0.09, gives an estimate for the mean value of the reconstruction efficiency for single pions. Taking into account that the pions coming from

Parameter	Value
$M_{\psi(2S)}$	3.6815 ± 0.0004
$\sigma_{1\,\psi(2S)}$	0.024 ± 0.002
$\sigma_{2\,\psi(2S)}$	0.050 ± 0.003
$N_{\psi(2S)}$	13080 ± 170
N_{bkg}	19740 ± 190
$S/B_{2\sigma}(\psi(2S)$	2.90 ± 0.05
χ^2_{fit}	1.21

Table 4.8: *Parameters obtained from the fit to the $\mu^+\mu^-$ invariant mass spectrum.*

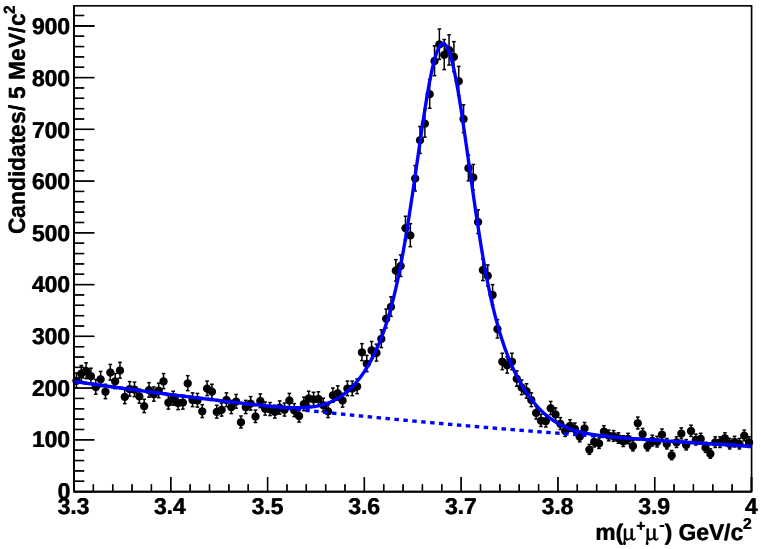

Figure 4.14: *$\mu^+\mu^-$ invariant mass spectrum in the region $p_T > 8$ GeV and $|y| < 2.2$.*

$\mathcal{B}(\psi(2S) \to J/\psi\pi^+\pi^-)$	33.6 ± 0.4 %
$\mathcal{B}(\psi(2S) \to \mu^+\mu^-)$	$(7.7 \pm 0.8) \times 10^{-3}$
$\mathcal{B}(J/\psi \to \mu^+\mu^-)$	(5.93 ± 0.06)%

Table 4.9: *Branching Ratios.*

the $\psi(2S)$ have lower momentum than the ones from X(3872), this result for the single pion reconstruction efficiency indicates that the analysis has been performed in a region where the tracking efficiency of the detector is sufficient. Fig. 4.17 shows a scan of the result for variation of the pion pair selection. The excellent agreement between data and Monte Carlo simulations gives further confidence that the pion pair reconstruction is well described in the simulation, within the uncertainties of the method.

4.9 Final result

From the fit of the invariant mass distribution (Fig. 5.13) the following numbers of $X(3872)$ and $\psi(2S)$ candidates are obtained:

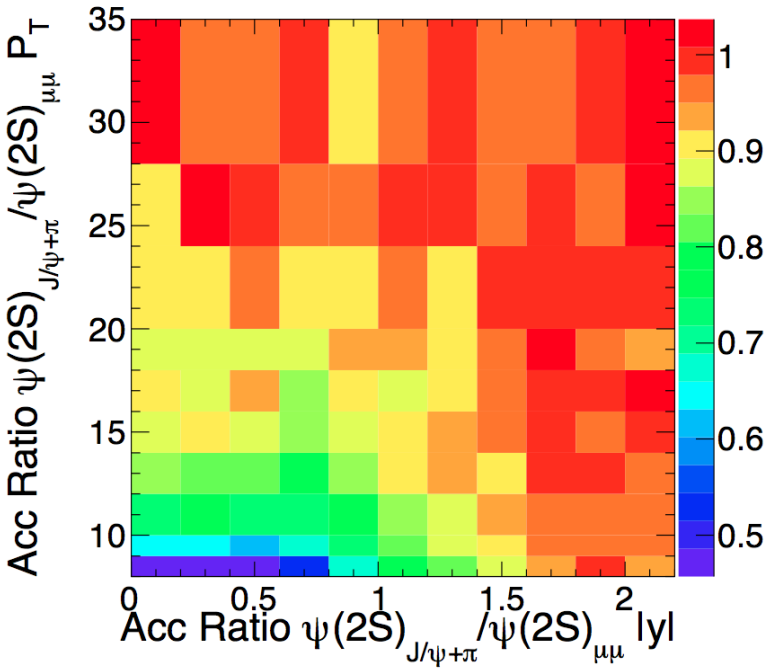

Figure 4.15: *Acceptance ratio for* $\psi(2S) \to J/\psi\pi^+\pi^-$ *and* $\psi(2S) \to \mu^+\mu^-$

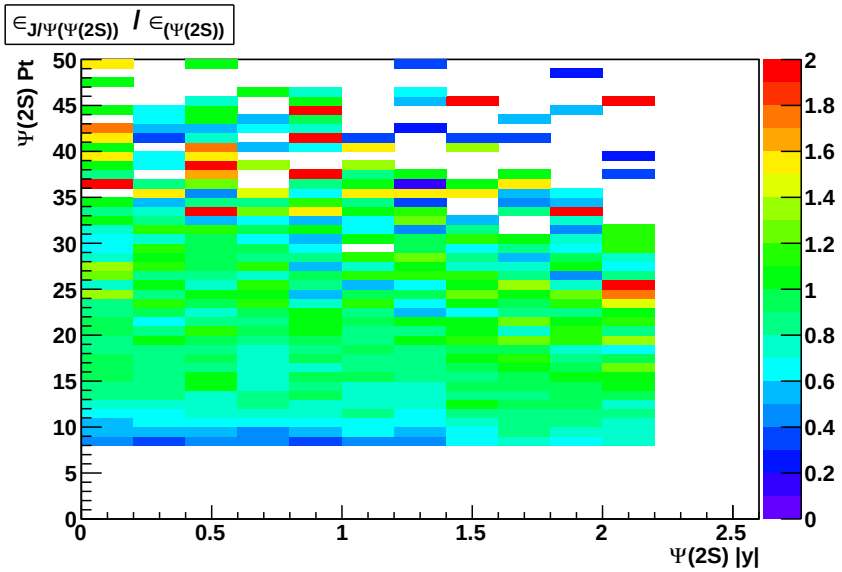

Figure 4.16: *Efficiency ratio for* $\psi(2S) \to J/\psi\pi^+\pi^-$ *and* $\psi(2S) \to \mu^+\mu^-$

$$N_{X(3872)} = 548 \pm 104(stat.) \tag{4.11}$$

and

$$N_{\psi(2S)} = 7346 \pm 155(stat.), \tag{4.12}$$

where the error refers to the statistical uncertainty, as listed in Table 5.2.

The ratio of acceptance-corrected yields is then

$$R = \frac{N_{X(3872)}}{N_{\psi(2S)}}/C = \frac{\sigma(pp \to X(3872) + \text{anything}) \times \mathcal{B}(X(3872) \to J/\psi\pi^+\pi^-)}{\sigma(pp \to \psi(2S) + \text{anything}) \times \mathcal{B}(\psi(2S) \to J/\psi\pi^+\pi^-)} \quad (4.13)$$

Applying the correction $C = 0.863 \pm 0.015$ to the ratio of measured signal yields, a value

$$R = 0.087 \pm 0.017(stat.) \pm 0.009(syst.) \quad (4.14)$$

is obtained, where the first error arises from the statistical uncertainty of the signal yield in the data, and the second error is the systematic uncertainty, as detailed in Section 5.10.

4.10 Study of kinematic distributions

A sideband subtraction method is used to remove continuum background from the data distributions and thus facilitate direct comparisons between the data and Monte Carlo simulations of signal events. The method makes use of the invariant mass spectrum (Fig. 4.18) and assumes that the continuum events in the sideband regions, i.e. in the regions close to, but outside the invariant mass signal window, have the same properties and distributions as the background events inside the mass signal window.

A sideband subtracted distribution is constructed by determining the distribution of events separately in the signal and sideband regions, and subtracting distributions in the sidebands, normalized to their width, from the signal distribution. Specifically, here, the sideband distributions are extracted separately from two regions below and above the signal region. Subsequently, the two sideband distributions are summed and the summed sideband distribution is normalized to the signal distribution using the integral of the background function in the central and sideband regions. Fig. 4.18 shows the choices made for the central and sideband regions for both $\psi(2S)$ and $X(3872)$ signal, using as a discriminatory factor the invariant mass of the $J/\psi\pi^+\pi^-$ system.

The shapes of the background subtracted distributions of the p_T for the candidate and J/ψ are shown in Fig. 4.19 and Fig. 4.20 respectively. In Fig. 4.21 and Fig. 4.22 the pion p_T is presented, separated between the lower momentum (soft) and higher momentum (hard) pion in the pair. The shapes of the distributions for the $\psi(2S)$ show a good agreement between data and Monte Carlo, with deviations usually within the statistical errors. However, the $X(3872)$ distributions are strongly statistics limited, due to the poor signal to background ratio.

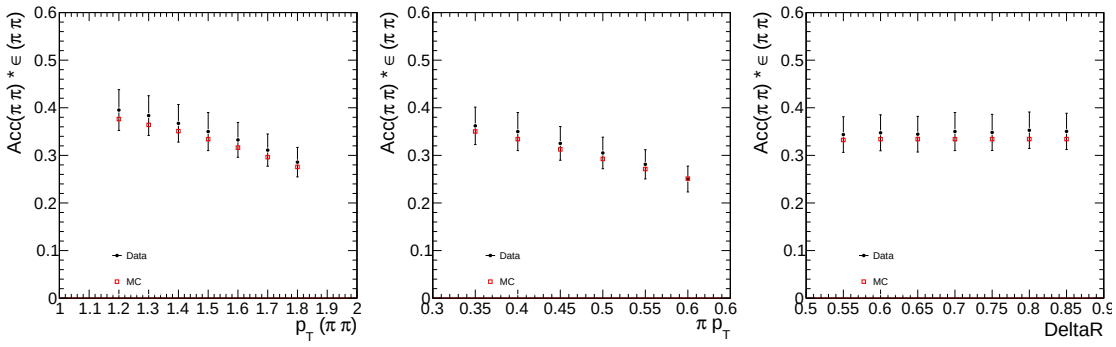

(a) (b) (c)

Figure 4.17: *Acceptance and efficiency of the pion pair for Monte Carlo simulation (red squares) and data (black circles) as a function of different cuts on $p_T(\pi^+\pi^-)$ (a), $p_T(\pi)$ (b) and ΔR (c).*

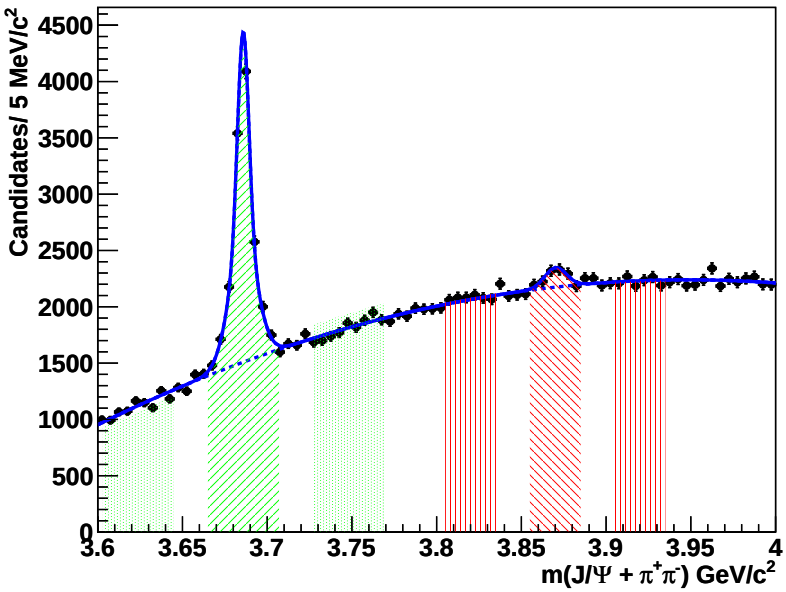

Figure 4.18: *$J/\psi\pi^+\pi^-$ mass spectrum. In green the signal and sideband regions for the $\psi(2S)$, in red the ones for the $X(3872)$*

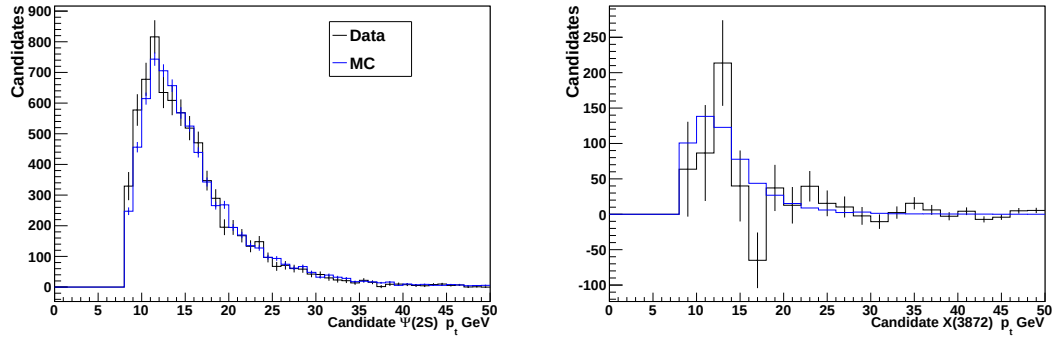

(a) (b)

Figure 4.19: *Candidate p_T after sideband subtraction, compared with the MC distribution for $\psi(2S)$ (a) and $X(3872)$ (b)*

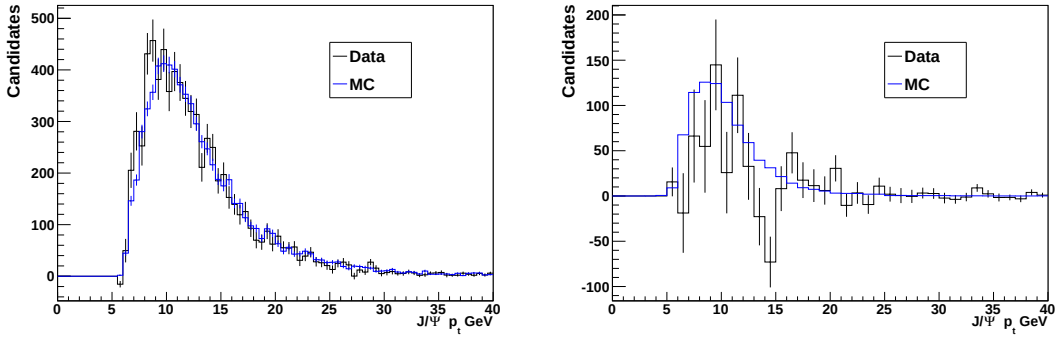

(a) (b)

Figure 4.20: *Distribution of the J/ψ p_T after sideband subtraction, compared with the MC distribution for $\psi(2S)$ (a) and $X(3872)$ (b)*

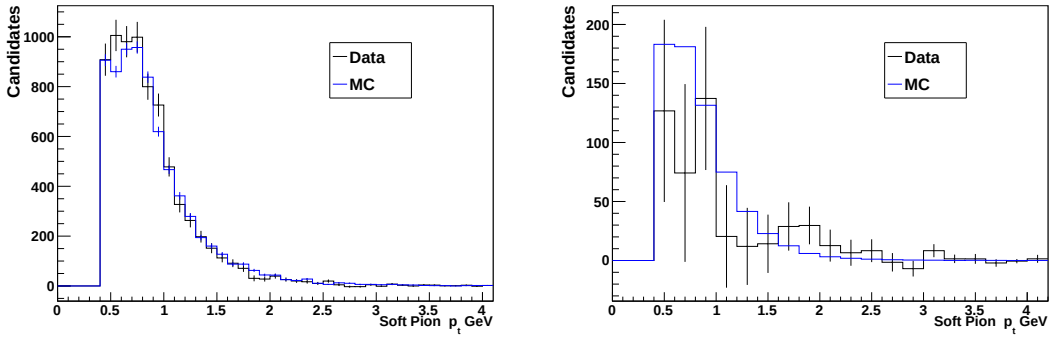

(a) (b)

Figure 4.21: *Lower momentum pion π p_T after sideband subtraction, compared with the MC distribution for $\psi(2S)$ (a) and $X(3872)$ (b)*

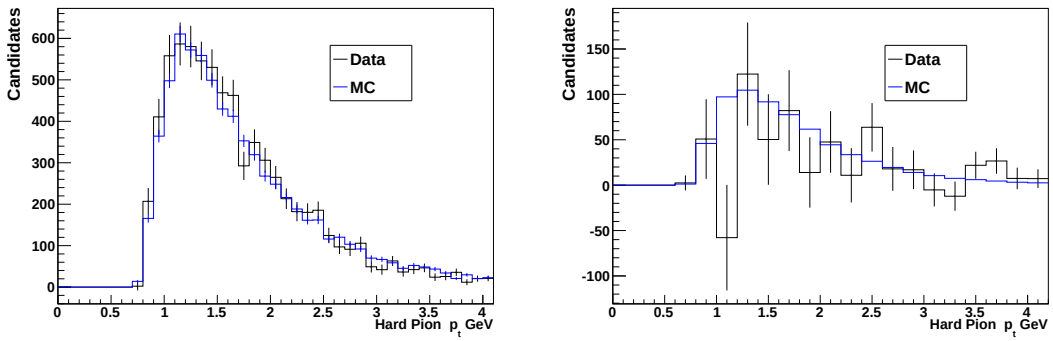

(a) (b)

Figure 4.22: *Higher momentum π p_T after sideband subtraction, compared with the MC distribution for $\psi(2S)$ (a) and $X(3872)$ (b)*

4.11 Conclusion and Discussion

In this chapter has been shown how, with just the first data coming from LHC collisions, a clear signal for the $X(3872)$ has been established by the CMS experiment.

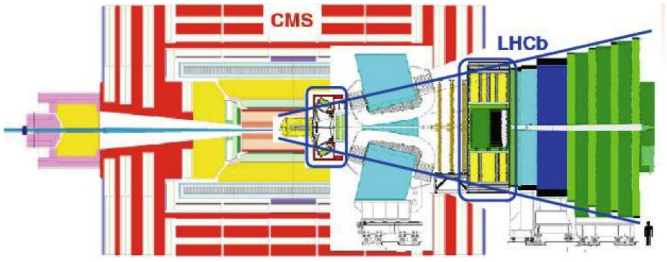

Figure 4.23: *Comparison of the LHCb and CMS detectors.*

The measurement of the production cross section ratio presented is the first of its kind, and the first result on the $X(3872)$ in pp collision at $\sqrt{7}$ TeV.

During 2011 the LHCb collaboration has also presented its analysis on the data sample collected during 2010 [9], containing a precise measurement of the mass and a cross section determination. The acceptance region of the LHCb detector is complementary to the CMS one (see Fig. 4.23), and its cross section measurement is given for X(3872) with p_T within 5 and 20 GeV/c and a rapidity between 2.5 and 4.5. LHCb obtains

$$\sigma(pp \to X(3872)+anything)\times(X(3872) \to J/\psi\,\pi^+\pi^-) = 4.74\pm1.1\ (stat)\ \pm0.7\ (syst)nb \quad (4.15)$$

LHCb compares the result with the predictions of $13.0\pm2.7\ nb$ made in [25] from NRQCD calculation for the molecular model, finding a 2.8σ difference. Following LHCb procedure, the cross section in the acceptance region of the present analysis can be estimated as

$$\sigma(pp \to X(3872) + anything) \times (X(3872) \to J/\psi\,\pi^+\pi^-) = \frac{N_{X(3872)}}{\mathcal{B}(J/\psi \to \mu^+\mu^-) \cdot \mathcal{L}_{int} \cdot C_{X(3872)}} \quad (4.16)$$

where $C_{X(3872)}$ contains all the efficiency corrections for the $X(3872)$ taken from the simulation. Taking into account only statistical errors (that are expected to dominate the systematic uncertainties) the cross section results:

$$\sigma(pp \to X(3872) + anything) \times (X(3872) \to J/\psi\,\pi^+\pi^-) = 5.2 \pm 1.2\ (stat) \quad (4.17)$$

for $X(3872)$ candidates in kinematic region $p_T(X) > 8$ GeV/c and $|y(X)| < 2.2$.

Montecarlo Simulation can be used to extract acceptance conversion factor between different kinematic regions in order to compare this result In [25] the expected kinematic region for CMS was of candidates with $p_T > 5$ GeV/c and $|y| < 2.4$, for which a cross section of 57.2 ± 14.5 nb was calculated. Rescaling the acceptance through simulation in that region, the cross section would result 24.9 ± 4.2 (stat) nb, with an excess of 2.2σ with respect to data, similar to the LHCb observation.

Using the same method it's finally possible to make a direct comparison with the LHCb result (with all the caveats linked to the correct description in the simulation of the real $X(3872)$ kinematic distribution). The CMS cross section rescaled in the LHCb acceptance region results 5.6 ± 1.1 (stat) nb. The two results seem perfectly compatible, and could also imply that the kinematic distribution of the $X(3872)$ is quite similar to the one of a conventional charmonium state with $J^{PC} = 1^{++}$, like the one used in our simulation.

Chapter 5

Differential Cross Section Ratio

5.1 Introduction

In this section it's presented the measure of the ratio between the production cross section of the $X(3872)$ and $\psi(2S)$ into their decay channel $J/\psi\pi^+\pi^-$ as a function of their transverse momentum, using the data collected during 2011 by the CMS detector in pp collisions at $\sqrt{s} = 7\,TeV$. This analysis follows the same methods for the measurement described in Chapter 4, adapting it to the 2011 running condition.

5.2 Data samples

During 2011 LHC has gradually increased the instantaneous luminosity, up to $3.54 \times 10^{33}\,cm^{-1}s^{-1}$. This improvement has offered at the same time a great opportunity and a great challenge for quarkonium study with the CMS experiment.

In fact such instantaneous luminosity permits to largely increase data available: more than $5\,fb^{-1}$ of data have been delivered to CMS. On the other side the bandwidth available for low energy physics study is limited, and high rate events, like the production of J/ψ, with the trigger selection of 2010 would have rapidly saturated it.

The strategy followed in CMS to overcome this limitation and still obtain enough statistic for various low energy analysis in the charmonium and bottomium mass region, has been to develop specific HLT trigger paths for every analysis. Every trigger path has been studied to guarantee an high level of purity for the selected object. The cuts used in this paths have followed the evolution of the LHC luminosity in order to maintain a similar rate throughout the year.

The evolution of the trigger path is shown in Fig. 5.1. In these plots the di-muon mass distribution obtained from overlapping several specific HLT trigger paths is plotted for different trigger *menu*. A trigger *menu* is the collection of the trigger paths actually used at HLT level, and different trigger *menu* are designed for different LHC instantaneous luminosity, from which they take the name. In Fig. 5.1(a) and Fig. 5.1(b) is shown the di-muon spectrum in the same period of data taking (for $L_{max} = 5 \times 10^{32}$, so $5E33menu$) for a generic trigger, which requires two muons with $p_T > 3$ GeV/c, and for the sum of specific triggers path developed to point to quarkonium resonances. Fig. 5.1(c) and Fig. 5.1(d) show the evolution of the dimuon mass spectrum for the $1E33$ and $1p4E33$ trigger *menus*, respectively.

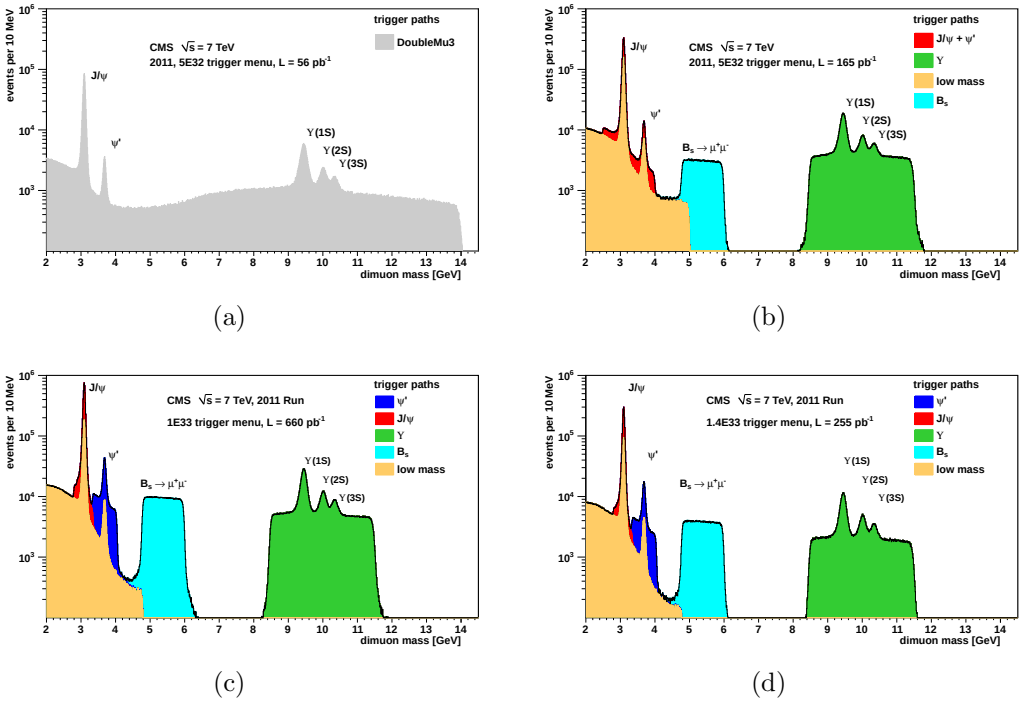

(a) (b)

(c) (d)

Figure 5.1: *Evolution of the di-muon trigger paths for studies regarding quarkonium in CMS*

For the $X(3872)$ studies the triggers of interest are the ones developed for the J/ψ, in order to reconstruct the $X(3872)$ and $\psi(2S)$ in their $J/\psi\pi^+\pi^-$ decay channel. These triggers require oppositely charged di-muon invariant mass between 2.95 and 3.25 GeV, with a di-muon rapidity cut of $|y(\mu\mu)| < 1.25$ and a p_T threshold for the pair of muons that increased from 6.5 to 10 GeV over time. The rapidity region limited to the barrel has been chosen in order to keep the region with the better momentum resolution and lower background. Due to the trigger the fiducial region for the analysis has been limited to $|y(X_{cand})| < 1.25$, $p_{T\,Xcand} > 10 GeV/c$, with additionally $p_{T\,J/\psi} > 6.5\ GeV/c$ and $|y(J/\psi)| < 1.25$. The data from higher trigger cuts on the J/ψ have been used to populate only the higher bins in the differential analysis. A run-dependent trigger selection is applied to the data. In order to have consistent trigger types during the analysis, the di-muon trigger, used in the first period of data taking, and the last trigger *menu*, where the J/ψ was requested to be over 12.5 GeV/c, were not used.

With these requirements the data sample used for the measurement of the differential cross section ratio is equivalent to 4.5 fb^{-1} of integrated luminosity.

Another challenge with respect to the Chapter 4 analysis is the increased pile-up, with a average number of about 10 inelastic pp collisions per bunch crossing in the CMS interaction point. At HLT trigger level a pile-up protection has been implemented, based on the distance between the two muons, in order not to fire the di-muon trigger if the two muons come from different primary vertexes. For what regards the analysis, studies conducted on data and simulation showed no strong effects on the efficiency due to the higher pile-up.

For the analysis described in this chapter, simulation samples similar to the one described in Section 4.2 have been used, changing the acceptance region in order to mirror

the new fiducial region for the measurement ($p_T > 7\ GeV$ and $|y| < 1.5$ for the $\psi(2S)$ and $X(3872)$ and $p_T > 2.5\ GeV$ for the muons - see Section 5.5).

5.3 Selection of $J/\psi \to \mu\mu$ events

The reconstruction of J/ψ candidates follows the selection described in Section 4.3, with just some differences on the kinematic region for the muons and the final J/ψ candidates. Following more detailed study on the muon acceptance (see Fig. 5.2) the kinematic requirements imposed on the muon candidate tracks are:

$$p_T > 4 \text{ GeV/c} \quad \text{for} \quad |\eta| < 1.2$$
$$p_T > 3.3 \text{ GeV/c} \quad \text{for} \quad 1.2 < |\eta| < 2.4$$

In order to satisfy the requirements introduced at trigger level, cuts on the J/ψ kinematics such as $p_T > 7$ GeV/c and $|y| < 1.25$ are applied, following the trigger evolution.

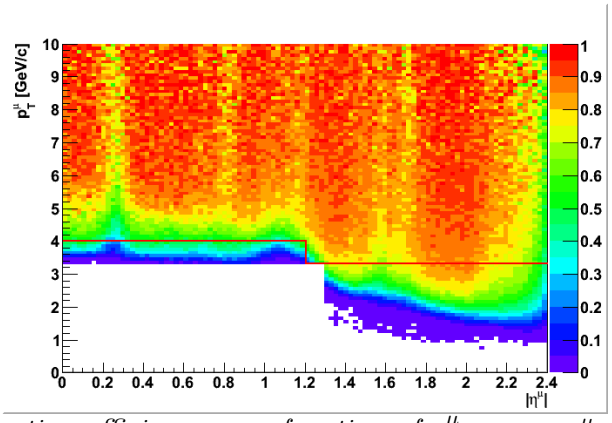

Figure 5.2: *Muon detection efficiency as a function of p_T^μ versus η^μ. The red line shows the cuts defining the single-muon acceptance region [8]*

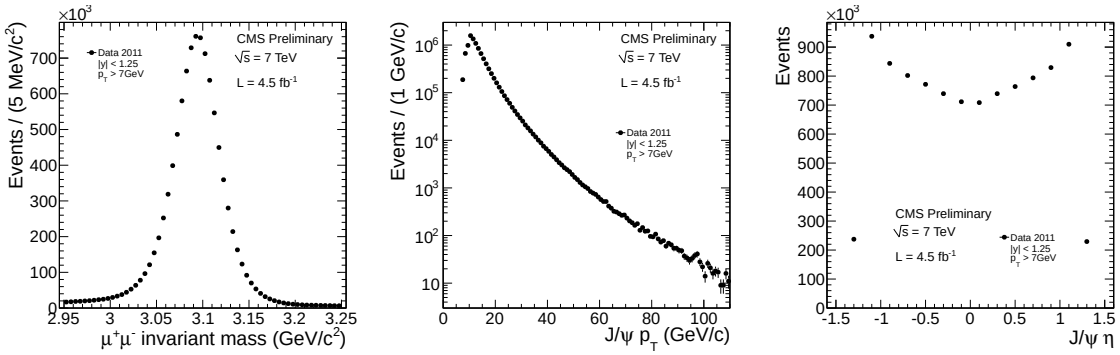

(a) (b) (c)

Figure 5.3: *The invariant mass (a), p_T (b) and rapidity (c) distribution of the two opposite charged muons after the selection cuts for the J/ψ*

In Fig 5.3 the invariant mass distribution in data of the two opposite charged muons is shown, corresponding to about 10^7 J/ψ.

Figure 5.4 shows the stability over time of the J/ψ yield. The vertical drops corresponds to the introduction of a new trigger *menu*. The fluctuations in the last period of data taking are due to prescale factor applied to the used trigger path.

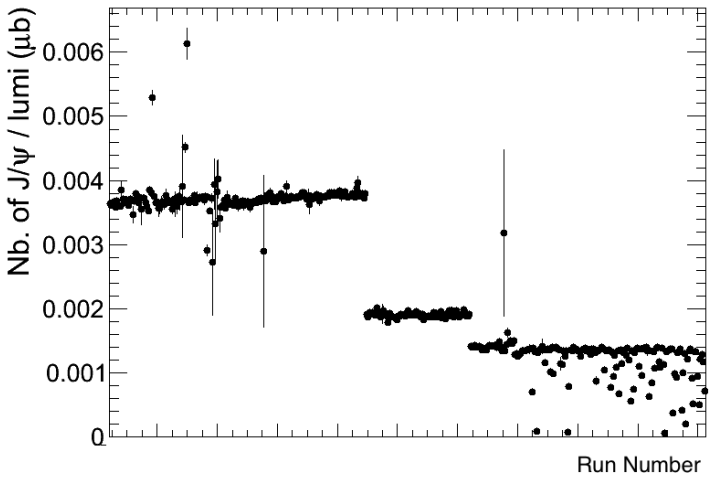

Figure 5.4: *J/ψ uncorrected yield as a function of run number. The vertical drop corresponds to the introduction of a new trigger menu.*

In order to select the J/ψ meson candidates for further analysis, a window in the invariant mass distribution of $3019 < M_{J/\psi} < 3167$ is defined, corresponding to a 2.5 σ region with mass resolution $\sigma = 29$ MeV.

The J/ψ meson candidates are combined with a pair of opposite charge pion track candidates. With respect to 2010, some selection cuts on the pions have been changed. This reflect both the fact that the analysis is made in a different kinematic region (for example a $X(3872)$ with higher p_T more likely generates higher p_T pions) and the more detailed data-driven studies are possible (thanks to the higher statistic). Pion tracks are selected if they have at least two hits in the pixel detector, at least seven hits in the strip detector and a $\chi^2/NDF < 5$. To reduce the combinatorial background to a reasonable level, the transverse momenta of the pions are required to be larger than 600 MeV/c. The pions track candidates that match kinematically with the muon tracks are removed to avoid duplicates.

To suppress the combinatorial background arising from tracks originating from different vertices, the probability of the 4-track vertex fit is required to be larger than 0.05. The behaviour of the 4-track vertex probability in simulation (Fig 5.5) shows that this requirement is particularly effective in the non-prompt case. In fact when the J/ψ comes from the displaced vertex of the B-meson decay if a track coming from the collision point is used to build a vertex instead of the correct pions, it gives a low 4-track vertex probability.

The optimal cut is found from the behaviour of $X(3872)$ yields and signal-over-background ratio (Fig. 5.6).

The opening angle between the pion pair and the J/ψ (ΔR) is used as further selection criteria. The impact on the $X(3872)$ yield of various ΔR thresholds is reported in Fig. 5.7, showing that with $\Delta R > 0.55$ the available statistic starts to decrease. Based on these findings a cut $\Delta R < 0.55$ is applied. From Monte Carlo studies shown in Fig. 5.8 the

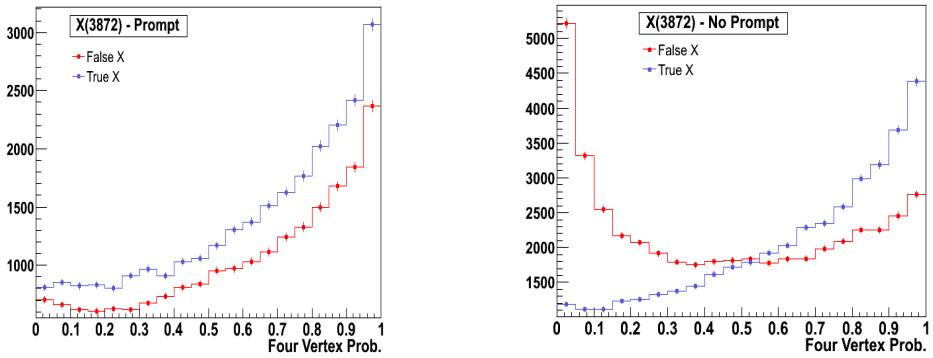

Figure 5.5: *The 4-track vertex probability distribution in prompt $X(3872)$ simulation (left) and in non-prompt $X(3872)$ simulation (right) for both candidates matched to the MC truth (True X) and not matched with the MC truth (False X).*

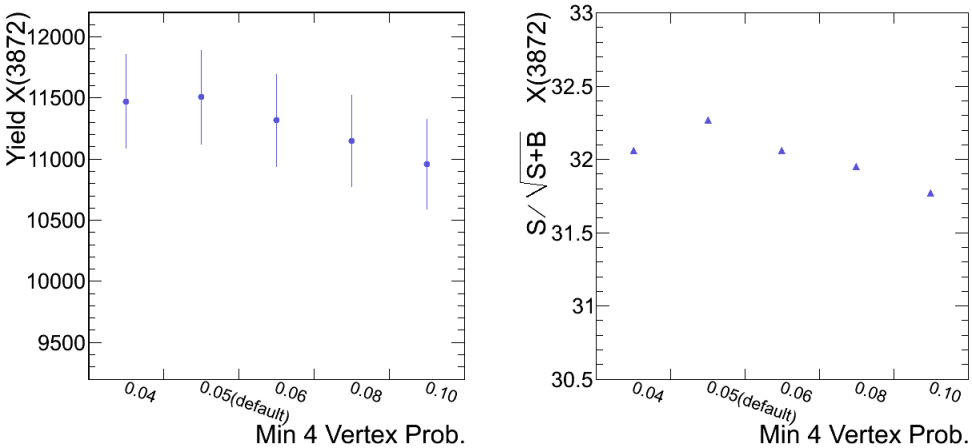

Figure 5.6: *The $X(3872)$ yield (left) and $S/\sqrt{S+B}$ (right) extracted from data as a function of 4-track vertex probability thresholds.*

requirement $\Delta R < 0.55$ reduces the background by 7% while keeping 99% of the signal.

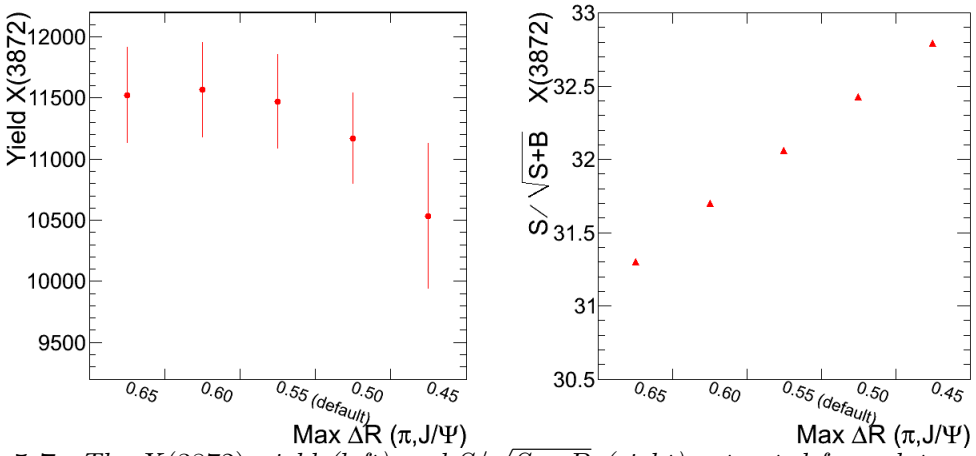

Figure 5.7: *The $X(3872)$ yield (left) and $S/\sqrt{S+B}$ (right) extracted from data as a function of $\Delta R(\pi, J/\psi)$ thresholds.*

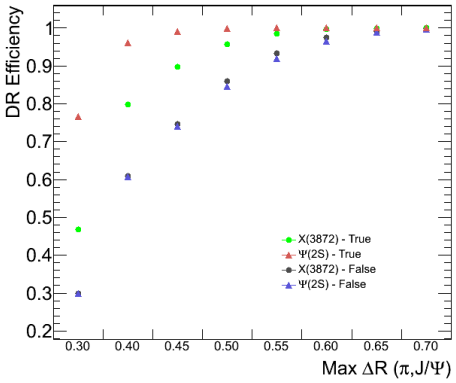

Figure 5.8: *Efficiency of various $\Delta R(\pi, J/\psi)$ cuts for both signal (i.e. candidate matched with the MC truth) and background events, estimated from $X(3872)$ and $\psi(2S)$ Simulation.*

A powerful selection criteria to reduce the background is to cut on the quantity:

$$Q = M_{\mu\mu\pi\pi} - M_{J/\psi}(PDG) - M_{\pi\pi}. \tag{5.1}$$

The $X(3872)$ yield and signal over background ratio, as a function of different Q-value cuts, in Fig. 5.9 shows that tightening the Q value cut increase the signal significance at the price of loss in statistic. From Monte Carlo calculations is clear that a tight requirement on the Q value removes a significant fraction of the signal too, as illustrated in Fig. 5.10. A cut $Q < 0.3\ GeV/c^2$, that removes about 20% of the background while retaining 97% of the $X(3872)$ signal, and all the $\psi(2S)$ signal is used in this analysis. Such cut corresponds to a minimum of 470 MeV/c^2 for the di-pions invariant mass coming from the $X(3872)$ candidate.

As mentioned above, the $J/\psi \to \mu\mu$ trigger paths used are restricted to the barrel region and require a di-muon transverse momentum above 7 GeV/c. Sufficiently large

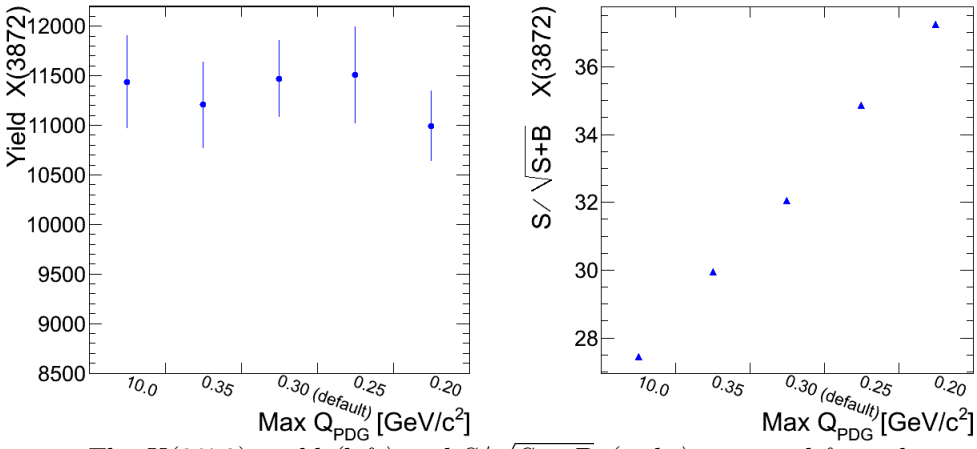

Figure 5.9: *The $X(3872)$ yield (left) and $S/\sqrt{S+B}$ (right) extracted from data as a function of Q-value.*

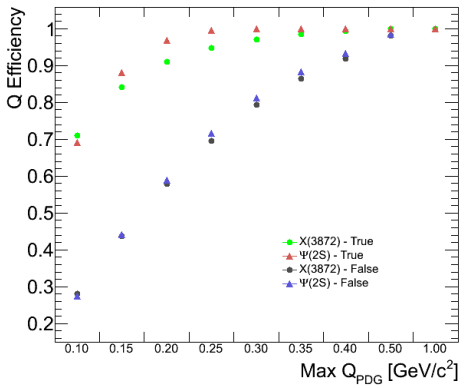

Figure 5.10: *Efficiency of various Q value cuts for both signal (i.e. candidate matched with the MC truth) and background events, estimated from $X(3872)$ and $\psi(2S)$ simulation.*

muon selection	
muon track fit χ^2/NDF	< 1.8
number of hits in Pixel	≥ 2
number of hits in Tracker	≥ 11
$p_T(\mu)$ for $\|\eta\| < 1.2$	> 4 GeV/c
$p_T(\mu)$ for$1.2 < \|\eta\| < 2.4$	> 3.3 GeV/c
di-μ vertex probability	> 0.01
$m_{\mu\mu}$	3019$-$3167 MeV/c^2
$p_T(\mu\mu)$	> 7 GeV/c
$\|y(\mu\mu)\|$	< 1.25
pion selection	
pion track fit χ^2/NDF	< 5
number of hits in Pixel	≥ 2
number of hits in Strip	≥ 7
$p_T(\pi)$	> 600 MeV/c
$J/\psi\pi\pi$ selection	
4-track fit vertex probability	> 0.05
$\Delta R(\pi, J/\psi)$	< 0.55
Q value	< 0.3 GeV/$c^2 \equiv ((m_{\pi\pi})^{min} > 470$ MeV)
p_T	> 10 GeV/c
$\|y\|$	< 1.25

Table 5.1: *The list of final cuts on the $J/\psi\pi^+\pi^-$ system.*

acceptance is found for the $X(3872)$ in the kinematic region $p_T(X) > 10\ GeV/c$ and $|y(X)| < 1.25$ that is chosen as fiducial region for the analysis.

The list of final cuts is given in table 5.1.

5.4 Signal and background determination

The ratio of signal yields is extracted from the $J/\psi\pi^+\pi^-$ invariant mass spectrum in the kinematic region in which the $J/\psi\pi^+\pi^-$ system has a transverse momentum $p_T > 10$ GeV/c and the absolute value of rapidity $|y| < 1.25$. To extract the inclusive yields from the $J/\psi\ \pi^+\pi^-$ invariant mass distribution an unbinned log likelihood fit is performed in two mass windows around the $\psi(2S)$ and $X(3872)$ peaks. The sum of two Gaussians is used for the description of the $\psi(2S)$ signal while a single Gaussian is used for the $X(3872)$ signal. The background is modelled by a second order Chebyshev polynomial.

The complete fits of the mass distribution for the $X(3872)$ and $\psi(2S)$ are reported in Fig. 5.11 and in Fig. 5.12 respectively.

The typical statistical error in each bin is around 10-15% for the $X(3872)$.

The mass spectrum for the $X(3872)$ in the whole kinematic region $p_T > 10$ GeV/c and $|y| < 1.25$ is shown in Fig 5.13. The statistical error is of the order of 4%. The full set of parameters returned from the unbinned fit are given in Table 5.2.

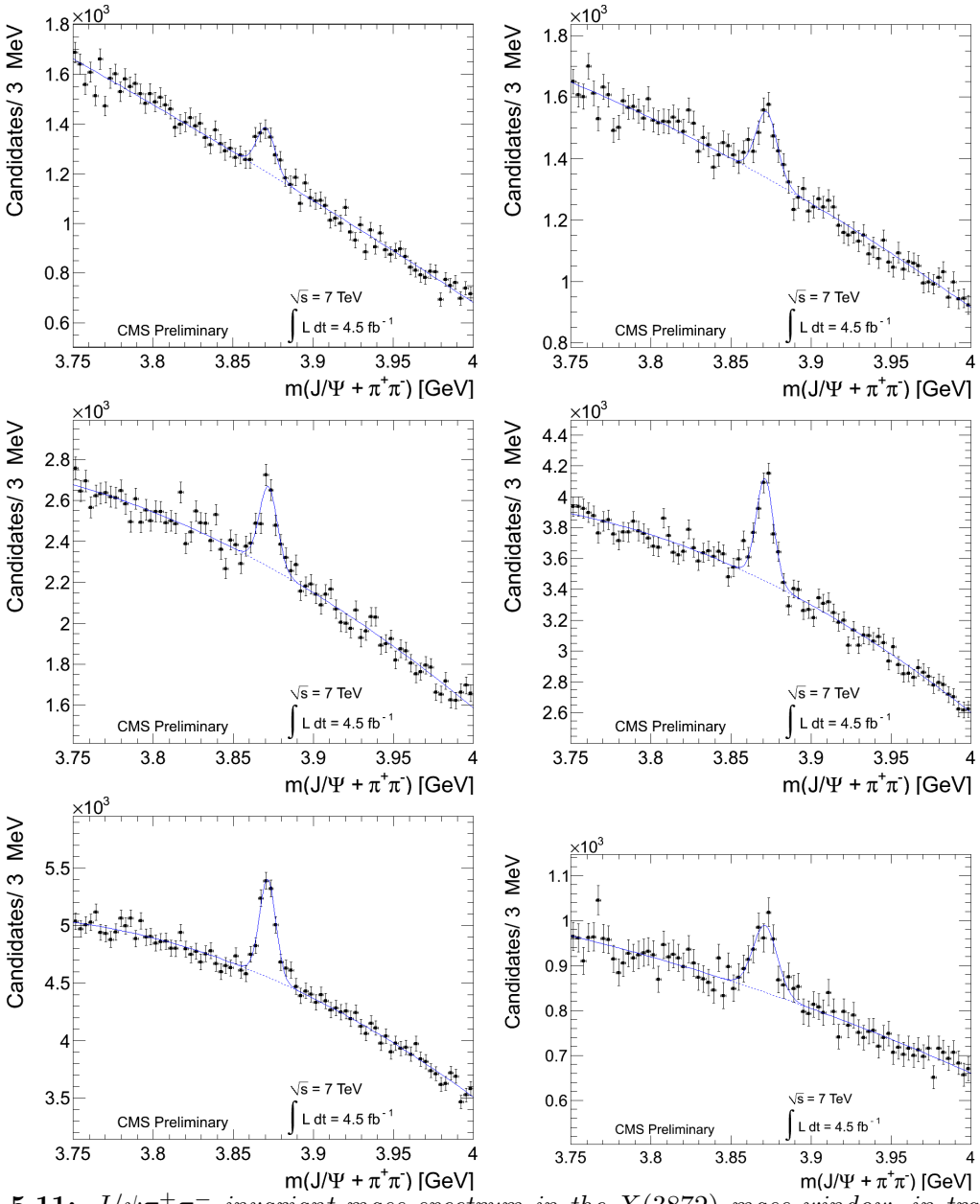

Figure 5.11: *$J/\psi\pi^+\pi^-$ invariant mass spectrum in the $X(3872)$ mass window, in transverse momentum bins: 10-12GeV , 12-13.5GeV, 13.5-15GeV, 15-18GeV, 18-30GeV, 30-50GeV*

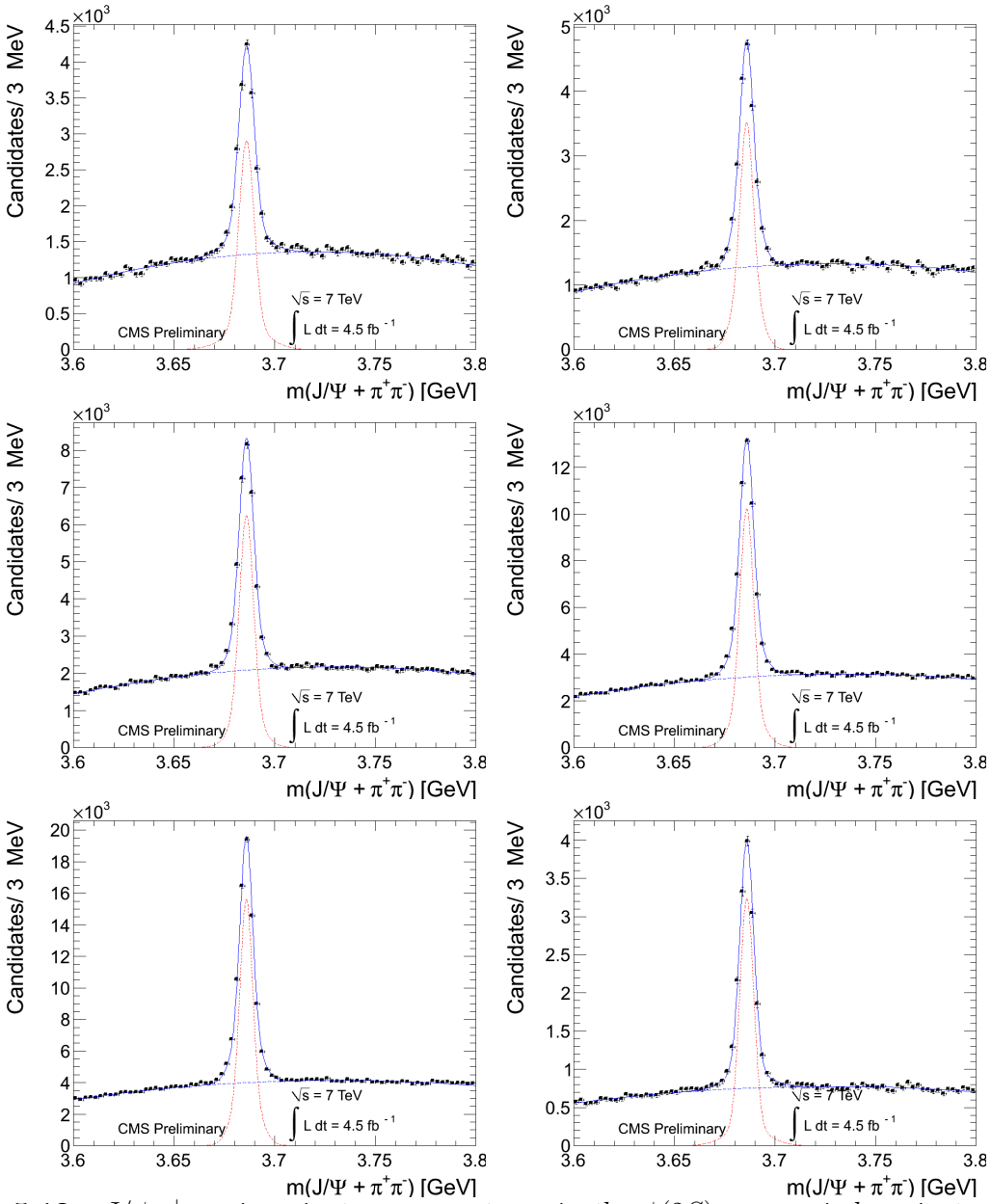

Figure 5.12: *$J/\psi\pi^+\pi^-$ invariant mass spectrum in the $\psi(2S)$ mass window, in transverse momentum bins: 10-12GeV , 12-13.5GeV, 13.5-15GeV, 15-18GeV, 18-30GeV, 30-50GeV*

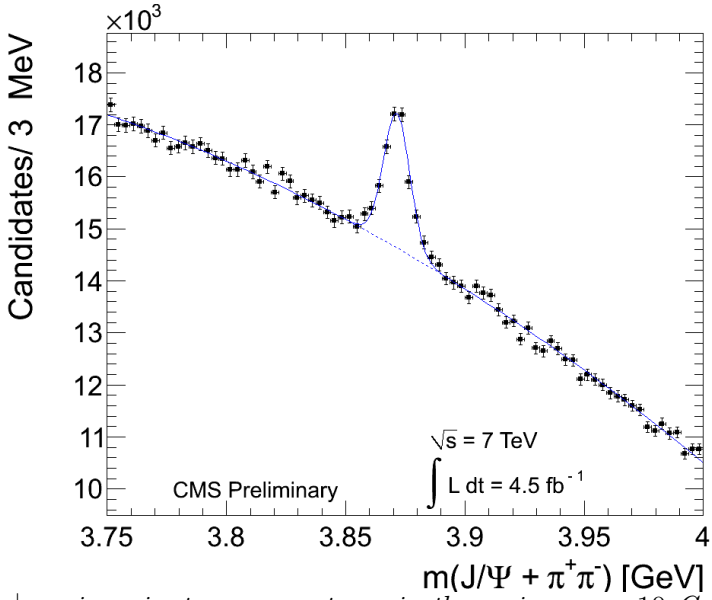

Figure 5.13: *$J/\psi\pi^+\pi^-$ invariant mass spectrum in the region $p_T > 10$ GeV/c and $|y| < 1.25$. The curve represents the result from an unbinned log likelihood fit.*

Parameter	Value
$M_{X(3872)}$	3.8714 ± 0.0002
$\sigma_{X(3872)}$	0.0055 ± 0.0002
$N_{X(3872)}$	11419 ± 412
N_{bkg}	1144910 ± 1136
$S/B_{2\sigma}(X(3872)$	0.105
χ^2_{fit}	1.06

Table 5.2: *Parameters obtained from the fit to the invariant mass spectrum in the $X(3872)$ region.*

5.5 Acceptance

The finite geometrical coverage and kinematic reach of the CMS muon detectors affect the ability to detect muons. Both generated muons should lay within the geometric acceptance of the muon detector defined in Equation 5.1. In addition, the $J/\psi \to \mu^+\mu^-$ should pass the selection criteria imposed by the trigger: $|y(\mu\mu)| < 1.25$ and $p_T(\mu\mu) > 7$ GeV/c or $p_T(\mu\mu) > 10$ GeV/c, depending on the trigger evolution due to the instantaneous luminosity increase during the data taking.

The acceptance A_{dimuon} is defined as the fraction of detectable $J/\psi \to \mu^+\mu^-$ decays among all the generated ones:

$$A_{dimuon}(p_T, y) = \frac{N_{det}(p_T, y)}{N_{gen}(p_T, y)} \tag{5.2}$$

where N_{gen} is the total number of generated $X(3872)$ (or $\psi(2S)$) in the kinematic region $p_T > 10$ GeV/c and $|y| < 1.25$ and N_{det} is the number of those with J/ψ satisfying the trigger criteria at generator-level ($p_T(\mu\mu) > 10$ GeV/c and $|y(\mu\mu)| < 1.25$) and with muons in the geometric acceptance mentioned above.

In Fig. 5.14 the acceptance A_{dimuon} is shown for the measurement of $X(3872)$ and $\psi(2S)$ production as a function of their p_T, when the requirement on the dimuon transverse momentum is $p_T > 7$ GeV/c.

Sufficiently large acceptance is found in the kinematic region of $p_T(X) > 10$ GeV/c and $|y|(X) < 1.25$. The ratio of the A_{dimuon} terms between the $X(3872)$ and the $\psi(2S)$ in this kinematic region is close to unity (Fig. 5.14), steeply decreasing at the smallest values of p_T as summarized in Table 5.3.

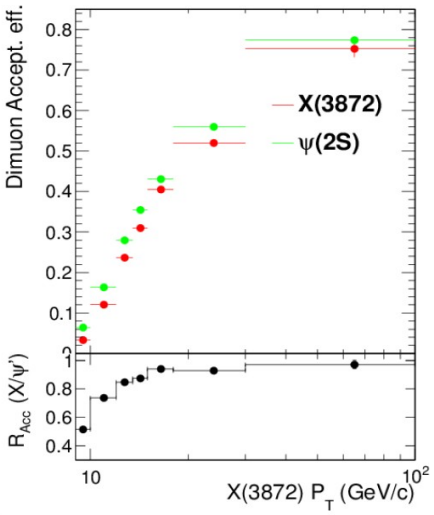

Figure 5.14: *Ratio between the acceptance for $X(3872)$ prompt and $\psi(2S)$ prompt, as a function of p_T. Requirement on the dimuon system are: $|y(\mu\mu)| < 1.25$ and $p_T(\mu\mu) > 7$ GeV/c.*

p_T(GeV/c)	$A_{dimuon}(X(3872))/A_{J/\psi}(\psi(2S))$ $p_T > 7$ GeV/c	$p_T > 10$ GeV/c
9-10	0.514 ± 0.012	
10-12	0.740 ± 0.009	0.247 ± 0.009
12-13.5	0.847 ± 0.012	0.660 ± 0.011
13.5-15	0.875 ± 0.014	0.860 ± 0.014
15-18	0.941 ± 0.013	0.941 ± 0.013
18-30	0.929 ± 0.012	0.929 ± 0.012
30-100	0.972 ± 0.029	0.972 ± 0.029

Table 5.3: *Ratio between acceptance maps for $X(3872)$ prompt and $\psi(2S)$ prompt as a function of the transverse momenta of the $J/\psi\pi\pi$ system.*

As expected the behaviour for the prompt and non-prompt component is the same both for the $X(3872)$ and $\psi(2S)$, as shown in Fig. 5.15 and only the acceptance terms from prompt production are used in the analysis.

It has been verified that the effect of Final State Radiation (FSR), estimated as the difference in acceptance computed with dimuon or J/ψ variables, is negligible.

Since the deployment of the $3E33$ trigger menu, the dimuon transverse momentum threshold in the J/ψ trigger was increased from 7 GeV/c to 10 GeV/c. An integrated luminosity of about $L_{int} = 1.98 fb^{-1}$ corresponds to the data taken with the trigger using

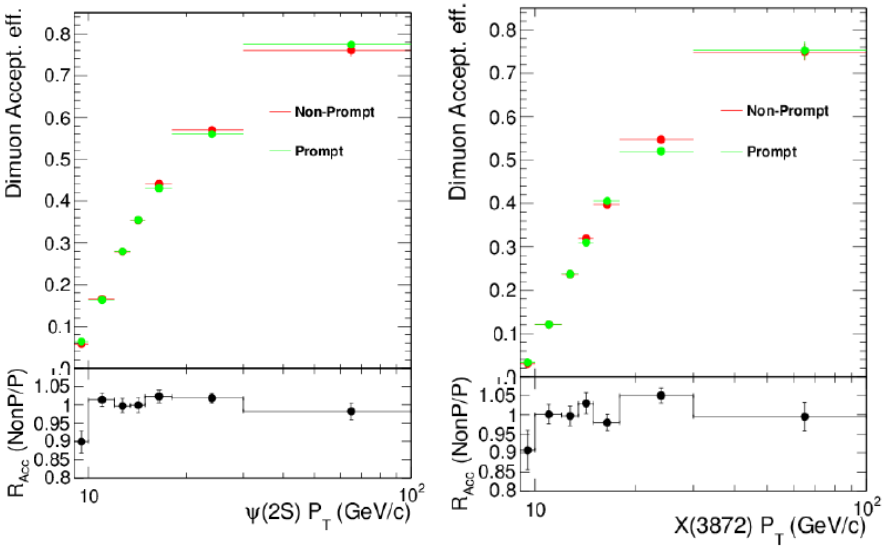

Figure 5.15: *Acceptance A_{dimuon} as a function of p_T for prompt and non-prompt $\psi(2S)$ production and their ratio (left) and for prompt and non-prompt $X(3872)$ production and their ratio (right)*

dimuon $p_T > 7$ GeV/c. About $L_{int} = 2.53 fb^{-1}$ corresponds to the data taken with the dimuon $p_T > 10$ GeV/c. Increasing the requirement on dimuon p_T to 10 GeV/c affects the $X(3872)$ and $\psi(2S)$ acceptance in the low p_T region, as shown in Fig. 5.16.

The impact is slightly different for $X(3872)$ and $\psi(2S)$ at low p_T, so that the acceptance ratio falls more steeply with respect to the case with di-muon $p_T > 7$ GeV/c. In order to avoid effects due to acceptance boundaries, the adopted strategy is to remove the data taken with dimuon p_T trigger threshold of 10 GeV/c for the $X(3872)$ and $\psi(2S)$ yields measurement up to $p_T \leq 13.5$ GeV/c. For $p_T > 13.5$ GeV/c all the data taken are considered.

5.6 Efficiency and correction factors

The Monte Carlo samples are also used to study the efficiency for $\psi(2S)$ and $X(3872)$ as a function of their transverse momentum.

The correction of the signal yield can be factorized into three components, i.e. the efficiency $\epsilon_{J/\psi}$ for the reconstruction of the J/ψ, the acceptance correction for the kinematic cuts imposed on the pion pair $A_{\pi\pi}$ and the reconstruction efficiency of the pion pair $\epsilon_{\pi\pi}$. The correction C on the ratio of $X(3872)$ and $\psi(2S)$ signals is then given by:

$$C = \frac{\epsilon_{J/\psi}(X(3872)) \cdot A_{\pi\pi}(X(3872)) \cdot \epsilon_{\pi\pi}(X(3872))}{\epsilon_{J/\psi}(\psi(2S)) \cdot A_{\pi\pi}(\psi(2S)) \cdot \epsilon_{\pi\pi}(\psi(2S))}. \tag{5.3}$$

where the acceptance and efficiency for the two pions is computed for events where the

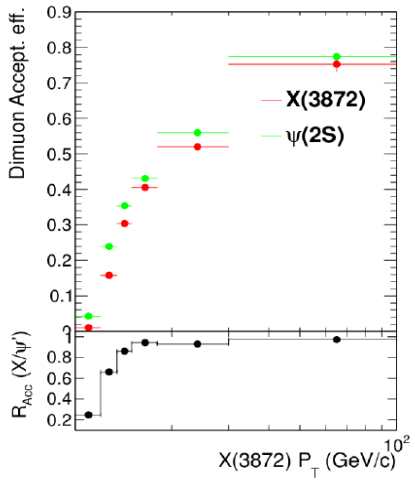

Figure 5.16: *Ratio between the acceptance for $X(3872)$ prompt and $\psi(2S)$ prompt, as a function of p_T. Requirement on the dimuon system are: $|y(\mu\mu)| < 1.25$ and $p_T(\mu\mu) > 10$ GeV/c.*

J/ψ has passed selection criteria.

The term $\epsilon_{J/\psi}$ accounts for the J/ψ reconstruction and trigger efficiency. The transverse momentum dependence of $\epsilon_{J/\psi}$ and the ratio $\epsilon_{J/\psi}(X(3872))/\epsilon_{J/\psi}(\psi(2S))$ is shown in Fig. 5.17 for prompt MC.

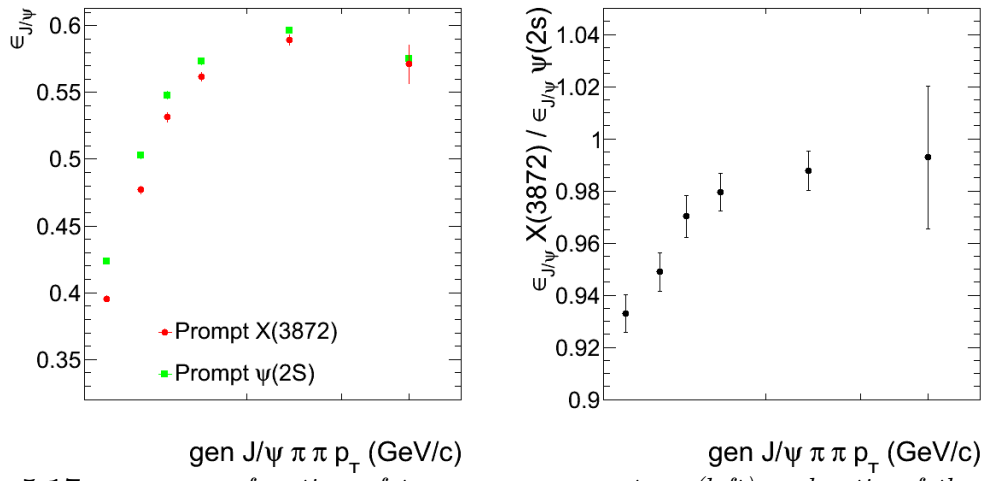

Figure 5.17: *$\epsilon_{J/\psi}$ as a function of transverse momentum (left) and ratio of the $\epsilon_{J/\psi}$ terms between the $X(3872)$ and$\psi(2S)$ (right).*

The behaviour of the term $A_{\pi\pi} \cdot \epsilon_{\pi\pi}$ for $X(3872)$ and $\psi(2S)$ as a function of transverse momentum is shown in Fig. 5.18.

The correction factor as a function of the candidate's transverse momentum is shown in Fig. 5.19. The reference correction factor is obtained from the prompt MC, however the correction was also computed from the non-prompt MC and with a mixture assuming a 25% of non-prompt fraction for the $X(3872)$ and 45% of non-prompt fraction for the $\psi(2S)$, as reported in Fig. 5.20. The behaviour of the correction factor from prompt

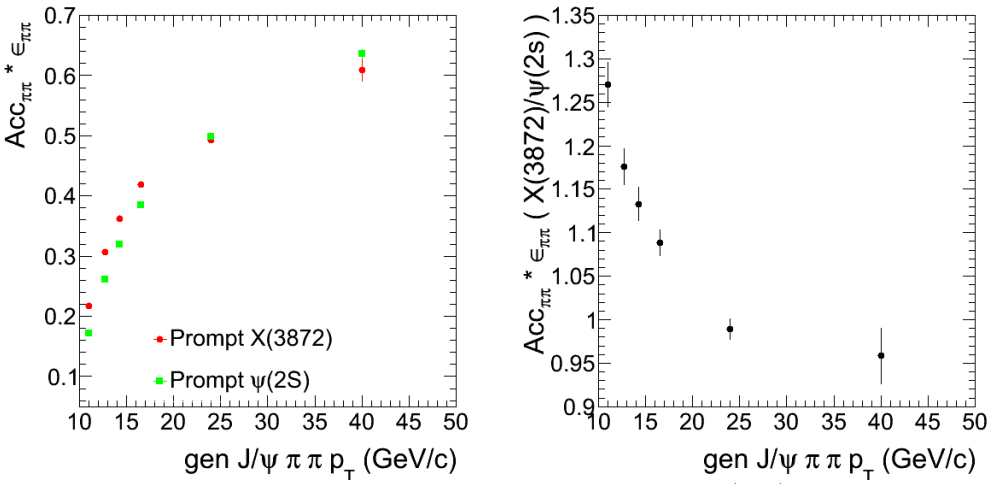

Figure 5.18: *$A_{\pi\pi} \cdot \epsilon_{\pi\pi}$ as a function of transverse momentum (left) and ratio of the $A_{\pi\pi} \cdot \epsilon_{\pi\pi}$ terms between the $X(3872)$ and$\psi(2S)$ (right).*

and non-prompt simulation are similar, with differences typically below 2%. Variation on the assumption of non-prompt fraction for $X(3872)$ and $\psi(2S)$ (20%-45%, 30%-45%,20%-50%,30%-40%) are well below 0.5% and are neglected.

The effect of muons that are not within the muon detector geometrical acceptance at generation level, but are however reconstructed as passing the muon selection criteria, has been investigated. The fraction of candidates with muons in the acceptance at reconstruction level that have also muons in the acceptance at generator-level is at worst about 98% for $10 < p_T < 12$ GeV/c for both $X(3872)$ and $\psi(2S)$. The effect is negligible in the yields ratio. The candidates that are reconstructed in the fiducial region ($p_T > 10$ GeV/c and $|y| < 1.25$) and that are not in that region at generator level, affect the first p_T bin, slightly differently for $X(3872)$ and $\psi(2S)$, thus implying a correction of 3% to the yields ratio. These effects have been evaluated within a MC closure test. Using the simulation as if they were data, it has been verified that the correction factors applied give the result of the MC truth. This is illustrated in Fig. 5.21 for $X(3872)$ and Fig. 5.22 for $\psi(2S)$, where the correction factors are applied to the yield obtained in the simulation with the same selection used in the analysis.

The term $f_{migration}$ is the fraction of candidates that pass the generator level acceptance criteria among those that survive the selection based on reconstructed variables. The generator level acceptance criteria are:

- generated candidate $p_T > 10$ GeV/c and $|y| < 1.25$
- generated J/ψ $p_T > 7$ GeV/c and $|y| < 1.25$
- generated muons in acceptance.

The effect is shown in Fig. 5.23 for both $X(3872)$ and $\psi(2S)$.

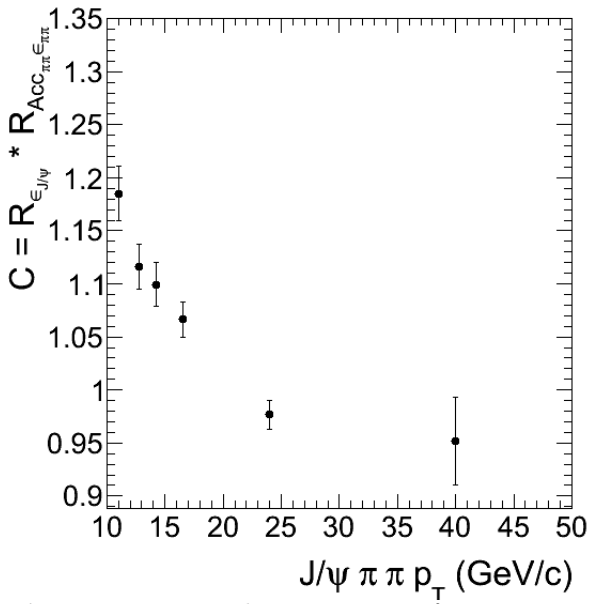

Figure 5.19: *The correction factor due to J/ψ and pions efficiencies, as a function of transverse momentum, from prompt MC.*

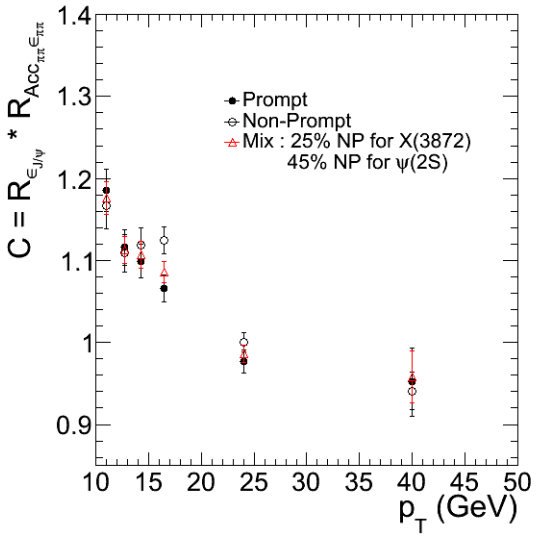

Figure 5.20: *The correction factor as a function of transverse momentum, obtained using prompt MC, non-prompt MC or a combination of the two assuming 25%(45%) of non-prompt fraction for the $X(3872)$ ($\psi(2S)$).*

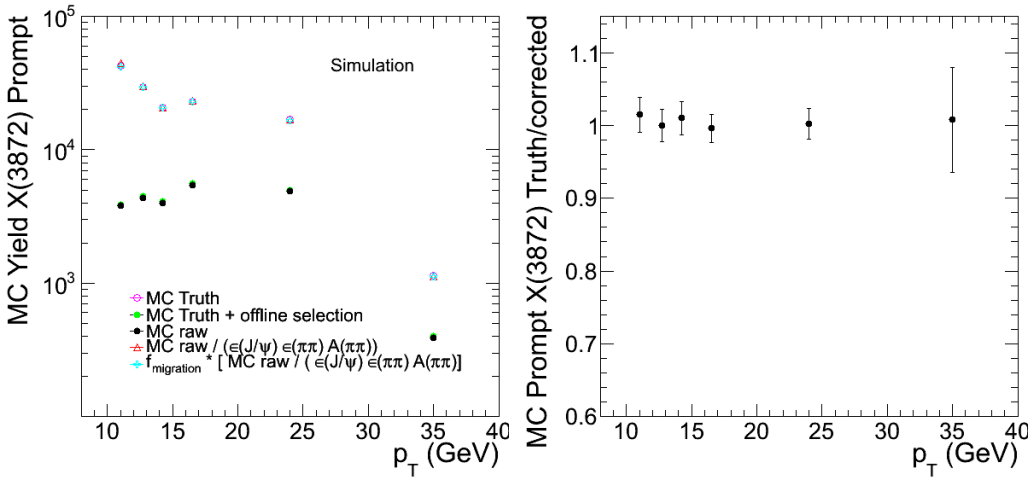

Figure 5.21: *Yields for $X(3872)$ using MC truth information (MC Truth) and extracting the yield as if the MC were data (MC raw). The MC raw yields are corrected for the efficiencies terms $\epsilon_{J\psi} \cdot A_{\pi\pi} \cdot \epsilon_{\pi\pi}$ and taking also into account the migration from candidates that don't pass the generator level acceptance criteria ($f_{migration}$).*

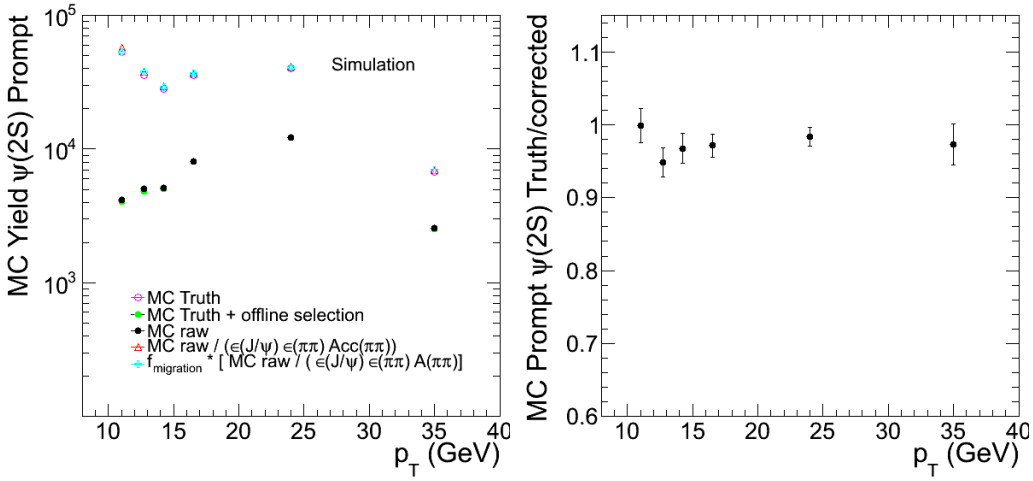

Figure 5.22: *Yields for $\psi(2S)$ using MC truth information (MC Truth) and extracting the yield as if the MC were data (MC raw). The MC raw yields are corrected for the efficiencies terms $\epsilon_{J\psi} \cdot A_{\pi\pi} \cdot \epsilon_{\pi\pi}$ and taking also into account the migration from candidates that don't pass the generator level acceptance criteria ($f_{migration}$).*

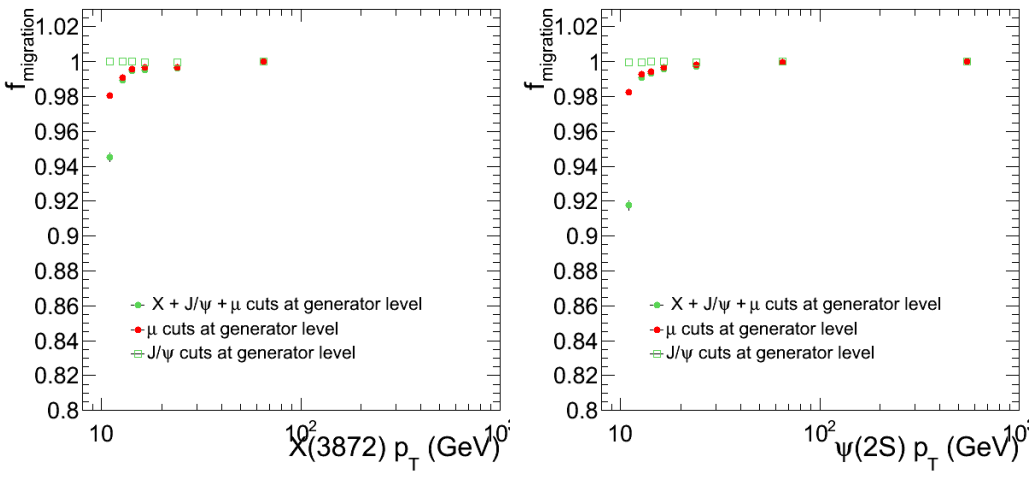

Figure 5.23: *Fraction of the candidates after reconstruction selection that pass also the generator level acceptance criteria*

5.7 Cross-section ratio determination

The ratio of the $X(3872)$ to $\psi(2S)$ cross-sections is given by the ratio of corrected yields for the $X(3872)$ and $\psi(2S)$ signals. The kinematic region considered is $p_T > 10$ GeV/c and $|y| < 1.25$ for the $J/\psi\pi^+\pi^-$ system.

The ratio of the fitted signal yields $N_{X(3872)}$ and $N_{\psi(2S)}$ are corrected for the detector efficiencies:

$$R_{\text{“}fiducial\text{”}} = \frac{N_{X(3872)}}{N_{\psi(2S)}} \cdot \frac{1}{C} \tag{5.4}$$

where C includes all the correction terms obtained from simulation in Section 5.6. This provides a “fiducial” result within the muon detector acceptance.

The fully corrected cross-section ratio takes into account also the detector dimuon acceptance:

$$\begin{aligned} R &= \frac{N_{X(3872)}}{N_{\psi(2S)}} \cdot \frac{1}{C_{tot}} \\ C_{tot} &= \frac{A_{dimuon}(X)}{A_{dimuon}(\psi(2S))} \cdot C \end{aligned}$$

Fig. 5.24 shows both the fully corrected cross-section ratio and the “fiducial” ratio as a function of $J/\psi\pi^+\pi^-$ p_T.

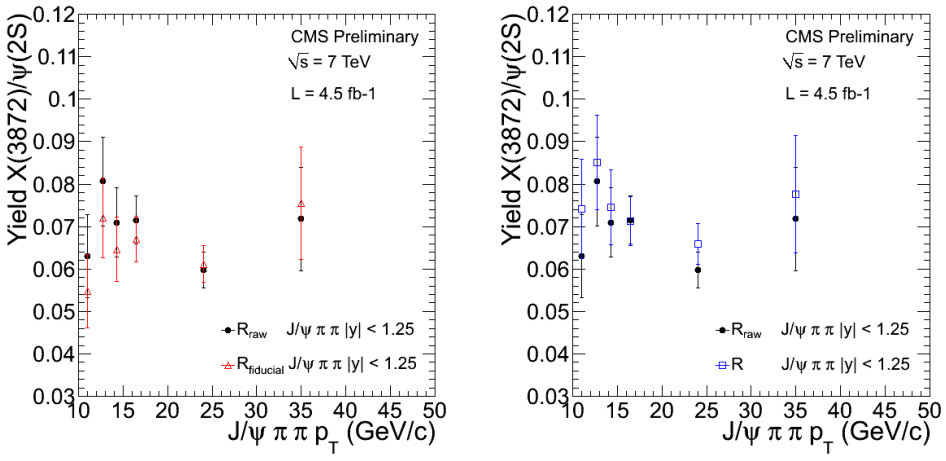

Figure 5.24: *Differential cross-section as a function of p_T. The ratio of the fitted signal yields extracted from data (R_{raw}) is shown together with the ratio of corrected yields for efficiencies term ($R_{fiducial}$) (left) and including also the acceptance term (R) (right). The uncertainties shown reflect the statistical uncertainty only.*

5.8 Data-driven muon efficiency

The single muon efficiencies can be factorized into muon identification efficiency, muon reconstruction efficiency and trigger efficiencies:

$$\epsilon_\mu = \epsilon_{ID} \cdot \epsilon_{reco} \cdot \epsilon_{trigger} \tag{5.5}$$

These efficiencies can be estimate using the Tag & Probe method. In this method events are selected with strict selection requirements on one muon (the 'tag' muon), and with a more relaxed selection on the other muon (the 'probe' muon), such that the selection applied to the probe muon does not bias the efficiency desired.

The fraction of probe muons which passes the selection under study gives an estimate of its efficiency.

For muons in CMS, tracks reconstructed using only the inner tracker are used as probes, while global muons are 'tag'. The number of passing probe is extracted by the yield of J/ψ form the di-muon mass spectrum formed by combination of one 'tag' and one 'probe'. A more detailed description of the method can be found in [61]. The results of these efficiencies estimated from data and simulation with a Tag & Probe method in 2011 data are available in the muon acceptance region [46]

$$\begin{aligned} |\eta| < 1.1 \quad & p_T \quad 4.6 \to 4 \text{ GeV/c} \\ 1.1 < |\eta| < 1.4 \quad & p_T \quad 4 \to 2.75 \text{ GeV/c} \\ 1.4 < |\eta| < 2.4 \quad & p_T \quad 2.75 \to 2 \text{ GeV/c} \end{aligned}$$

The dimuon efficiency is the product of the two single muon efficiency $\epsilon_{\mu 1} \cdot \epsilon_{\mu 2}$ in the event. To obtain the efficiency for each bin in $X(3872)$ p_T, the average efficiency for each generated event within acceptance is computed using the $X(3872)$ Monte Carlo sample. The efficiency can be estimated relying on the single muon efficiencies obtained from Tag & Probe both in data or in J/ψ Monte Carlo sample, thus providing a scale factor that takes into account differences between data and Monte Carlo:

$$\epsilon_X^{DATA}(p_T) = \epsilon_X^{MC}(p_T) \cdot R_\epsilon \quad \text{with} \quad R_\epsilon = \frac{\epsilon_{X,T\&P}^{DATA}(p_T)}{\epsilon_{X,T\&P}^{MC}(p_T)}$$

The same approach is followed for the $\psi(2S)$. The scale factors for $X(3872)$ and $\psi(2S)$ are shown in Fig. 5.25, together with their ratio. The results are limited by the statistical uncertainty on Tag & Probe muon efficiencies from data.

The muon data driven efficiency determination has an impact on the ratio of $X(3872)$ to $\psi(2S)$ efficiencies within 0.8%.

5.9 Data-driven pion acceptance and efficiency

A data-driven verification of the simulated pion pair acceptance and efficiency is performed by measurement of the candidate yields of the two decay channels of the $\psi(2S)$ into $(J/\psi \to \mu^+\mu^-)\pi^+\pi^-$ and directly into $\mu^+\mu^-$, following the same method described in Section 4.8.

In order to extract the yields from data, different trigger paths have to be used for the two charmonium states. In order to have similar sample and not to add additional correction factor, a reduced sample has been used with respect to the complete analysis. The only trigger paths kept are the ones in which the dimuon pair (J/ψ or $\psi(2S)$) has a minimum p_T requirement of 7 GeV/c.

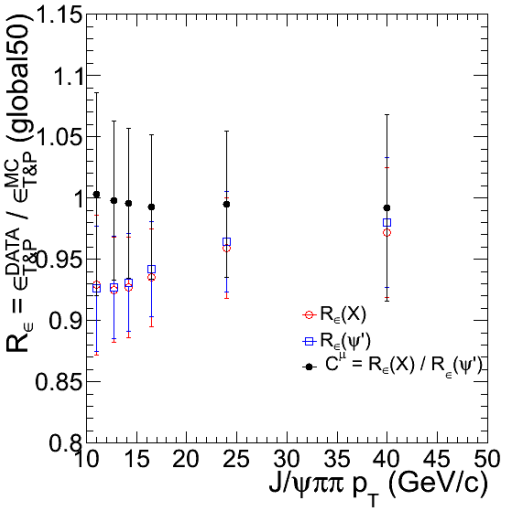

Figure 5.25: *Differences from DATA and MC single muon efficiencies expressed as a function of candidate p_T muon selection .*

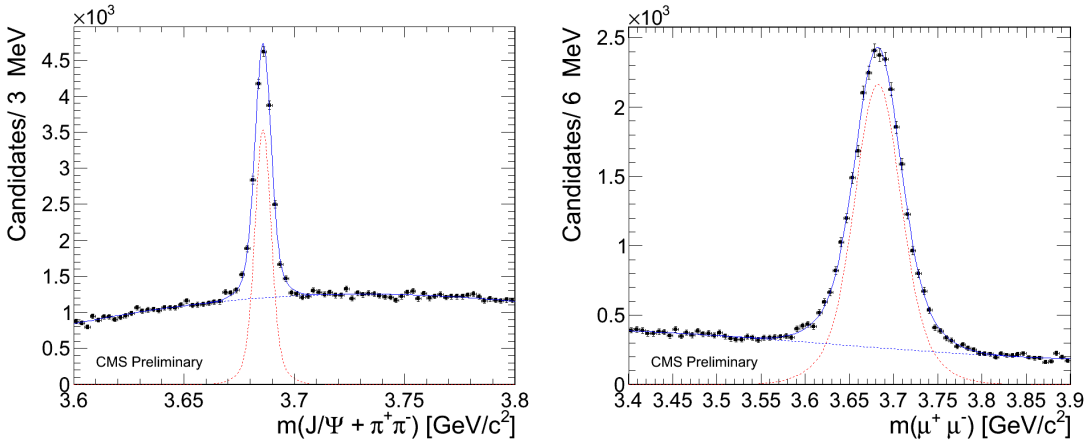

Figure 5.26: *The $J/\psi\pi^+\pi^-$ invariant mass dstribution (left) and the $\mu^+\mu^-$ invariant mass (right) in the $\psi(2S)$ region for the bin: $13.5 < p_T < 15 GeV/c$.*

The sum of two Gaussian functions is used for the description of the $\psi(2S) \to J/\psi\pi^+\pi^-$ signal while the background is modelled by a second order Chebyshev polynomial. For the $\psi(2S) \to \mu^+\mu^-$ peak the sum of two Gaussians and an exponential tail function, simultaneously taking into account FSR and resolution, is used and a third order Chebyshev polynomial describes the background.

Fig. 5.26 shows an example of a fitted mass distribution for the $\psi(2S) \to J/\psi\pi^+\pi^-$ and $\psi(2S) \to \mu^+\mu^-$ decays in the transverse momentum region $13.5 < p_T < 15\ GeV/c$.

The ratio of the fitted signal yields $N_{\psi(2S)\to J/\psi\pi^+\pi^-}$ and $N_{\psi(2S)\to\mu^+\mu^-}$ is corrected according to:

$$A_{\pi\pi} \cdot \epsilon_{\pi\pi} = \frac{N_{\psi(2S)\to J/\psi\pi^+\pi^-}}{N_{\psi(2S)\to\mu^+\mu^-}} \cdot \frac{1}{C} \cdot \frac{1}{C_{BR}} \tag{5.6}$$

where C takes into account the acceptance and efficiencies terms:

$$C = \frac{A_{J/\psi}(\psi(2S) \to J/\psi\pi^+\pi^-)}{A_{dimuon}(\psi(2S) \to \mu^+\mu^-)} \cdot \frac{\epsilon_{J/\psi}(\psi(2S) \to J/\psi\pi^+\pi^-)}{\epsilon_{J/\psi}(\psi(2S) \to \mu^+\mu^-)} \tag{5.7}$$

and C_{BR} the branching ratios correction:

$$C_{BR} = \frac{\mathcal{B}(\psi(2S) \to J/\psi\pi^+\pi^-) \cdot \mathcal{B}(J/\psi \to \mu^+\mu^-)}{\mathcal{B}(\psi(2S) \to \mu^+\mu^-)} \tag{5.8}$$

The branching ratios are summarized in Table 5.4. In order to reduce the final uncertainty, instead of the uncertainty related to the knowledge of $\mathcal{B}(\psi(2S) \to \mu^+\mu^-)$ the uncertainty on the $\mathcal{B}(\psi(2S) \to e^+e^-)$ is used.

$\mathcal{B}(\psi(2S) \to J/\psi\pi^+\pi^-)$	33.6 ± 0.4 %
$\mathcal{B}(\psi(2S) \to \mu^+\mu^-)$	$(7.7 \pm 0.8) \times 10^{-3}$
$\mathcal{B}(J\psi \to \mu^+\mu^-)$	(5.93 ± 0.06)%
$\mathcal{B}(J\psi \to e^+e^-)$	(5.94 ± 0.017)%

Table 5.4: *Branching Ratios.*

The acceptance ratio for the two decay channels is shown in Fig. 5.27. The ratio of the efficiencies for the reconstruction of $\psi(2S)$ in the decay channel $\psi(2S) \to J/\psi\pi^+\pi^-$ and in the channel $\psi(2S) \to \mu^+\mu^-$ is also shown.

The acceptance and efficiency for the dipion system is reported in Fig. 5.28. Finally, the average pion-pair efficiency is estimated dividing the value extracted from the data by the pion pair acceptance as determined from MC, as shown in the same figure.

The difference between data and Monte Carlo simulation on the pion-pair efficiency is of the order of 5% at low p_T and negligible at higher p_T, as summarized in Fig. 5.29. In Table 5.5 the value of $\epsilon_{\pi\pi}$ are proposed in the six bins of the analysis and also integrated in a low p_T region (10-15 GeV/c) and a hight p_T region (15-100 GeV/c).

5.10 Systematic uncertainties

The systematic error on the cross-section ratio is composed of the contributions to the uncertainty that are uncorrelated between the $X(3872)$ and the $\psi(2S)$. The list of these contributions is given in the following:

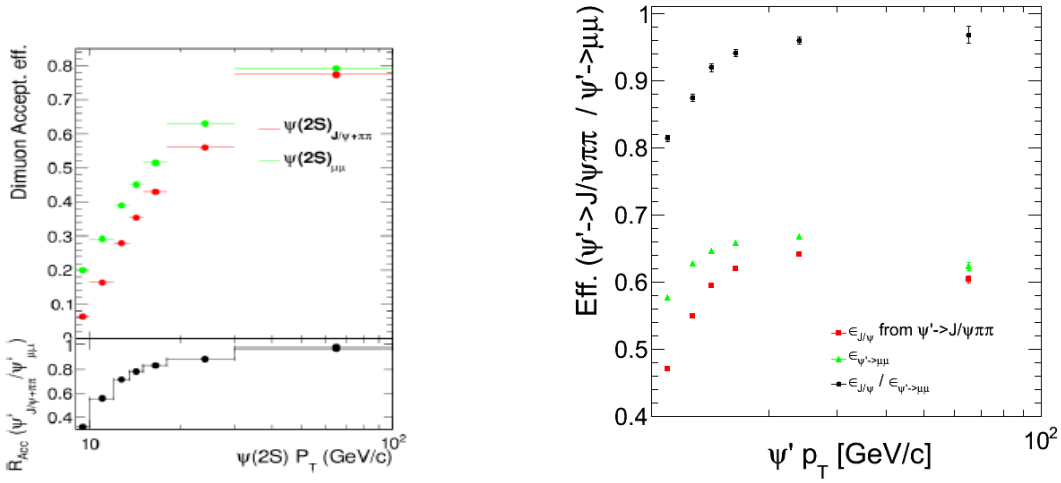

Figure 5.27: *Acceptance for $\psi(2S) \to J/\psi\pi\pi$ and $\psi(2S) \to \mu\mu$ (left) and efficiencies (right), as a function of p_T.*

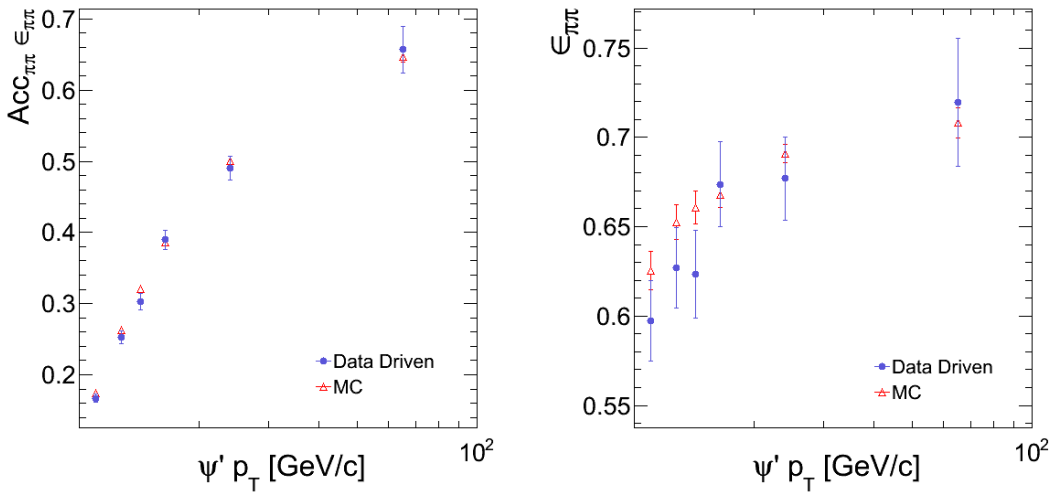

Figure 5.28: *$A_{\pi\pi} \cdot \epsilon_{\pi\pi}$ (left) and efficiency of the dipion system (right), as a function of p_T, obtained from the data driven technique in comparison with the simulation.*

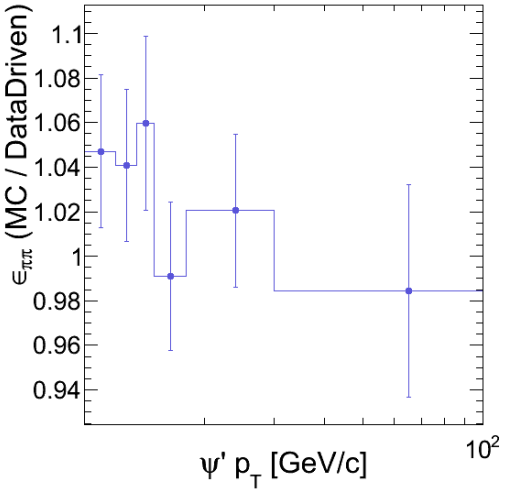

Figure 5.29: *Variation of the pion-pair efficiency from Monte Carlo simulation and from data-driven method.*

p_T(GeV/c)	$\epsilon_{\pi\pi}(MC/data)$
10-12	+4.7 ± 3.4 %
12-13.5	+4.1 ± 3.4 %
13.5-15	+6.0 ± 3.9 %
15-18	-0.9 ± 3.3 %
18-30	+2.0 ± 3.4 %
30-100	-1.6 ± 4.8 %
10-15	4.8 ± 2.1 %
15-100	0.1 ± 2.1 %

Table 5.5: *Ratio between the $\epsilon_{\pi\pi}$ from Monte Carlo simulation and from the data-driven technique.*

- *Signal and background parametrization.* The systematic error on the signal extraction is determined by variation of the fit parametrization. For the $\psi(2S)$ background a third order Chebyshev polynomial is used and for the signal the sum of a two Gaussian and an exponential tail is used. The maximum variation is around 2.4% in the first p_T bin and below 1% at higher transverse momentum. Variation of the $X(3872)$ background yields differences below 1% for all transverse momenta.

- *Muon efficiency.* The differences between the muon selection efficiency obtained from Monte Carlo simulation and from data using a Tag and Probe method largely cancel in the cross-section ratio measurement, as described in section 5.8, giving a contribution below 1% well within the statistical uncertainty of the Tag and Probe method from data.

- *Pion pair efficiency.* A data driven technique that compares the yields for $\psi(2S) \to J/\psi\pi^+\pi^-$ and $\psi(2S) \to \mu^+\mu^-$ decays is used to verify the pion pair efficiency obtained from simulation, as described in section 5.9. The difference between data and Monte Carlo simulation on the pion-pair efficiency is of the order of 5% at low p_T ($p_T < 15$ GeV/c) and negligible at higher transverse momenta.

- *Simulation statistic.* The uncertainty introduced by statistical effects, due to limited size of the fully reconstructed Monte Carlo samples, has been estimated to be of the order of 1%, except for the $30 < p_T < 100$ GeV/c bin where it goes up to 3% . The uncertainty on dimuon acceptance estimate, due to the limited size of the un-filtered Monte Carlo sample, is of the same order.
- *X(3872) production mechanism.* The production mechanism of the $X(3872)$ is unknown and the p_T dependence of the result is evaluated modifying the prompt $X(3872)$ p_T distribution. The generated $X(3872)$ p_T spectrum is reweighted to the transverse momentum distribution observed in data using a sideband subtracted technique, as described in Section 4.10 . Fig. 5.30 shows the $X(3872)$ p_T spectrum in data in comparison to the Monte Carlo simulation. The statistical uncertainty of the data distribution is taken into account as variation to the reweighting function. On the basis of this event by event weight, all the correction factors are recalculated. The maximum difference is around 9% for the first bin and below 2-3% elsewhere.
- *Differences in $\psi(2S)/;p_T$ spectrum.* The variation introduced by reweighting the generated $\psi(2S)$ p_T spectrum to the transverse momentum distribution observed in data, using a sideband subtracted technique, is quoted as systematic uncertainty. Fig. 5.31) shows the $\psi(2S)$ p_T spectrum in data in comparison to the MC Simulation. The statistical uncertainty of the data distribution is taken into account as variation to the reweighting function. The maximum difference is around 9% for the first bin and below 4% elsewhere.

The summary of relative systematic uncertainties is reported in Table **??**.

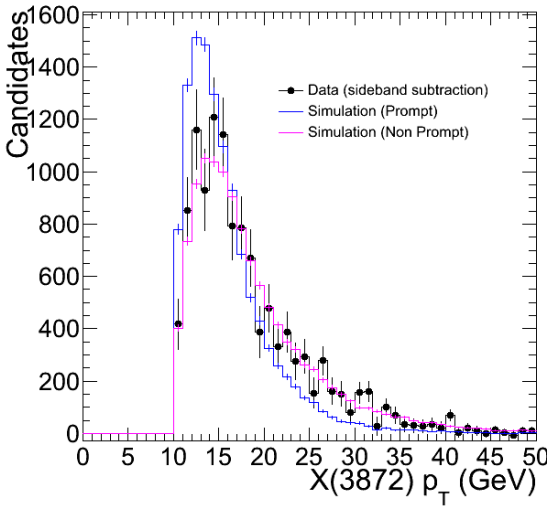

Figure 5.30: $X(3872)$ *transverse momentum from data with a sideband subtraction technique, in comparison with Monte Carlo simulation*

5.11 Distribution from sideband subtraction

A sideband subtraction method is used to remove continuum background from the data distributions and thus facilitate direct comparisons between the data and Monte Carlo

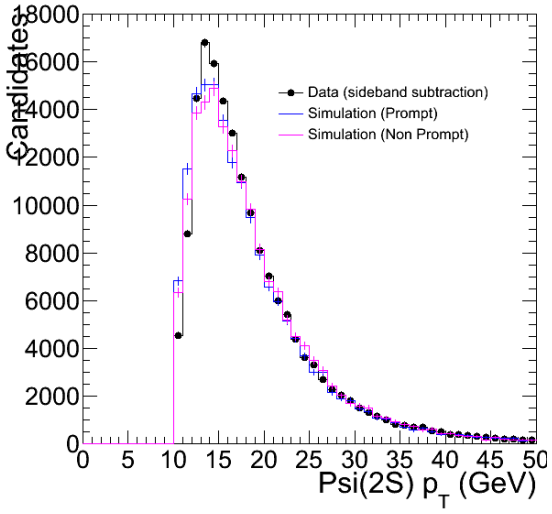

Figure 5.31: *$\psi(2S)$ transverse momentum from data with a sideband subtraction technique, in comparison with Monte Carlo simulation*

	Relative uncertainty (%)					
p_T range (GeV/c)	10-12	12-13.5	13.5-15	15-18	18-30	30-50
Fiducial cross-section ratio						
fit	2.4	1.0	1.0	1.1	0.9	1.3
p_T shape	8.7	0.6	0.2	1.4	3.5	1.7
$\psi(2S)p_T$ shape	9.4	0.7	0.2	0.9	4.1	1.2
$\epsilon_{\pi\pi}$	4.8	4.8	4.8	-	-	-
ϵ_{μ}	0.3	0.2	0.4	0.7	0.5	0.8
MC statistic	1.4	1.2	1.2	1.0	1.0	3.1
Acceptance corrected cross-section ratio						
MC statistic($Acc_{\mu\mu}$)	1.2	1.4	1.6	1.4	1.3	3.0

Table 5.6: *Summary of the relative systematic uncertainties (%). For the acceptance corrected cross-section ratio the uncertainties affecting the di muon acceptance ratio are also reported.*

simulations of signal events. The detailed description of the method is reported in Section 4.10. Specifically, here, in figure 5.32, the sideband distributions are extracted separately from two regions below (3.76−3.83 GeV/c^2) and above (3.92−3.99 GeV/c^2) the signal region (3.855−3.888 GeV/c^2). Similar distributions for $\psi(2S)$ are shown in Fig. 5.33.

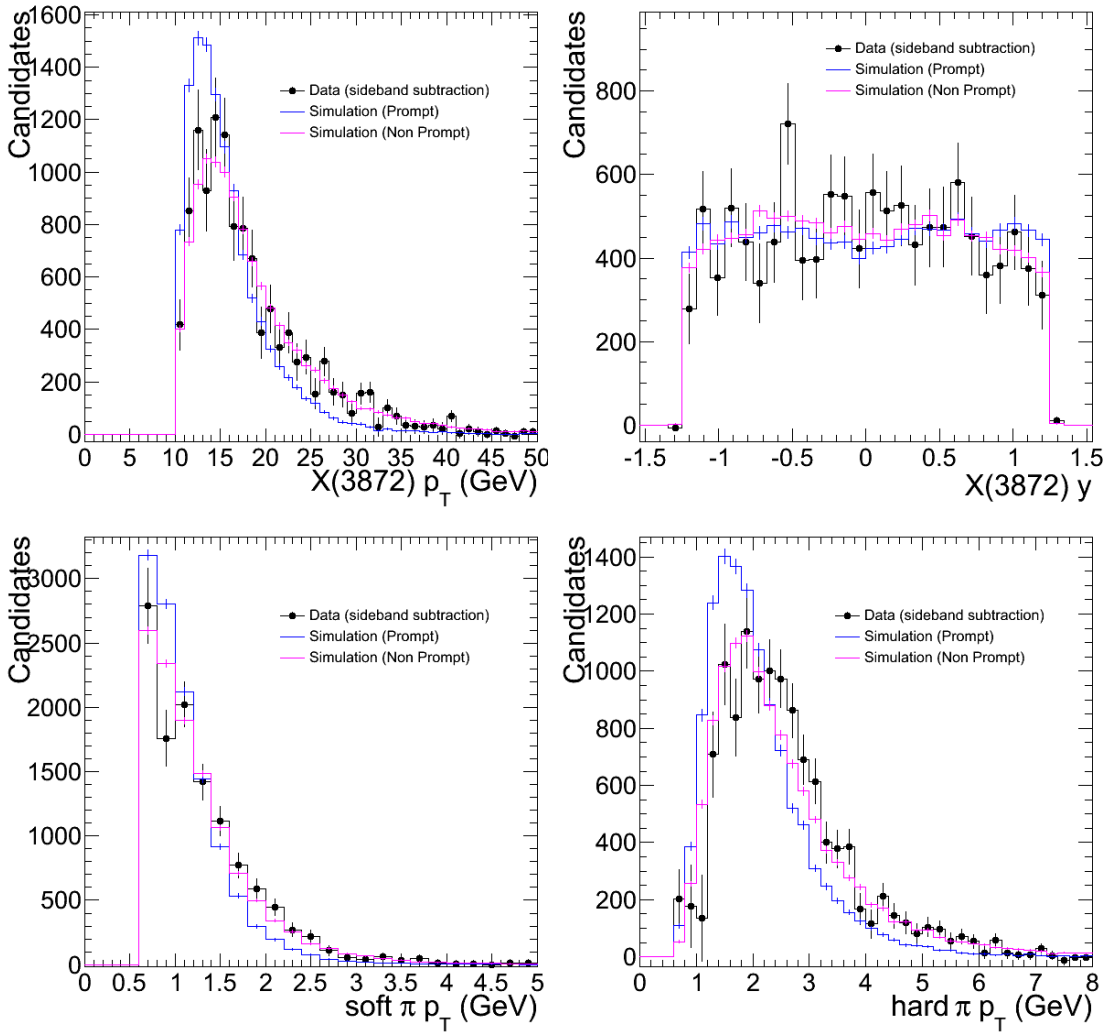

Figure 5.32: *(top) Transverse momentum (left) and rapidity (right) of the $X(3872)$ obtained from data after sidebands subtraction. (bottom) Transverse momentum of the soft (left) and hard (right) pions for the $X(3872)$ obtained from data after sidebands subtraction. The prompt and non-prompt MC distributions, normalized to the data, are used as comparison.*

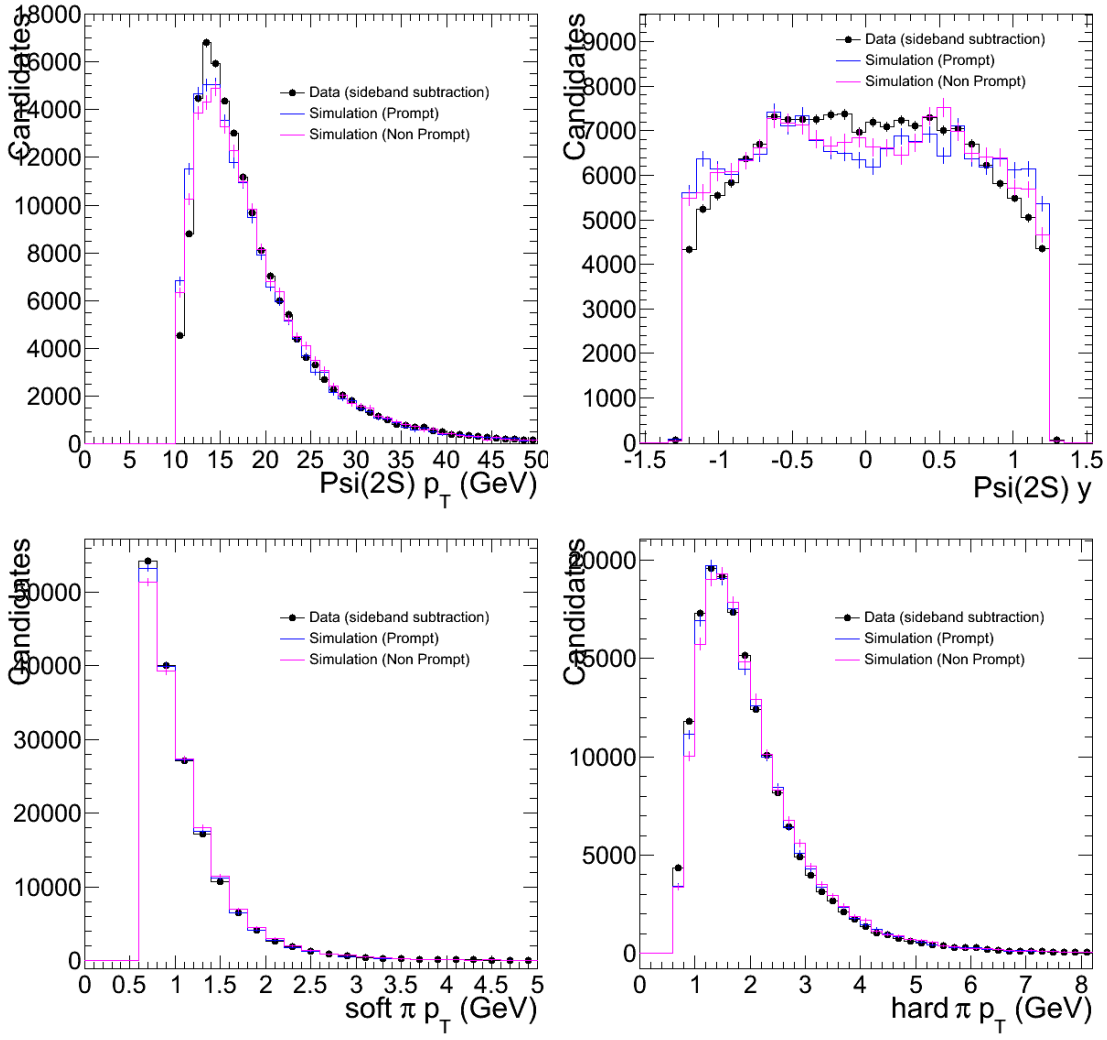

Figure 5.33: *(top) Transverse momentum (left) and rapidity (right) of the $\psi(2S)$ obtained from data after sidebands subtraction. (bottom) transverse momentum of the soft (left) and hard (right) pions for the $\psi(2S)$ obtained from data after sidebands subtraction. The prompt and non-prompt MC distributions, normalized to the data, are used as comparison.*

5.12 Final Result

The measured differential cross-section ratio for $X(3872)$ over $\psi(2S)$ as a function of p_t is shown in Fig. 5.34 without (left) and with (right) correction for the muon acceptance. The corresponding values are reported in Table 5.7. The measurements are provided within $J/\psi\ \pi^+\pi^-$ rapidity below 1.25 and null polarization scenario is assumed. No particular trend of the ratio is visible within the experimental errors.

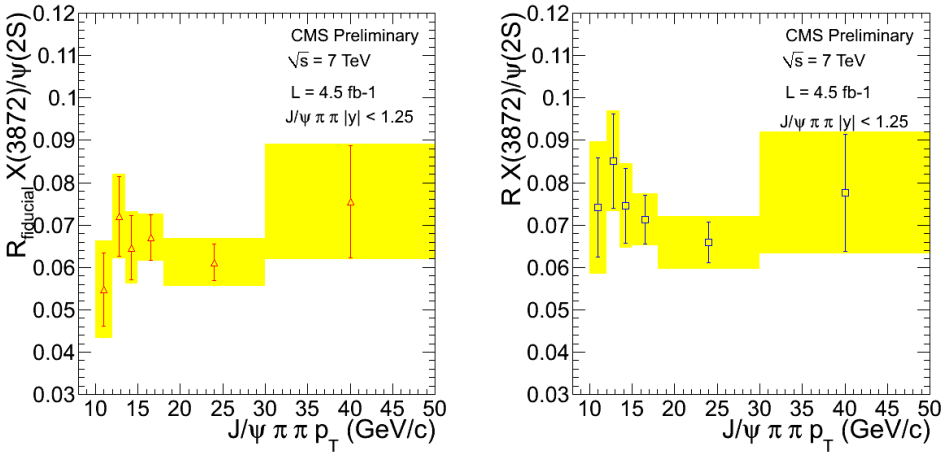

Figure 5.34: *Differential cross-section as a function of p_T. The ratio of the fitted signal yields exctracted from data corrected yields for efficiencies term ($R_{fiducial}$) (left) and including also the acceptance term (R) (right). The error bars shown include the statistical uncertainty. The coloured bands indicate the total uncertainty.*

p_T range (GeV/c)	$R_{fiducial}\ \frac{X(3872)}{\psi(2S)}$	Acceptance corrected $R\ \frac{X(3872)}{\psi(2S)}$
10-12	0.055 ± 0.009(stat) ± 0.008(sys)	0.074 ± 0.012(stat) ± 0.010(sys)
12-13.5	0.072 ± 0.009(stat) ± 0.003(sys)	0.085 ± 0.011(stat) ± 0.004(sys)
13.5-15	0.065 ± 0.008(stat) ± 0.004(sys)	0.075 ± 0.009(stat) ± 0.005(sys)
15-18	0.067 ± 0.005(stat) ± 0.002(sys)	0.071 ± 0.006(stat) ± 0.002(sys)
18-30	0.061 ± 0.004(stat) ± 0.004(sys)	0.066 ± 0.005(stat) ±0.004(sys)
30-50	0.075 ± 0.013(stat) ± 0.003(sys)	0.078 ± 0.014(stat) ± 0.004(sys)

Table 5.7: *Measured differential cross-section ratio for $X(3872)$ over $\psi(2S)$ without ($R_{fiducial}$) and with (R) the muon acceptance corrections. Null polarization scenario is assumed. The measurements are provided within $J/\psi\ \pi^+\pi^-$ rapidity below 1.25.*

Chapter 6

X(3872) Lifetime Analysis

In this section it's presented the extraction of the non-prompt component of the X(3872) from the 4.5 fb^{-1} of data collected during 2011 by the CMS experiment (the sample described in Section 5.2). In order to verify the procedure used, it is at the same time applied also to the $\psi(2S)$ resonance.

6.1 Experimental procedure

The fraction of the $X(3872)$ and $\psi(2S)$ from B-hadron decays is extracted using a 2-dimensional technique already applied in the CMS Collaboration in the study of the non-prompt component for J/ψ and $\psi(2S)$ in the decay channels $J/\psi \to \mu^+\mu^-$ [50] and $\psi(2S) \to \mu^+\mu^-$ [50].

The measurement of the fraction of $X(3872)$ coming from the decays of the B-hadrons relies on the discrimination of the $X(3872)$ produced away from the pp collision vertex (contrary to the prompt part), by the distance between the 4-track vertex and the primary vertex in the plane orthogonal to the beam line.

The primary vertex for the event is calculated with a common fit to all tracks, excluding the four tracks forming the $X(3872)$ candidate and using adaptive weights to avoid bias from displaced secondary vertices (see Section 3.3).

Due to the presence of pile-up in the data samples, the primary vertex in the event is not unique: according to MC studies, the best assignment of the correct primary vertex is achieved by requiring the minimum distance in the z-coordinate w.r.t. the X(3872) secondary vertex.

As a rough estimate of the B-hadron decay length, for each $X(3872)$ candidate, the quantity

$$\ell_{xy}^{X(3872)} = \frac{L_{xy}^{X(3872)} \cdot m_{X(3872)}}{p_T} \tag{6.1}$$

is computed, where m is mass of the $X(3872)$ candidate and L_{xy} is the most probable transverse decay length in the laboratory frame [5, 59], defined as

$$L_{xy} = \frac{\mathbf{u}^T \sigma^{-1} \mathbf{x}}{\mathbf{u}^T \sigma^{-1} \mathbf{u}^T} \quad , \tag{6.2}$$

where $\mathbf{x}$ is the distance between the vertex of the four tracks and the primary vertex of the event computed in the transverse plane, $\mathbf{u}$ is the unit vector of the $X(3872)$ p_T and

σ is the sum of the primary and secondary vertex covariance matrices. $\ell_{xy}^{X(3872)}$ is usually called *pseudo-proper decay length* to distinguish it from the *proper decay length* defined as

$$\ell_{xy}^{B} = \frac{L_{xy}^{B} \cdot m_B}{p_T^B} \tag{6.3}$$

where m_B and p_T^B are the mass and transverse momentum of the B-hadron. While ℓ_{xy}^{B} has an exponential behaviour, the distribution of $\ell_{xy}^{X(3872)}$ from B-hadrons is not perfectly exponential, since the transverse momentum of the $X(3872)$ does not coincide with the transverse momentum of the B-hadron.

To determine the fraction f_B of $X(3872)$ from B-hadron decays in the data, an unbinned maximum-likelihood fit is performed in bins of p_T.

The $J/\psi\,\pi^+\pi^-$ mass spectrum and the $\ell_{X(3872)}$ distribution were simultaneously fitted by a log-likelihood function,

$$\ln L = \sum_{i=1}^{N} \ln F(\ell_{X(3872)}, M_{J/\psi\,\pi^+\pi^-}) \quad , \tag{6.4}$$

where N is the total number of events and $M_{J/\psi\,\pi^+\pi^-}$ is the invariant mass in the $X(3872)$ fit region. The general expression for $F(\ell_{X(3872)}, m_{J/\psi\,\pi^+\pi^-})$ is given by

$$\begin{aligned} F(\ell_{X(3872)}, m_{J/\psi\,\pi^+\pi^-}) = & f_{Sig} \cdot F_{Sig}(\ell_{X(3872)}) \cdot M_{Sig}(m_{J/\psi\,\pi^+\pi^-}) \\ & + (1 - f_{Sig}) \cdot F_{Bkg}(\ell_{X(3872)}) \cdot M_{Bkg}(m_{J/\psi\,\pi^+\pi^-}) \end{aligned} \tag{6.5}$$

where:

- f_{Sig} is the fraction of events attributed to $X(3872)$ sources coming from both prompt and non-prompt components.
- $M_{Sig}(m_{J/\psi\,\pi^+\pi^-})$ and $M_{Bkg}(m_{J/\psi\,\pi^+\pi^-})$ are the functional forms describing the invariant mass distributions for the signal and background, respectively. These are the same functions used to extract the signal yields in Section 5.4.
- $F_{Sig}(\ell_{X(3872)})$ is the functional form describing the $\ell_{X(3872)}$ distribution for the signal. This part is given by a sum of prompt and non-prompt components,

  $$F_{Sig}(\ell_{X(3872)}) = f_B \cdot F_B(\ell_{X(3872)}) + (1 - f_B) \cdot F_p(\ell_{X(3872)}) \quad , \tag{6.6}$$

  where f_B is the fraction of $X(3872)$ from B-hadron decays, and $F_p(\ell_{X(3872)})$ and $F_B(\ell_{X(3872)})$ are the $\ell_{X(3872)}$ distributions for prompt and non-prompt $X(3872)$, respectively. Since $\ell_{X(3872)}$ should be zero in an ideal detector for prompt events, $F_p(\ell_{X(3872)})$ is described simply by a resolution function.

  The $\ell_{X(3872)}$ shape of the non-prompt component is described by an exponential decay of the B-hadron with a smearing function that accounts for the difference between the proper decay length, defined by $\ell_{X(3872)}$, and the one of the B-hadron. To evaluate this effect at Monte Carlo truth level, it can be observed that the relation between the pseudo-proper and the proper decay lengths, given by:

  $$\frac{\ell_{X(3872)}}{\ell_{X(3872)}^{B}} = \frac{M_{X(3872)}}{p_{T\,X(3872)}} \cdot \frac{p_T^B}{M^B} \tag{6.7}$$

is sufficiently described by a Gaussian function:

$$G_{MC}(\ell_{X(3872)} - \ell^B_{X(3872)}|0, \sigma_{MC}). \tag{6.8}$$

Hence, the function that approximates the $\ell_{X(3872)}$ distribution for the B-hadron component at Monte Carlo truth level will be:

$$F_B^{true}(\ell_{X(3872)}) = e^{-\ell^B_{X(3872)}/c\tau_B} \otimes G_{MC}(\ell_{X(3872)} - \ell^B_{X(3872)}|0, \sigma_{MC}) \tag{6.9}$$

where $e^{-\ell^B_{X(3872)}/c\tau_B}$ describes the exponential part, and G_{MC} the correction.

In the final step of the fit σ_{MC} is a constant previously fixed from a fit to the MC-truth decay length, while the τ_B parameter is left free (this is expected to be close to the average B-hadron lifetime, but is still an effective parameter, since Eq. 6.5 is not an exact relation).

- $F_{Bkg}(\ell_{X(3872)})$ is the functional form describing the $\ell_{X(3872)}$ distribution for background. This functional has a more complicated shape due to the various sources of combinatorial background in the signal and sideband region. The expression follows the one used by CDF [16] and combines a series of tail functions with the same resolution function used for the signal.

The functional $F_{Bkg}(\ell_{X(3872)})$ and $F_{Sig}(\ell_{X(3872)})$ can be written in the general form:

$$F_{Sig,Bkg}(\ell_{X(3872)}) = \sum_i F^{true,sideband}_{Sig,Bkg}(\ell_{X(3872)}) \otimes R_i(\ell_{X(3872} - \ell'_{X(3872}|\mu, \sigma_i), \tag{6.10}$$

combining a description for the exponential tail, that come from the Monte Carlo for the signal and from sidebands fit for background, and a resolution function (R_i).

The resolution can be described by a function that depends on the "per-event error", i.e. the uncertainty on the pseudo-proper decay length, as determined event by event from the covariance matrices of the primary and secondary vertex, is used as the standard deviation of the resolution Gaussian.

In this way, a single Gaussian is sufficient to describe the core of the resolution and a second Gaussian, with a very small fraction (usually $< 1\%$) parametrizes incorrect primary vertex assignments. Without this technique, at least 4 Gaussians are needed to describe properly the prompt component in high statistics bins and the fit quality is anyway poorer.

In this way Eq. 6.6 becomes

$$\begin{aligned} F(\ell_{X(3872)}, m_{J/\psi\,\pi^+\pi^-}) \;=\; & \int [f_{Sig} \cdot D_{Sig}(\sigma_\ell) F_{Sig}(\ell_{X(3872)}, \sigma_\ell) \cdot M_{Sig}(m_{\mu\mu}) + \\ & (1 - f_{Sig}) \cdot D_{Bkg}(\sigma_\ell) F_{Bkg}(\ell_{X(3872)}, \sigma_\ell) \cdot & (6.11) \\ & M_{Bkg}(m_{J/\psi\,\pi^+\pi^-})] d\sigma_\ell & (6.12) \end{aligned}$$

and the expressions for the signal and background functionals F change to

$$F_{Sig,Bkg}(\ell_{X(3872)}, \sigma_\ell) = \sum_i F^{true,sidebands}_{Sig,Bkg}(\ell_{X(3872)}) \otimes R_i(\ell_{X(3872)} - \ell'_{X(3872)}|\mu, s_i\sigma_\ell), \tag{6.13}$$

$D_{Bkg,Sig}(\sigma_\ell)$ in Eq. 6.11 are the distributions of the per-event errors separately for signal and background. These distributions for the signal and background are obtained respectively from the mass signal region, after sideband subtraction, and from the mass sideband regions (defined as Table 6.1). No fit is performed to these distributions, the step PDF obtained from a suitable binning of the variable is used.

	Signal Region (GeV/c)	Lower Bkg Region (GeV/c)	Upper Bkg Region (GeV/c)
X(3872)	[3.855 - 3.888]	[3.76 - 3.83]	[3.92 - 3.99]
$\Psi(2S)$	[3.667 - 3.703]	[3.56 - 3.64]	[3.72 - 3.8]

Table 6.1: *Region of the $J/\psi\pi^+\pi^-$ used for sideband subtraction*

The fit procedure follows these steps:

- A fit of the $J/\psi\pi^+\pi^-$ is performed, using the same technique described in 5.4 . The number of signal events and some of the shape parameters defining the mass function are then kept fixed in the next steps.

- A resolution function for the prompt decay length of signal is fitted on the prompt MC sample. Some of the shape parameters are then kept fixed in the next steps.

- The shape of the decay length for the background is extracted from a fit of this distribution on the sidebands of the $J/\psi\pi^+\pi^-$ mass spectrum (Table 6.1). Some of the fitted parameters are fixed for the next step.

- The measured two-dimensional (mass and decay length) event distribution is fitted using a combination of the previous functions in order to obtain all the parameters not fixed in the previous steps. The starting values for the function describing the non prompt decay of the signal is estimated from Monte Carlo. The results of the projection of the fit function along the lifetime variable are shown in Fig. 6.2 and Fig. 6.3 for $X(3872)$ and $\psi(2S)$.

The result in the different p_T bins are summarized in table 6.2. The behaviour of the B-fraction as a function of the candidate p_T for both the $X(3872)$ and $\psi(2S)$ and the ratio of B-fraction between the two states are shown in Fig. 6.1.

p_T range (GeV/c)	$f_B X(3872)$	$f_B \psi(2S)$	$f_{BX(3872)}/f_{B\psi(2S)}$
10-12	0.192 ± 0.054	0.395 ± 0.006	0.486 ± 0.137
12-13.5	0.204 ± 0.034	0.424 ± 0.003	0.482 ± 0.081
13.5-15	0.171 ± 0.054	0.458 ± 0.005	0.374 ± 0.119
15-18	0.235 ± 0.028	0.494 ± 0.004	0.475 ± 0.057
18-30	0.302 ± 0.025	0.569 ± 0.003	0.531 ± 0.045
30-50	0.311 ± 0.050	0.649 ± 0.005	0.479 ± 0.077

Table 6.2: *X(3872) and $\psi(2S)$ non-prompt component values as a function of the particle p_T and the ratio of this fraction between the two states*

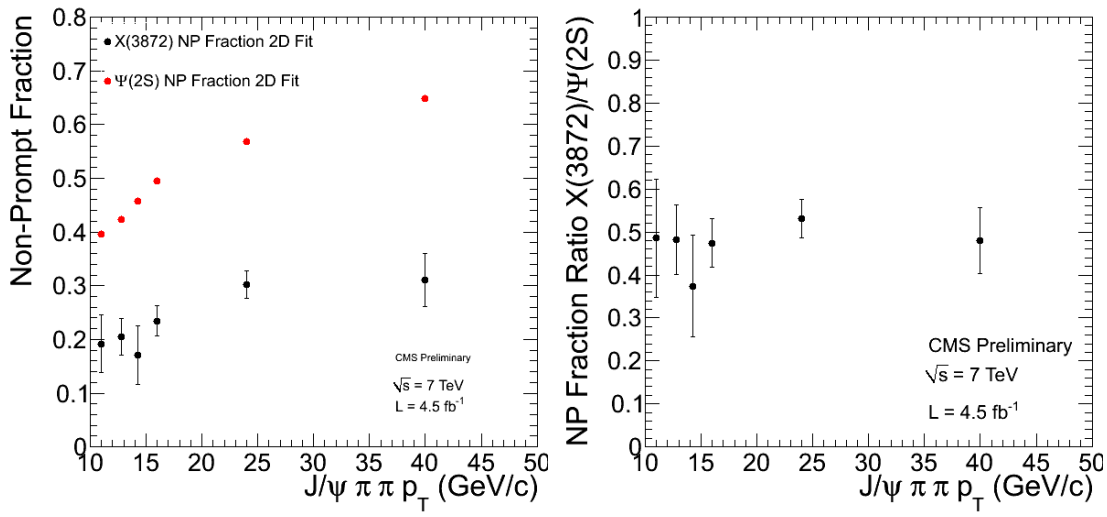

Figure 6.1: *$X(3872)$ and $\psi(2S)$ non-prompt component as a function of the particle p_T (left) and the ratio of this fraction between the two states (right)*

6.1.1 Cross-checks on non-prompt fractions extraction

Due to the harsh environment for $X(3872)$ non-prompt fraction extraction related to the high background, an alternative approach is also used as a cross-check. A B-enriched sample is obtained with a further selection based on the pseudo proper decay length in the transverse plane, requiring it to be $> 100\mu m$. Due to the lack of statistics, the fit for the extraction of the X(3872) yield in this sample is done keeping the same parameters for the signal function obtained from fit of the complete sample in the same p_T region.

The ratio of the fitted signal yields in the B-enriched sample ($N_{c\tau>100\mu m}$) and in the whole sample (N_{all}) are corrected to:

$$fraction_{NP} \sim \frac{N_{c\tau>100\mu m}}{N_{all}} \cdot \frac{1}{\epsilon^{NP}(c\tau > 100\mu m) - \epsilon^{P}(c\tau > 100\mu m)} \tag{6.14}$$

taking into account the efficiencies of the $c\tau > 100\mu m$ selection criteria estimated from prompt and non-prompt MC simulation and summarized in Table 6.3. The corrected non prompt fraction of the $X(3872)$ and $\psi(2S)$ are reported in Table 6.4, and the comparison with the 2D fit resuls are shown in Fig. 6.4.

	$\epsilon^{NP}(c\tau > 100\mu m)$	$\epsilon^{P}(c\tau > 100\mu m)$
$X(3872)$	79 %	0.1 %
$\psi(2S)$	78 %	0.06%

Table 6.3: *Efficiencies of the $c\tau > 100\mu m$ cut estimated from prompt and non-prompt simulation.*

Additionally the non-prompt component of the $\psi(2S)$ has been extracted in the same kinematic region and with the same binning of [50] using both methods.The comparison between the two measurements is shown in Fig. 6.5 and the results are compatible within the statistical error.

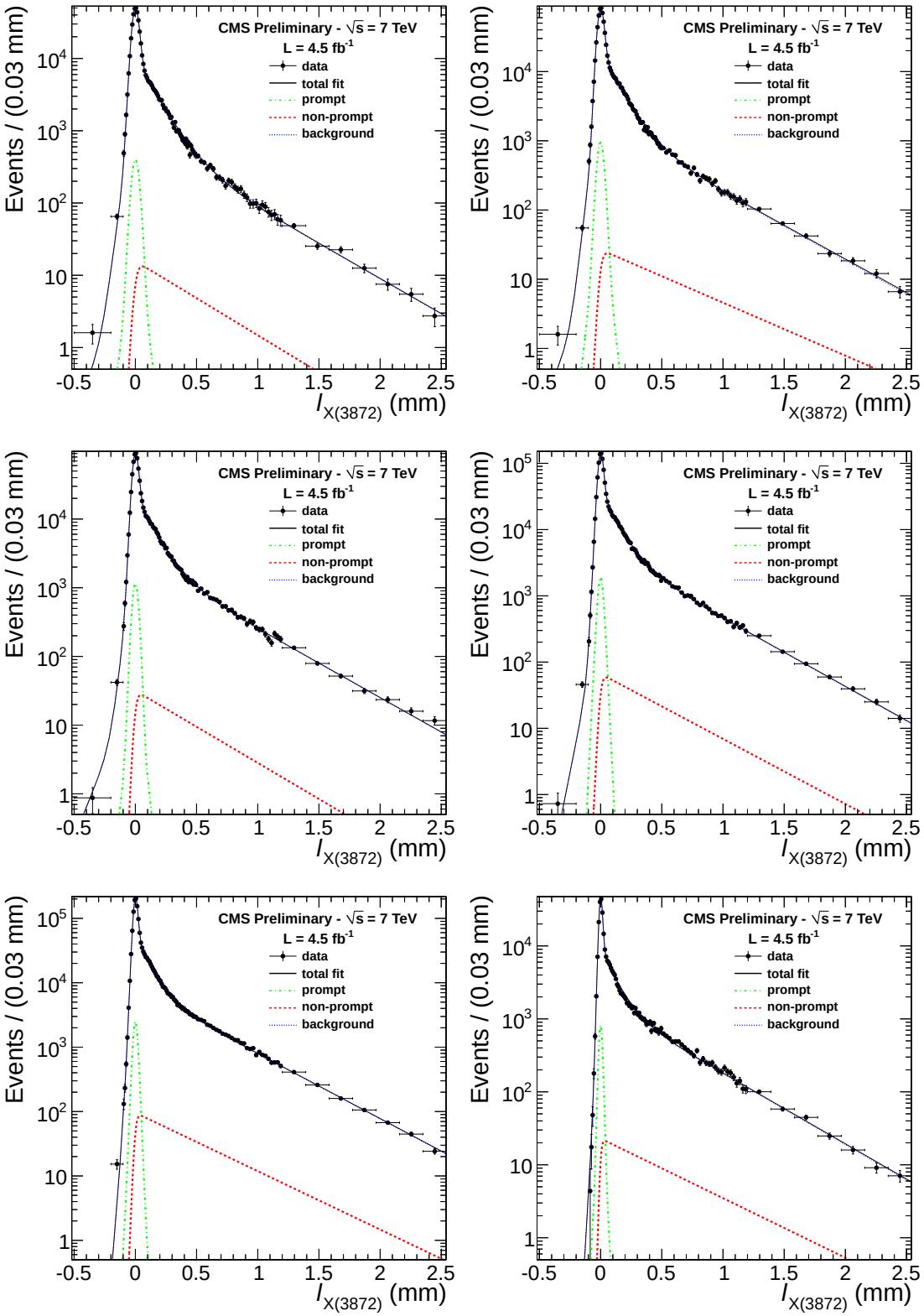

Figure 6.2: $X(3872)$ *non prompt component fit*

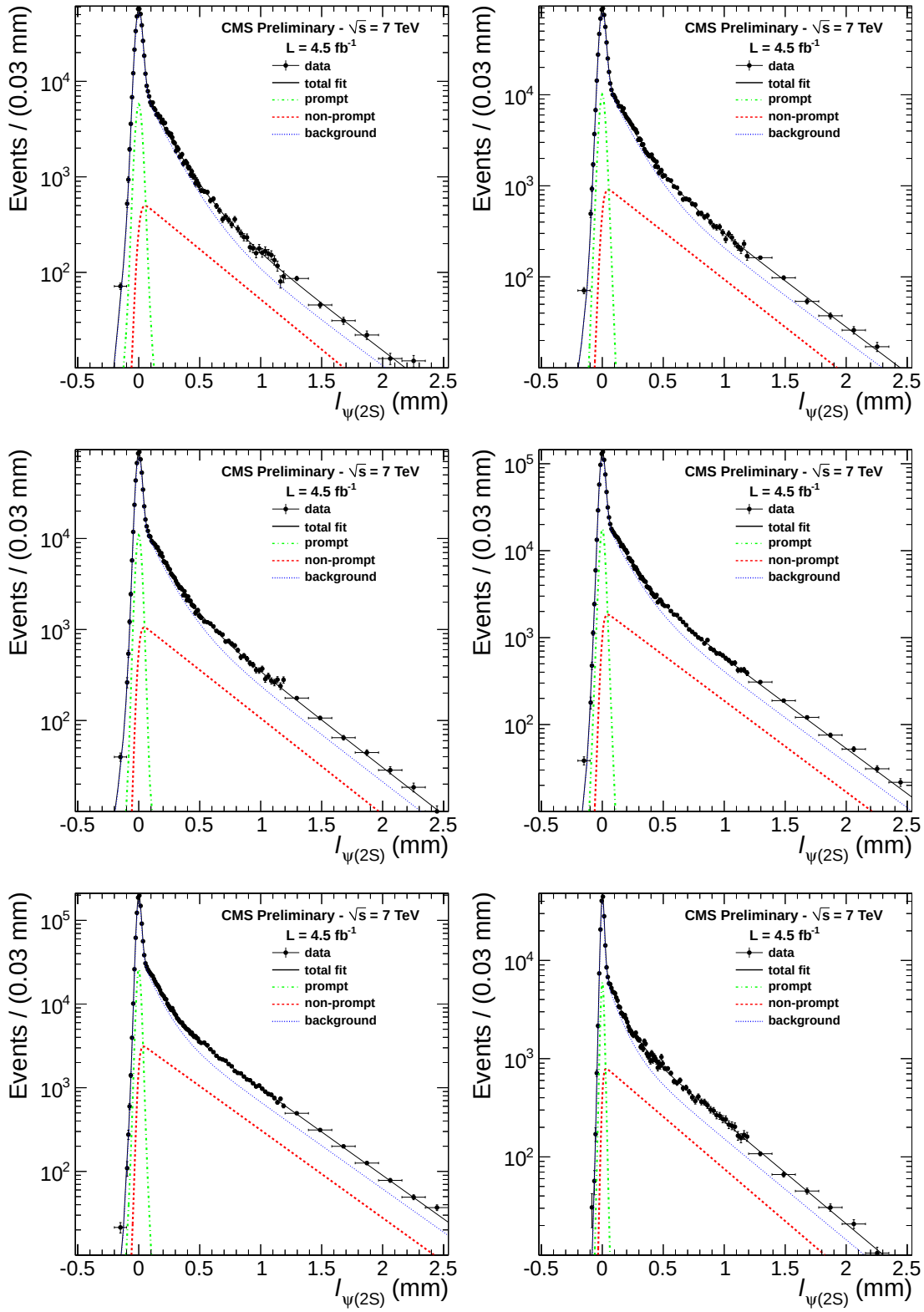

Figure 6.3: *$\psi(2S)$ non prompt component fit*

p_T range (GeV/c)	$f_B X(3872)$	$f_B \Psi(2S)$	$f_{BX(3872)}/f_{B\Psi(2S)}$
10-12	0.300 ± 0.084	0.389 ± 0.015	0.771 ± 0.218
12-13.5	0.237 ± 0.058	0.416 ± 0.013	0.571 ± 0.141
13.5-15	0.198 ± 0.052	0.449 ± 0.014	0.440 ± 0.117
15-18	0.241 ± 0.042	0.488 ± 0.012	0.493 ± 0.086
18-30	0.294 ± 0.041	0.567 ± 0.010	0.518 ± 0.074
30-50	0.345 ± 0.095	0.648 ± 0.025	0.532 ± 0.148

Table 6.4: *Non-prompt fraction results for the $X(3872)$ from the B-enriched sample with $c\tau > 100\mu m$.*

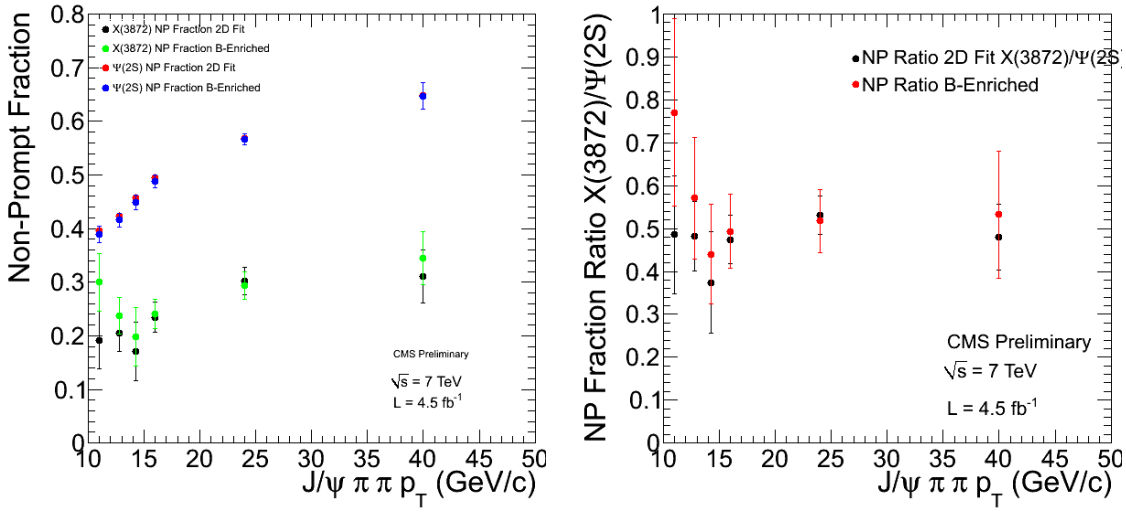

(a) (b)

Figure 6.4: *In (a) $X(3872)$ non-prompt component extracted with the 2D fit and from the B-enriched sample, in (b) the ratio of the b-fractions between $X(3872)$ and $\psi(2S)$*

p_T range (GeV/c)	10-12	12-13.5	13.5-15	15-18	18-30	30-50
Differemce %	2.0 ± 2.4	3.2 ± 2.0	2.1 ± 1.9	0.3 ± 1.5	1.7 ± 1.4	7.4 ± 4.7

Table 6.5: *Difference (%) in prompt and non-prompt efficiencies from $X(3872)$ simulation.*

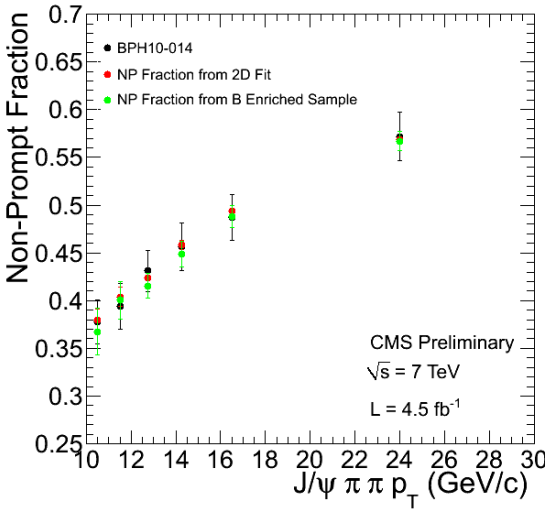

Figure 6.5: *$\psi(2S)$ non-prompt component in comparison with the public CMS result [50]*

6.1.2 Systematic uncertainties on non-prompt fractions

Several sources of systematic uncertainty have been evaluated and are the following:

- *Resolution model.* The pseudo-proper decay length per event resolution is modelled by a double Gaussian. The difference using a Single Gaussian model is taken as a systematic uncertainty.

- *Background Fit.* The systematic uncertainty related to the background is evaluated changing the size of the sidebands regions. Instead of using the bands defined in Table 6.1, the entire region of mass outside the signal peak is used.

- *Different prompt and non-prompt efficiency.* Possible difference between prompt and non-prompt efficiency can affect the measurement of the non-prompt fraction. The full difference between prompt and non-prompt efficiency estimated from simulation is taken as a systematic uncertainty, although limited by statistics (Table 6.5).

- *Extraction method.* The alternative non-prompt fraction extraction based on the B-enriched method (Section 6.1.1) is used to asses possible systematic uncertainty related to the 2D fit method. The effect is evaluated for the $\psi(2S)$ where statistic uncertainty is small.

- *Vertex assignment.* The primary vertex is chosen as the one with smaller longitudinal impact parameter for the $X(3872)$ candidate instead of the one closest in z to the 4-tracks vertex. The difference between the fitted B-fractions is taken as systematic uncertainty.

- *Estimate of possible effect of the pile-up.* Variation of the non-prompt fraction as a function of the number of the primary vertexes in the event are taken as a systematic uncertainty. The slight increase of non-prompt fraction as a function of primary vertexes is shown in Fig. 6.6 for the $\psi(2S)$. The bulk of the events has an average number of seven primary vertexes. Half of the difference between

events with less than four vertexes and events with 10 to 15 vertexes is taken as a systematic uncertainty, accounting for 2%.

The summary of all systematic uncertainties for the non-prompt fraction is given in Table 6.6.

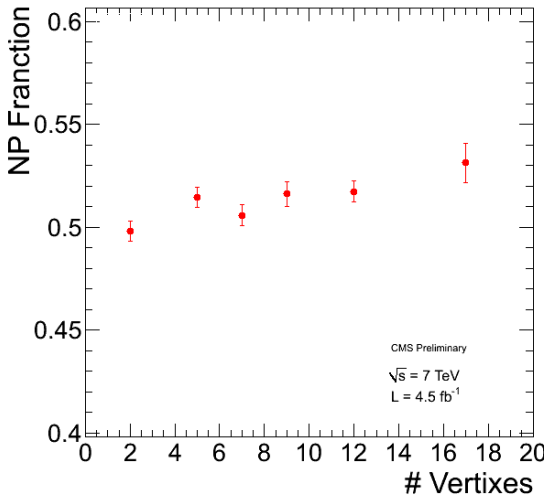

Figure 6.6: *$\psi(2S)$ non-prompt component as a function of the number of vertexes in the event*

Relative uncertainty (%)						
p_T range (GeV/c)	10-12	12-13.5	13.5-15	15-18	18-30	30-50
Background fit	3.9	6.1	5.5	0.5	0.1	3.8
Resolution Model	4.5	1.6	2.3	1.9	2.1	1.0
Efficiency P,NP	2.	3.2	2.1	0.3	1.7	7.4
2D/B-enriched	1.6	1.9	2.0	1.3	0.3	0.2
Vertex estimation	1.6	1.2	1.9	2.3	0.7	0.2
PileUp	2	2	2	2	2	2
Total Systematic	6.9	7.7	7.2	3.8	3.5	8.6

Table 6.6: *Summary of the relative systematic uncertainties (%) on $X(3872)$ non-prompt fraction.*

6.2 Final Result

Taking into account the systematic uncertainties studies reported in Section 6.1.2, the measurement of the X(3872) non-prompt fraction as a function of transverse momentum result as in Fig. 6.7.

We can compare our result of the $X(3872)$ with the results for $\psi(2S)$ and J/ψ from another CMS publication [44]. In Fig 6.8 the trend for the b-fraction of $\psi(2S)$ and J/ψ are showed in the barrel rapidity region. As for the $X(3872)$ the b-fraction increase with the p_T, even if the values are sensibly higher than the $X(3872)$. In Table 6.7 the values of the B-fraction for extracted from the $\psi(2S)$ from its decay in a pair of muon are reported,

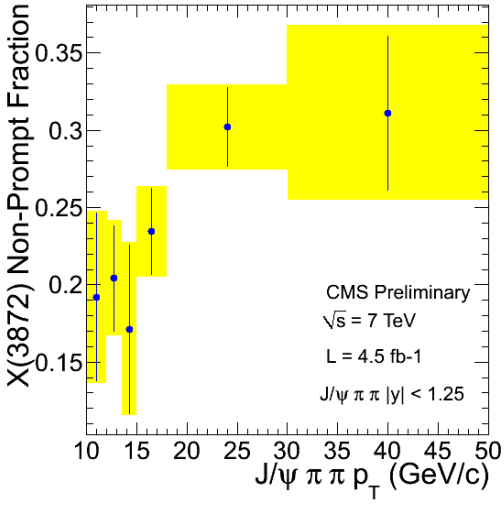

Figure 6.7: *Fitted $X(3872)$ non-prompt fraction as a function of p_T. The error bars represent the statistical uncertainties only. The coloured area are the quadratic sum of statistical and systematic uncertainties.*

with also the ratio w.r.t. the J/ψ . It can be see that the ratio tends to unity as hight p_T for these two quarkonium states. That's not true for the ratio of the b-fractions between X(3872) and $\psi(2S)$, has be seen in Fig 6.4(b), that remains stable to 0.5 at the increase of the p_T.

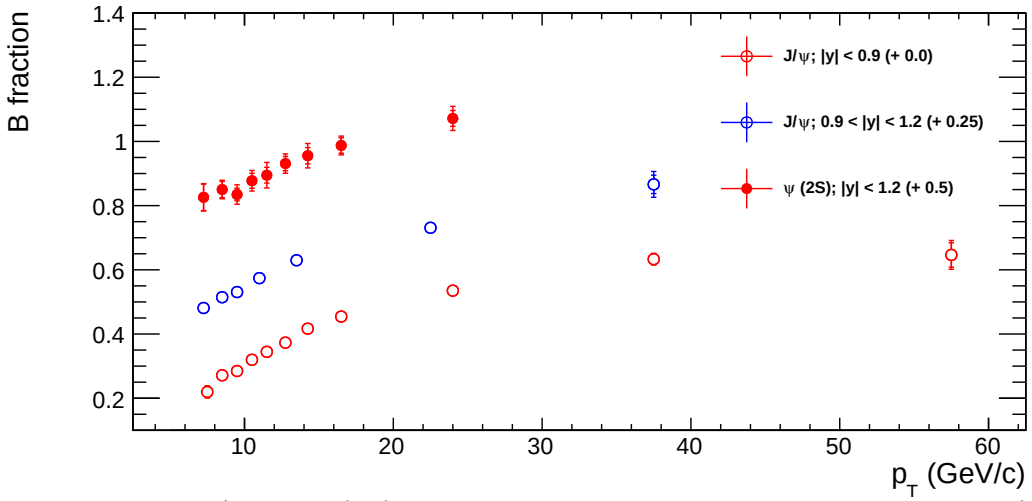

Figure 6.8: *Fitted J/ψ and $\psi(2S)$ b-fractions plotted as a function of p_T for $0 < |y| < 1.2$. Constant factors reported in the legend are added for plotting clarity.*

Finally we have seen in Section 1.3.2 that from NRQCD calculation for the molecular hypothesis for the $X(3872)$ the fraction of events from b-hadron decay was predicted to increase from 10% at $p_T = 5\ GeV/c$ to 35% at $p_T = 50GeV$. The value predicted for $p_T = 50GeV$ is perfectly compatible with the value extracted for the higher p_T of this analysis.

$\|y\|$	p_T (GeV/c)	$f_B(J/\psi)$
$0.0 - 0.9$	$7.0 - 8.0$	$0.220 \pm 0.016 \pm 0.011$
	$8.0 - 9.0$	$0.271 \pm 0.006 \pm 0.003$
	$9.0 - 10.0$	$0.285 \pm 0.005 \pm 0.004$
	$10.0 - 11.0$	$0.320 \pm 0.005 \pm 0.004$
	$11.0 - 12.0$	$0.345 \pm 0.005 \pm 0.007$
	$12.0 - 13.5$	$0.373 \pm 0.005 \pm 0.003$
	$13.5 - 15.0$	$0.417 \pm 0.006 \pm 0.005$
	$15.0 - 18.0$	$0.454 \pm 0.006 \pm 0.004$
	$18.0 - 30.0$	$0.535 \pm 0.006 \pm 0.004$
	$30.0 - 45.0$	$0.633 \pm 0.015 \pm 0.010$
	$45.0 - 70.0$	$0.646 \pm 0.038 \pm 0.024$

Table 6.7: *Fit results for the determination of the fraction of J/ψ from b-hadrons in p_T and $|y|$ bins. The b-fraction column shows the statistical and systematic errors*

Summary

In this thesis are reported the results on the studies performed on the $X(3872)$ state with the CMS experiment in its first two years of operations. These studies have been primary focalized to give a detailed description of the production of the $X(3872)$ in pp collision at $\sqrt{s} = 7$ TeV. Two different data samples have been used.

The first one covers the data collected by the CMS experiment during 2010, and corresponds to an integrated luminosity of 40 nb^{-1}. This sample have been collected taking advantage of the whole acceptance region of the detector, and about 500 $X(3872)$ have been reconstructed in the kinematic region $p_T > 8$ GeV/c and $|y| < 2.2$. With this sample the ratio

$$R = \frac{\sigma(pp \to X(3872) + \text{anything}) \times \mathcal{B}(X(3872) \to J/\psi\pi^+\pi^-)}{\sigma(pp \to \psi(2S) + \text{anything}) \times \mathcal{B}(\psi(2S) \to J/\psi\pi^+\pi^-)} \tag{6.15}$$

have been calculated obtaining

$$R = 0.087 \pm 0.017(stat.) \pm 0.009(syst.) \tag{6.16}$$

The second sample used covers the data collected by CMS during 2011, corresponding to $4.5 fb^{-1}$ of integrated luminosity. Due to the different trigger condition it has been possible to reconstruct the candidates only in the kinematic region $p_T > 10$ GeV/c and $|y| < 1.25$. The results of two measurements on this sample have been presented in this thesis: the cross section ratio R and the non-prompt component of the $X(3872)$, both as a function of p_T.

In the ratio of the differential cross section no particular feature has been found for the $X(3872)$ with respect to the other charmonium states, within the experimental error. For what regards the non-prompt fraction, it seems to scale with p_T with a similar shape to standard charmonium, and its ratio with respect to the $\psi(2S)$ one remains stable at about 0.5.

Starting from the results shown in this analysis, there are interesting prospectives for new results on the $X(3872)$ from the CMS experiment in the near future. The large sample collected will permit to perform a precise measurement of the mass and angular study will try to solve the remaining doubts on the $X(3872)$ quantum numbers.

Acknowledgements

I would like to thank all the fantastic people I worked with in these year in the CMS Collaboration. First of all Marina Giunta, who have pointed me to the right direction both for the data analysis and for the technical activities on the detector, and Alessandra Fanfani for all the work done together on the $X(3872)$ and for the sleepless night spent to keep up to the deadlines.

I would also like to thank all the people who have collaborated on the $X(3872)$ analysis, in particular A. Meyer, F. Palla, X. Wang, J. Wang and M. Dall'Osso for their contributions towards the final result. Then I would also like to mention all the people of the CMS Quarkonia Working Group for their advices and support, in particular H. Woehri, R. Covarelli, C. Lourenco and L. Martini.

For his unceasing work for the Drift Tube detector and all the help and life lessons given, I would like also to thank Alberto Benvenuti, who is an example for every physicist. And with him I would like to thank all the people I've worked with for the operation of the detector.

I would also thanks all the friends I've made during this years spent in Geneva, without who my life would have been very boring.

And finally I would like to thanks my family, and in particular my mother, becouse without her I wouldn't have finished this thesis on schedule!

Bibliography

[1] http://mathworld.wolfram.com/chebyshevpolynomialofthefirstkind.html.

[2] *QCD and Collider Physics*. Cambridge Monographs.

[3] The lifetime distribution of $X(3872)$ Mesons Produced in $p\bar{p}$ Collisions at CDF.

[4] *LEP design report*. CERN, Geneva, 1984. Copies shelved as reports in LEP, PS and SPS libraries.

[5] *Erratum-ibid. B*, 325:537–538, 1994.

[6] Measurement of Tracking Efficiency. *CMS PAS*, TRK-10-002, 2010.

[7] Inelastic *pp* cross section at 7 tev. 2011.

[8] J/psi and psi(2S) production in pp collisions at sqrt(s) = 7 TeV. 2011.

[9] R. Aaij et al. Observation of X(3872) production in pp collisions at sqrt(s)= 7 TeV. 2011.

[10] T. Aaltonen et al. Precision Measurement of the X(3872) Mass in $J/\psi\pi^+\pi^-$ Decays. *Phys. Rev. Lett.*, 103:152001, 2009.

[11] V. M. Abazov et al. Observation and properties of the $X(3872)$ decaying to $J/\psi\pi^+\pi^-$ in $p\bar{p}$ collisions at $\sqrt{s} = 1.96TeV$. *Phys. Rev. Lett.*, 93:162002, 2004.

[12] K. Abe et al. Properties of the X(3872) at Belle. 2004.

[13] A. Abulencia et al. Measurement of the dipion mass spectrum in $X(3872) \to J/\psi\pi^+\pi^-$ decays. *Phys.Rev.Lett.*, 96:102002, 2006.

[14] A. Abulencia et al. Analysis of the quantum numbers J(PC) of the X(3872). *Phys. Rev. Lett.*, 98:132002, 2007.

[15] Andrea Achilli et al. Total and inelastic cross-sections at LHC at CM energy of 7 TeV and beyond. 2011.

[16] D. Acosta et al. Measurement of the J/ψ meson and $b-$hadron production cross sections in $p\bar{p}$ collisions at $\sqrt{s} = 1960$ GeV. *Phys.Rev.*, D71:032001, 2005.

[17] Darin E. Acosta et al. Observation of the narrow state $X(3872) \to J/\psi\pi^+\pi^-$ in $\bar{p}p$ collisions at $\sqrt{s} = 1.96$ TeV. *Phys. Rev. Lett.*, 93:072001, 2004.

[18] I. Adachi et al. Study of the B to X(3872)(D*0 anti-D0) K decay. 2008.

[19] I. Adachi et al. Study of $X(3872)$ in B meson decays. 2008.

[20] W. Adam et al. Description and performance of the cms track and primary vertex reconstruction. CMS AN-11-172, 2011.

[21] S. Agostinelli et al. GEANT4: A simulation toolkit. *Nucl. Instrum. Meth.*, A506:250., 2003.

[22] John Allison et al. Geant4 developments and applications. *IEEE Trans. Nucl. Sci.*, 53:270, 2006.

[23] J. Alwall, P. Demin, S. de Visscher, R. Frederix, M. Herquet, F. Maltoni, T. Plehn, D. L. Rainwater, and T. Stelzer. Madgraph/madevent v4: the new web generation. *JHEP*, 09:028, 2007.

[24] C. Amsler et al. Review of particle physics. *Phys. Lett.*, B667:1, 2008.

[25] Pierre Artoisenet and Eric Braaten. Production of the X(3872) at the Tevatron and the LHC. *Phys. Rev.*, D81:114018, 2010.

[26] Bernard Aubert et al. A Study of $B \to X(3872)K$, with $X_{3872} \to J/\Psi\pi^+\pi^-$. *Phys. Rev.*, D77:111101, 2008.

[27] Bernard Aubert et al. Study of Resonances in Exclusive B Decays to anti-D(*) D(*) K. *Phys.Rev.*, D77:011102, 2008.

[28] Bernard Aubert et al. Evidence for $X(3872) \to \psi_{2S}\gamma$ in $B^\pm \to X_{3872}K^\pm$ decays, and a study of $B \to c\bar{c}\gamma K$. *Phys.Rev.Lett.*, 102:132001, 2009.

[29] E. Barberio, B. van Eijk, and Z. Was. Photos a universal montecarlo for qed radiative corrections in decays. *Comput. Phys. Commun.*, 66:115, 1991.

[30] M. Bargiotti and V. Vagnoni. *LHCb-2007-042*, 2007.

[31] Eric Braaten and James Stapleton. Analysis of $J/psipi^+pi^-$ and D0 anti-D0 pi0 Decays of the X(3872). *Phys.Rev.*, D81:014019, 2010.

[32] N. Brambilla et al. Heavy quarkonium: progress, puzzles, and opportunities. 2010.

[33] R Brunelire. Cms electromagnetic calorimeter performance and test beam results. *Nucl. Instrum. Methods Phys. Res., A*, 572(1):33–35, 2007.

[34] CERN. Lhc design report. Technical report, 2004.

[35] Serguei et al Chatrchyan. Performance of CMS Muon Reconstruction in Cosmic-Ray Events. *JINST*, 5:T03022, 2010.

[36] Ludmila Cherkasova, Diwaker Gupta, Eygene Ryabinkin, Roman Kurakin, Vladimir Dobretsov, and Amin Vahdat. Optimizing Grid Site Manager Performance with Virtual Machines. In *Proceedings of the 3rd USENIX Workshop on Real Large Distributed Systems*, December 2006.

[37] S. K. Choi et al. Observation of a new narrow charmonium state in exclusive $B^{\pm} \to K^{\pm}\pi^{+}\pi^{-}J/\psi$ decays. *Phys. Rev. Lett.*, 91:262001, 2003.

[38] S.-K. Choi, S.L. Olsen, K. Trabelsi, I. Adachi, H. Aihara, et al. Bounds on the width, mass difference and other properties of X(3872) $\to$ *pi*$^{+}$*pi*$^{-}$*J/psi* decays. *Phys.Rev.*, D84:052004, 2011.

[39] CMS Collaboration. Cms physics tdr: Volume 1, detector performance and software. *CERN/LHCC 2006-001*, 2006.

[40] CMS Collaboration. The CMS experiment at the CERN LHC. *JINST*, 0803:S08004, 2008.

[41] UK. Cobham, Vector Fields Ltd.

[42] CMS collaboration. Cms analysis note, an-10-083.

[43] CMS Collaboration. The cms software framework cmssw.

[44] CMS Collaboration. j/ψ and $\psi(2s)$ production in pp collisions at $\sqrt{s}$=7 tev. *CMS Physics Analysis Summary*, CMS-BPH-10-014, CERN-PH-EP-2011-177, 2010.

[45] The CMS collaboration. Cms analysis note, an-10-453.

[46] The CMS collaboration. Cms analysis note, an-11-417.

[47] The CMS Collaboration. "the muon project: Technical design report". *CERN/LHCC 97-32*, 1997.

[48] The CMS Collaboration. The tridas project technical design report, vol- ume 1: The trigger systems. *CERN/LHCC 2000-038*, CMS TDR 6.1, 2000.

[49] The CMS Collaboration. The tridas project technical design report, vol- ume 2: Data acquisition and high-level trigger. *CERN/LHCC 2002- 26*, CMS TDR 6.2, 2002.

[50] The CMS collaboration. J/psi and psi (2s) production in pp collisions at sqrt (s)= 7 tev. 2011.

[51] Susanna Cucciarelli, Marcin Konecki, Danek Kotlinski, and Teddy Todorov. Track reconstruction, primary vertex finding and seed generation with the pixel detector. Technical Report CMS-NOTE-2006-026. CERN-CMS-NOTE-2006-026, CERN, Geneva, Jan 2006.

[52] P. del Amo Sanchez et al. Evidence for the decay X(3872) $\to$ J/ psi omega. *Phys.Rev.*, D82:011101, 2010.

[53] S. Dobbs et al. Search for X(3872) in gamma gamma fusion and ISR at CLEO. *Phys.Rev.Lett.*, 94:032004, 2005.

[54] Aaron Dominguez. The cms pixel detector. Technical Report CMS-CR-2009-142. CERN-CMS-CR-2009-142, CERN, Geneva, Jun 2009.

[55] N. Drenska, R. Faccini, F. Piccinini, A. Polosa, F. Renga, et al. New Hadronic Spectroscopy. *Riv.Nuovo Cim.*, 033:633–712, 2010.

[56] S. Dubynskiy, A. Gorsky, and M.B. Voloshin. Holographic Hadro-Quarkonium. *Phys.Lett.*, B671:82–86, 2009.

[57] S. Dubynskiy and M.B. Voloshin. Hadro-Charmonium. *Phys.Lett.*, B666:344–346, 2008.

[58] W. Erdmann. Offline Primary Vertex Reconstruction with Deterministic Annealing Clustering. *CMS Analysis Note*, 2011/014, 2011.

[59] D. Buskulic et al. Measurement of the $\bar{B}^0$ and B^- meson lifetimes. *Phys. Lett. B*, 307:194–208, 1993.

[60] Eck et Al. *LHC computing Grid: Technical Design Report. Version 1.06 (20 Jun 2005).* Technical Design Report LCG. CERN, Geneva, 2005.

[61] N. Adam et al. Generic tag and probe tool for measuring efficiency at cms with early data. *CMS Analysis Note*, (111), June 2009.

[62] S. Chatrchyan et al. "performance of the cms chatode strip chambers with cosmic rays". *JINST*, 5:T03018, 2010.

[63] S. Chatrchyan et al. "performance of the cms drift tube chambers with cosmic rays". *JINST*, 5:T03015, 2010.

[64] S. Chatrchyan et al. "performance study of the cms barrel resistive plate chambers with cosmic rays". *JINST*, 5:T03017, 2010.

[65] J. J. Aubert et al. [E598 Collaboration]. *Phys. Rev. Lett. 33*, 1974.

[66] K. Nakamura et al. (Particle Data Group). 2011 review of particle physics. *Journal of Physics G37, 075021*, 2010.

[67] S. Eidelman et al. [Particle Data Group]. *Phys. Lett. B 592 1*, 2004.

[68] J. E. Augustin et al. [SLAC-SP-017 Collaboration]. *Phys. Rev. Lett. 33*, 1974.

[69] R. Fruhwirth. Application of Kalman filtering to track and vertex fitting. *Nucl.Instrum.Meth.*, A262:444–450, 1987.

[70] R Fruhwirth, Wolfgang Waltenberger, and Pascal Vanlaer. Adaptive vertex fitting. *CMS NOTE*, 2007/008, 2007.

[71] Iliopoulos J. Glashow S. L. and Maiani L. *Phys. Rev. D, 2*, 1970.

[72] G. Gokhroo et al. Observation of a near-threshold $D^0\overline{D^0}\pi^0$ enhancement in $B \to D^0\overline{D^0}\pi^0 K$ decay. *Phys. Rev. Lett.*, 97:162002, 2006.

[73] Rose K. Deterministic Annealing for Clustering, Compression, Classification, Regression and related Optimisation Problems. *Proceedings of the IEEE*, Vol. 86, Issue 11, 1998.

[74] M. Krämer. *Prog. Part. Nucl. Phys.*, 47:141, 2001.

[75] D.J. Lange. The `evtgen` particle decay simulation package. *Nucl. Instrum. Meth.*, A462:152–155, 2001.

[76] Ting Miao, N Leioatts, Hans Wenzel, and Francisco Yumiceva. Beam position determination using tracks. *CMS NOTE*, 2007/021, 2007.

[77] Colin Morningstar and Mike J. Peardon. Glueballs from improved lattice actions. 1996.

[78] K. Nakamura et al. Psi(2s) publication. *J. Phys. G*, 37:075021, 2010.

[79] M. Pioppi. Iterative Tracking. *CMS Internal Note*, 2007/065, 2008.

[80] J. Pumplin et al. New generation of parton distributions with uncertainties from global QCD analysis. *JHEP*, 07:012, 2002.

[81] S. Frixione, P. Nason, and C. Oleari. Matching nlo qcd computations with parton shower simulations: the powheg method. 2007.

[82] Thomas Speer, Kirill Prokofiev, R Fruhwirth, Wolfgang Waltenberger, and Pascal Vanlaer. Vertex fitting in the cms tracker. *CMS NOTE*, 2006/032, 2006.

[83] Daniele Trocino. *Muon Reconstruction and Momentum Scale Calibration and Their Application to Standard Model Higgs Searches with the CMS Experiment*. PhD thesis, Università degli Studi di Torino, 2010.

[84] T. T.Sjoestrand, S. Mrenna, and P.Z. Skands. Pythia 6.4 physics and manual. *JHEP*, 05:026, 2006.

[85] Wouter Verkerke and David P. Kirkby. The RooFit toolkit for data modeling. *eConf*, C0303241:MOLT007, 2003.

[86] Jingzhi Zhang. Charmonium spectroscopy and decays. 2011.

[87] Nicolas Zwahlen. Study of the B rightarrow X(3872) K $\rightarrow$ D*0 anti-D0 K decay at Belle. 2008.